TECHNICAL UNIVERSITY OF CRETE
SCHOOL OF PRODUCTION ENGINEERING & MANAGEMENT
TURBOMACHINES & FLUID DYNAMICS LABORATORY

On the Numerical Solution of High Mach number Flows

By

Angelos Klothakis

A dissertation submitted in partial fulfilment of the requirements for the degree of

Doctor of Philosophy (PhD)

Supervisor: Dr. Ioannis K. Nikolos, Professor

ΕΠΤΑΜΕΛΗΣ ΕΞΕΤΑΣΤΙΚΗ ΕΠΙΤΡΟΠΗ

Τίτλος (ελληνικά/αγγλικά): Αριθμητική επίλυση ροών υψηλού αριθμού Mach / On the numerical solution of high Mach number flows.

ΔΙΔΑΚΤΟΡΙΚΗ ΔΙΑΤΡΙΒΗ

Άγγελος Κλωθάκης

ΤΡΙΜΕΛΗΣ ΣΥΜΒΟΥΛΕΥΤΙΚΗ ΕΠΙΤΡΟΠΗ:

1. **Ιωάννης Κ. Νικολός,** Καθηγητής Σχολής Μ.Π.Δ., Πολυτεχνείου Κρήτης.
2. **Ανάργυρος Ι. Δελής,** Καθηγητής Σχολής Μ.Π.Δ., Πολυτεχνείου Κρήτης.
3. **Michael Gallis (Μιχαήλ Γαλλής),** Researcher, Sandia National Laboratories, USA.

Εγκρίθηκε από την Επταμελή Εξεταστική Επιτροπή την 27-9-2024.

1. **Δρ. Ιωάννης Κ. Νικολός, Καθηγητής Σχολής Μ.Π.Δ., Πολυτεχνείο Κρήτης (Επιβλέπων).** **(υπογραφή)** Ioannis Nikolos Digitally signed by Ioannis Nikolos Date: 2024.09.28 08:28:44 +03'00'

2. **Δρ. Ανάργυρος Ι. Δελής, Καθηγητής Σχολής Μ.Π.Δ., Πολυτεχνείου Κρήτης (Μέλος Τριμελούς Συμβουλευτικής Επιτροπής).** Anargiros Delis Digitally signed by Anargiros Delis Date: 2024.09.29 22:12:30 +03'00'

3. **Dr. Michael Gallis (Μιχαήλ Γαλλής), Researcher, Sandia National Laboratories, USA (Μέλος Τριμελούς Συμβουλευτικής Επιτροπής).** Gallis 1/10/2024

4. **Dr. Vassilis Theofilis (Βασίλης Θεοφίλης), Professor, Department of Aerospace Engineering, Technion - Israel Institute of Technology, Israel.** Vassilis Theofilis

5. **Δρ. Γεώργιος Καρατζάς, Καθηγητής Σχολής Χημικών Μηχανικών & Μηχανικών Περιβάλλοντος, Πολ. Κρήτης** Digitally signed by Georgios Karatzas Date: 2024.09.29 22:36:35 +03'00'

6. **Δρ. Γεώργιος Αραμπατζής, Αν. Καθηγητής Σχολής Μ.Π.Δ. Πολ. Κρήτης.**

Georgios Arampatzis
Digitally signed by Georgios Arampatzis
Date: 2024.09.30 00:33:38 +03'00'

7. **Δρ. Δημήτριος Κουμπογιάννης, Αν. Καθηγητής Σχολής Μηχανικών, Τμ. Ναυπηγών Μηχανικών, ΠΑ.Δ.Α.**

Dimitrios Koumpogiannis
Digitally signed by Dimitrios Koumpogiannis
Date: 2024.09.30 13:15:34 +03'00'

To Vassoula and my family

“Intentionally left blank”

Abstract

In this study the simulation and analysis of rarefied hypersonic flows is outlined. The study is divided in two parts. The first part is devoted the enhancement of the in-house academic Computational Fluid Dynamics solver *Galatea* to encounter such simulations is reported in this study. In case of rarefied gas flows and particularly for fluids in slip flow regime (Knudsen number greater than 0.01) the no-slip condition on solid wall surfaces is no longer valid; hence, velocity slip conditions as well as temperature jump ones have to be included instead. Furthermore, to increase accuracy at that regime the second-order accurate spatial slip model of Beskok and Karniadakis has been incorporated, which avoids the numerical difficulties, entailed by the evaluation of the second derivative of slip velocity when complex geometries along with unstructured hybrid grids are encountered. Due to oscillations that might appear, especially during the initial steps of the iterative procedure, a normalization scheme is additionally employed, to allow for the gradual increase of the corresponding slip/jump values. *Galatea* is validated against a benchmark test case concerning rarefied laminar flow (inside the slip flow regime) over a wing with a NACA0012 airfoil in different angles of attack. The obtained results were compared with those of obtained by the parallel open-source DSMC code SPARTA. According to this last approach, the flow domain is divided into a finite number of computational cells, while the required sample macroscopic flow properties are retrieved assuming intermolecular collisions of the simulated particles inside such cells. An excellent agreement was achieved between the results obtained by *Galatea* and SPARTA as well. In the second part base flows produced by the DSMC method are extensively analyzed by linear stability theory in order to recover underlying flow transition mechanisms and flow modes. It was found that in cases where oscillations where imposed or physically generated in the boundary layer, the characteristics of these oscillations are predicted accurately by linear stability analysis. Most interestingly, in one specific case, the effect of the generated perturbation is felt well outside of the boundary layer, generating oscillations of the leading-edge shock that synchronize with linear perturbations inside the boundary layer. Finally, the design methodology, simulation and analysis of a hypersonic high-altitude waverider is presented.

Keywords: Hypersonic flows, Direct Simulation Monte Carlo, linear stability analysis theory, hypersonic vehicles design, rarefied flows, high Mach number flows, rarefied gas dynamics.

Περίληψη
(Extended Abstract in Greek)

Σκοπός της παρούσας διατριβής ήταν η προσομοίωση και ανάλυση ροών σε χαμηλή πίεση και υπερηχητική ταχύτητα. Οι συγκεκριμένες ροές παρατηρούνται γύρω από ιπτάμενα οχήματα στα άνω όρια της ατμόσφαιρας και σε οχήματα κατά τη διάρκεια της επανεισόδου στην ατμόσφαιρα. Η διατριβή είναι χωρισμένη σε δυο μέρη.

Πιο συγκεκριμένα στο πρώτο μέρος, παρουσιάζεται η τροποποίηση του ακαδημαϊκού κώδικα *Γαλάτεια* με την ενσωμάτωση των οριακών συνθηκών για τον υπολογισμό της ταχύτητας ολίσθησης (velocity slip) και θερμοκρασιακού άλματος (temperature jump) σε επιφάνειες που βρίσκονται εντός υπερηχητικών ροών χαμηλής πίεσης. Ο κώδικας *Γαλάτεια* χρησιμοποιεί τις εξισώσεις Navier-Stokes για τη μοντελοποίηση της ροής. Η διακριτοποίηση των εξισώσεων εγινε με χρήση της κεντροκομβικής μεθόδου πεπερασμένων όγκων (Finite Volume Method) επί υβριδικών μη-δομημένων υπολογιστικών πλεγμάτων. Για τον υπολογισμό των μη-συνεκτικών διανυσμάτων ροής εφαρμόστηκε ο προσεγγιστικός επιλύτης του Roe, θεωρώντας ένα τοπικό μονοδιάστατο πρόβλημα Riemann στη διεπαφή γειτονικών όγκων ελέγχου. Αύξηση στην υπολογιστική ακρίβεια του προαναφερθέντος υπολογισμού επιτυγχάνεται με την εφαρμογή χωρικού σχήματος ακρίβειας δεύτερης τάξης βασισμένο στη τεχνική MUSCL (Monotonic Upwind Scheme for Conservation Laws). Το εν λόγω σχήμα συνδυάστηκε με δύο κατάλληλες συναρτήσεις περιορισμού (Van Albada – Van Leer ή Min-mod) οι οποίες χρησιμοποιήθηκαν για την διασφάλιση της μονοτονίας μεταξύ των τιμών των μεταβλητών σε γειτονικούς όγκους ελέγχου. Ο υπολογισμός των συνεκτικών διανυσμάτων της ροής απαιτεί τον πρώτερο υπολογισμό των παραγώγων των συνιστωσών της ταχύτητας και της θερμοκρασίας στη διεπαφή των όγκων ελέγχου, η οποία συμπίπτει με το μέσο της ακμής που συνδέει τους αντίστοιχους υπολογιστικούς κόμβους. Γι’αυτόν τον υπολογισμό χρησιμοποιήθηκε η μέθοδος του κομβικού μέσου όρου (nodal averaging) κατα την οποία οι παράγωγοι προκύπτουν από τις αντίστοιχες τιμές των παραγώγων των ακραίων κόμβων της υπο εξέταση ακμής. Ο υπολογισμός τόσο των μη-συνεκτικών όσο και των συνεκτικών διανυσμάτων ροής επιτυγχάνεται με σάρωση των ακμών του πλέγματος, χρησιμοποιώντας κατάλληλες δομές δεδομένων (edge-based data structures), που επιτρέπουν τη μείωση του υπολογιστικού χρόνου με σκοπό την επιτάχυνση της επίλυσης της ροής. Η ολοκλήρωση στο χρόνο καθώς κι η τελική κατάσταση της
ροής υπολογίζονται επαναληπτικά χρησιμοποιώντας τη μέθοδο Runge-Kutta τεσσάρων βημάτων (RK4) και δεύτερης τάξης χρονική ακρίβεια. Για την αύξηση

της ακρίβειας των οριακών συνθηκών ταχύτητας ολίσθησης και θερμοκρασιακού άλματος πάνω στα όρια επιφανειών που βρίσκονται μέσα στη ροή, χρησιμοποιηθήκε το δεύτερης τάξης ακρίβειας σχήμα των Beskok και Καρνιαδάκη. Το εν λόγω μοντέλο χρησιμοποιήθηκε διότι λόγω της ευκολίας εφαρμογής του σε μη δομημένα ή υβριδικά πλέγματα μπορεί να υπερκεράσει αριθμητικές δυσκολίες που προκύπτουν από τον υπολογισμό της δεύτερης παραγώγου της ταχύτητας ολίσθησης. Επιπλέον για τον περιορισμό των διακυμάνσεων κατα τα αρχικά βήματα της επαναληπτικής διαδικασίας που προκαλούνται λόγω του Dirichet τύπου των οριακών συνθηκών ολίσθησης/άλματος, χρησιμοποιήθηκε το σχήμα ομαλοποίησης των Ferras, Nobregal και Pinho που επιτρέπει τη σταδιακή αύξηση της ταχύτητας ολίσθησης και του θερμοκρασιακού άλματος.

Το δεύτερο μέρος της διατριβής παρουσιάζει τη χρήση της μεθόδου DSMC για την παραγωγή βασικών υπερηχητικών ροών γύρω από διάφορες γεωμετρίες με σκοπό την μαθηματική «γραμμική ανάλυση ευστάθειας» (Linear Stability Analysis) για την εύρεση των ιδιοτιμών και ιδιομορφών της ροής. Οι ιδιοτιμές της ροής προβλέπουν αν η ροή σε μεταγενέστερο χρόνο θα παραμείνει στρωτή ή αν υπάρχει κάποιος υποθάλπων φυσικός μηχανισμός που θα αναγκάσει τη ροή να γίνει τυρβώδης. Για την πιστοποίηση της ποιότητας της βασικής ροής γίνεται σύγκριση του οριακού στρώματος που υπολογίστηκε από τη μέθοδο DSMC με τις εξισώσεις αναλυτικού υπολογισμού του οριακού στρώματος. Από τις συγκρίσεις διαφαίνεται η αποτελεσματικότητα της μεθόδου για την παραγωγή βασικών ροών για γραμμική ανάλυση ευστάθειας, τόσο ως προς την ακρίβειά της όσο κι ως προς την αποδοτικότητας της. Λόγω του ότι η μέθοδος DSMC είναι μια στατιστική μέθοδος υπολογισμού της ροής, υπάρχει θόρυβος (noise) στα παραγώμενα αποτελέσματα. Ο θόρυβος αυτός προκαλεί μεγάλες αριθμητικές αποκλίσεις στη γραμμική ανάλυση ευστάθειας. Γι'αυτό, η παρούσα έρευνα καταδεικνύει τεχνικές με τις οποίες μπορεί να μειωθεί ο θόρυβος στα αποτελέσματα διατηρώντας παράλληλα αναλλοίωτες τις βασικές πληροφορίες της ροής. Επιπλέον συγκρίνονται κλασικές και προηγμένες τεχνικές μείωσης θορύβου και παρουσιάζεται ο αντίκτυπος που έχει κάθε τεχνική στα αποτελέσματα. Τέλος παρουσιάζονται επίσης διάφορες τεχνικές γραμμικής ανάλυσης ευστάθειας και γίνεται σύγκριση μεταξύ τους για την εύρεση και τεκμηρίωση τόσο ποσοτικών όσο και ποιοτικών διαφορών. Επιπρόσθετα, γίνονται προσομοιώσεις υπερηχητικών ροών με θερμοχημικές αντιδράσεις και γίνεται ανάλυση των διαταραχών που παρατηρούνται στη ροή. Επιπλέον γίνεται ανάλυση της μεθοδολογίας σχεδίασης και προσομοίωση ενός υπερηχητικού οχήματος για μεγάλο υψόμετρο. Πέραν από τη παρουσίαση των αποτελεσμάτων γίνεται και μελέτη της αεροδυναμικής ικανότητας του εν λόγω οχήματος για υπερηχητική πτήση σε περιβάλλον χαμηλής πίεσης.

Συνοψίζοντας όλα τα παραπάνω και λαμβάνοντας υπόψη παρόμοιες μελέτες διαθέσιμες στη βιβλιογραφία η συνεισφορά της παρούσας εργασίας συνοψίζεται στα ακόλουθα:

- Βελτίωση κι επέκταση των υπολογιστικών δυνατοτήτων του ακαδημαϊκού τριδιάστατου κώδικα *Γαλάτεια* με την υλοποίηση οριακών συνθηκών για την ολίσθηση της ροής πάνω σε επιφάνειες καθώς και τον υπολογισμό του θερμοκρασιακού άλματος σε συνθήκες χαμηλής πίεσης.

- Κατασκευή κατάλληλης μεθοδολογίας για τη χρήση βασικών ροών που έχουν παραχθεί με τη μέθοδο DSMC για «γραμμική ανάλυση αστάθειας» (linear stability analysis)

- Μελέτη και ανάλυση κατανομών ταχύτητας στο εσωτερικό κυμάτων κρούσης.

- Μελέτη αλληλεπίδρασης κρουστικών κυμάτων χωρίς/με θερμοχημικές αντιδράσεις.

- Μελέτη αλληλεπίδρασης κυλινδρικού στοιχείου τραχύτητας (roughness element) με υπερηχητική ροή πάνω σε επίπεδη πλάκα (flat plate).

- Εφαρμογή σε τρισδιάστατες υπερηχητικές ροές τεχνικών ανάλυσης ευστάθειας καθοδηγούμενων από δεδομένα που παρήχθησαν με τη μέθοδο DSMC.

- Σχεδιασμός αεροδυναμική ανάλυση και προσομοίωση ενός υπερηχητικού οχήματος για μεγάλο υψόμετρο.

Acknowledgements

I would like to express my deepest gratitude and appreciation to all those who have supported me throughout my PhD journey.

First and foremost, I am deeply grateful to my advisors Prof. Ioannis K. Nikolos, Dr. Michael A. Gallis, and Prof. Vassilis Theofilis for their unwavering guidance, expertise, and encouragement throughout my research journey. Their passion for fluid dynamics and their mentorship have been instrumental in shaping my academic and personal growth. I am truly fortunate to have had the opportunity to learn from their wealth of knowledge and experience. A special thanks goes to Prof. Deborah Levin and Prof. Helen Reed for all the thoughtful and insightful discussions.

I would also like to express my gratitude to Dr. Georgios N. Lygidakis for providing, running and supporting the *Galatea* code used in this research. His contributions have been essential in the successful completion of this work, and I am grateful for his assistance.

Furthermore, I am thankful to Mr. Kamil Dylewicz and Dr. Helio Jr. Quintanilha for their support in the LiGHT code and for providing the stability analyses results shown in this work. Their expertise and contributions have been invaluable in advancing this research and I am grateful for that. I am also thankful to Dr. Anton Burtsev for his valuable suggestions on how to effectively plot and visualize some results presented in this work. Special thanks also to Dr. Nicolas Cerulus, Dr. Saurabh S. Sawant and Dr. Madeline McMillan for their collaboration and discussions in the last stages of my PhD.

Last but certainly not least, I would like to express my deep gratitude to my wife, Dr. Vasiliki Chalkiadaki, who has been a pillar of support, understanding, and motivation throughout my PhD “mission”. Her encouragement, belief in my abilities, and sacrifices have been a driving force behind my achievements. I am also grateful to my mother, Despina Linaraki, my sister, Thomais Klothaki, and my father, George Klothakis (whom I wish were here), for their constant support and belief in my aspirations. Their presence and tireless support have been instrumental in my pursuit of academic excellence. This thesis is dedicated to all of them.

This work was funded by Office of Naval Research under grant no. N00014-1-20-2195 "Multi-scale modelling of unsteady shock-boundary layer hypersonic flow instabilities" (Dr. Eric Marineau, PO) and IAMD-COE grants under the project entitled “Overview of international hypersonic programs, and potential ways to exploit related physical phenomena to improve surveillance capabilities”. The research was conducted in this work with the computational resources provided by UKTC and EPSRC on the ARCHER2 supercomputing facility via project EP/X035484/1.

This work was also funded by contracts 22-10 - Study Report “Analysis of the related Physical Phenomena and Aerodynamic Performance of Hypersonic Vehicle(s) and possible ways of exploiting those data in order to improve Surveillance Capabilities” and 22-04 “Writing, delivering and publishing of review paper-report” between the IAMD COE and the Technical University of Crete-Special Account for Research Funding.

The computational time on ARCHER2 Supercomputing facility was provided via project EP/R029326/1.

“Intentionally left blank”

Contents

Abstract ..... **v**
Περίληψη ..... **vi**
Acknowledgements ..... **ix**
Nomenclature ..... **xv**
1. Introduction **1**
1.1 Objectives *1*
1.2 Literature review *2*
1.2.1 Fluid flow modeling using the Navier-Stokes equations *2*
1.2.2 Fluid flow modeling using the Direct Simulation Monte Carlo method *4*
1.3 Present study *9*
1.3.1 Overview *9*
1.3.2 Contributions *10*
1.3.3 Outline *11*
1.4 List of publications *11*
1.4.1 International Journals, with peer-review *11*
1.4.2 International Conference Proceedings, with peer-review *12*
1.4.3 International Conferences *12*
2. Fluid flow **14**
2.1 Statistical representation of gas flows *14*
2.1.1 Boltzmann equation *14*
2.1.2 The Direct Simulation Monte Carlo method *17*
2.1.3 Discretization in space and time *17*
2.1.4 Particle movement *18*
2.1.5 Boundary and surface interactions *19*
2.1.6 Collision mechanics *21*
2.1.7 Collision models *24*
2.1.8 Sampling of flow Macro-Properties *27*
2.2 The Navier-Stokes equations *28*
2.2.1 Governing equations *28*
2.2.2 Reynolds Averaged Navier-Stokes (RANS) equations *31*
2.2.3 Spatial Discretization *34*
2.2.4 Inviscid fluxes *36*
2.2.5 Viscous fluxes *37*
2.2.6 High-order schemes and slope limiters *38*

2.2.6 Boundary conditions *40*
2.2.7 Time integration *42*
2.3 Linear stability theory **45**
2.3.1 Equations of motion *45*
2.3.2 Linearized Navier-Stokes equations (LNSE) *46*
2.3.3 Data driven stability analysis – The residuals algorithm *49*
2.3.4 Data driven stability analysis – Dynamic mode decomposition *50*
2.4 Introduction to hypersonic and waverider vehicles design **52**
3. Numerical Results **59**
Definitions *59*
3.1 Rarefied flow over a NACA 0012 wing *61*
3.2 Rarefied gas flow over a re-entry space capsule geometry *67*
3.3 Slip effects and stability analysis of a DSMC generated supersonic boundary layer ... *75*
3.4 Hypersonic flow around a flat plate at range of $4.5 \leq M\infty \leq 9$ *85*
3.5 Investigation of the Instabilities of Hypersonic Flow over a Blunt Geometries *98*
3.6 Hypersonic flow over a complex suborbital vehicle *104*
3.7 Hypersonic flow over a complex suborbital vehicle with stability analysis *117*
3.8 Hypersonic flow over a flat plate with a roughness element *127*
3.9 Hypersonic flow over a cone with a swept fin *148*
3.10 Hypersonic flow over a Mach 7 waverider *157*
4. Conclusions **170**
4.1 Summary *170*
4.2 Contributions *173*
4.3 Future work *174*
5. References **177**

“Intentionally left blank”

Nomenclature

$\underline{\tilde{A}}$	Jacobian matrix
a	normalization coefficient
a_c	energy accommodation coefficient
a_n	surface normal accommodation coefficient
a_{rot}	rotational energy accommodation coefficient
a_t	tangential energy accommodation coefficient
a_{ref}	reference speed of sound
b	undisturbed particle trajectory
c	particle velocity
c_p	constant pressure specific heat
c_V	constant volume specific heat
c_1, c_2	viscosity coefficients
CFL	Courant-Friedrichts-Lewy number
C_L	coefficient of lift
C_P	coefficient of pressure
CD	coefficient of drag
d	particle diameter
E	total flow energy per unit mass
E_c	Eckert number
E_{in}	particle internal energy
E_t	particle translational energy
E_{tot}	total particle energy
e	flow energy per unit mass
erf	error function

$\dot{e}$	angle between refence plane and collision plane
$\vec{F}, \vec{G}, \vec{J}$	Navier-Stokes PDEs' vectors
F	Boltzmann equation force term
f	frequency
f_P	probability distribution function
g	generic function
$\vec{H}^{inv}$	inviscid fluxes vector evaluated at the middle of an edge
h	height
$\dot{h}$	enthalpy
h_t	specific total enthalpy
Kn	Knudsen number
k_B	Boltzmann's constant
ke	kinetic energy
L	length
L_x	periodicity length along streamwise direction
L_y	periodicity length along spanwise direction
$\mathcal{L}$	linear operator
M	Mach number
m	mass
$\dot{m}$	center of mass
N	particle probability
N_d	number density
$\dot{N}$	molecular flux
$\vec{n}$	surface normal unit vector
P	probability

Pr	Prandtl number
p	pressure
$\dot{p}_i$	momentum component
$\dot{Q}$	energy flux
Q_i	heat flux vector
q	general vector of flow quantities
$\overline{q}$	general vector of mean flow quantities
$\tilde{q}$	small perturbated vector
$\hat{q}$	amplitude function
$\dot{q}_i$	thermal tensor
R_{gas}	gas specific constant
Re	Reynolds number
$\dot{r}_i$	position coordinate
s	speed ratio
T	temperature
t	time
u, v, w	velocity components
$\widetilde{U}$	averaged Roe value of a primitive variable
U_s	slip velocity
U_w	wall velocity
V_i	volume of control volume of node i
$\overrightarrow{W}$	conservatives' variables vector
$\overrightarrow{W}_{PQ}^{L}, \overrightarrow{W}_{PQ}^{R}$	conservative variables vectors on the left and right side of an edge PQ
$\dot{x}$	particle deflection angle

$\boldsymbol{x}$	space vector coordinator

Greek symbols

α	wavenumber in the streamwise direction
$\dot{\beta}$	wavenumber in the spanwise direction
β	particle most probable velocity
γ	gas constant
Δt	timestep
δ	mean molecular spacing
δ_{ij}	Kronecker's delta
ε	infinitely small perturbation
η	self-similar variable, transformed wall normal direction
θ	angle between a particle and a surface
ϑ	scaled temperature variable
λ	mean free path
μ	viscosity
ξ	transformed streamwise direction
ρ	density
σ	collision cross section
σ_T	total collision section
σ_μ	viscosity cross section
σ_M	momentum transfer cross section
σ_t	tangential momentum accommodation cross section
σ_u	tangential velocity momentum accommodation coefficient
τ_{ij}	stress tensor
$\vec{\Phi}$	inviscid fluxes vector

Φ	limiter function
ϕ	tangential momentum flux accommodation coefficient
ω	complex eigenvalue
$\widehat{\omega}$	least stable eigenmode
$\overline{\omega}$	molecular viscosity exponent
Ω	solid angle

Subscripts and superscripts

$incident$	incident particle property
inv	inviscid variables vector
MCS	mean collision time
n	normal
$part$	particle
r	relative
ref	reference value
$reflected$	reflected particle property
rot	rotational
s	surface property
t	tangential
tr	translational
tot	total
vis	viscous variables vector
w	wall property
x, y, z	x, y, z coordinates values

“Intentionally left blank”

1. Introduction

1.1 Objectives

As the title of this thesis suggests, its main objective is the simulation and extensive analysis of rarefied hypersonic flows over complex geometries. The study of rarefied hypersonic flows over complex geometries is crucial for a wide range of aerospace and engineering applications. In this thesis, is presented a comprehensive investigation of this phenomenon, utilizing a multi-faceted approach that utilizes the strengths of both continuum and particle-based methods. More specifically, a Navier-Stokes solver has been modified in order to incorporate temperature jump and velocity slip boundary conditions, enabling the simulation of hypersonic flows in the rarefied regime. Furthermore, the Direct Simulation Monte Carlo (DSMC) method has been employed to capture the rarefaction effects accurately and compare with the Navier-Stokes modification. In addition, base flows calculated by the DSMC method have been utilized to conduct linear stability analysis of these flows. By combining these techniques, a robust framework for the simulation and analysis of rarefied hypersonic flows over complex geometries has been introduced, which has the potential to advance our understanding of important flow phenomenon and improve the design of high-speed aerospace vehicles. To achieve the aforementioned goal, the following objectives were successfully completed:

- Modify an in-house developed Navier-Stokes solver with temperature jump and velocity slip boundary conditions to accurately simulate rarefied hypersonic flows over complex geometries.
- Utilize the Direct Simulation Monte Carlo (DSMC) method to capture the rarefaction effects and improve the accuracy of hypersonic flow simulations.
- Conduct linear stability analysis of hypersonic flows using base flows calculated by the DSMC method.
- Investigate the effects of various parameters on the rarefied hypersonic flows, including gas properties, geometric configurations, and flow conditions.
- Compare and validate the results obtained from the modified Navier-Stokes solver and the DSMC method, and assess the limitations and applicability of each method.
- Compare the results obtained from linear stability analysis using DSMC based flows with results available in the open literature for the same flows calculated by Navier-Stokes methods.
- Apply the developed methodology framework to practical engineering problems, such as the design of hypersonic vehicles and roughness effects in a hypersonic flow.
- Provide insights into the physical mechanisms and flow structures of rarefied hypersonic flows, and contribute to the development of theoretical models and numerical methods for the analysis of these flows.

This Chapter continues with a literature review, concerning the fluid flow modeling using the Navier-Stokes equations and the DSMC method, while in the final section an overview of the methods used with its original contributions is summarized.

1.2 Literature review

1.2.1 Fluid flow modeling using the Navier-Stokes equations

The roots of Computational Fluid Dynamics (CFD) can be traced back to the early 1920s, when English mathematician L.F. Richardson made an attempt to predict weather by solving Partial Differential Equations (PDEs). Richardson's work included the main four features of CFD: a practical problem, PDEs to model the problem, a numerical scheme, and human computers to perform the calculations [Tor97]. However, it was not until the early 1970s [Bla01], when computer capabilities had sufficiently advanced, that the modern era of CFD began to take shape. Since then, CFD has evolved into a multidisciplinary field that combines physics, numerical analysis, and computer science to simulate fluid flows. It has been widely applied in various scientific and engineering fields, including aeronautics, marine engineering, turbomachinery, meteorology, oceanography, astrophysics, oil recovery, and architecture [Tor97, Bla01].

The first hypersonic Navier-Stokes code ever developed is a matter of debate as several researchers and groups claim to have developed the first code. However, some of the early codes that were developed for hypersonic Navier-Stokes simulations include the HYENA code developed by the US Air Force in the 1970s [And77], the TURMOIL code developed by NASA in the late 1970s [Buy80], and the NPARC code developed by the US Air Force and NASA in the early 1980s [Elm95]. In modern times, CFD algorithms have become an integral tool for aerodynamic and hypersonic vehicle designers, allowing them to reduce the cost and time spent on wind tunnel experiments. This is particularly true for CFD codes based on the Reynolds Averaged Navier-Stokes (RANS) equations, which enable a shorter design cycle. However, even the most widely used CFD methodologies sometimes fail to produce results that match the corresponding wind tunnel experimental data. As the accuracy of numerically derived flow is a critical factor affecting lift, drag, and general aerodynamic payload, which in turn influences the final design of aircraft, there is a continuous demand for more accurate and efficient methods in the ever-evolving field of CFD. While various academic and commercial compressible flow solvers have been developed over the years, issues related to grid generation, discretization, flux computation, turbulence modeling, and other factors continue to be subjects of ongoing research.

Given the context, the initial and crucial aspect to address when designing a CFD algorithm is the grid type adopted to represent the physical domain. Structured grids, either algebraically generated or via PDEs, were initially preferred in early solvers, with overlapping grids also being used for complex cases through Chimera techniques [Bla01]. However, constructing such grids was a time-consuming process that could take weeks, especially in military aircraft scenarios. To address this issue, researchers shifted their attention towards the creation of unstructured grid generators [And94, Bla01]. Unstructured grids are a type of mesh used in CFD simulations that offer high flexibility in modeling complex geometries and require minimal user intervention for their generation and adaptation. These grids are typically composed of tetrahedral elements, or triangular faces in two dimensions. However, in the case of viscous flow simulations, it is recommended to use a hybrid mesh consisting of prismatic or

hexahedral elements in the boundary layer region to effectively resolve the severe anisotropy of the flow in this area. Smaller spacing is necessary in this region, and tetrahedral elements are used for the rest of the domain, with pyramids filling the transition region between the two element types. This approach not only improves the accuracy of the final solution but also reduces the number of required elements, faces, and edges, resulting in decreased computational effort and memory requirements. This technique has been extensively studied and discussed in the literature, with references such as [Kim03] and [Bla01]. Unstructured grids are favored over structured grids for problems involving external aerodynamic flow over complex geometries such as aircrafts or hypersonic vehicles, due to their ability to adapt mesh size to local geometrical and flow features. Despite their arbitrary nodal distribution, which results in approximately twice the number of edges compared to a corresponding structured hexahedral mesh and consequently doubles computational and memory cost when using an edge-based technique, unstructured meshes remain the preferred choice for such simulations. Furthermore, unstructured meshes have the advantage of easy adaptation, which can be performed during the solution procedure to capture localized phenomena such as shocks. This feature is analyzed in further detail in the following paragraph by several researchers [Bar92, Kal96, Bla01, Sor03].

To numerically approximate the governing equations for the discretization of the computational field, an appropriate modeling strategy is needed. The most commonly used method in three-dimensional flow simulations is the finite-volume method, which divides the computational domain into finite control volumes, where the variables are assumed to be constant (for first-order schemes) [Bla01]. This method can be applied to both structured and unstructured grids and can be classified into two types: cell-centered and node-centered. In the cell-centered approach, the mesh elements serve as control volumes and the variables are stored at their barycenters. On the other hand, the control volumes in the node-centered approach are constructed around the nodes of the grid. Various methods have been developed for constructing these control volumes, such as connecting lines defined by edge midpoints, barycenters of faces, and barycenters of elements sharing a node [Kim03]. Although the cell-centered scheme includes many more Degrees of Freedom (DoFs) than the node-centered one, it is still widely used, along with the node-centered scheme [Bla01]. Additionally, some studies suggest that the node-centered method may have equal or even superior accuracy potential compared to the cell-centered method, even when the same number of Degrees of Freedom (DoFs) are used [Del11].

The selection of an appropriate scheme for the computation of numerical fluxes is another crucial aspect in CFD methods. The upwind method is commonly used and involves solving an one-dimensional Riemann problem along the normal vector of each face of a finite control volume, making it suitable for evaluating inviscid fluxes. This method has been widely accepted as the most appropriate approach, with approximate Riemann solvers like Roe, Osher-Engquist, and HLLC developed to solve the problem [Roe81, Osh84, Bar89], since the exact solution would require a considerable amount of computational effort. Studies have confirmed the effectiveness of this method in several CFD applications [Bar89, Bla01]. The discretization of the continuous computational field into finite control volumes results in significant numerical diffusion. To address this issue, higher-order spatial schemes such as the Monotonic Upstream Scheme for Conservation Laws (MUSCL) have been developed to reconstruct the variables' values at computational nodes using Taylor series expansion. Various slope limiters, including Van Albada-Van Leer, Min-mod, Barth-Jespersen, and Superbee, are also employed to control the total variation of the reconstructed field and ensure monotonicity between adjacent control volumes. These schemes have been extensively studied and applied in the literature [VanA82, Bar89, Bar92, And94, Kal96, Lan98, Bla01]. For the viscous fluxes, methods such as nodal-averaging or element-based approaches (e.g., approximate Galerkin

finite-element approach, face-centered control volume approach) are used to evaluate the temperature and velocity components' gradients at the control volumes' interfaces [Kal96, Bla01]. Although the nodal-averaging approach is susceptible to odd/even oscillations, it is often selected over the element-based approach due to the latter's relatively higher computational cost.

CFD involves numerical methods, and one crucial aspect that needs to be determined is the iterative approximation method used to solve the equations for flow and turbulence models, either strongly or loosely coupled [Bla01]. One straightforward approach to iterative solutions for a system of PDEs is by using an explicit scheme [And94, Kal96, Kim03, Sor03], such as a multi-stage Runge-Kutta method [Lal88]. With this method, the temporal derivative of conservative variables is discretized using a finite-difference formulation at each time step, followed by the evaluation of the flux sum at the same step [Ven95]. Explicit methods require only simple updates, making them easy to parallelize and requiring less memory. However, for large-scale flow simulations involving millions or tens of millions of computational nodes, the rate of convergence slows down considerably, resulting in relatively inefficient solution schemes. Implicit schemes may be more appropriate for fine grids, as they allow for larger CFL (Courant-Friedrichs-Lewy) numbers and, consequently, larger time steps, accelerating the solution process [Ven95]. Nevertheless, implicit methods are more complex to implement, particularly in a parallel computational environment, and require increased memory storage. Point-implicit schemes, a category of implicit iterative methods, typically implemented with the Jacobi or the Gauss-Seidel iterative algorithms, retain the simplicity of explicit schemes, even in parallelized simulations, and permit the use of large time steps [Kou03].

Over the years, several techniques have been developed to increase the convergence rate and accelerate the solution procedure in large-scale flow problems, regardless of the iterative scheme used (explicit or implicit). Using unstructured grids increases computational effort and memory requirements, especially hybrid ones. To address this, a more advanced data structure with indirect addressing, such as an edge-based one, can be employed [Bar92, Eva92, Bla01, Sor03]. This method enables the solver to obtain information from the mesh as sets of nodes connected by an edge, concealing the hybrid mesh's nature from the primary calculation loops, enhancing the solver's ability to handle grids composed of complex elements [Eva92]. In addition to the main solver, h-refinement methodologies take advantage of the edge-based data storage, introducing new nodes that enrich the mesh at the middle of the existing edges [Eva92]. Another widely used acceleration method is the local time-stepping technique, which determines the maximum allowable time step for each computational node, thereby improving the simulation's convergence [Bla01]. For explicit iterative schemes with relatively low convergence rates, an implicit residual smoothing technique may be employed, which introduces implicit features and permits the use of larger CFL numbers [Kim03]. Finally, methods that reduce the required wall-clock simulation time are parallel computation [Ven95] and the multigrid method [Bla01, Sor03].

1.2.2 Fluid flow modeling using the Direct Simulation Monte Carlo method

The DSMC method was first introduced by Graeme A. Bird [Bir63]. Since then, Bird has written three books on the method [Bir76], [Bir94] and [Bir13] and thousands of research papers have been published that report on development and application of the technique. The significance of the DSMC technique has been its ability over 50 years of development to provide a method of analysis for high Knudsen number flows (conditions ranging from continuum to free-molecular). Strong nonequilibrium in a flow is characterized by large

Knudsen numbers ($Kn = \lambda / L > 0.01$), where L is a characteristic length of interest in the flow. A DSMC simulation emulates the same physics as the Boltzmann equation. In fact, it has been demonstrated that DSMC converges to the solution of the Boltzmann equation in the limit of a very large number of particles [Bir94]. For low Knudsen numbers ($Kn = \lambda / L < 0.01$), through Chapman-Enskog theory [Vin75], the Boltzmann equation reduces exactly to the Navier–Stokes equations, which are the governing equations for computational fluid dynamics (CFD) simulations. Therefore, DSMC and CFD methods provide a highly consistent modeling capability for gas flows spanning the entire Knudsen range. DSMC collision models are very flexible in that they can be formulated to be consistent with continuum thermochemical rate data or they can directly incorporate quantum chemistry results. This flexibility in physical modeling enables DSMC to provide high fidelity calculations of multispecies gases in strong thermochemical nonequilibrium. For example, DSMC has been used to support the Columbia Space Shuttle orbiter accident investigation [Gal05], to support the 2001 Mars Odyssey aerobraking mission [Cla05], and to analyze the post-flight data from the Stardust mission [Wil99], [Zho08], [Boy10] and [Boy10a]. The utility of DSMC and its range of applications continues to expand in-step with advances in computational resources.

At first DSMC was used to analyze ground based hypersonic experiments. For many years the formation of rarefied hypersonic flows in ground based experimental facilities was a major technical challenge, thus very few datasets exist that can be used for validation of the various DSMC codes. Several years ago, a common code validation exercise was the hypersonic viscous interactions generated on slender body geometries. A lot of experiments were performed in the LENS experimental facility for a number of different geometries such as biconics and cylinder flares [Hol01]. The most popular comparison of DSMC simulations with the measured data were provided by Moss and Bird [Mos05] for a Mach 15.6 flow of nitrogen over a 25/55-degree biconic. Results from two different codes (DS2V and SMILE) are presented. Both show very good agreement with the experimental measurements. Similar results are also provided in [Erd94] for a Mach 12.4 flow of nitrogen over a flared cylinder. For both of these flows, the flow conditions didn't activate the vibrational energy of the nitrogen molecules, so there were no chemical reactions.

Furthermore, the Bow-Shock Ultra-Violet-2 (BSUV-2) flight experiment was flown in 1991 [Erd94]. This vehicle consisted of a capped 15-degree cone with a nose radius of *10* cm. BSUV-2 reentered the atmosphere of earth at *5.1* km/s and provided useful data for the altitude between 60 and 110 km. During this flight there was ultra-violet radiation emission due to nitric oxide and vacuum ultra-violet emission due to the presence of the atomic oxygen. The experimental data were obtained by on-board instrumentation. The chemically reacting flow was simulated using both continuum [Lev92, Lev93, Can93] and particle methods [Boy97]. Afterwards the ultra-violet emissions were calculated using the NASA nonequilibrium code NEQAIR [Whi96]. The first comparisons using the DSMC method had very poor agreement at high altitude. This fact led to the study of oxygen dissociation and nitric oxide formation at high altitudes by implementing chemistry models in the DSMC simulations [Boy97], [Boy95]. After that there was not only very good agreement with radiance but also the spectral features were simulated very accurately. Also, the atomic oxygen emissions were measured very accurately. The BSUV-2 experiment indicated that access to experimental data is needed in order to make significant advances in thermochemical modeling by using DSMC [Boy97].

Another very important issue which was studied extensively was the communications blackout during reentry. To study this effect, the Radio Attenuation Measurement (RAM) experiments started. During these experiments a series of reentry flights were performed. The communications blackout is a very important issue for all hypersonic vehicles and is related to the plasma formation at very high speeds which interferes with the radio waves sent from and to the vehicle. To perform the experiment, the RAM-C II hypersonic vehicle was used. It

consists of a cone with a spherical cap of radius *0.1524* m, a cone angle of 9-degrees, and a total length of *1.3* m. During reentry the RAM-C II obtains an orbital velocity of *7.8* km/s and the experiments were carried out at an altitude of *90* to *60* kilometers. The electron number density was measured in several different locations in the plasma layer surrounding the vehicle [Gra70], [Lin72]. A series of reflectometers were also used to measure the plasma density along lines normal to the vehicle's surface in 4 different locations. Finally, several Langmuir probes were used to measure the variation in plasma density across the plasma layer near the rear of the vehicle. The DSMC simulations of the RAM-C II vehicle were performed by Boyd [Boy07] with the intent of developing DSMC procedures for simulating charged species, i.e, electrons and ions in trace amounts. The DSMC results were compared with the measurements from the vehicle and it was concluded that the model employed for the dissociation chemistry needs to be investigated. The two models tested were the Total Collision Energy (TCE) and the Vibrationally Favored Dissociation (VFD). Both models showed very good agreement with the measurements [Boy07]. The generation of high-quality experimental data in the rarefied hypersonic regime continues to be a significant challenge till today.

The DSMC algorithm scales linearly with the number of particles used and the number of total timesteps till the final solution. Thus, any method that reduces the total number of particles used and the number of timesteps while maintaining accuracy can offer huge computational gains. Even when the computational cells are perfectly adapted to the local mean free path the number of particles per cell changes with changes with the flow density. An ideal simulation should employ enough particles per cell for obtaining statistical accuracy and during the simulation the total number of particles must remain close to this number.

A number of efficient strategies for the DSMC method have been proposed by Kennenber and Boyd several years before [Kan00]. The most famous strategy for reducing the number of simulation timesteps and also maintain some control on the number of particles is the cell-based timestep for steady state flows. In this technique a ray-tracing strategy has been used to move the particles from one cell to another, while each cell has its own timestep adapted to the local mean collision time. More specifically each cell stores the value $\Delta t_{ratio} = \tau_c/\Delta t_{ref}$where Δt_{ref} is a global reference timestep. Then on each timestep of Δt every particle is moved for $\Delta t_{ratio} \times \Delta t$. As it can be observed the larger the timestep used the fewer particles will end in that cell. To overcome this difficulty a particle weight of $W_p = \Delta t_{ratio} \times W_{p-ref}$ is assigned to each cell. With this technique we can maintain a constant particles number during a simulation by cloning or deleting particles and with minor changes to the DSMC algorithm [Kan00]. In general, the particle weighting schemes can precisely control the total number of particles in three dimensional flows. Here, by cloning or deleting particles we try to obtain the total number of particles to a constant level. Conserving momentum and energy on average when cloning particles can lead to random walk errors. Furthermore, collisions between particles of different weight conserves mass, momentum and energy only on average, which can also lead to random walk errors [Bir76].

In order to reduce the total number of computational cells and therefore the total number of particles LeBeau developed the Virtual Sub-Cell (VSC) method [Leb03], while Bird developed the Transient Adaptive Sub-Cell (TASC) method [Bir06]. Both methods try to lower the mean collision separation between selected collision pairs which are no longer selected at random with a computational cell. Thus, the cell size can increase to some degree while still maintaining a low mean collision separation. The VSC performs a nearest-neighbor search to select collision partners [Leb03], while the TASC subdivides each cell into a number of sub cells that are used only during the collision routine to sort the collision pairs in order to minimize the mean collision separation [Bir06]. To avoid the same pair undergoing repeated collisions, it is necessary to track the last collision partner and if the last collision partner is chosen again this particle is excluded and we choose the next nearest particle instead.

Moreover, since the collision rate is computed within each cell (not sub cell), there is a limit on the increase in cell size, before the assumption of a constant collision rate within a large cell leads to simulation inaccuracy. Another method for reducing the size of the computational grid was proposed by Gallis et al. according to which a collision partner is selected within a sphere with radius the distance the particle travels in one timestep [Gal11]. The advantage of this scheme is that it can relax the computational grid since it does not consider the cell size for precise collisions. However, an adequate number of particles is necessary to ensure accurate collision modeling.

A few years ago, Burt et al. [Bur12] introduced an interpolation scheme for the collision rate within the computational cells combined with the techniques mentioned. This scheme was shown to enable an increase in cell size while maintaining full accuracy. Bird has also proposed some substantial algorithm modifications [Bir09, Bir13] to the DSMC method with the same goals of reducing the number of timesteps and total number of particles. Like the schemes above the mean collision separation is minimized in these new algorithms but now all particles store their own timestep. This allows the simulation to iterate with small time steps and particles can only move when the global time step catches up with their timestep. Like that, only a small number of particles are moved during a global timestep iteration [Gal09]. These new algorithms produced a factor of 2 speedup for Fourier flow simulations compared to the standard DSMC algorithm. However, the formation of nearest-neighbor collision pairs after particles moved for large timesteps is physically inconsistent and leads to inaccuracies in the simulation [Gal09]. Inaccuracies were also reported when a constant collision rate was applied to large cells [Gal09]. In summary, the utilization of these new DSMC algorithms has greatly aided in the investigation of hypersonic flows characterized by large density gradients.

When the flow pressure is close to the continuum regime the DSMC method becomes computationally expensive compared to its continuum counteparts, due the requirement to resolve the mean free path and the resulting large number of collisions between computational particles. However, in the continuum regime the Navier-Stokes equations can predict the flow field accurately. Various researchers propose a hybrid DSMC-CFD numerical schemes in which the continuum regions of the flow domain are solved using the Navier-Stokes equations whereas the rarefied regions are solved by the DSMC algorithm. For these different methods to work together the particle and the continuum regions must be coupled by transferring flow information between their interfaces [Has96, Hass96, Rov98, Rov00, Wan03, Wij04, Sch07, Bur09]. A novel approach of hybrid simulations named Modular Particle Continuum (MPC) is described by Schwartzentruber in [Sch07] and was developed particularly for steady-state hypersonic flows.

At first the MPC method was developed for 1-D shock waves [Sch06] and for a hypersonic flow over a 2-D cylinder geometry [Sch06]. Afterwards it was applied to flows over blunt bodies [Sch08a, Sch08b], shock interaction flows [Sch08c], reentry flows using reaction control jets [Des08], and also has been extended to model non equilibrium gas flows [Sch08c, Des11]. The MPC method couples loosely the rarefied and continuum regions of the flow domain and these regions are updated by using different timesteps. This approach lets spatial and temporal scale decoupling while still remaining a modular implementation [Sch07a], using state of the art DSMC and NS code, with the appropriate modifications, within its code. Generally, MPC simulations can accurately reproduce full DSMC simulations to the level of velocity and energy distribution functions using less computational resources.

A study completed in 2009 by Holman and Boyd [Hol01] compared DSMC and CFD simulations for a hypersonic flow over cylinders and spheres for a wide range of Mach and Knudsen numbers. The most important conclusions of these study were that sufficient computational resources were used to fully resolve the DSMC simulations and that all physical models were formulated consistently between DSMC and CFD. More specifically the

viscosity, thermal conductivity, rotational relaxation and vibrational relaxation models used by DSMC and CFD were ensured to be consistent in the near-equilibrium limit. As it was revealed the agreement between CFD and DSMC was improved as the Knudsen number decreased. This type of consistency is very crucial for any hybrid simulation since the information is transferred across DSMC-CFD interfaces in near-equilibrium regions of the flow. In a hybrid simulation even minor inconsistencies in the physical models can produce severe errors. The specific application of the MPC method to hypersonic flows typically results in high flow speeds near particle-continuum interfaces ($\left|\vec{V}\right| > 10\ m/s$ for example) and the application to steady-state flows enables loose coupling where boundary conditions do not need to be updated at each timestep. These two results enable any statistical scatter involved in information transfer from DSMC regions to CFD regions to be strictly controlled with simple averaging techniques [Sun05]. For hypersonic steady-state flows with no trace species, statistical scatter is generally not a limiting factor for hybrid DSMC-CFD simulations, however, further research will be necessary for chemically reacting flows involving trace species.

One interesting study was the influence on the hybrid solution due to a minor change in the vibrational energy relaxation model. Specifically, the DSMC model was implemented to be consistent with the Landau–Teller expression with a temperature dependent vibrational relaxation rate from Millikan and White [Mil63]. If the DSMC model is based on the cell-based (CB) temperature, then the DSMC model can be shown to analytically match the continuum model in the equilibrium limit although not necessarily satisfying detailed balance. Therefore, models dependent only on collision properties (not cell averaged properties) are preferred in DSMC since velocity and energy distributions can be highly nonequilibrium. Thus, a second DSMC model was tested, herein referred to as the velocity-based (VB) model. The VB model does not have an analytical limit that precisely matches the Landau–Teller equation with a Millikan and White relaxation constant. This is a subtle, but important, issue with many DSMC models that has been investigated in several articles [Lum91], [Haa94], [Wys98]. Since most continuum thermochemical rate models are curve-fits to experimental data, there is no guarantee that the integration of a physics-based molecular model has the same functional form as the empirical fitting function used for the continuum model. Thus, perfect consistency in the continuum limit is not always possible between existing DSMC and CFD model formulations. Indeed, future research will require the formulation of new models that are consistent at the molecular and continuum levels and also with experimental data. To conclude, the accuracy of hybrid DSMC-CFD simulations and physical model has dramatically increased over the past few years. Further research is required on multispecies flows and flows involving chemistry, where the coupling between the DSMC and CFD models must be very consistent and the statistical scatter associated with trace species needs to be addressed.

In addition to the advancements made in the past few decades, the substantial increase in computational power over the last five years has been a crucial factor in expanding the practicality of the DSMC method. Recently DSMC has been used to study turbulence in the continuum and close to continuum regime [Gal17a, Gal18, Gal20, Gal21]. In [Gal17] DSMC and DNS comparisons are made in calculating the turbulent energy decay in the Taylor-Green vortex. Both methods showed very good agreement and were able to reproduce similar turbulent energy cascades. Furthermore, in several flow conditions DSMC reproduced richer physics that could not be captured by the equivalent DNS simulations [Gal21, Gal20]. Additionally, DSMC has been extremely useful in researching hydrodynamic instabilities because of its molecular structure [Gal15, Gal16, Gal16a, Lee19]. It provides a physical approach to examine physical phenomena that arise during the progression and expansion of hydrodynamic instabilities, without enforcing any preconceptions or particular flow models.

Based on the aforementioned applications in this work the DSMC method was used as a benchmark to assess the accuracy of an in-house developed Navier-Stokes solver named *Galatea* in the slip regime, simulate flows over complex configurations. For the first time, the ability of DSMC to produce accurate base flows that satisfy the stringent linear stability analysis requirements is demonstrated. For the latter, results are compared qualitatively and quantitatively with predictions made by the linear stability analysis theory. Finally, velocity distributions within shocks will be showcased along with the effects of chemical reactions on flows over complex geometries.

1.3 Present study

1.3.1 Overview

As per the main objective of this thesis, the in-house developed Navier-Stokes solver, *Galatea*, was modified to extend its application range to the slip flow regime. The modified code was then used to simulate low-density, high-altitude hypersonic flows and compared with solutions obtained from the DSMC method. To represent the computational domains, three-dimensional unstructured grids are used for the *Galatea* solver, while Cartesian grids with varying levels of refinement are employed for the SPARTA DSMC solver. The unstructured grids contain tetrahedral, prismatic, and pyramidical elements to resolve the significant anisotropy of boundary layers in viscous flows. The Cartesian grids mainly consist of cubical elements with triangular prismatic elements utilized where surfaces intersect the computational grid. Additionally, the thesis applies the linear stability analysis theory (LST) to analyze hypersonic base flows, comparing chemically reacting and non-reacting flows.

The numerical results of rarefied gas cases obtained with the *Galatea* solver utilized the RANS PDE's implementation of the code without any turbulence models, and were compared against the results obtained from the DSMC method, which is the dominant method for solving rarefied gas flows. Among the slope limiters implemented in the Galatea solver, the Van Albada-Van Leer and Min-Mod were used as they limited numerical diffusion and demonstrated effective smoothing abilities, yielding the most accurate results. The Navier-Stokes equations are insufficient to simulate rarefied gas flows without appropriate boundary conditions. Hence, velocity slip and temperature jump boundary conditions were implemented to enhance the solver's ability to simulate rarefied gas flows. Both first-order and second-order accurate methods were employed, and it was shown that the code was capable of simulating flows with Knudsen numbers well into the slip regime. No significant difference was observed between the first-order and second-order methods in the cases examined, due to the use of very fine grids in the simulations. The modified Navier-Stokes implementation exhibits excellent agreement with the solutions obtained from the DSMC method and experimental results, whenever available. To simulate complex geometries, a normalization coefficient was introduced to the implemented models to reduce residual oscillations during initial timesteps and facilitate the gradual increase of velocity slip and temperature jump values.

In addition to the modified Navier-Stokes solver, this thesis also reports on the ability of the DSMC method to produce high-quality flows suitable for stability analysis. Stability analysis requires a high level of convergence, typically eight digits, to produce accurate results.

Although DSMC is a stochastic statistical method for simulating rarefied gas flows, this work demonstrates that with careful treatment of the grid and simulation parameters, DSMC can provide highly resolved base flows for stability analysis that are comparable to those obtained by solving the Navier-Stokes equations, albeit without eight-digit convergence. The boundary layers are fully resolved, and perturbations inside the boundary layers match those predicted by LST theory. Enabling chemical reactions in the flow revealed interesting physical phenomena. The introduction of chemistry causes perturbations in the flow that usually propagate downstream the entire flow field.

Last but not least, an attempt has been made in this work to design a Mach 7 waverider. The method used is the well-known method of the osculating cones to extract the geometry profile of the waverider. Firstly, the three-dimensional flow field around a 7-degree cone with a blunt leading edge was calculated. The resulting geometry produced a lift/drag coefficient of 2.18. Although this may seem small compared to lift/drag ratios found in literature, it should be noted that the flow conditions were set to those occurring at *90* km altitude, where air is very rarefied, whereas waveriders in literature are simulated at *25-40* km altitudes. Despite this, a lift/drag ratio of 2.18 demonstrates that the vehicle is capable of flying under these rarefied conditions. The simulation data also revealed that for the on-design conditions examined, the shock wave is fully attached at the tip and leading edges of the vehicle.

1.3.2 Contributions

Considering analogous research published in literature, this thesis presents the following contributions:

- Improvements to a three-dimensional Navier-Stokes solver developed in-house, incorporating velocity slip and temperature jump boundary conditions.
- Evidence of the DSMC method's capability to generate high-quality flow patterns suitable for stability analysis.
- Documentation and analysis of velocity distribution functions within shocks.
- Quantification of shock-shock interactions with and without chemistry, and the consequent flow oscillations.
- An exploration of the impact of a cylindrical roughness element on a Mach 6 flow.
- Application of data-driven stability analysis techniques to three-dimensional DSMC data.
- Design, simulation and quantification of flow effects of a Mach 7 waverider in conditions of highly rarefied flow and off-design conditions with realistic leading edges.

The aforementioned contributions have been published in twelve Journal and Conferences papers listed below.

1.3.3 Outline

This thesis is organized as follows. Chapter 2 provides a theoretical background on DSMC, Navier-Stokes, and Linear Stability Theory (LST). The DSMC section gives a short introduction to the DSMC method, Boltzmann equation, Knudsen number, flow regimes, time and spatial discretization, molecular models, collision mechanics, and boundary conditions. The Navier-Stokes portion discusses governing equations, discretization methods, numerical flux computation, iterative solution, while the LST section covers linear stability analysis theory, analysis of compressible boundary layer, and outlines the necessary steps for stability analysis. The final portion of Chapter 2 introduces data-driven stability analysis techniques. In Chapter 3 of this thesis, a comprehensive analysis is presented that compares the results obtained from DSMC and Navier-Stokes simulations, along with the DSMC method integrated with linear stability analysis theory. The chapter not only showcases the comparison between these methods, but also displays the base flows generated through DSMC simulations. Furthermore, the stability analysis of these flows is also presented, providing an in-depth understanding of the underlying physics of the rarefied gas flows. Finally, in Chapter 4, the conclusions drawn from the research presented in the preceding chapters are discussed in detail. The significance of the results obtained in the context of the broader research area is highlighted, along with their implications and potential applications. Additionally, ongoing and future work that builds upon the findings presented in this thesis is outlined, providing direction for further research in this field. The limitations of the current research are also discussed, and avenues for future investigation are suggested.

1.4 List of publications

1.4.1 International Journals, with peer-review

1. Klothakis A., and Nikolos I.K., “Design and Evaluation of a Hypersonic Waverider Vehicle Using DSMC”, *Computation*, vol. 12(7), p. 140, https://doi.org/10.3390/computation12070140, 2024.

2. A. Klothakis, and I.K. Nikolos, “Comprehensive Evaluation of the Massively Parallel Direct Simulation Monte Carlo Kernel “Stochastic Parallel Rarefied-Gas Time-Accurate Analyzer” in Rarefied Hypersonic Flows—Part A: Fundamentals”, *Computation*, vol. 12(10), no. 198, 2024.

3. A. Klothakis, and I.K. Nikolos, “Comprehensive Evaluation of the Massively Parallel Direct Simulation Monte Carlo Kernel “Stochastic Parallel Rarefied-Gas Time-Accurate Analyzer” in Rarefied Hypersonic Flows—Part B: Hypersonic Vehicles”, *Computation*, vol. 12(10), no. 200, 2024.

4. Klothakis A., Quintanilha Jr H., Sawant S.S., Protopapadakis E., Theofilis V., and Levin D.A., “Linear stability analysis of hypersonic boundary layers computed by a kinetic approach: a semi-infinite flat plate at 4.5≤ M∞ ≤ 9”, *Theoretical and Computational Fluid Dynamics*, vol. 36(1), pp.117-139, 2022.

1.4.2 International Conference Proceedings, with peer-review

1. Klothakis A., Dylewicz K., Theofilis V. and Levin D.A., “Computation of hypersonic flow around an isolated roughness element using kinetic methods”, In *AIP Conference Proceedings*, vol. 2996(1), AIP Publishing, 2024.

2. Dylewicz K., Cerulus N., Klothakis A., Theofilis V., and Levin D.A., “Linear stability of couette flow with DSMC-informed boundary conditions”, In *AIP Conference Proceedings*, vol. 2996(1), AIP Publishing, 2024.

3. Klothakis A.G., Lygidakis G.N., and Nikolos I.K., “Rarefied gas flow analysis of a suborbital shuttle with the academic CFD code Galatea”, In *ASME International Mechanical Engineering Congress and Exposition*, vol. 58349, p. V001T03A002, 2017.
4. Klothakis A.G., Nikolos I.K., Koehler T.P., Gallis M.A., and Plimpton S.J., “Validation simulations of the DSMC code SPARTA”, In *AIP Conference Proceedings*, vol. 1786(1), p. 050016, 2016.

5. Klothakis A.G., Lygidakis G.N., Leloudas S.N., and Nikolos I.K., “Revisiting rarefied gas experiments with recent simulation tools”, In *6th European Conference on Computational Mechanics (ECCM 6)*, Glasgow, UK, 11-15 June 2018.

6. Klothakis A., Lygidakis G.N., and Nikolos I.K., “Numerical analysis of rarefied gas flows using the academic CFD code Galatea”, In *Proceedings of the ECCOMAS Conference*, 2016.

1.4.3 International Conferences

1. Klothakis A., and Nikolos I.K., “Simulation of a Mach-7 waverider in off-design Conditions”, *3rd IAMD-COE Conference*, June 19-20, 2024 (In Press).

2. Francis A.A., Dylewicz K., Klothakis A., Theofilis V., and Jewell J.S., “Instability measurements on a cone-slice-flap in Mach-6 quiet flow”, In *AIAA SCITECH 2024 Forum*, p. 0500-2024, 2024.

3. Lappas V., Klothakis A., Nikolos I., and Theofilis V., “On the Design of Miniature Reentry Vehicles for Mesosphere Exploration. Part I: Theoretical Considerations”, In *AIAA SCITECH 2024 Forum*, p. 1160-2024, 2024.

4. Klothakis A., Dylewicz K., Theofilis V., and Levin D.A., “Analysis of Hypersonic Flow Behind an Isolated Roughness Element Using Kinetic Methods”, In *AIAA SCITECH 2023 Forum*, paper 2023-0680, 2023.

5. Peck M.M., Riha A.K., Reed H.L., Klothakis A., Dylewicz K., and Theofilis V., “Comparative Studies on the Hypersonic Finned Cone”, In *AIAA SCITECH 2023 Forum*, paper 2023-0859, 2023.

6. Klothakis A., and Nikolos I.K., “An overview of international hypersonic flight programs and related technologies”, *2nd IAMD-COE Conference*, June 13-14, 2023.

7. Klothakis A., Nikolos I.K., “Numerical Simulations of the Flow Around Hypersonic Vehicles at High Altitude”, *1st IAMD-COE Conference*, September 29-30, 2022.

8. Klothakis A., Dylewicz K., Theofilis V., Sawant S.S., and Levin, D.A., “The effect of an isolated cylindrical roughness element on a semi-infinite flat plate in rarefied Mach 6 flow is studied using Direct Simulation Monte Carlo methods”, In *AIAA AVIATION 2022 Forum*, p. 4029, 2022.

9. Dylewicz K., Cerulus N., Klothakis A., Theofilis V., and Levin D.A., “Time-stepping global stability analysis using open-source DNS and DSMC codes”, *Bulletin of the American Physical Society*, 2022.

10. Klothakis A., Dylewicz K., and Theofilis V., “Stability Analysis of a Rarefied Flow Around a Re-entry Vehicle Model”, *Bulletin of the American Physical Society*, 2022.

11. Klothakis A., Sawant S.S., Quintanilha H., Theofilis V., and Levin, D.A., “Slip effects on the stability of supersonic laminar flat plate boundary layer”, In *AIAA Scitech 2021 Forum*, p. 1659, 2021.

12. Klothakis A., Quintanilha Jr. H., Sawant S.S., Protopapadakis E., Theofilis V., and Levin D.A., “On the effect of velocity slip and temperature jump on flat plate boundary layer stability at Mach 4.5”, In *APS Division of Fluid Dynamics Meeting Abstracts*, pp. H05-003, 2020.

2. Fluid flow

2.1 Statistical representation of gas flows

2.1.1 Boltzmann equation

In 1872 Ludwig Boltzmann introduced an equation which can describe which is valid in all flow regimes, from continuum flow to free molecular flow [Cer02, Ced02]. A brief introduction in the derivation of this equation will be given in this section. Before that, a short description of the phase space and density function concepts will be given.
Considering a small volume containing a finite number of particles, each particle that lies within that volume can be described by a set of three coordinates $\dot{r}$, one for each position coordinate, $\dot{r}_x, \dot{r}_y, \dot{r}_z$ and another set of three coordinates $\dot{p}$, for each momentum component $\dot{p}_x, \dot{p}_y, \dot{p}_z$. This is a six-dimensional space in which each point inside that space can be described by $(\dot{r}, \dot{p}) = (\dot{r}_x, \dot{r}_y, \dot{r}_z, \dot{p}_x, \dot{p}_y, \dot{p}_z)$ and each coordinate is pameterized by time t. Mathematically, this small volume can be expressed as:

$$\mathrm{d}^3\dot{r}\mathrm{d}^3\dot{p} = \mathrm{d}\dot{r}_x\mathrm{d}\dot{r}_y\mathrm{d}\dot{r}_z\mathrm{d}\dot{p}_x\mathrm{d}\dot{p}_y\mathrm{d}\dot{p}_z \tag{2.1.1}$$

The probability of N molecules all having $\dot{r}$ and $\dot{p}$ within $\dot{d}^3\dot{r}\dot{d}^3\dot{p}$ is given by a function f which gives the probability per unit length cubed per momentum cubed at a time t and is called the probability density function and is defined so that [Str05]:

$$\mathrm{d}N = f_P(\dot{r}, \dot{p}, t)\mathrm{d}^3\dot{r}\dot{\mathrm{d}}^3\dot{p} \tag{2.1.2}$$

where dN is the number of molecules that all lie within a volume element $\dot{d}^3\dot{r}$ and have their momentum within the momentum space $\dot{d}^3\dot{p}$ at time t. Then f_P can be expressed in a phase space description problem and the total number of molecules inside that volume is given by:

$$\begin{aligned} \mathrm{N} = & \int_{position} \mathrm{d}^3\dot{r} \int_{momentum} \mathrm{d}^3\dot{p} \\ & = \iiint_{position} \iiint_{momentum} f(\dot{r}_x, \dot{r}_y, \dot{r}_z, \dot{p}_x, \dot{p}_y, \dot{p}_z, t)\mathrm{d}\dot{r}_x\mathrm{d}\dot{r}_y\mathrm{d}\dot{r}_z\mathrm{d}\dot{p}_x\mathrm{d}\dot{p}_y\mathrm{d}\dot{p}_z) \end{aligned} \tag{2.1.3}$$

The generalized Boltzmann equation is composed of three terms and is written as [Str05]:

$$\frac{\partial f_P}{\partial t} = \left(\frac{\partial f_P}{\partial t}\right)_{force} + \left(\frac{\partial f_P}{\partial t}\right)_{diffusion} + \left(\frac{\partial f_P}{\partial t}\right)_{collision} \tag{2.1.4}$$

where the $force$ term expresses an external force acting to the particles of the system, the $diffusion$ term corresponds to the diffusion among particles and the $collision$ term accounts for the force exerted by molecules when colliding with each other.

Let F be an external force acting to the particles described by f. At time t a number of particles will have a position within the volume $\dot{d}^3\dot{r}$ that will be described by $\dot{r}$ and momentum in the $\dot{d}^3\dot{p}$ that will be described by $\dot{p}$. If force F acts instantly then at time $t + \Delta t$ the position of the particles will be:

$$\dot{r} + \Delta\dot{r} = \dot{r} + \frac{\dot{p}}{m}\Delta t \tag{2.1.5}$$

and momentum:

$$\dot{p} + \Delta\dot{p} = \dot{p} + F\Delta t \tag{2.1.6}$$

In the absence of collisions in the system then the probability density function f must be equal to:

$$f_P\left(\dot{r} + \frac{\dot{p}}{m}\Delta t, \dot{p} + F\Delta t, t + \Delta t\right)\mathrm{d}^3\dot{r}\mathrm{d}^3\dot{p} = f_P(\dot{r}, \dot{p}, t)\mathrm{d}^3\dot{r}\mathrm{d}^3\dot{p} \tag{2.1.7}$$

In equation (2.1.7) we can safely assume that the small volume $\mathrm{d}^3\dot{r}\mathrm{d}^3\dot{p}$ is constant due to the fact that all particles obey Hamilton's equation of motion, and according to Liouville's theorem, volumes of phase space along Hamiltonian trajectories are conserved [Str05]. In reality though, collisions do occur and thus the particle density in the small volume $\mathrm{d}^3\dot{r}\mathrm{d}^3\dot{p}$ changes such as:

$$\begin{aligned}\mathrm{d}N_{collission} &= \left(\frac{\partial f_P}{\partial t}\right)_{coll}\Delta t\mathrm{d}^3\dot{r}\mathrm{d}^3\dot{p} \\ &= f_P\left(\dot{r} + \frac{\dot{p}}{m}\Delta t, \dot{p} + F\Delta t, t + \Delta t\right)\mathrm{d}^3\dot{r}\mathrm{d}^3\dot{p} - f_P\left(r, \dot{p}, t\right)\mathrm{d}^3\dot{r}\mathrm{d}^3\dot{p} \\ &= \Delta f_P\mathrm{d}^3\dot{r}\mathrm{d}^3\dot{p}\end{aligned} \tag{2.1.8}$$

where Δf denotes the total change in f_P. If we divide equation (2.1.8) by $\mathrm{d}^3\dot{r}\mathrm{d}^3\dot{p}\Delta t$, in the limits $\Delta t \to 0$ and $\Delta f \to 0$ we get:

$$\frac{\mathrm{d}f_P}{\mathrm{dt}} = \left(\frac{\mathrm{d}f_P}{\mathrm{dt}}\right)_{collission} \tag{2.1.9}$$

and the total differential of f_P can be written as:

$$\begin{aligned}\mathrm{d}f_P &= \frac{\partial f_P}{\partial t}\mathrm{d}t + \left(\frac{\partial f_P}{\partial x}\mathrm{dx} + \frac{\partial f_P}{\partial y}\mathrm{dy} + \frac{\partial f_P}{\partial z}\mathrm{dz}\right) \\ &\quad + \left(\frac{\partial f_P}{\partial \dot{p}_x}\mathrm{d}\dot{p}_x + \frac{\partial f_P}{\partial \dot{p}_y}\mathrm{d}\dot{p}_y + \frac{\partial f_P}{\partial \dot{p}_z}\mathrm{d}\dot{p}_z\right) \\ &= \frac{\partial f_P}{\partial t}\mathrm{d}t + \nabla f_P \cdot \mathrm{d}\dot{r} + \frac{\partial f_P}{\mathrm{d}\dot{p}} \cdot \mathrm{d}\dot{p} \\ &= \frac{\partial f_P}{\partial t}\mathrm{d}t + \nabla f_P\frac{\dot{p}}{m}\mathrm{d}t + \frac{\partial f_P}{\partial \dot{p}} \cdot F \cdot \mathrm{d}t\end{aligned} \tag{2.1.10}$$

By dividing (2.1.10) with dt and substituting to equation (2.1.9) we get:

$$\frac{\partial f_P}{\partial t} = \frac{\dot{p}}{m} \cdot \nabla f_P + F \cdot \frac{\partial f_P}{\partial \dot{p}} = \left(\frac{\partial f_P}{\partial t}\right)_{collision} \tag{2.1.11}$$

which is a more well-known form of equation (2.1.4) in which the force field $F(\dot{r}, \dot{p})$ is the one that acts upon the particles and m is the mass of the particles. The right-hand side term describes the collisions between particles and if set to zero then the flow is collision less. This collision term is the most difficult to calculate due to fact that it's a statistical term and requires knowledge of the distribution the particles obey. Nevertheless, there are methods in the literature that approximate this term and the most well-known are the Bhatnagar, Gross and Krook (BGK) method [Bha54] and the Direct Simulation Monte Carlo (DSMC) [Bir94]. The latter is used in this work and will be discussed in the next session.

Before describing the numerical methods used in this work a description of the flow regimes will be given. An overview of the flow regimes along with the corresponding applicable numerical method for each regime can be seen in Figure *2.1*.

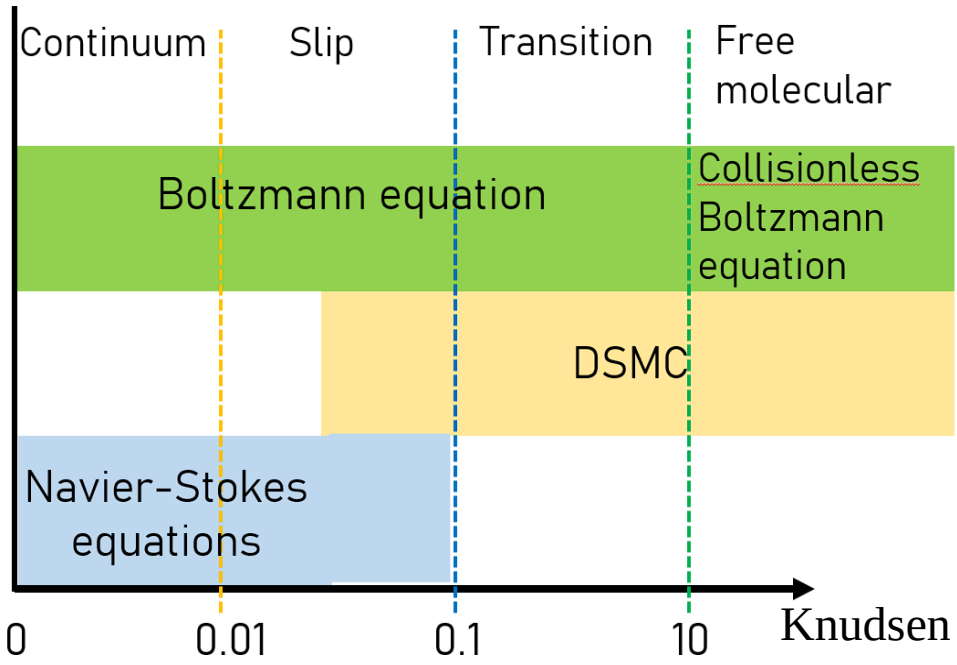

Figure 2.1. *Flow regimes.*

The Knudsen number used to determine each flow regime is given by:

$$\mathrm{Kn} = \frac{\lambda}{L_{ref}} \tag{2.1.12}$$

where is the mean free path (MFP) denoted by:

$$\lambda = \frac{1}{\sqrt{2}\pi d_{ref}^2 N_d \left(\frac{T_{ref}}{T}\right)^{\bar{\omega}-\frac{1}{2}}} \quad (2.1.13)$$

where d_{ref} is the particle characteristic diameter, N_d is the number density, T_{ref} a characteristic temperature (*273.15 K* in this work) and $\bar{\omega}$ is the viscosity exponent of the gas.

2.1.2 The Direct Simulation Monte Carlo method

The DSMC method was first introduced by Graeme Bird in the early 1960s [Bir94]. It is a particle-based statistical method, made for the study of rarefied flows in a direct physical way instead of solving partial differential equations. In other words, the evolution of a large number of simulated particles, which represent a fraction of the real molecules in the flow field, is simulated. Modeling is implemented by uncoupling the particles motion and calculating the intermolecular collisions between the simulated particles over a time interval smaller than the mean collision time. It has been proved mathematically that the method for a large number of particles per cell converges to the Boltzmann equation presented in the previous section [Wag92]. In general, the DSMC method consists of four steps:

1. Moving of particles
2. Indexing particles into cells
3. Performing the intermolecular collisions
4. Sampling particles properties

To locate the particles and track their movements, the whole computational domain is partitioned into a number of cells, which can contain sub-cells in a predefined structure. Initially, a set of particles are randomly distributed in each cell. Each of the particles is assigned a position, velocity components and energy. Then, the mentioned steps are repeated in each timestep in order to simulate the evolution of flow in time. The macroscopic quantities of the flow, such as velocity, pressure, density, temperature and so on, are measured on each cell and can be obtained from weighting averages of microscopic properties. For all simulations in this work the DSMC method as described by Graeme Bird [Bir94] and implemented in the Stochastic PArallel Rarefied-gas Time-accurate Analyzer developed in Sandia National Laboratories [Gal14], has been used to analyze the examined flows.

2.1.3 Discretization in space and time

The essential assumption in DSMC simulations is that over a timestep Δt smaller than the local mean collision time the molecular motion is independent of the intermolecular collisions. Accordingly, each molecule is moved by its corresponding distance traveled during this time interval, interacting with flow boundaries deterministically. After the calculation of the molecular moves the time is advanced by one time step and an appropriate set of intermolecular

collisions is selected. By alternating moving and colliding the flow develops in a time accurate manner from its initial state to its final state. Usually, a uniform flow is chosen as the initial state of the gas, which is specified by means of the macroscopic stream velocity, and two state variables, such as number density and temperature. Accordingly, neither an initial estimate of the flow field nor any kind of iteration is needed. All simulations are unsteady in the sense that they employ a time parameter which can be identified with physical time in real flow. However, if the flow parameters or the flow nature allow the formation of a steady flow, the steady state may be attained as a cumulative average of the unsteady flow over time. The uncoupling of the molecular motion and intermolecular collisions, is valid as long as the time step is small compared to the local mean collision time. If this condition is met the discretization error in the results can be kept below the uncertainty in the transport properties, which is about 2%. [Bir94].

As mentioned earlier, in the DSMC method a grid is required. The grid serves a two-fold objective. It divides the simulation domain in cells which, on one hand, serve the purpose of selecting the appropriate collision partners within each grid cell and on the other hand they are used to sample the macroscopic flow properties. The more molecules per grid cell used in a simulation the smaller the grid cell is the more accurate representation of the real flow behavior becomes. In fact, it has been shown that DSMC converges quadratically in terms of spatial and temporal discretization and 1/N, with the number of simulators per cell. Thus, the quality of the results is improved. The computation time of the DSMC routines is generally proportional to the number of simulated molecules, this is at the cost of higher computational efforts. This tradeoff gains importance at low Knudsen numbers and shorter mean free paths such as in the continuum regime. Bird in 2005 [Bir05] proposed the ratio of mean collision separation (MCS) to the mean free path (MFP) as the most important quality criterion for DSMC simulations and recommended an upper limit of:

$$\frac{t_{MCS}}{\lambda} < 0.2 \tag{2.1.14}$$

Higher values of equation (2.1.14) can increase the discretization error in the results. Furthermore, in order to reduce the computational cost flow symmetries or grid adaption can be employed. In areas where the flow gradients are very steep the grid cells can be refined to get a better representation and coarsened in areas where the flow gradients are practically constant.

2.1.4 Particle movement

In a DSMC simulation particles move in space according to their velocity taking into account the timestep. In the absence of external force fields, the change in their position is given by:

$$\Delta x = u\Delta t \tag{2.1.15}$$

Equation (2.1.15) can be applied to all problems regarding of their dimensionality (1d, 2d or 3d). In DSMC particle velocities are always three-dimensional regardless of the dimensionality

of the problem. To decrease the problem from three-dimensional to two-dimensional or one-dimensional the movement in the homogenous direction is ignored.

Axisymmetric flows yield a degree of difficulty due to the fact that it is necessary to account for the rotation around the axis of symmetry [Bir94]. An axisymmetric flow is assumed to occur in a single radial plane of a three-dimensional flow domain. The existence of the azimuthal velocity component causes the particles to exit this plane when following their physical three-dimensional trajectories. In order to account for that and return the particles inside the simulation plane their final position and velocity vectors are transformed such as to rotate the particle around the axis of symmetry and back into the initial simulation plane. This transformation maps a straight-line trajectory to a hyperbolic path in the simulation domain.

2.1.5 Boundary and surface interactions

For the simulations presented in this work four different boundaries were used namely, inflow, outflow, symmetry and surfaces. From the inflow boundary particles enter the simulation domain and the particles flux inserting the simulation domain from a grid cell face per unit time is calculated by [SPARTA21]:

$$\dot{N}_i = \frac{e^{\frac{[(-s^2 cos^2(\theta))+\sqrt{\pi} s\, cos(\theta)(1+erf(s\, cos\, \theta))]}{2\sqrt{\pi}}}}{\beta} N_d,$$

$$\beta = \sqrt{2R_{gas}T}$$

$$s = \frac{u}{\sqrt{2R_{gas}T}} \tag{2.1.16}$$

$$erf(a) = \frac{2}{\sqrt{\pi}} \int_0^a e^{-x^2} dx$$

where β is the particle most probable velocity, s is the speed ratio, u is the macroscopic flow velocity, erf is an error function and $\dot{N}_i$ the incoming molecular flux per unit time and N_d is the flow number density. Furthermore, in order to calculate the total number of particles to be inserted the ratio of simulator particles to real particles ($FNUM$), flow properties such as number density, velocity, thermal temperature and the area of the grid cell face relative to the streaming velocity are also considered [SPARTA21]. If a boundary is defined as outflow, then particles crossing this boundary are deleted from the simulation domain whereas if defined as symmetry the particles reflect back such that the angle of incidence is equal to the angle of departure with no change in energy. A visual representation of a specular reflection can be seen in Figure *2.2*. The different types of surface reflections used in this work will be presented next.

When a particle hits a surface boundary two events are happening. The reflection of the particle and the accommodation of the particle to the surface temperature. As seen in Figure

2.1 different types of surface reflection used in this work. The specular reflection in which the incident angle is equal to the reflection angle. In specular reflection the energy of the particle is the same before and after the collision with the surface, whereas in diffuse reflection nor the reflection angle nor the energy after the collision with the surface boundary are the same [Bir94]. In some cases, where an adiabatic surface was needed, a more sophisticated model was used to model it, that of Cercignagni-Lampis as modified by Lord [Lor91] for use in DSMC. This model differentiates the normal and tangential reflection [Cer71, Lor91].

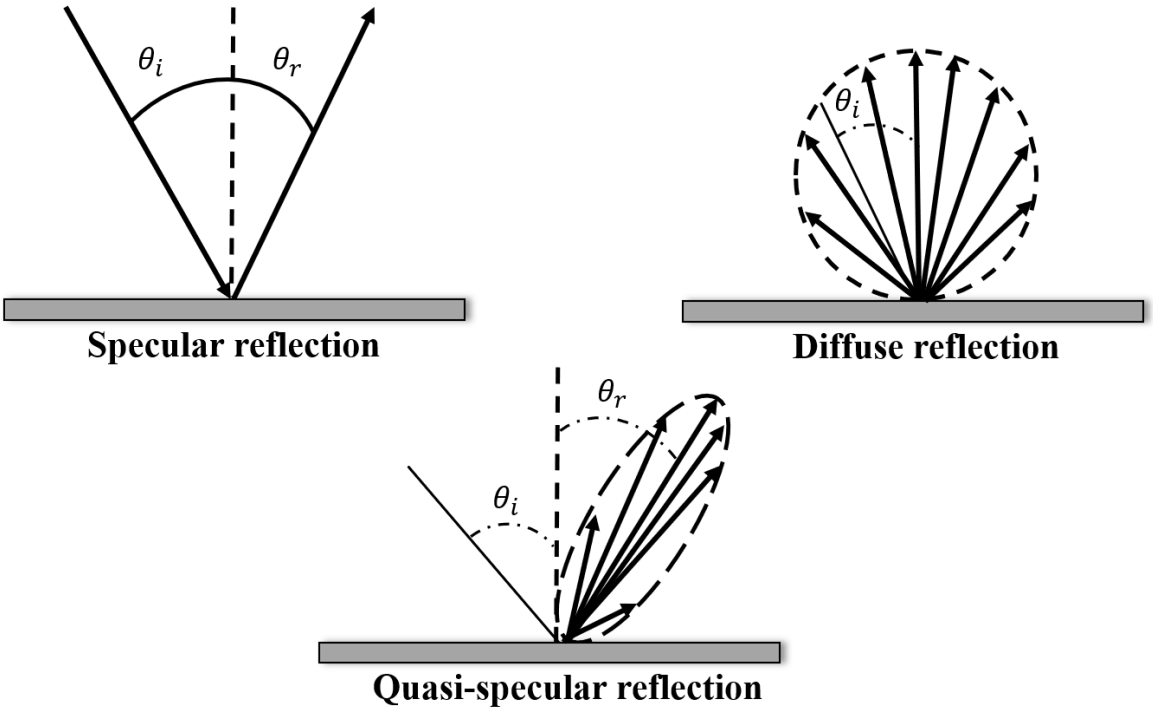

Figure 2.2. *Different types of surface and boundary reflections.*

The energy accommodation is used to account for the difference in temperature between the gas particles colliding with the surface and the surface temperature itself. In realistic engineering cases the gas is not always in thermodynamic equilibrium with the surface, so there's a difference of temperature before and after the particles collide with the surface. The energy accommodation coefficient, denoted here as a_c is the ratio between the energy given to the surface by the reflected particles and the energy given to the surface if the particles were reflected at the surface temperature [Bir94]. When $a_c = 1$ the reflected particles are at the same temperature as the surface so that they have exchanged with the surface all their energy. The energy accommodation coefficient is given by:

$$a_c = \frac{\dot{Q}_{incident} - \dot{Q}_{reflected}}{\dot{Q}_{incident} - \dot{Q}_{surface}} \tag{2.1.17}$$

where $\dot{Q}_{incident}$ and $\dot{Q}_{reflected}$ are the incident and reflected energy fluxes respectively and $\dot{Q}_{surface}$ is the energy flux that would be carried away in diffuse reflection with temperature $T_{reflected} = T_w$.

The Cercignani-Lampis model is able to reproduce more realistic surface reflections due to the ability to model quasi-specular reflections. Lord modified that model later in order to include the surface accommodation [Lor91]. The model was then renamed to Cercignani-Lampis-Lord (CLL) and requires five coefficients to be defined one for the surface normal direction accommodation, denoted as a_n, one for the tangential surface accommodation denoted as a_t, one for the rotational modes a_{rot}, one for the vibrational modes a_{vib} and one for the surface accommodation denoted here as $a_{partial}$. There is also another coefficient connecting with a_t, namely the tangential momentum accommodation σ_t. The equations of the model are:

$$a_n = \frac{ke_{incident} - ke_{reflected}}{ke_{incident} - ke_{surface}} \tag{2.1.18}$$

$$\sigma_t = \frac{\phi_{incident} - \phi_{reflected}}{\varphi_{incident}} \tag{2.1.19}$$

$$\begin{cases} a_t = \sigma_t(2 - \sigma_t) \\ 0 \leq \sigma_t \leq 1 \end{cases} \tag{2.1.20}$$

where $ke_{incident}$ and $ke_{reflected}$ are the kinetic energy for the incident and the reflected flux respectively for the normal to the surface velocity component, $ke_{surface}$ is the kinetic energy for the most probable normal velocity component in thermal equilibrium with the surface and $\phi_{incident}$ and $\phi_{reflected}$ are the tangential momentum accommodation coefficients for the incident and the reflected momentum flux respectively. If $a_n = a_t = a_{partial} = 1$ then the model reduces to a diffuse reflection with full surface temperature accommodation whereas if $a_{partial} = 0$ the model represents a diffuse reflecting adiabatic surface.

2.1.6 Collision mechanics

In DSMC there are two types of collisions occurring during a simulation regarding how is energy processed during the collision. Since DSMC is meant to simulate dilute gases only binary collisions are considered. The probability of having three particles in the same place during one timestep is negligibly small. Therefore, two types of collisions take place. Elastic collisions where only an exchange of translational energy occurs and inelastic collisions where rotational and vibrational energies are exchanged as well.

When an elastic collision occurs, energy and momentum are conserved. In the equations below the subscripts 1 and 2 denote of the two colliding particles, $\dot{m}$ denotes the center of mass of the particle and the superscript $(*)$ denotes the post collision properties. The conservation of energy and momentum can then be written as [Bir94]:

$$\dot{m}_1 c_1 + \dot{m}_2 c_2 = m_1 c_1^* + m_2 c_2^* = (\dot{m}_1 + \dot{m}_2) c_m \tag{2.1.21}$$

$$\dot{m}_1 c_1^2 + \dot{m}_2 c_2^2 = \dot{m}_1 c_1^{*2} + \dot{m}_2 c_2^{*2} \tag{2.1.22}$$

Defining also the relative velocity between the two particles before and after the collision as:

$$c_r = c_1 - c_2$$
$$c_r^* = c_1^* - c_2^* \tag{2.1.23}$$

where c is the velocity of the particle. Combining equations (2.1.21) and (2.1.22) with (2.1.23) we can write:

$$c_1^* = c_m + \frac{\dot{m}_2}{\dot{m}_1 + \dot{m}_2} c_r^* \tag{2.1.24}$$

$$c_2^* = c_m - \frac{\dot{m}_2}{\dot{m}_1 + \dot{m}_2} c_r^* \tag{2.1.25}$$

$$\dot{m}_1 c_1^2 + \dot{m}_2 c_2^2 = (\dot{m}_1 + \dot{m}_2) c_m^2 + \dot{m}_r c_r^2 \tag{2.1.26}$$

$$\dot{m}_1 c_1^{*2} + \dot{m}_2 c_2^{*2} = (\dot{m}_1 + \dot{m}_2) c_m^2 + \dot{m}_r c_r^{*2} \tag{2.1.27}$$

where $\dot{m}_r$ is the reduced mass and is defined as:

$$\dot{m}_r = \frac{\dot{m}_1 \dot{m}_2}{\dot{m}_1 + \dot{m}_2} \tag{2.1.28}$$

All of the above equations show that $c_r^* = c_r$ and that the post collisional velocities c_1^* and c_2^* can be calculated from the pre-collision velocities. This means that the calculation of the post-collision velocities can be known if the deflection angle $\dot{x}$ is known and additionally that the pre- and post- collision velocities are on the same plane. The deflection angle can be seen visually in Figure *2.3* adapted by [Bir94]. Furthermore, the knowledge of the separation of the undisturbed particle trajectories b are required for the calculation of the collisional cross-section. The undisturbed particle trajectory is the distance of the closest approach of the two colliding particles. The collision cross-section can be defined as [Bir94]:

$$\sigma \mathrm{d}\Omega = b db d\dot{e} \tag{2.1.29}$$

where $\dot{e}$ as seen in Figure *2.3* is the angle between a reference plane and the collision plane. Defining $d\Omega$ as [Bir94]:

$$\mathrm{d}\Omega = \sin \dot{x}\, d\dot{x} d\dot{e} \tag{2.1.30}$$

The total collision section can be defined and written as [Bir94]:

$$\sigma_T = \int_0^{4\pi} \sigma d\Omega = 2\pi \int_0^{\pi} b \left| \frac{db}{d\dot{x}} \right| d\dot{x} \tag{2.1.31}$$

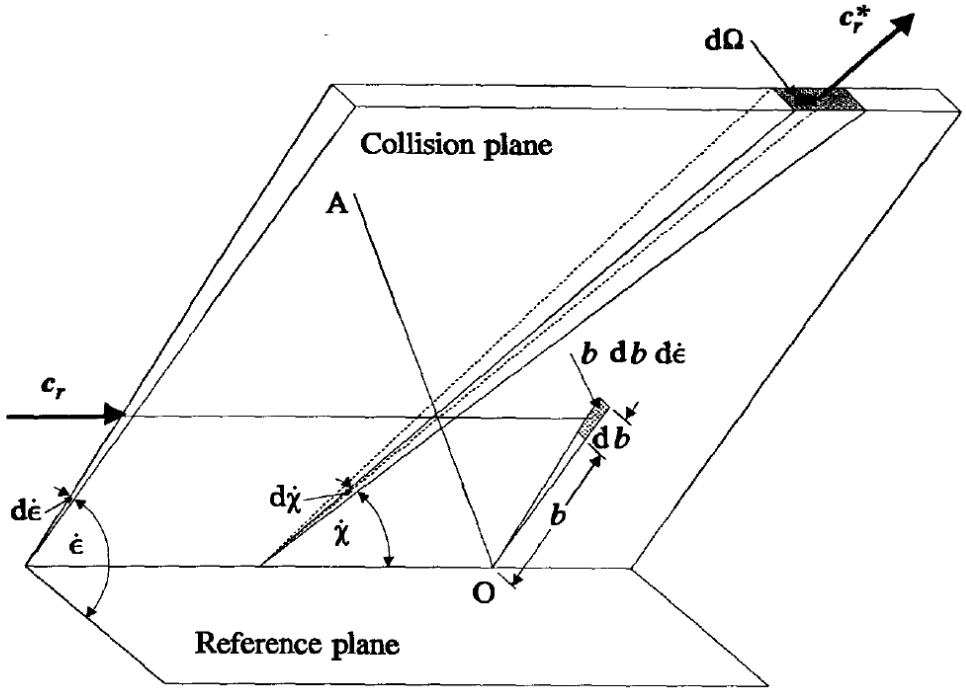

Figure 2.3. *Collision parameters. Adapted from [Bir94].*

The viscosity cross-section σ_μ and the momentum transfer cross section σ_M can also be derived from equation (2.1.31) and are equal to:

$$\sigma_\mu = \int_0^{4\pi} sin^2(\dot{x})\sigma d\Omega \tag{2.1.32}$$

$$\sigma_M = \int_0^{4\pi} (1 - cos\, x)\sigma d\Omega \tag{2.1.33}$$

Apart from the elastic collisions discussed previously, as mentioned before, there are also inelastic collisions occurring during a DSMC simulation. During an inelastic collision, besides translational energy, rotational and vibrational energies are exchanged as well. A very well-known model for inelastic collisions, which is almost universally used is the Larsen-Borgnakke model [Lar74, Bir94]. A detailed description of this model is given in [Bir94]. Here, for the sake of simplicity only one aspect of the model will be presented, that of a simple gas. A simple gas has its viscosity proportional to the temperature at the viscosity exponent $\bar{\omega}$ with a degree of freedom δ. The model assumes that the rotational modes of a particle are spherically symmetric. Thus, the relaxation rate can be defined as the rate at which a particle's internal mode approaches equilibrium and is related to the fraction of inelastic collisions [Lar74, Bir94]. The total translational energy E_t is equal to the sum of the translational energy of each particle and the same also applies for the internal energy E_{in}. The probability of a system to have a given translational or internal energy is given by [Bir94]:

$$P_{E_t} \propto E^{\frac{3}{2}-\bar{\omega}} e^{(-E_t/k_B T)} \tag{2.1.34}$$

$$P_{E_i} \propto E^{\frac{\delta}{2}-1} e^{(-E_i/k_B T)} \tag{2.1.35}$$

The total energy of a system is equal to the sum of translational and internal energy. According to that, the probability for a particle to be in the state $(E_t . E_i)$ is equal to [Lar74, Bir94]:

$$P_{E_t,E_i} \propto E^{\frac{3}{2}-\bar{\omega}} (E_c - E_t)^{\delta-1} e^{(-E_c/k_B T)} \tag{2.1.36}$$

where E_c is the total energy of the system. Furthermore, the temperature T can be linked to the total energy so that the probability denoted by equation (2.1.36) depends only on E_c but not from its distribution on translation or internal energy. The maximum of this probability is given by [Bir94]:

$$\frac{E_t}{E_{tot}} = \frac{3/2 - \bar{\omega}}{\delta + 1/2 - \bar{\omega}} \tag{2.1.37}$$

To obtain the post-collision energies E_t^* and E_i^* the acceptance-reception method is used. According to this principle, E_t^* is generated according to P_{E_t,E_i} as given by equation (2.1.36) and also a random number between 0 and 1 is generated as well. If accepted, then E_i^* is calculated as $E_i^* = E_c - E_t^*$. After the redistribution of the total energy into total translational and total internal energy is completed, the latter need also to be distributed on the two colliding particles. The same is done, knowing that the probability of having a particle with internal energy $E_{i,part}^*$ is:

$$P_{E_{i,part}^*} \propto E_{i,part}^{*\frac{\delta}{2}-1} \left(E_i^* - E_{i,part}^*\right)^{\frac{\delta}{2}-1} \tag{2.1.38}$$

Then the post-collision relative velocity in the center of mass is given by:

$$c_r^* = \sqrt{\frac{2E_t^*}{\dot{m}_r}} \tag{2.1.39}$$

2.1.7 Collision models

In DSMC collisions between the particles are treated in a statistical manner using models for the collision cross section and the scattering angle as well. Two collision models have been used in this work the Variable Hard Sphere (VHS) [Bir94] and the Variable Soft Sphere (VSS) of Koura and Matsumoto [Kou91, Kou92]. Before describing these complicated models, the simplest model of all will be described namely the Hard Sphere (HS) model [Bir94]. The hard sphere model assumes that:

$$\mathrm{b} = \frac{1}{2}(d_1 + d_2)\, cos\frac{\dot{x}}{2} \tag{2.1.40}$$

So that:

$$\sigma = \frac{(d_1 + d_2)^2}{16} \tag{2.1.41}$$

Denoting a total collision cross-section of [Bir94]:

$$\sigma_T = \int_0^{4\pi} \sigma d\Omega = \frac{\pi}{4}(d_1 + d_2)^2 \tag{2.1.42}$$

The advantage of the HS model is that since the collision cross-section is finite it has an isotropic scattering on the reference plane of the center of mass.

The isotropic scattering law of the HS model, although simple to calculate is also unrealistic. Moreover, the collision cross-section is independent of the relative translational energy of the collision. The viscosity in the HS model is proportional to temperature in viscosity exponent $\bar{\omega}$, with $\bar{\omega}$ equal to 0.5 although according to [Bir94] this number is closer to 0.5.

$$\mu \propto T^{\bar{\omega}} \tag{2.1.43}$$

This fact, led to a viscosity model such that [Bir94]:

$$\mu = \mu_{ref}\left(\frac{T}{T_{ref}}\right)^{\bar{\omega}} \tag{2.1.44}$$

As it will be shown in the next section this temperature dependency on the viscosity is known from the Sutherland's law [Luo05, Sut93]. Introducing a Sutherland coefficient denoted as A_s and a Sutherland temperature denoted as T_s equation (2.1.43) can be transformed to:

$$\mu = \frac{A_s\sqrt{T}}{1 + \frac{T_s}{T}} \tag{2.1.45}$$

This model is more realistic than the hard sphere model and differs to the fact that in the VHS particles have a diameter with is a function of the relative velocity such as [Bir94]:

$$\mathrm{d} = d_{ref}\left(\frac{c_{r,ref}}{c_r}\right)^{v} \tag{2.1.46}$$

where $v = \bar{\omega} - 1/2$. In the VHS model the deflection angle $\dot{x}$ is equal to [Bir94]:

$$\dot{x} = cos^{-1}\left(\frac{b}{d}\right) \tag{2.1.47}$$

The reference diameter of the VHS model can be derived from the viscosity power law as:

$$d_{ref} = \left(\frac{15\sqrt{\dot{m}k_B T_{ref}/\pi}}{2(5-2\bar{\omega})(7-2\bar{\omega})\mu_{ref}}\right)^{\frac{1}{2}} \tag{2.1.48}$$

where k_B is the Boltzmann constant. In the VHS model the collision cross-section is determined from the viscosity coefficient exponent while the viscosity and momentum cross-sections are given by the equations (2.1.32) and (2.1.33).

One deficiency of the VHS model is that the collision cross-section must be determined from the viscosity exponent coefficient of the gas while the ration of momentum to the viscosity collision cross-section follow the hard sphere rule [Bir94]. This ratio though varies in case of the inverse power law model varies with the power law resulting in values different from the hard sphere values. To tackle this deficiency, Koura and Matsumoto introduced the Variable Soft Sphere (VSS) model [Kou91, Kou92]. In this model the impact parameter b instead of defined as in equation (2.1.40) is now defined as [Kou91]:

$$\mathrm{b} = dcos^{a_{VSS}}\left(\frac{\dot{x}}{2}\right) \tag{2.1.49}$$

where a_{VSS} is the exponent of the cosine of the reflection angle. This exponent can be found in the gas data in open literature [Kou92] and all the other parameters of the model are directly linked to the value of a [Kou91]. As seen from equation (2.1.46) for a value of a equal to *1.0* the VSS is reduced to the VHS and can be proved that both models (VHS and VSS) yield the same computational cost [Kou91]. The deflection angle $\dot{x}$ for the VSS model is given by:

$$\dot{x} = 2cos^{-1}\left(\frac{b}{d}\right)^{1/a_{VSS}} \tag{2.1.50}$$

while the reference diameter d_{ref} for this model is given by [Kou91, Kou92]:

$$d_{ref} = \left(\frac{5(a_{VSS}+1)(a_{VSS}+2)\sqrt{\dot{m}k_B T_{ref}/\pi}}{4a_{VSS}(5-2\bar{\omega})(7-2\bar{\omega})\mu_{ref}}\right)^{\frac{1}{2}} \tag{2.1.51}$$

For this specific model, the total collision cross-section σ_T still remains equal to πd^2 [Kou91], while the viscosity and collision cross-sections can be written as [Bir94]:

$$\sigma_\mu = \frac{4a_{VSS}}{(a_{VSS}+1)(a_{VSS}+2)}\sigma_T \tag{2.1.52}$$

$$\sigma_M = \frac{2}{(a_{VSS}+1)}\sigma_T \tag{2.1.53}$$

In DSMC simulations, the collisions between particles are the primary means to represent the evolution of physical phenomena in a gas flow. For large simulations though, the calculation of the particle's trajectories, impact parameters and angle of incidence would be prohibitively expensive. For that reason, collisions are calculated in a statistical manner between particles in the same cell. Within a computational cell, particles are paired and a list of possible collision partners is formed. Then an accept-reject method is used to determine which collision pairs will collide. The probability for a collision to occur depends on the collision model and the collision partners selection scheme and is a function of the flow density, the relative velocity of the collision pair and the collision cross-section [Bir94]. This probability is also proportional to the timestep and the ratio of simulator to real particles ($FNUM$) [Bir94]. The pair is selected for collision if the collision probability is greater than a random number generated in [0,1]. The number of collision pairs examined and the collision probabilities are such that the average collision rate is equal to that given by kinetic theory.

Several collision partners selection schemes exist in open literature [Bar90, Bir94, Bir09, Bir05]. The selection scheme used in this work is based on the one described in [Bir05, Gal09] as modified by *Gallis et al.* [Gal11]. In this modified scheme the nearest-neighbor scheme of [Bir05] is replaced by a near-neighbor scheme according to which the collision partner of a particle is selected from a sphere with radius equal to the distance the particle travels in one timestep. Comparative studies and convergence behavior of the latter can be found in [Gal11].

2.1.8 Sampling of flow Macro-Properties

In the DSMC method the macroscopic properties of the flow are calculated as averages of the particles micro-properties. Properties such as density, velocity and temperature are the zeroth, first and second moments of the velocity distribution function. Since DSMC is able to simulate the evolution of the particle distribution function, it is valid to calculate the flow field properties by sampling particle properties and computing the moments of the sampled data. In each computational grid of the simulation domain the particles residing within the cell are grouped and their properties are averaged such as one value of the property is computed for each computational cell.

In areas with steep gradients and sudden changes of flow properties a large number of cells is required to capture the steep gradients to calculate smooth flow properties. The magnitude of statistical fluctuations varies with the inverse root of the sample size. A real gas is generally subjected to these fluctuations but the magnitudes are much smaller due to a sample size which is orders of magnitudes larger than the one available in a DSMC simulation. Although as the simulation ratio $FNUM$ approaches 1.0 it has been proven that the fluctuations found in a DSMC simulation represent the actual fluctuations of the real gas [Gar86, Gar87, Gar90].

If the number of particles per cell is relatively small to provide a reasonable sample, then the number of particles has to be either increased, if possible, or the samples size has to be increased in order to reduce the fluctuations. In steady flows examined in this work sampling was occurring for as many iterations as possible to obtain smooth results. On the other hand, in time accurate flows the sampling time was lower than corresponding flow times. If an acceptable sample couldn't be obtained then timestep was decreased accordingly in order to obtain more samples within the same time window.

2.2 The Navier-Stokes equations

2.2.1 Governing equations

According to Navier-Stokes theory a compressible viscous flow can be described by Partial Differential Equations (PDEs) named by the French mathematician Claude Louis Navier and the English engineer Sir George Gabriel Stokes. Navier-Stokes equations can be directly derived from the aforementioned Boltzmann equation. The PDEs are derived by the conservation of mass, momentum and energy [Bla01]. In the three-dimensional space, arranged into convective (inviscid), diffusive (viscous) and source terms, the equations can be written in differential form as:

$$\frac{\partial \vec{W}}{\partial t} + \frac{\partial \vec{F}^{inv}}{\partial x} + \frac{\partial \vec{G}^{inv}}{\partial y} + \frac{\partial \vec{J}^{inv}}{\partial z} - \frac{\partial \vec{F}^{vis}}{\partial x} - \frac{\partial \vec{G}^{inv}}{\partial y} - \frac{\partial \vec{J}^{inv}}{\partial z} = \vec{S} \tag{2.2.1}$$

The conservative variables vector $\vec{W} = (\rho, \rho u, \rho v, \rho w, \rho E)^T$, the inviscid vectors $\vec{F}^{inv}, \vec{G}^{inv}, \vec{J}^{inv}$, the viscous flux vectors $\vec{F}^{vis}, \vec{G}^{vis}, \vec{J}^{vis}$, and the source term vector $\vec{S}$ are expressed in terms of primitive variables (ρ, u, v, w, p). For the simulations presented in this work the source term was set to zero and the inviscid terms are defined as [Koo00, Lyg14e] such as:

$$\vec{F}^{inv} = \begin{pmatrix} \rho u \\ \rho u^2 + p \\ \rho uv \\ \rho uw \\ (\rho E + p)u \end{pmatrix}, \vec{G}^{inv} = \begin{pmatrix} \rho v \\ \rho vu \\ \rho v^2 + p \\ \rho vw \\ (\rho E + p)v \end{pmatrix}, \vec{J}^{inv} = \begin{pmatrix} \rho w \\ \rho wu \\ \rho w^2 + p \\ \rho wv \\ (\rho E + p)w \end{pmatrix} \tag{2.2.2}$$

$$\vec{F}^{vis} = \begin{pmatrix} 0 \\ \tau_{xx} \\ \tau_{xy} \\ \tau_{xz} \\ u\tau_{xx} + v\tau_{xy} + w\tau_{xz} + q_x \end{pmatrix}, \vec{G}^{vis} = \begin{pmatrix} 0 \\ \tau_{yx} \\ \tau_{yy} \\ \tau_{yz} \\ u\tau_{yx} + v\tau_{yy} + w\tau_{yz} + q_y \end{pmatrix},$$

$$\vec{J}^{vis} = \begin{pmatrix} 0 \\ \tau_{zx} \\ \tau_{zy} \\ \tau_{zz} \\ u\tau_{zx} + v\tau_{zy} + w\tau_{zz} + q_z \end{pmatrix} \tag{2.2.3}$$

When considering an inviscid flow only the inviscid flux vectors $(\vec{F}^{inv}, \vec{G}^{inv}, \vec{J}^{inv})$ are considered, which lead to the Euler equations. On the contrary, for a viscous flow the diffusive flux vectors $(\vec{F}^{vis}, \vec{G}^{vis}, \vec{J}^{vis})$ are taken into account, based on the components of the stress tensor $(\tau_{xx}, \tau_{xy}, \tau_{xz}, \tau_{yy}, \tau_{yz}, \tau_{zz})$, which are defined for Newtonian fluids as [Hir90]:

$$\tau_{ij} = \mu\left[\left(\frac{\partial u_i}{\partial x_j} + \frac{\partial u_j}{\partial x_i}\right) - \frac{2}{3}\left(\nabla \cdot \vec{V}\right)\delta_{ij}\right] \quad (2.2.4)$$

where μ is the dynamic viscosity coefficient and for a calorically perfect gas depends strongly on the temperature and less on the pressure [Bla01]. It can be computed from the local temperature field expressed in Kelvin vis the Sutherland equation such as [Luo05, Sut93]:

$$\mu = \frac{c_1 T^{3/2}}{T + c_2} \quad (2.2.5)$$

where the coefficients c_1 and c_2 are equal to $1.458\times10^{-6} kgm^{-1}sec^{-1}K^{-1/2}$ and $110.4\ K$ respectively. Another formulation of the same equation according to [Luo05] is:

$$\mu = \mu_{ref}\left(\frac{T}{T_{ref}}\right)^{\frac{3}{2}} \frac{T_{ref} + c_2}{T + c_2} \quad (2.2.6)$$

The three-dimensional Navier-Stokes equations are defined by a set of five equations with five conservative unknown variables $(\rho, \rho u, \rho v, \rho w, \rho E)$ which contain seven unknown field variables namely (ρ, u, v, w, E, T) requiring two more equations for the solution of the system. In the aerodynamics the fluid media is considered to be a calorically perfect gas, so the perfect gas state equation can be included in the set [Lan98] expressed as:

$$p = \rho R_{gas} T \quad (2.2.7)$$

where the gas constant for air is equal to $287.04\ m^2\ sec^{-2}\ K^{-1}$ and can be associated with the pressure and volume specific heat coefficients with the following two equations

$$R_{gas} = c_p - c_v, \gamma = c_p/c_v \quad (2.2.8)$$

while c_p and c_v are defined as:

$$\dot{h} = c_p T, \quad e = c_v T \quad (2.2.9)$$

in which $\dot{h}$ and e are the enthalpy and internal energy of the gas per mass unit. These specific heat coefficients are considered constants, although for different gases have different values, for air for example are equal to $c_p=1004.64\ m^2sec^{-2}K^{-1}$ and $c_v=171.6\ m^2sec^{-2}K^{-1}$ and $\gamma=1.4$ [Lan98]. The last equation to complete the system, connects pressure p with the total energy per unit:

$$\begin{aligned} \rho E &= \rho e + \frac{1}{2}\rho(u^2 + v^2 + w^2) = \rho T c_v + \frac{1}{2}\rho(u^2 + v^2 + w^2) = \\ &\frac{p}{R_{gas}} c_v + \frac{1}{2}\rho(u^2 + v^2 + w^2) = \frac{p}{(\gamma - 1)} + \frac{1}{2}\rho(u^2 + v^2 + w^2) \end{aligned} \quad (2.2.10)$$

where ρe is the internal energy per unit volume. The corresponding specific total enthalpy h_t is associated to pressure p and the total energy per unit volume ρE as:

$$h_t = \frac{\rho R + p}{\rho} = \frac{\gamma p}{\rho(\gamma - 1)} + \frac{1}{2}(u^2 + v^2 + w^2) \tag{2.2.11}$$

The heat flux vector in the equation of energy is defined accordingly to the stress tensor as [Bla01]:

$$Q_i = x\nabla T, \quad x = \frac{\mu c_p}{Pr} \tag{2.2.12}$$

where the conductivity coefficient x depends on the Prandtl number Pr which is generally considered constant across the entire flow domain and equal to *0.72* for a perfect gas.

A common strategy in CFD and experiments as well is to write the governing equations in a dimensionless form. The variables normalization is performed using a characteristic length L_{ref}, the free-stream velocity V_{ref}, the free-stream density ρ_{ref}, the free-stream dynamic viscosity μ_{ref} and the constant volume specific heat coefficient c_v as:

$$\tilde{x}_i = \frac{x_i}{L_{ref}}, \tilde{u}_i = \frac{u_i}{V_{ref}}, \tilde{\rho} = \frac{\rho}{\rho_{ref}}, \tilde{\mu} = \frac{\rho}{\mu_{ref}}, \tilde{R}_{gas} = \frac{R_{gas}}{c_v} = \gamma - 1 \tag{2.2.13}$$

Taking into account the aforementioned normalizations, the rest of the variables, included in equations (2.2.1-2.2.3) and (2.2.10-2.2.11), are expressed as:

$$\tilde{p} = \frac{p}{\rho_{ref} V_{ref}^2}, \tilde{\rho E} = \frac{\rho E}{\rho_{ref} V_{ref}^2}, \tilde{h}_t = \frac{h_t}{V_{ref}^2}, \tilde{T} = \frac{T}{V_{ref}^2 / c_v}, \tilde{t} = \frac{t}{L_{ref}/V_{ref}} \tag{2.2.14}$$

taking into account the dimensionless Reynolds number defined as [Mun98]:

$$\mathrm{Re} = \frac{\rho_{ref} V_{ref} L_{ref}}{\mu_{ref}} \tag{2.2.15}$$

the dynamic viscosity μ in the equations for the stress tensor and the heat flux vector is replaced by the term $\tilde{\mu}/Re$ and the equation is expressed as:

$$\tau_{ij} = \frac{\tilde{\mu}}{Re}\left[\left(\frac{\partial \tilde{u}_i}{\partial \tilde{x}_j} + \frac{\partial \tilde{u}_j}{\partial \tilde{x}_i}\right) - \frac{2}{3}(\nabla \cdot V)\delta_{ij}\right] \tag{2.2.16}$$

$$\tilde{Q}_i = \frac{\tilde{\mu}\gamma}{RePr}\nabla\tilde{T} \tag{2.2.17}$$

Furthermore, the constant pressure and the volume specific heat coefficients are normalized such as $c_p = \gamma$ and $c_v = 1$ while the perfect gas equation is written as:

$$\mathrm{p} = \rho R_{gas} T \rightarrow \tilde{p}\rho_{ref} V_{ref}^2 = \tilde{\rho}\rho_{ref}\tilde{R}_{gas} c_v \tilde{T}\left(V_{ref}^2/c_v\right) \rightarrow \tilde{p} = \tilde{\rho}\,\tilde{R}_{gas}\tilde{T} \rightarrow \tag{2.2.18}$$

$$\tilde{p} = \tilde{\rho}(\gamma - 1)\tilde{T}$$

The dimensionless dynamic is assumed to be equal to unity in compressible flow simulations evaluated by the Sutherland law using the dimensionless temperature as [Mar07]:

$$\begin{aligned}\tilde{\mu} &= \left(\frac{T}{T_{ref}}\right)^{\frac{3}{2}} \frac{T_{ref} + c_2}{T + c_2} = \left(\frac{\tilde{T}\left(V_{ref}^2/c_v\right)}{\tilde{T}_{ref}\left(V_{ref}^2/c_v\right)}\right)^{\frac{3}{2}} \frac{\tilde{T}_{ref}\left(V_{ref}^2/c_v\right) + c_2}{\tilde{T}\left(V_{ref}^2/c_v\right) + c_2} \\ &= \left(\frac{\tilde{T}}{\tilde{T}_{ref}}\right)^{\frac{3}{2}} \frac{\tilde{T}_{ref} + \dfrac{c_2}{\left(V_{ref}^2/c_v\right)}}{T_{ref} + \dfrac{c_2}{\left(V_{ref}^2/c_v\right)}} = \left(\frac{\tilde{T}}{\tilde{T}_{ref}}\right)^{\frac{3}{2}} \frac{\tilde{T}_{ref} + \dfrac{c_2\tilde{T}_{ref}}{\tilde{T}_{ref}}}{T_{ref} + \dfrac{c_2\tilde{T}_{ref}}{\tilde{T}_{ref}}}\end{aligned} \tag{2.2.19}$$

where $\tilde{T}$ is the dimensionless local temperature, whereas T_{ref} and $\tilde{T}_{ref}$ are the dimensional and dimensionless reference temperatures respectively. Lastly two more equations are used in the implementation of N-S equations in this work which concerns the local speed of sound at a node *P* [Lan98]:

$$\tilde{c}_p = \sqrt{\gamma \tilde{R}_{gas}\tilde{T}_p} = \sqrt{\gamma(\gamma - 1)\tilde{T}_p} = \sqrt{\frac{\gamma \tilde{p}_P}{\tilde{\rho}_P}} \tag{2.2.20}$$

and finally, equation for the Mach number in node *P* is defined as [Mun98]:

$$M_P = \frac{\sqrt{\tilde{u}_P^2 + \tilde{v}_P^2 + \tilde{w}_P^2}}{\tilde{c}_P} \tag{2.2.21}$$

For simplicity the accent ~ used as a superscript for the normalized variables will be neglected throughout this section.

2.2.2 Reynolds Averaged Navier-Stokes (RANS) equations

Navier-Stokes equations can theoretically account for turbulence without any models but only through Direct Numerical Simulation (DNS) but their use is limited to relatively simple problems at low Reynolds numbers due to their excessive computational requirements for spatial resolution and computation time. Instead, approximation methods such as Large Eddy Simulation (LES) or the Reynolds Averaged Navier-Stokes are preferred in order to simulate more complicated flows. The latter is implemented in the in-house code *Galatea* used in this work [Lyg13]. According to RANS model the flow variables are decomposed into a mean and a fluctuating part and each flow variable can be written as:

$$U_i = \overline{U}_i + U_i', \quad U_i' = 0 \tag{2.2.22}$$

where the turbulent fluctuation is described by a prime and the mean value defined as:

$$\bar{U}_i = \lim_{T\to\infty} \frac{1}{T} \int_t^{t+T} U_i dt \tag{2.2.23}$$

Equations (2.2.22) and (2.2.23) according to Blasius [Bla01] can be implemented only in incompressible flows where density can be assumed constant. In a compressible flow density is applied to certain variables such as velocity, enthalpy and energy whereas for density and pressure the Reynolds averaging approach holds [Bla01]. With that in mind the previous equations can be transformed for velocity, enthalpy and energy as:

$$U_i = \widetilde{U}_i + U_i'', \quad \widetilde{\rho U_i''} = 0 \tag{2.2.24}$$

$$\widetilde{U}_i = \frac{1}{\bar{\rho}} \lim_{T\to\infty} \frac{1}{T} \int_t^{t+T} \rho U_i dt \tag{2.2.25}$$

In the governing equations the turbulent kinetic energy $\tilde{k}$ has to be included and is defined using the velocity fluctuations as:

$$\bar{\rho}\tilde{k} = \frac{1}{2} \bar{\rho} \widetilde{u_i'' u_j''} \tag{2.2.26}$$

Using the aforementioned approaches, the Favre and Reynolds Averaged Navier-Stokes equations are derived [Lyg14] as:

$$\frac{\partial \overrightarrow{W}}{\partial t} + \frac{\partial \vec{F}^{inv}}{\partial x} + \frac{\partial \vec{G}^{inv}}{\partial y} + \frac{\partial \vec{J}^{inv}}{\partial z} - \frac{\partial \vec{F}^{vis}}{\partial x} - \frac{\partial \vec{G}^{inv}}{\partial y} - \frac{\partial \vec{J}^{inv}}{\partial z} = \vec{0} \tag{2.2.27}$$

$$\vec{F}^{inv} = \begin{pmatrix} \rho u \\ \rho u^2 + p \\ \rho uv \\ \rho uw \\ (\rho E + p)u \end{pmatrix}, \vec{G}^{inv} = \begin{pmatrix} \rho v \\ \rho vu \\ \rho v^2 + p \\ \rho vw \\ (\rho E + p)v \end{pmatrix}, \vec{J}^{inv} = \begin{pmatrix} \rho w \\ \rho wu \\ \rho w^2 + p \\ \rho wv \\ (\rho E + p)w \end{pmatrix} \tag{2.2.28}$$

$$\vec{F}^{vis} = \begin{pmatrix} 0 \\ \tau_{xx} \\ \tau_{xy} \\ \tau_{xz} \\ u\tau_{xx} + v\tau_{xy} + w\tau_{xz} + q_x + E_{tx} \end{pmatrix}, \tag{2.2.29}$$

$$\vec{G}^{vis} = \begin{pmatrix} 0 \\ \tau_{yx} \\ \tau_{yy} \\ \tau_{yz} \\ u\tau_{yx} + v\tau_{yy} + w\tau_{yz} + q_y + E_{ty} \end{pmatrix},$$

$$\vec{J}^{vis} = \begin{pmatrix} 0 \\ \tau_{zx} \\ \tau_{zy} \\ \tau_{zz} \\ u\tau_{zx} + v\tau_{zy} + w\tau_{zz} + q_z + E_{tz} \end{pmatrix}$$

where the mean total energy per unit volume ρE and the corresponding mean specific total enthalpy h_t can be evaluated as per [Koo00]:

$$\rho E = \frac{p}{(\gamma - 1)} + \frac{1}{2}\rho(u^2 + v^2 + w^2) + \rho k \tag{2.2.30}$$

$$h_t = \frac{\rho E + p}{\rho} = \frac{\gamma p}{\rho(\gamma - 1)} + \frac{1}{2}(u^2 + v^2 + w^2) + k \tag{2.2.31}$$

In the same manner the viscous stress tensor is extended in the momentum and energy equation by the Favre analogous averaged turbulent stress tensor τ_{ij}^t as defined in [Bla01]:

$$\tau_{ij}^t = -\bar{\rho}\widetilde{u_i'' u_j''} \tag{2.2.32}$$

According to the Boussineq hypothesis a linear relationship is assumed between the turbulent shear stress and the mean strain rate, the total averaged stress tensor τ_{ij}, divided in the laminar part denoted by the superscript l and the turbulent part denoted by the superscript t and is defined as [Koo00]:

$$\tau_{ij} = \tau_{ij}^l + \tau_{ij}^t = \left[\frac{\mu}{Re}\left[\left(\frac{\partial u_i}{\partial x_j} + \frac{\partial u_j}{\partial x_i}\right) - \frac{2}{3}(\nabla \cdot \vec{V})\delta_{ij}\right]\right] + \left[\mu_t\left[\left(\left(\frac{\partial u_i}{\partial x_j} + \frac{\partial u_j}{\partial x_i}\right) - \frac{2}{3}(\nabla \cdot \vec{V})\delta_{ij}\right)\right] - \frac{2}{3}\rho k\delta_{ij}\right] = \left(\frac{\mu}{Re} + \mu_t\right)\left[\left(\frac{\partial u_i}{\partial x_j} + \frac{\partial u_j}{\partial x_i}\right) - \frac{2}{3}(\nabla \cdot \vec{V})\delta_{ij}\right] - \frac{2}{3}\rho k\delta_{ij} \tag{2.2.33}$$

The total averaged thermal vector Q_i is expressed to the total averaged stress tensor as [Lyg14a]:

$$Q_i = Q_i^l + Q_i^t = \frac{\mu\gamma}{RePr}\nabla T + \frac{\mu_t\gamma}{Pr_t}\nabla T \tag{2.2.34}$$

in which Pr_t is the turbulent Prandtl number which in general is again assumed constant through the entire flow field and equal to *0.9* for air or a calorically perfect gas. For completion, the partial derivative of the turbulent kinetic energy term E_{tx_i} will be defined although it is not used in this work.

$$E_{tx_i} = \left(\frac{\mu}{Re} + \frac{\mu_t}{\sigma_k}\right)\frac{\partial k}{\partial x_i} \tag{2.2.35}$$

which for *k-ω* and the SST turbulent model is defined as:

$$E_{tx_i} = \left(\frac{\mu}{Re} + \mu_t \sigma_k\right)\frac{\partial k}{\partial x_i} \tag{2.2.36}$$

The term μ_t is the turbulent dynamic viscosity and σ_k is a constant. For the evaluation of these terms and for computing the turbulent kinetic energy *k* appropriate turbulence models have to be implemented and paired with the RANS equations.

2.2.3 Spatial Discretization

In order to discretize the fluid domain *Galatea* uses a node-center finite volume scheme [Lyg15a]. According to this scheme the computational grid is divided in a finite number of control volumes, across each the magnitude of the conservative variables is considered constant. Figure *2.4* illustrates a control volume around a node P. The control volume is defined by a set of linear segments connected to the midpoint of each edge and to the barycenter of its corresponding neighboring face [Kal96, Lyg12b, Sar14].

In a three-dimensional grid the control volume of a node *P* is comprised of a set of connecting lines defined by the edges midpoint, faces barycenters and elements barycenters that are sharing this specific node [Kal96, Lyg12, Sar14, Bla01, Koo00]. Based on that scheme the volume of every element is divided equally to the control volumes of its nodes. Thus, the volume of a tetrahedral element can be computed based on the coordinates of its nodes as [Lyg15a]:

$$V_T = \frac{1}{3!}\begin{vmatrix} x_1 & y_1 & z_1 & 1 \\ x_2 & y_2 & z_2 & 1 \\ x_3 & y_3 & z_3 & 1 \\ x_4 & y_4 & z_4 & 1 \end{vmatrix} \tag{2.2.37}$$

whereas the calculation of the volume of prisms and pyramids is performed by their subdivision in tetrahedra.

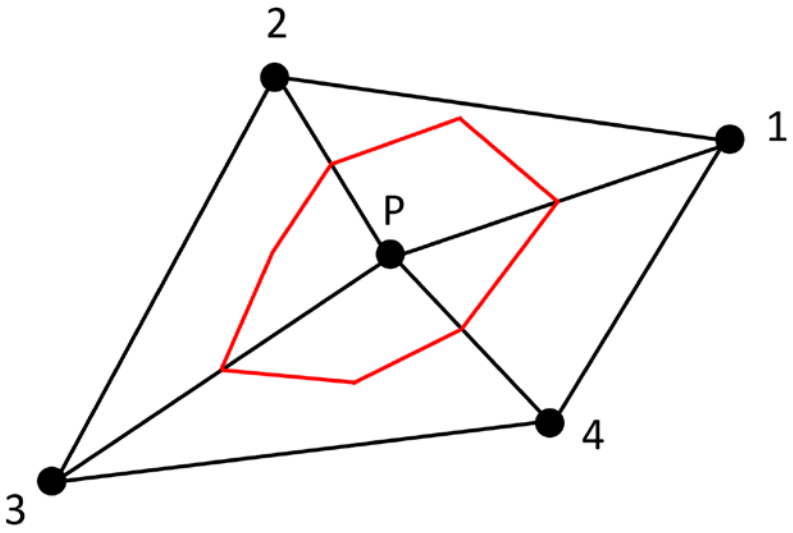

Figure 2.4. *Control volume around a node P in a two-dimensional grid.*

By utilizing this scheme equation (2.2.1) is integrated over the control volume CV_P of each node such as:

$$\iiint_{CV_P} \frac{\partial \vec{W}}{\partial t} dxdydz + \iiint_{CV_P} \frac{\partial \vec{F}^{inv}}{\partial x} + \frac{\partial \vec{G}^{inv}}{\partial y} + \frac{\partial \vec{J}^{inv}}{\partial z} - \frac{\partial \vec{F}^{vis}}{\partial x} - \frac{\partial \vec{G}^{inv}}{\partial y} - \frac{\partial \vec{J}^{inv}}{\partial z} dxdydz = \iiint_{CV_P} \vec{S} dxdydz \tag{2.2.38}$$

and by employing the Green-Gauss divergence theorem equation (2.2.38) is transformed to:

$$\iiint_{CV_P} \frac{\partial \vec{W}}{\partial t} dxdydz + \iint_{\partial CV_P} \left(\vec{\hat{H}}^{inv} - \vec{\hat{H}}^{vis}\right) ds = \iiint_{CV_P} \vec{S} dxdydz \tag{2.2.39}$$

where ∂CV_P are the boundaries of the control volume of a node P as defined by the facets constructed around the edges connecting node P with each neighboring node Q. In case ∂CV_{PQ} is the interfacing part of ∂CV_P and ∂CV_Q, with $K_N(P)$ is the set of neighboring nodes of P and Γ as the external boundary then ∂CV_P is defined as:

$$\partial CV_P = \bigcup_{Q \in K_N(P)} \partial CV_{PQ} + (\partial CV_P \cap \Gamma) \tag{2.2.40}$$

With $\vec{\hat{H}}$ as the vector of the inviscid or viscous fluxes, evaluated at the middle point of an edge connected to node P, that point then coincides with the interface between the adjacent control volumes of node P and Q interconnected to that edge. An edge-based data structure is used to accelerate the solution and ease the computational effort by utilizing the outward normal vector $\overrightarrow{\hat{n}_{PQ}}$ of the corresponding ∂CV_{PQ} face of the control volume. These vectors are described by the following equations [Lyg15a, Koo00, Kou03]:

$$\vec{\hat{H}}^{inv} = n_{PQ,x}\vec{\hat{F}}^{inv} + n_{PQ,y}\vec{\hat{G}}^{inv} + n_{PQ,z}\vec{\hat{J}}^{inv}$$

$$\vec{\hat{H}}^{vis} = n_{PQ,x}\vec{\hat{F}}^{vis} + n_{PQ,y}\vec{\hat{G}}^{vis} + n_{PQ,z}\vec{\hat{J}}^{vis} \tag{2.2.41}$$

$$\vec{\hat{n}}_{PQ} = \frac{\vec{n}_{PQ}}{\left|\hat{n}_{PQ}\right|} = \left(\hat{n}_{PQ,x}, \hat{n}_{PQ,y}, \hat{n}_{PQ,z}\right)$$

where $\vec{\hat{n}}_{PQ}$ is the vector sum of the outward normal vector of all the facets forming the face of the control volume ∂CV_{PQ}.
According to all of the above equation (2.2.39) is can be written as:

$$\iiint_{CV_P} \frac{\partial \vec{W}}{\partial t} dxdydz + \sum_{Q \in K_N(P)} \iint_{\partial CV_P} \left(\vec{\hat{H}}^{inv} - \vec{\hat{H}}^{vis}\right) ds + \iint_{\partial CV_P \cap \Gamma} \left(\vec{\hat{H}}^{inv} - \vec{\hat{H}}^{vis}\right) ds = \iiint_{CV_P} \vec{S} dxdydz \tag{2.2.42}$$

By assuming that the conservative variables at any node *P* are equal to their mean values counterparts over the control volume CV_P the first term of equation (2.2.42) is written as:

$$\iiint_{CV_P} \frac{\partial \vec{W}}{\partial t} dxdydz = \left(\frac{d\vec{W}}{dt}\right)_P \iiint_{CV_P} dxdydz = \left(\frac{d\vec{W}}{dt}\right)_P V_P \tag{2.2.43}$$

by expressing the integrals of numerical fluxes as a summation of fluxes through the faces comprising the control volume of a node *P*, equation (2.2.42) can be written as:

$$\left(\frac{d\vec{W}}{dt}\right)_P V_P + \sum_{Q \in K_N(P)} \vec{\Phi}_{PQ}^{inv} + \sum_{(K_{out} \in \partial CV_P \cap \Gamma)} \vec{\Phi}_{P,out}^{inv} - \sum_{Q \in K_N(P)} \vec{\Phi}_{PQ}^{vis} + \sum_{(K_{out} \in \partial CV_P \cap \Gamma)} \vec{\Phi}_{P,out}^{vis} = \iiint_{CV_P} \vec{S} dxdydz \tag{2.2.44}$$

$$\vec{\Phi}_{PQ}^{inv} = \iint_{\partial CV_P} \vec{\hat{H}}^{inv} ds = \vec{f}\left(\vec{W}_{PQ}^{L}, \vec{W}_{PQ}^{R}, \vec{n}_{PQ}\right), \vec{\Phi}_{PQ}^{vis} = \iint_{\partial CV_P} \vec{\hat{H}}^{vis} ds = \vec{g}\left(\vec{W}_{PQ}^{L}, \vec{W}_{PQ}^{R}, \vec{n}_{PQ}\right)$$

$$\vec{\Phi}_{P,out}^{inv} = \iint_{\partial CV_P \cap \Gamma} \vec{\hat{H}}^{inv} ds = \vec{f}\left(\vec{W}_{P}, \vec{W}_{out}, \vec{n}_{out}\right), \vec{\Phi}_{PQ}^{vis} = \iint_{\partial CV_P \cap \Gamma} \vec{\hat{H}}^{vis} ds = \vec{g}\left(\vec{W}_{P}, \vec{W}_{out}, \vec{n}_{out}\right) \tag{2.2.45}$$

where $\vec{W}_{PQ}^{L}$ and $\vec{W}_{PQ}^{R}$ are the vectors of conservative variables on the left and right side of an edge *PQ* respectively, whereas $\vec{W}_{out}$ is the vector on the boundary.

2.2.4 Inviscid fluxes

The computation of the inviscid fluxes in this work was accomplished by solving a one-dimensional Riemann problem in the direction of the normal vector of each face of the control volume of a node *P*. The exact solution of this problem is very computationally intensive [Lan98]. In order to ease the computation an upwind scheme was employed using the Roe's

approximate Riemann solver [Roe81]. The inviscid fluxes at the middle point of the edge *PQ* connecting node *P* and its neighbor node *Q* are calculated as:

$$\vec{\Phi}_{PQ}^{inv} = \frac{1}{2}\left(\vec{H}^{inv}\left(\vec{W}_{PQ}^{L}, n_{PQ}\right) + \vec{H}^{inv}\left(\vec{W}_{PQ}^{R}, n_{PQ}\right)\right) - \frac{1}{2}\left|\underline{\tilde{A}}_{PQ}\right|\left(\vec{W}_{PQ}^{R} - \vec{W}_{PQ}^{L}\right) \tag{2.2.46}$$

where $\underline{\tilde{A}}$ is the Jacobian matrix of the convective flux vector $\vec{H}^{inv}$ evaluated at the middle point of the edge *PQ* as well, utilizing the Roe's averaged values of the primitive variables [Roe81, Koo00, Kou03] denoted as:

$$\vec{\tilde{U}}_{PQ} = \frac{\sqrt{\rho_L}\vec{U}_L + \sqrt{\rho_R}\vec{U}_R}{\sqrt{\rho_L} + \sqrt{\rho_R}} \tag{2.2.47}$$

where $\vec{U}_L$ and $\vec{U}_R$ are the values of the primitive variables on the left and right side of edge *PQ* respectively, for a first order scheme. Utilizing the next equation (2.2.48), equation (2.2.46) is transformed to the form that was used in this work [Roe81, Lan98, Lyg15a]:

$$\vec{H}^{inv}\left(W_{PQ}^{R}\right) - \vec{H}^{inv}\left(W_{PQ}^{L}\right) = \underline{\tilde{A}}_{PQ}\left(W_{PQ}^{R} - W_{PQ}^{L}\right) \tag{2.2.48}$$

$$\vec{\Phi}_{PQ}^{inv} = \vec{H}^{inv}\left(W_{PQ}^{L}, \vec{n}_{PQ}\right) + \underline{\tilde{A}}_{PQ}\left(W_{PQ}^{R} - W_{PQ}^{L}\right) \tag{2.2.49}$$

As mentioned in [Lyg14, Lyg15] due to the edge-wise data structure of *Galatea* the evaluation of convective fluxes is accomplished with a single edge loop as no information is needed about the cell topology.

2.2.5 Viscous fluxes

Viscous fluxes are computed based on the components of velocity and temperature at the middle of the examined edge of the grid. For the evaluation of these derivatives a nodal-averaging method was used in this work [Bla01] and will be described in this section. This method is very popular because the gradients can be calculated by a single edge loop, which is used anyway for the calculation of convective fluxes. Thus, no additional computational requirements are needed. By using the gradients at the end points *P* and *Q* of an examined edge, along with the directional derivative in these nodes $(\partial U/\partial l)_{PQ}$, a mathematical scheme described in [Bla01, Lyg14, Lyg15] is used:

$$(\nabla\bar{U})_{PQ} = \frac{1}{2}\left((\nabla U)_P + (\nabla U)_Q\right) \tag{2.2.50}$$

$$\left(\frac{\partial U}{\partial l}\right)_{PQ} \approx \frac{U_Q - U_P}{\left|\vec{r}_{PQ}\right|}, \vec{\hat{r}}_{PQ} = \frac{\vec{r}_{PQ}}{\left|\vec{r}_{PQ}\right|} \tag{2.2.51}$$

$$(\nabla U)_{PQ} = (\nabla \bar{U})_{PQ} - \left[(\nabla \bar{U})_{PQ} \cdot \vec{\hat{r}}_{PQ} - \left(\frac{\partial U}{\partial l}\right)_{PQ}\right]\vec{\hat{r}}_{PQ} \tag{2.2.52}$$

For consistency, the equations computing the gradients at each node of the grid are written in this section and defined as:

$$(\nabla U)_P = \frac{1}{V_P}\sum_{Q\in K_N(P)} \frac{1}{2}(U_P + U_Q)\cdot \vec{n}_{PQ} \tag{2.2.53}$$

If *P* is a boundary node, then equation (2.2.53) has to be modified in order to include the boundary interfaces and is written as [Lyg13]:

$$(\nabla U)_P = \frac{1}{V_P}\left(\sum_{Q\in K_N(P)} \frac{1}{2}(U_P + U_Q)\cdot \vec{n}_{PQ} + \sum_{(K_{out}\in \partial C_P \cap \Gamma)} U_P \cdot \vec{n}_{out}\right) \tag{2.2.54}$$

2.2.6 High-order schemes and slope limiters

In case of a first order accurate spatial scheme the left and right states of an edge *PQ* are approximated by the values at the nodes *P* and *Q* respectively. For higher order schemes these states are approximated by Taylor series expansions, accounting for the values of more nodes when calculating numerical fluxes. The higher order scheme implemented in *Galatea* is based on MUSCL (Monotonic Upstream Scheme for Conservation Laws) reconstruction of the primitives or conservative variables, using also slope limiters to control the total variation of the reconstructed field. The left and right state for a primitive or conservative variable *U* at the middle of the edge *PQ* is calculated by [Bla01, Lyg13a, Sar14, Bar92]:

$$U_{PQ}^{L} = U_P + \frac{1}{2}\cdot(\nabla U)^L \cdot \vec{r}_{PQ} \tag{2.2.55}$$

$$U_{PQ}^{R} = U_Q + \frac{1}{2}\cdot(\nabla U)^R \cdot \vec{r}_{PQ} \tag{2.2.56}$$

where the right-hand side terms are the left and right node values of the variable *U* and $\vec{r}_{PQ}$ is the vector connecting these nodes. For a second order accurate scheme the gradients $(\nabla U)^L$ and $(\nabla U)^R$ are equal to the gradients $(\nabla U)_P$ and $(\nabla U)_Q$ on the nodes *P* and *Q* respectively. To evaluate these derivatives the element-by-element approach as described by [Bar92] is employed, which for a node *P*, being the common vertex of the neighboring tetrahedra *T* is written as:

$$(\nabla U)_P = \frac{1}{V_P}\sum_{T\in K_T(P)} \frac{V_T}{4}(\nabla U)_T \tag{2.2.57}$$

where V_P and V_T are the volumes of the node *P* and adjacent element *T* control volumes. Since *Galatea* uses an edge-based data structure an equivalent expression derived by Green-Gauss is used within the code which is described by equation (2.2.53) and in case of a boundary node by equation (2.2.54).

Within the code three slope limiters are used in total [Lyg15a] but for the cases simulated in this work only two of them were used namely the Min-mod [Swe84] and the Van Albada - Van Leer [Van82]. The main characteristic of the Min-mod limiter is the smoothing of the solution by choosing the slope with the smallest magnitude. In order to maintain the monotonicity between the values at the end points *P* and *Q* of the edge *PQ*, the limiter is based on the centered $(\nabla U)^c_{PQ}$ and upwind gradients $(\nabla U)^u_P, (\nabla U)^u_Q$ defined by the following set of equations:

$$\begin{aligned} (\nabla U)^c_{\mathrm{PQ}} \cdot \vec{r}_{PQ} &= U_{\mathrm{Q}} - U_P \\ (\nabla U)^u_P &= 2(\nabla U)_P - (\nabla U)^c_{\mathrm{PQ}} \\ (\nabla U)^u_{\mathrm{Q}} &= 2(\nabla U)_{\mathrm{Q}} - (\nabla U)^c_{\mathrm{PQ}} \end{aligned} \tag{2.2.58}$$

When these gradients are calculated then equations (2.2.55) and (2.2.56) can be written as [Bla01, Lyg13c]:

$$U^L_{\mathrm{PQ}} = U_P + \frac{1}{2} \cdot \Phi\left((\nabla U)^u_P \cdot \vec{r}_{PQ}, (\nabla U)^u_{\mathrm{PQ}} \cdot \vec{r}_{\mathrm{PQ}}\right) \tag{2.2.59}$$

$$U^R_{\mathrm{PQ}} = U_{\mathrm{Q}} + \frac{1}{2} \cdot \Phi\left((\nabla U)^u_{\mathrm{Q}} \cdot \vec{r}_{PQ}, (\nabla U)^u_{\mathrm{PQ}} \cdot \vec{r}_{\mathrm{PQ}}\right) \tag{2.2.60}$$

where Φ is the limiter function and is defined as [Swe84]:

$$\Phi(a,b) = \begin{cases} a & if\ |a| < |b|\ and\ ab > 0 \\ b & if\ |b| < |a|\ and\ ab > 0 \\ 0 & if\ ab \leq 0 \end{cases} \tag{2.2.61}$$

The Van Albada – Van Leer [Van82] limiter has exactly the same formulation as Min-mod, differing only in the limiting function Φ. For this specific limiter the Φ function is defined as:

$$\Phi(a,b) = \begin{cases} \dfrac{(a^2+e)b + (b^2+e)a}{a^2+b^2+2e}, & if\ ab > 0 \\ 0, & if\ ab \leq 0 \end{cases} \tag{2.2.62}$$

where *e* is a very small number with a typical value of 1.0×10^{-16} basically used to avoid division by zero.

2.2.6 Boundary conditions

If surfaces exist inside the fluid domain, then the contribution of these surfaces in the flux balance of the appropriate nodes must be considered. In the cases examined in this work boundary conditions such as wall, inlet, outlet and symmetry are used. Those boundary conditions are already implemented in *Galatea* and more information about the implementation can found in [Lyg15a]. In this section only the necessary boundary conditions used for the cases in the Results section will be described.

If a face is defined as inlet, then a one-dimensional Riemann problem is assumed across the face barycenter and the far field in order to compute the convective fluxes. Then the acquired fluxes are shared to the corresponding boundary nodes. Sharing with the boundary nodes is solved by implementing the Steger-Warming scheme [Ste81, Lan98] as:

$$\vec{H}_{K,out}^{inv} = \underline{\tilde{A}}_K^+ \vec{W}_K + \underline{\tilde{A}}_K^- \vec{W}_{out} \tag{2.2.63}$$

where the subscript *K* denotes the barycenter of the boundary face and the subscript *out* is the far field. The values of the variables of the $\vec{W}_{out}$ vector are obtained either from the far field or the boundary barycenter depending if the flow is internal or external [Bla01]. The diffusive fluxes due to their low contribution are omitted away from the solid surfaces [Kou03]. The same practice described for the inlet faces is followed for the outlet faces. In the symmetry boundary condition free-slip is imposed on the boundary nodes such those for solid walls in inviscid flow.

Generally, in most CFD codes a no-slip boundary condition is imposed on the walls by explicitly zeroing the velocity components on the nodes located on the walls. Due to the rarefaction of the flows examined in this work this boundary condition is no longer valid especially if the Knudsen number is above *0.001* [Zha12, Ho98, Gad99]. In this case, the velocity slip and temperature jump must be taken into account on the walls. The main idea of the slip condition on the walls was first introduced by Navier [Zha12] and the first mathematical approach was proposed by Maxwell in 1879 [Max79]. According to Maxwell's approach the values of velocity and temperature on solid walls are defined by the corresponding normal to the boundary surface gradients [Gad99].

Since that time many researchers have proposed solutions for the prediction of rarefied gas flows using numerical methods in two-dimensional or three-dimensional grids, structured or unstructured with first or second order accurate spatial schemes over complicated geometries [Don09, Myo01, Myo04, Myo05, Mad08, Het08]. Moreover, significant effort has been exerted to develop high-order accurate spatial slip schemes in order to improve the steady state solution on the solid walls [Bes15, Kar02, She05, Ste15]. From all the aforementioned approaches the one from Beskok and Karniadakis [Kar02, Bes99] seems to be very effective and easy to implement. It avoids numerical difficulties resulting from the computation of the second derivative of velocity components when complex geometries are combined with unstructured or hybrid grids. Due to the wall function mode in which these boundary conditions are applied, the corresponding schemes are susceptible to produce residual oscillations (especially during the initial steps of the iterative procedure) or fail. A method to counter this shortcoming has been proposed by Ferras et al. [Fer13] in which a specific normalization strategy is followed, allowing for the gradual change of the velocity or temperature values on

the boundary nodes. A visual representation of the aforementioned boundary condition can be seen in Figure *2.5*.

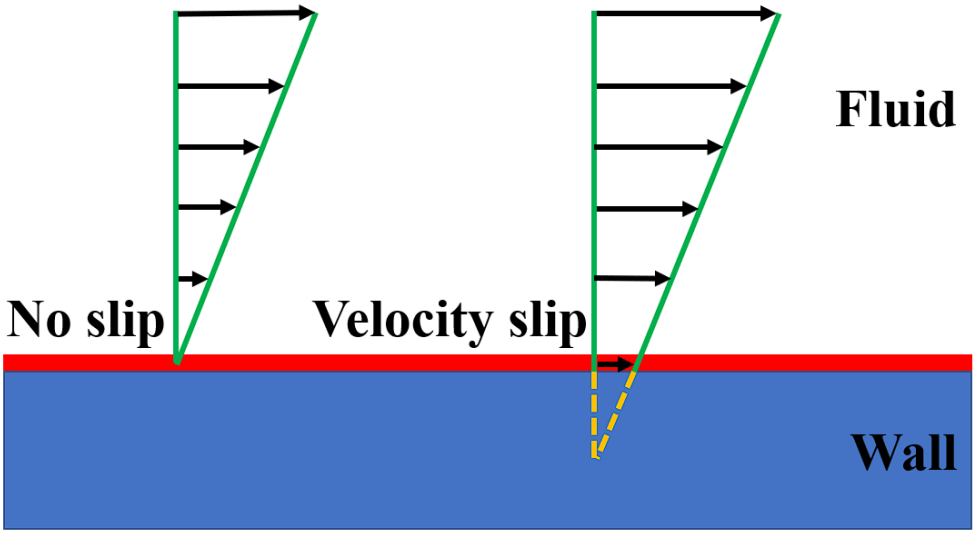

Figure 2.5. *Visual representation of the velocity slip boundary condition.*

Mathematically, this scheme, is described for the dimensionless slip velocity U_s as [Zha12, Max79, Bes99]:

$$U_s - U_w = \frac{2-\sigma_u}{\sigma_u} Kn \frac{\partial U_s}{\partial n} + \frac{3}{2\pi} \frac{(\gamma-1)}{\gamma} \frac{Kn^2 Re}{E_c} \frac{\partial T}{\partial s} \tag{2.2.64}$$

where U_w is the velocity of the wall surface, Kn is the Knudsen number, $\frac{\partial U_s}{\partial n}$ is the transverse velocity gradient, i.e., the derivative of the tangential slip velocity normal to the wall surface, denoted by the vector n [Het08], σ_u is the tangential momentum accommodation coefficient, which actually models the momentum exchange of the gas molecules impinging on the solid boundaries. It depends on the surface quality of the wall; small values of σ_u can increase the slip velocity even for low Knudsen numbers [Kar02]. In this work σ_u was set equal to unity [Klo16, Klo17, Klo20, Klo21, Fan01, Sho14]. The second right-hand side term includes the values of the dimensionless Reynolds number Re and Eckert number E_c along with the ideal gas constant γ and the tangential to the wall surface derivative of temperature accounting for the slip velocity contribution induced by the thermal creep. In this work this quantity is neglected as it is revealed to be relatively small in comparison with the right-hand side term. In common engineering problems there is only a very small temperature change across the wall surfaces [Het08].

The temperature jump condition is implemented in a similar as the velocity slip one and is described by the following equation [Het08]:

$$T_s - T_w = \frac{3-\sigma_T}{\sigma_T} \frac{2\gamma}{\gamma+1} \frac{Kn}{Pr} \frac{\partial T}{\partial n} \tag{2.2.65}$$

where T_s is the temperature slip, T_w is the wall temperature and the term $\frac{\partial T}{\partial n}$ denotes the derivative of the temperature normal to the wall surface. Pr is the dimensionless Prandtl number and σ_T is the thermal energy accommodation coefficient. Similarly, to the momentum coefficient σ_u the thermal energy accommodation coefficient depends on the surface quality [Bes99]. In this work it was set equal to unity [Fan01, Sho14].

For the improvement of the solution on the solid wall boundaries, several second order accurate spatial schemes can be employed [Bes99, Kar02, She05, Ste15]. However, most of them are based on the reconstruction of the first right-hand side term of equation (2.2.64) with a Taylor expansion series [She05, Ste15]. Despite the fact that this reconstruction can be an easy task in a two-dimensional grid, for unstructured or hybrid three-dimensional grids with complex geometries is not a straight forward procedure. The computation of the second derivative of the tangential velocity in the normal direction to the surface usually introduces significant numerical errors, besides the a priori computational difficulty it poses in such cases [Bes99]. Considering this, the approach of Beskok and Karniadakis [Bes99] was implemented in this work, as it appears to avoid the aforementioned numerical difficulties [Kar02]. Following this approach, equation (2.2.64) can be rewritten as:

$$U_s - U_w = \frac{2-\sigma_u}{\sigma_u}\frac{Kn}{(1-bKn)}\frac{\partial U_s}{\partial n} \tag{2.2.66}$$

where b is the slip coefficient; which can be defined experimentally or from other methods depending on the Boltzmann equation of the DSMC approach [Bes99]. This coefficient actually stands for the vorticity flux exerted to the surface divided by the vorticity of the flow field on that surface as obtained by the no-slip approach. In this work this coefficient was set to *-1.0* as in [Bes99].

The velocity slip and temperature jump boundary conditions are implemented in a Dirichlet way; hence they are sensitive to residual oscillations especially during the initial timesteps of an explicit iterative scheme [Fer13, Klo16]. To address this problem the normalization scheme proposed by *Ferras et al.* [Fer13] was implemented in the *Galatea* solver. This scheme allowed for a gradual increase of the slip velocity and temperature values. The equation for this scheme is defined as [Fer13]:

$$U_s^i = aU_s^{i-1} + (1-a)U_s^i \tag{2.2.67}$$

where a is the normalization coefficient. It can be set to values smaller than unity. For the cases examined in this work a value of *0.95* was adequate. Since the *Galatea* simulations in this work are multigrid accelerated the velocity slip and temperature jump values are calculated solely at the finest resolution. Therefore, they are restricted to the coarser multigrid levels similar to the rest nodal values [Lyg16].

2.2.7 Time integration

For the time integration of the cases examined in this work an explicit second order temporal accurate four-stage Runge-Kutta scheme was used [Bla01, Lyg14, Sor03]. For the implementation of this scheme equation (44) is transformed to:

$$-V_P\left(\frac{d\vec{W}}{dt}\right)_P = -V_P\frac{\Delta\vec{W}_P^{n+1}}{\Delta t_P}$$
$$= \sum_{Q\in K_N(P)}\vec{\Phi}_{PQ}^{inv} + \sum_{K_{out}\in\partial CV_p\cap\Gamma}\vec{\Phi}_{P,out}^{inv} - \sum_{Q\in K_N(P)}\vec{\Phi}_{PQ}^{vis} - \sum_{K_{out}\in\partial CV_p\cap\Gamma}\vec{\Phi}_{P,out}^{vis} \quad (2.2.68)$$
$$-\vec{S}_P V_P = \vec{R}_P^n$$

where Δt_P is the local timestep on node *P* which depends on the type of the flow (laminar in this work) and is computed as [Kim03, Lyg11]:

$$\Delta t_P^{lam} = CFL\cdot\frac{\left(0.5a_{min\,l\,edge,P}\right)^2}{\left(\left|\vec{U}_P\right|+c_P\right)0.5a_{min\,l\,edge,P}+\frac{2\gamma\mu}{\rho_P RePr}} \quad (2.2.69)$$

where $\left|\vec{U}_P\right|$ is the velocity value on node *P*, c_P is the speed of sound on the same node and $a_{min\,l\,edge,P}$ is the length of the smallest edge connected to node *P*. Local time stepping in a widely used technique in CFD and assures that each control volume will be assigned the maximum permissible timestep. This leads to the acceleration of convergence to steady-state [Bla01]. If in any case a global timestep is required, this can be defined as the smallest of the local timesteps of all grid nodes.

As aforementioned in this work an explicit scheme was used along with a four-stage Runge-Kutta (RK4) [Bla01, Sor03, Sar14, Lyg14, Kal96] in order to solve equation (2.2.68) iteratively and is defined as:

$$\vec{W}_P^{n+1,0} = \vec{W}_P^n$$
$$\vec{W}_P^{n+1,k} = \vec{W}_P^n - a_k\frac{\Delta t_P}{V_P}\vec{R}\left(\vec{W}_P^{n-1,k-1}\right), k = 1,\dots,4 \quad (2.2.70)$$
$$\vec{W}_P^{n+1} = \vec{W}_P^{n+1,4}$$

where k is the number of the internal stage of the scheme. In most of this work the constants a_1, a_2, a_3, a_4 have values of *0.11*, *0.26*, *0.5* and *1.0* respectively yielding a second order temporal accuracy to the procedure [Bla01]. Taking into account the low convergence rate of the explicit time stepping, in order to assure the stability of time integration an implicit residual smoothing technique is implemented in *Galatea* solver [Lyg15a] which attributes implicit features to the scheme and allows the use of larger CFL numbers [Bla01, Kim03]. Based on that the modified residual of a node *P* is can now be defined as [Kim03]:

$$R_P^{m+1}\frac{R_P^0+\varepsilon\sum_{j=1}^{l}R_{Q_j}^m}{1+\varepsilon\sum_{j=1}^{l}1} \quad (2.2.71)$$

where Q_j are the neighboring nodes to node P and ε is a coefficient with typical values of *0.5-0.8* defining the blending degree [Bla01]. In this work ε was set to *0.5*.

2.3 Linear stability theory

2.3.1 Equations of motion

All viscous or Newtonian fluids that follow the perfect gas assumption are governed by the Navier-Stokes equations. These equations can be written in a nondimensional form as:

$$\frac{\partial \rho}{\partial t} + \nabla \cdot (\rho V) = 0 \tag{2.3.1}$$

$$\frac{\partial \rho V}{\partial t} + \nabla \cdot (\rho V V) = -\nabla p + \frac{1}{Re} \nabla \cdot \sigma \tag{2.3.2}$$

$$\rho \frac{\partial T}{\partial t} - E_c \frac{\partial p}{\partial t} = E_c (V \cdot \nabla p) - \rho V \nabla \cdot T + \frac{1}{RePr} \nabla \cdot (k \nabla T) + \frac{E_c}{Re} \left(\frac{1}{2} (\nabla V + \nabla V) : \sigma \right) \tag{2.3.3}$$

$$\mathrm{p} = \frac{\rho T}{\gamma M a^2} \tag{2.3.4}$$

where σ is the viscous stress tensor and is denoted as $\sigma = \left(\mu (\nabla V + (\nabla V)^T) \right) + \nabla \left(\tilde{\lambda} (\nabla \cdot V) \right)$, V is the velocity vector components $V = (u, v, w)^T$, ρ is the fluid density, T is the fluid temperature, k is the fluid thermal conductivity, while μ and $\tilde{\lambda}$ are the first and second coefficient of viscosity respectively. In order to obtain a non-dimensional form of the aforementioned equations we scale all velocities by a reference velocity U^*_{ref}, temperature by T^*_{ref}, pressure is scaled as:

$$p_{ref} = \rho_{ref} \left(U_{ref} \right)^2 \tag{2.3.5}$$

while all lengths are scaled by a characteristic length L^*_{ref} and the reference free-stream speed of sound is denoted as:

$$a_{ref} = \sqrt{\left(\gamma R T_{ref} \right)} \tag{2.3.6}$$

where γ as mentioned before is the ratio of specific heats and R is the specific gas constant. Herein, all variables with an asterisk $(*)$ denote dimensional quantities. Based on the aforementioned formulation Reynolds number (Re), Mach number (Ma), Prandtl number (Pr) and Eckert number (Ec) can be written as:

$$\mathrm{Re} = \frac{\rho_{ref} U_{ref} L_{ref}}{\mu_{ref}} \tag{2.3.7}$$

$$\mathrm{Ma} = \frac{U_{ref}}{\alpha_{ref}} \tag{2.3.8}$$

$$\mathrm{Pr} = \frac{c_{p,ref}\mu_{ref}}{k_{ref}} \tag{2.3.9}$$

$$E_c = (\gamma - 1)Ma^2 \tag{2.3.10}$$

Assuming Stokes hypothesis for calculating $\tilde{\lambda}$ and Sutherland's law [Sut93] for calculating μ the dimensional viscosity μ is defined similarly to equation (2.2.5) where the coefficients c_1 and c_2 for standard air are equal to $1.458\times10^{-6} kgm^{-1}sec^{-1}K^{-1/2}$ and $110.4\ K$ respectively.

2.3.2 Linearized Navier-Stokes equations (LNSE)

Defining the vector $q = (p, T, u, v, w)^T$ as the vector containing all physical flow quantities, the Linearised Navier-Stokes equations (LNSE) are derived by a linear decomposition of vector q to a steady laminar base flow $\bar{q}$ and a small amplitude perturbation $\tilde{q}$ formulated as:

$$\mathrm{q}(\boldsymbol{x}, t) = \bar{q}(\boldsymbol{x}, t) + e\tilde{q}(\boldsymbol{x}, t), \quad with\ e \ll 1 \tag{2.3.11}$$

where $\boldsymbol{x}$ is the space vector coordinator, t is time and e is a very small amplitude disturbance. The $O(1)$ equations derived from the above are those that govern the base state and are satisfied by construction. The resulting $O(e^2)$ equations are neglected, on account of smallness. The $O(e)$ remaining terms define the LNSE, that need to be solved, either as an eigenvalues problem (modal analysis) or as an initial value problem for non-modal analysis.

The decomposition of equation (2.3.11) is valid for one-, two- and three-dimensional base flows. While there are three main categories of stability analysis, local, non-local and global. For completeness Table 2.3.1 shows all modern linear stability analysis concepts. From these three main categories only, the local analysis was used for the stability analysis in this work along with other data-driven stability analysis methods that will be discussed in the next section. In local stability analysis, the wall-normal spatial direction is taken as inhomogeneous in both the base flow and the amplitude functions. Two-dimensional parallel flow is assumed and only the streamwise velocity and temperature flow components are extracted from the DSMC simulations. After performing separation of variables, these two directions are decomposed in Fourier space and the linearized equations of motion can be now written as a system of ordinary differential equations (ODE) and are discussed extensively by Mack [Mac65, Mac69, Mac84].

Assuming *x* and *z* directions are the homogeneous spatial directions, such that the base flow depends only on the *y* spatial direction, in a Cartesian frame of reference, then the modal perturbations can be written in a local context such as:

$$\tilde{q}(x, y, z, t) = \hat{q}(y)e^{i(ax+\beta z+\omega t)} \tag{2.3.12}$$

Table 2.3.1: *Classification of linear stability theories [Jun13]*

	Denomination	Base flow assumptions	Amplitude function	Phase function
Global	TriGlobal	-	$\hat{q}(x,y,z)$	ωt
	PSE-3D	$\partial_x \bar{q} \ll \partial_y \bar{q}$	$\hat{q}(X,y,z)$	$\int_0^X a(\xi)d\xi - \omega t$
	Biglobal	$\partial_x \bar{q} = 0$	$\hat{q}(y,z)$	$ax - \omega t$
Nonlocal	PSE	$\partial_x \bar{q} \ll \partial_y \bar{q}; \partial_z \bar{q} = 0$	$\hat{q}(X,y)$	$\int_0^X a(\xi)d\xi + \beta z - \omega t$
Local	OSE	$\partial_x \bar{q} = \partial_z \bar{q} = 0$	$\hat{q}(y)$	$ax + \beta z - \omega t$

In a temporal framework, the variables $a = 2\pi/L_x$ and $\beta = 2\pi/L_z$ are the wavenumbers in the streamwise and spanwise direction respectively, while ω is a complex eigenvalue we solve for. Its real part ω_r relates to the perturbation angular frequency whereas the imaginary part ω_i is the damping rate. As aforementioned the dimensional qualities of length are divided by L_{ref} to become dimensionless and the streamwise velocity is divided by the edge of boundary layer velocity u_e which will be discussed later.

By substituting equation (2.3.11) into the LNSE, the one-dimensional eigenvalue problem is formulated and can be solved as per [Mac69, Mac84]. This can be written as:

$$\mathcal{L}\hat{q} = \omega\hat{q} \tag{2.3.13}$$

where $\hat{q}$ is the one-dimensional amplitude function. By solving the eigenvalue problem, can be determined if the flow is stable or unstable [The11]. The latter depends on the sign of the complex parameter ω. If $\omega_i < 0$ then the flow is stable and the perturbations decay in time, while if $\omega_i > 0$ then the flow is considered unstable and the perturbations grow exponentially. The eigenvalue problem (2.3.13) is solved by using the in-house developed *Linear Global* instability for *Hypersonic Transition* (*LiGHT*) solver [Qui17, Qui19, Qui21, The20]. The code is developed in Fortran and is solving in parallel complex non-symmetric eigenvalue problems (EVP) and singular value decomposition problems arising in linear flow instability.

For completeness the equations governing the two-dimensional compressible boundary layer and the boundary conditions used will be discussed. The boundary layer equations in a Cartesian domain can be written as:

$$\frac{\partial(\rho u)}{\partial x} + \frac{\partial(\rho u)}{\partial y} = 0 \tag{2.3.14}$$

$$\rho u\frac{\partial u}{\partial x} + \rho v\frac{\partial v}{\partial y} = \rho_e u_e\frac{du_e}{dx} + \frac{\partial}{\partial y}\left(\mu\frac{\partial u}{\partial y}\right) \tag{2.3.15}$$

$$\rho u\frac{\partial h}{\partial x} + \rho v\frac{\partial h}{\partial y} = \rho_e u\frac{dh_e}{dx} + \frac{\partial}{\partial y}\left(k\frac{\partial T}{\partial y}\right) + \mu\left(\frac{\partial u}{\partial y}\right)^2 \tag{2.3.16}$$

where streamwise velocity and wall-normal velocity are denoted by u and v respectively, h is the height of the boundary layer and the subscript e denotes the conditions at the edge of the boundary layer [Cri03, Ill49, Mac65, Whi05].

As aforementioned when the flow becomes more and more rarefied (Knudsen number increases) slip flow exists and equations (2.3.14-2.3.16) will require velocity slip and temperature jump boundary conditions in order to be closed. Herein, the equations used for velocity slip and temperature jump are those of Von Smoluchowski [Smo69] with a correction to the Maxwell conditions [Max79] and are written as:

$$U_s = \frac{1}{2}[u_\lambda + (1-\sigma_u)u_\lambda + \sigma_u U_w] + \frac{3\sigma_u}{8}\frac{\mu}{\rho T}\frac{\partial T}{\partial \chi} \tag{2.3.17}$$

$$T_s = \frac{\frac{2-\sigma_T}{Pr}\frac{\gamma}{\gamma+1}T_\lambda + \sigma_T T_w}{\sigma_T + \frac{2-\sigma_T}{Pr}} \tag{2.3.18}$$

where u_λ and T_λ denote the values of the streamwise velocity and temperature respectively at a distance of one mean free path from the wall. This form of the equations according to [Bes99] can obtain solutions within the slip and transition regime (Kn~0.5). The accommodation coefficients σ_u and σ_T are set equal to unity [Bes99, Cha61, Klo17].

In order to perform stability analysis, the dimensional variables of equations (2.3.14 – 2.3.18) must be converted in a non-dimensional form. Therefore, velocities u, v, density ρ, dynamic viscosity μ and temperature T are scaled by their corresponding boundary layer edge values denoted by the subscript e. The spatial coordinates are scaled as proposed by Mack [Mac65] inducing:

$$\xi = x \; and \; \eta = \frac{y}{x}\sqrt{Re_x} \tag{2.3.19}$$

$$Re_x = \frac{\rho_e u_e x}{\mu_e} \tag{2.3.20}$$

The Reynolds number used in linear stability analysis then can be expressed as:

$$\mathrm{Re} = \sqrt{Re_x} \tag{2.3.21}$$

By substituting equation (2.3.21) to (2.3.14-2.3.16) we derive the system to be solved for a zero-pressure gradient compressible boundary layer as:

$$\rho v - \frac{1}{\sqrt{Re_x}}(\eta g' - g) = 0 \tag{2.3.22}$$

$$\frac{d}{d\eta}\left(\mu\frac{du}{d\eta}\right) + g\frac{du}{d\eta} = 0 \tag{2.3.23}$$

$$\frac{d}{d\eta}\left(\frac{\mu}{Pr}\frac{d\vartheta}{d\eta}\right) + g\frac{d\vartheta}{d\eta} + 2\mu\left(\frac{du}{d\eta}\right)^2 = 0 \tag{2.3.24}$$

where:

$$g' = \frac{dg}{d\eta} \equiv \frac{1}{2}\rho u \tag{2.3.25}$$

$$\vartheta = \frac{T - T_e}{T_0 - T_e} \tag{2.3.26}$$

$$T_0 = T_e + \frac{u_e^2}{2c_P} \tag{2.3.27}$$

$$\frac{T}{\tilde{T}_e e} \equiv \tilde{T} = 1 + \frac{\gamma - 1}{2} Ma_e^2 \vartheta \tag{2.3.28}$$

while herein Prandtl number is defined as:

$$\mathrm{Pr} = \frac{\mu_e c_P}{k_e} \tag{2.3.29}$$

In order to complete the aforementioned system closed form the dependency of viscosity to the temperature has to be considered and is defined as:

$$\mu = \mu_{ref} \left(\frac{T}{T_{ref}} \right)^{\bar{\omega}} \tag{2.3.30}$$

where μ_{ref} denotes the reference viscosity $\bar{\omega}$ is the viscosity exponent.

Finally, the boundary layer system defined herein, can be solved subjected to the boundary conditions:

$$\mathrm{u}(\eta = 0) = {}^{U_s}/_{u_e e} \tag{2.3.31}$$

$$\mathrm{u}(\eta \to \infty) = 1 \tag{2.3.32}$$

$$\mathrm{T}(\eta = 0) = 0 \quad or \quad T(\eta = 0) = T_w \tag{2.3.33}$$

$$\mathrm{T}(\eta \to \infty) = 1 \tag{2.3.34}$$

2.3.3 Data driven stability analysis – The residuals algorithm

During the past years Theofilis showed that the well-known flow properties residuals are directly linked to decay of the least-stable global eigenmode [The00]. This can be represented mathematically as:

$$\hat{\omega} = \frac{d}{dt}(ln|q(x,t) - q(x)|) \tag{2.3.35}$$

where, as mentioned in the previous section $q(x,t)$ is any flow variable at a specific location (x,y,z) in the flow field in time t, ω is the amplification rate of the global eigenmode while $\breve{q}(x)$ is the final value of the aforementioned variable at the examined location x of the flow field. The term residuals algorithm describes the method used in order to recover an amplification rate and the amplitude functions of the least-damped global flow eigenmode directly from a numerical simulation. In this work, time windows in which ω is practically constant will be referred as *linear decay regime*. When the decay rate of the least stable global is calculated, then the corresponding amplitude function can be recovered using the linear stability Antsaz as defined in equation (2.3.11). Based on equation (2.3.11) any flow field can be decomposed in a steady state $\bar{q}(x)$ and an infinitely small perturbation, $\varepsilon \ll 1$, $\varepsilon\tilde{q}(x,t)$ Herein, for the residuals algorithm the amplitude perturbation $\tilde{q}$ is formulated as follows:

$$\tilde{q}(x,t) = \hat{q}(x)e^{-\omega t} \tag{2.3.36}$$

where $\hat{q}(x)$ is the amplitude function of the damped disturbance. Equation (2.3.36) assumes a global stationary mode but the Ansatz as shown in [The00] can be easily generalized for travelling modes. Since the damping rate remains constant throughout the linear decay time window, two discrete times can be selected and a 2×2 can be formed from which the amplitude functions can be computed as:

$$\varepsilon\hat{q}(x) = \frac{\tilde{q}(x,t_1) - \tilde{q}(x,t_2)}{e^{-\omega t_1} - e^{-\omega t_2}} \tag{2.3.37}$$

where t_1 and t_2 are two subsequent timesteps within the linear decay regime from which the flow fields are extracted.

2.3.4 Data driven stability analysis – Dynamic mode decomposition

Dynamic mode decomposition (DMD) is a numerical technique usually used to identify coherent flow structures in experimental of simulation data [Sch10]. In order to do that, a collection of flow snapshots is required which are then decomposed and in case of the flow being in the linear decay regime (small perturbations in the base flow) the extracted modes are equivalent to the result of a global stability analysis for a nonlinear flow [Sch10]. The result of the aforementioned decomposition yields structures of a linear tangent approximation to the underlying flow and can provide a description of fluid elements that express the most dominant dynamic behavior that is captured in the examined flow snapshots [Sch10, Sch11]. The method does not utilize a matrix formulation but relies only on the input data, ignoring any information about the underlying system matrix [Sch10]. The outline of the DMD algorithm used in this work is outlined in this section.

Let s_i be one snapshot of a flow field in a particular time. Then a collection of the flow field snapshot is arranged in two matrices such as:

$$S_1 = [s_1, s_2, \dots, s_{m-1}], \qquad S_2 = [s_1, s_2, \dots, s_m] \tag{2.3.38}$$

Then the Singular Value Decomposition (SVD) of matrix S_1 can be written as:

$$S_1 = \mathbf{U}\Sigma V^* \tag{2.3.39}$$

where $\mathbf{U}$ is an orthogonal matrix whose column vectors are the left singular vector of S_1 and is of size $n \times r$, Σ is a diagonal matrix containing the singular values of S_1 and is of size $r \times r$ and $V$is a matrix whose columns contain the right singular vectors of S_1 while $V^*$is the conjugate transpose of V and is of size $m \times r$ and r is the truncated value. The superscript $(*)$ herein denotes the conjugate transpose matrix. Then matrix $\hat{A}$ is defined such as:

$$\hat{A} = \mathbf{U}^* S_2 V \Sigma^{-1} \tag{2.3.40}$$

The eigenvalues and eigenvectors of $\hat{A}$ are computed as:

$$\hat{A}\tilde{y} = \Lambda\tilde{y} \tag{2.3.41}$$

Finally, the DMD mode corresponding to the DMD eigenvalue Λ is given by:

$$\tilde{\Phi} = \mathbf{U}\tilde{y} \tag{2.3.42}$$

In this version of the DMD algorithm it is assumed that the data is a sequential dataset of vectors.

2.4 Introduction to hypersonic and waverider vehicles design

In this section a short introduction to hypersonic vehicles design will be given. The potential benefits derived from the practical implementation of reusable hypersonic flight vehicles are desirable for all developed societies. However, the natural phenomena that occur during a hypersonic flight within the atmosphere introduce huge technological challenges that render the design and development of such a hypersonic vehicle a very difficult task. The technical complexities associated with the development of reusable hypersonic vehicles that are capable of controlled performance while withstanding sustained high temperature in a low-density aerodynamic environment are enormous. These natural phenomena which define hypersonic speed are discussed by Anderson and are the following [And06]:

- shock waves causing large flow property and entropy gradients

- high level of viscous interaction between the fluid and the vehicle geometry causing high heat flux and thick boundary layers

- thin shock layers due to the close vicinity of the shock to the surface of the vehicle trapping high temperature flow around the hypersonic object.

All the aforementioned physical phenomena produce large heat loads, which pose a challenge to materials to endure for long time periods. Therefore, material options for hypersonic vehicles are very slim and the residence time in the hypersonic regime very limited. The major technological challenges are the undesirable properties of existing materials and limited capabilities of existing thermal protection systems.

Furthermore, there are limited options and capabilities of current propulsion systems to provide and sustain the thrust required for hypersonic speeds. This is the main reason why all successful hypersonic crafts use rockets to provide the thrust needed to achieve hypersonic speeds. Rockets, which have proven to be very effective, are expensively inefficient. The required fuel accounts for a large portion of the take-off weight and success of rocket propulsion requires a very accurate and precise design of explosions. Alternatively, with the recent successful test flights of the X-51A [Mil01] and X-43A [Vol06], the scramjet is showing promise as another feasible option for hypersonic propulsion. The scramjet is a dynamic thrust airbreathing propulsion system that uses oxygen from the atmosphere as fuel. This feature dramatically decreases the weight of the required onboard fuel and entails higher performance efficiency than rockets as shown in Figure *2.6*.

Research efforts are also made in field of the design of the Magneto hydrodynamics (MHD) supersonic turbojet engines which are projected to be capable of a wide range of speeds of Mach numbers and more specifically between *0* and *7* utilizing existing technology [Bla03]. Both the scramjet and MHD supersonic turbojet are immature technologies still undergoing research studies and are not yet ready for extensive practical use. Since its inception in the 1950s, the waverider has been an object of study [Lun15]. Once a conceptual design is devised, the next step is its analysis. Aerodynamic analyses of flight vehicle configurations are obtained through various means. The typical methods are the use of engineering correlations, flight tests,

wind tunnel testing and numerical simulations. These methods are not only used for analyses but also proof of concept and building of knowledge. In the subsonic regime, each method has shown to be effective in conclusively determining performance and gaining scientific perspective. However, in hypersonics, each method has shown to have some issues in its reliability and/or implementation. Still research continues to improve upon these methods to gain knowledge for mastering the hypersonic regime.

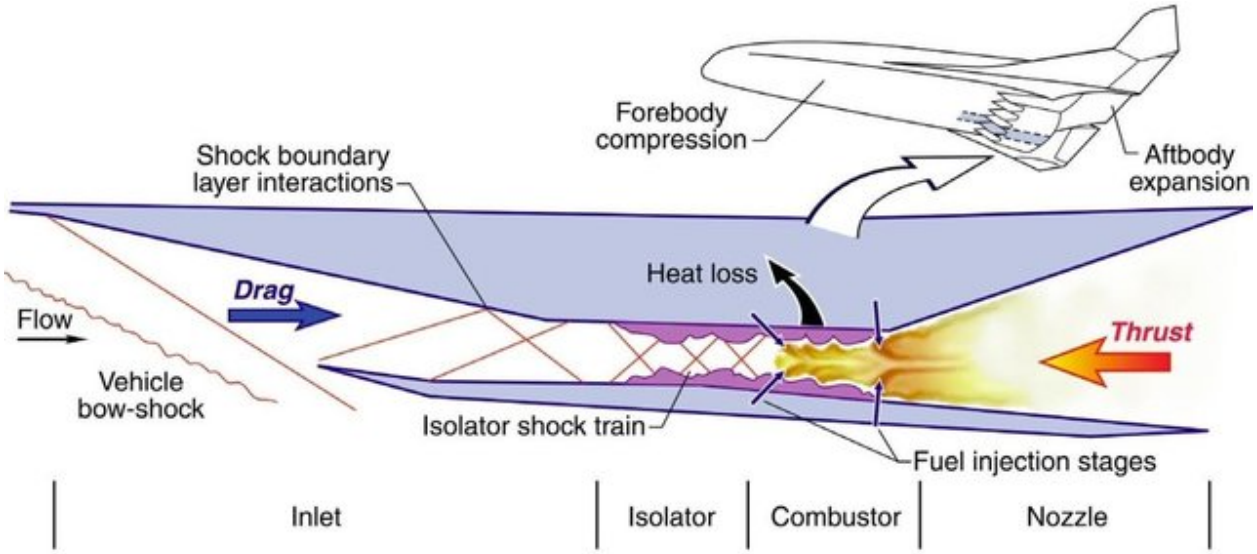

Figure 2.6. *Visual representation of a scramjet engine. Adapted from [Ser12].*

During the early quest for hypersonic flight, NASA designed, constructed and tested a hypersonic vehicle [And06]. The vehicle, illustrated in Figure *2.7*, demonstrated that it was capable of achieving speeds up to Mach 8 [Flo63]. However, a closer look at wind tunnel data revealed an interesting phenomenon. It was observed that the vehicle's aerodynamic performance parameter L/D decreased as Mach number increased [Flo63]. Consequently, Kuchemann et al. [Kuc78] conducted an extended number of empirical studies of supersonic/hypersonic research and vehicle performance of that time over a range of Mach numbers and documented the trend of the maximum L/D decrease as Mach number increased establishing a parameter called the L/D barrier. This attempt highlights another challenge in the realization of hypersonic flight vehicles; the traditional aerodynamic designs and design methodology were not effective in the hypersonic regime. Later on, Bowcutt, showed a method to optimize waverider configurations using a multidisciplinary approach yielding geometric configurations with relatively higher L/D ratios at higher Mach numbers [Bow01]. Bowcutt's findings were also supported by others [Coc94, Cor88]. Figure *2.8* illustrates the comparison of Kuchemann, Bowcutt and Corda findings; the non-filled circles represent experimental data obtained from flight tests and experiments. Kuchemann established the solid line and Bowcutt established the dashed line [Kuc78, Bow01]. The work of Bowcutt renewed interest in the waverider design technique that was first introduced in the 1950's by Nonweiler during his attempt to design a hypersonic wing for re-entry purposes. Figure*2.9*, established by Kuchemann, represents vehicle configurations that will likely achieve maximum L/D in their respective flight regime [Kuc78]. As evidenced, the trend shows a highly integrated vehicle configuration with aerodynamic and propulsion features fused together, would fare as the

optimum aerodynamic configuration for the hypersonic regime. The waverider design methodology inherently yields geometries that support this type of configuration.

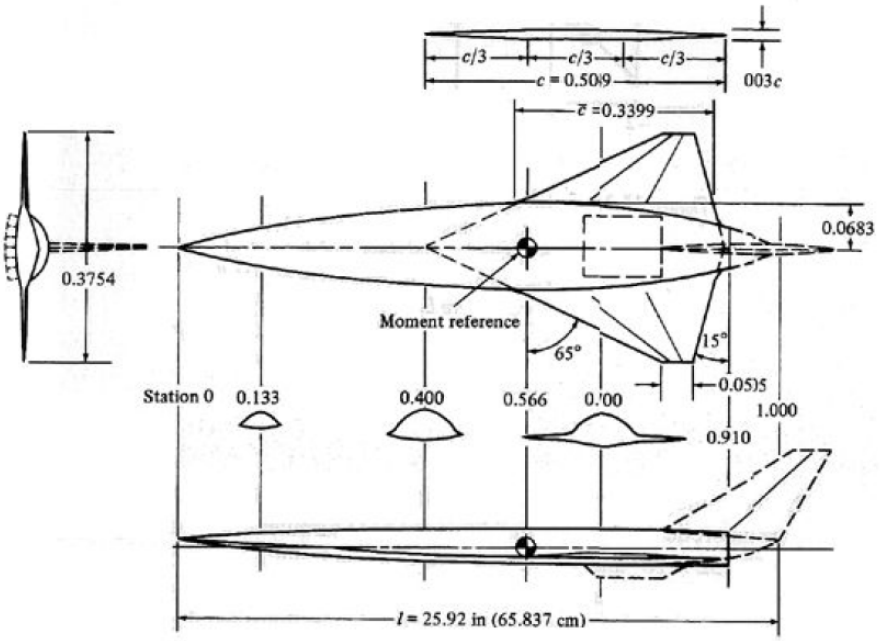

Figure 2.7. *NASA first hypersonic vehicle. Adapted from [Flo63].*

A waverider is a hypersonic vehicle configuration designed such that the high pressure due to the shockwave generated is only exerted to the lower surface of the vehicle. This configuration is achieved through an inverse design methodology that sets the leading edge of the geometry onto a generated shock. At the time of its creation, the waverider design concept solved a major re-entry problem by yielding configurations with the L/D needed for long-range glided re-entry landings. However, the leading edge of a waverider is inherently sharp which yields an extreme aerothermodynamic load. Also, early waverider configurations of the 1950's and 1960's were thin and presented limited 'volumetric efficiencies and their performance analysis did not consider viscous effects [Flo63]. Computational resources in the 1950s were not available to produce a wider range of configurations or perform viscous analysis due to their computational load. These circumstances rendered waveriders unrealistic at the time. However, the work of Bowcutt during the 1980s summarized in [Bow01] optimized waveriders by implementing established engineering relations and computational resources to predict the viscous effects on performance. However, even with the excitement of the waverider potential, the design methodology has yet to extend to a practical design of a working hypersonic vehicle.

Waveriders are designed as products of a hypersonic flow environment through an inverse design methodology. The inverse design approach uses the streamlines of a post shock inviscid flow field as the design space for the compression stream surface (usually the lower surface) of waverider geometries. The waverider methodology ideally produces a streamlined geometry for the hypersonic flow regime. The lower surface formed by a set of neighboring streamlines yields the attachment of the leading edge to the shock. Below a short version of a design algorithm for waverider generation is given:

- Selection and design of the cone to produce the basic flow field

- Solving the basic flow field using Taylor-Maccoll equation, or Euler or Navier-Stokes
- Tracing the streamlines
- Application of the osculating cone theory in the spanwise direction

- Remodel the final model

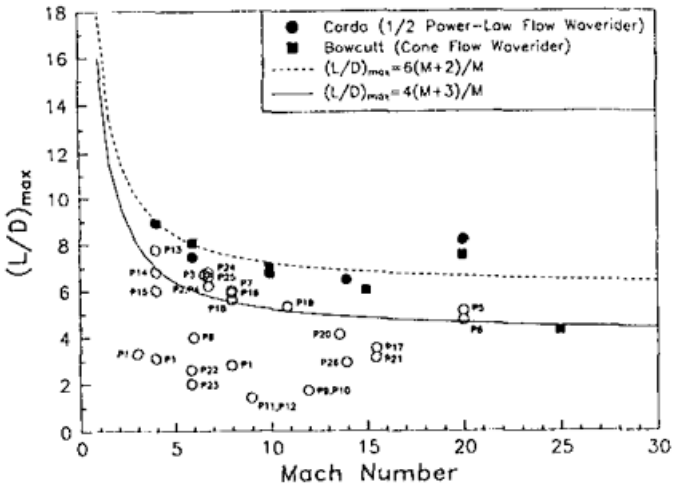

Figure 2.8. *L/D barriers. Adapted from [Cor88].*

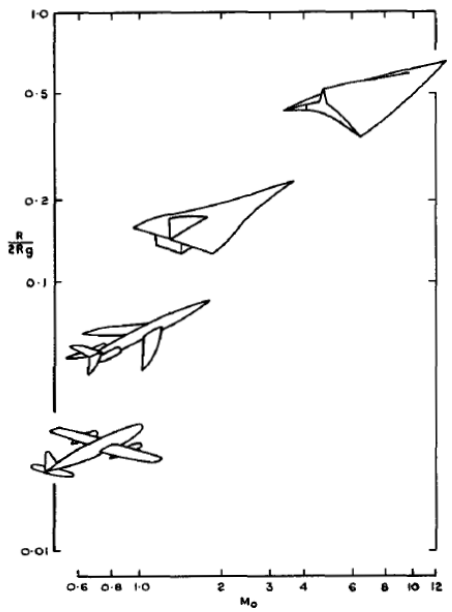

Figure 2.9. *Aircraft flight spectrum. Adapted from [Kuc78].*

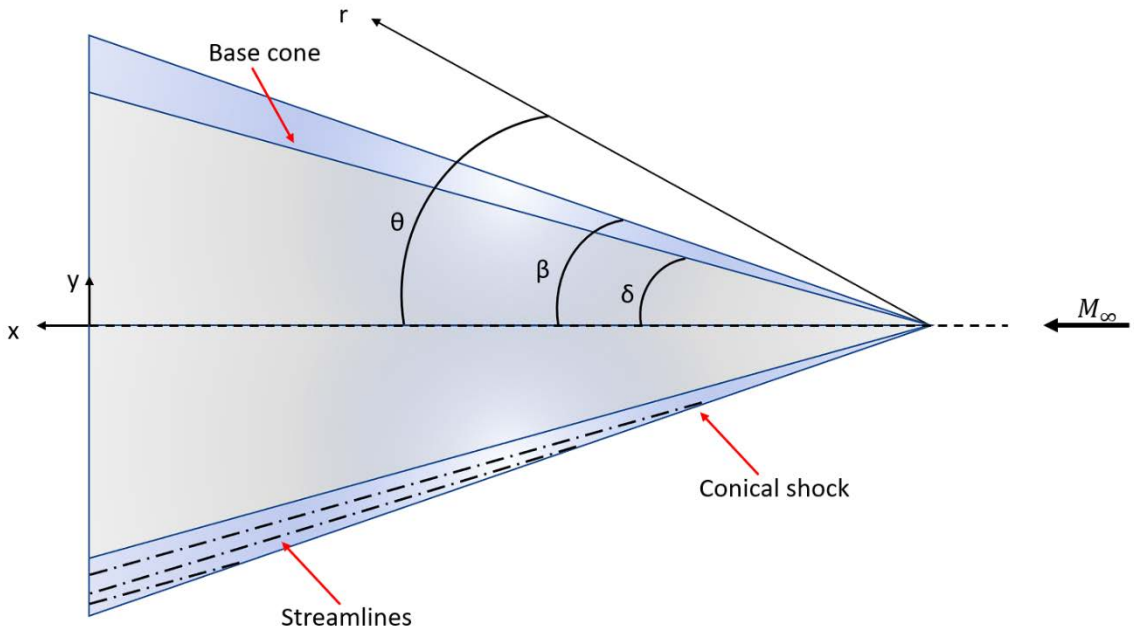

Figure 2.10. *Schematic approach of the design methodology.*

More specifically, to define the initial flow field from which the waverider will be derived a cone is designed with an angle δ. Then the inlet boundary conditions are defined such as Mach number, pressure and temperature and the flow field is calculated using a computational fluid dynamics method. After obtaining the flow field, the streamlines can be traced by numerically evaluating equation (2.3.1) by marching from points located on the shock to obtain streamline points. A schematic representation of the traced streamlines from the conical shock is shown in Figure *2.10*.

$$\frac{dr}{V_r} = \frac{r d\vartheta}{V_\vartheta} \tag{2.3.1}$$

In order to specify the waverider geometry using the osculating cone waverider derived method, firstly, a base curve must be specified. The base curve is then projected into the shock parallel to the freestream to obtain the leading edge. After that, streamlines are traced from the leading-edge locations on the shock back to the base plane to generate the compression (lower) surface of the waverider. Apart from the analytical equation (2.3.1) another more simplified technique also can be used to trace the streamlines as well. Streamlines can be traced tangential to the base cone surface to easily obtain the compression surface geometry. The base curve equation used for the waverider design is shown around the symmetry plane in Figure *2.11*. Denoted as l is the total width of the waverider, while l_u is the flat part of the curve. The curved part of the curve can be calculated by the equation shown in Figure *2.11*. The value of b can be calculated given the l_u,l and h which can be specified after the solution of the initial conical flow field.

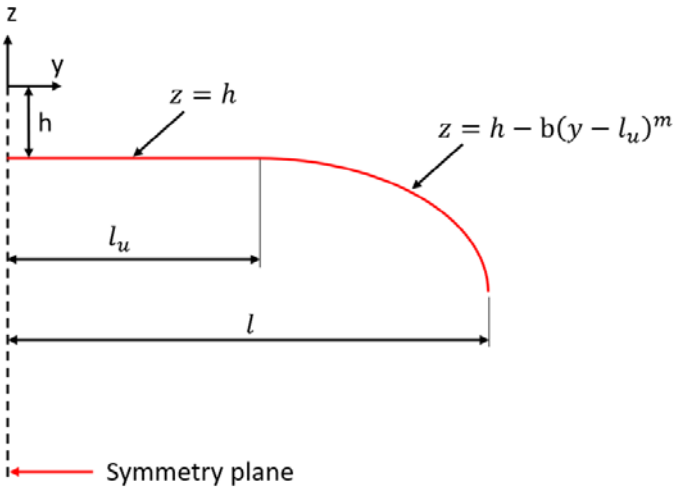

Figure 2.11. *Base curve equation.*

To produce a practical waverider design, the inherent sharp leading edge must be handled properly. Therefore, a practical design approach must incorporate blunting techniques to accomplish this task. Blunting the leading edge as well as areas where two stream surfaces meet relieves heating effects and yields a more realistic shape for manufacturing processes. On the other hand, blunting inherently deviates from a true waverider design and allows some leakage of pressure from the lower surface to upper surface. Hence, drag is increased and aerodynamic performance of a waverider is decreased. It has been shown through studies [San09, Che11] that blunting decreases the heat flux experienced by a vehicle while negatively affecting its L/D. Even with this effect, a blunted waverider design will still potentially provide exceptional aerodynamic performance compared to others. The seepage of pressure can be controlled and potentially minimized through the design of the leading edge. The amount and type of blunting must be determined through a compromise between minimizing heating and maximizing aerodynamic performance. As there is a variety of configurations for a waverider, there is a variety of designs for a blunt leading edge [Tin94]. There are two main approaches to blunting a leading edge as shown in Figure *2.12* [Tin94]. One approach removes material and the other adds material. Tincher and Burnett in their joint work suggested the addition of material will have less of an aerodynamic cost [Tin94].

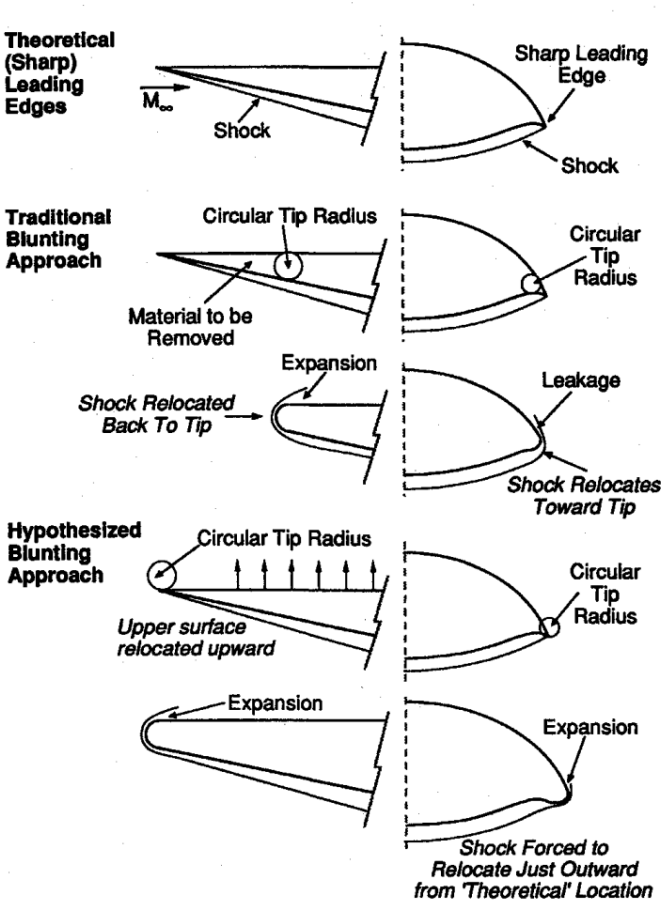

Figure 2.11. *The two main leading-edge curving techniques. Adapted from [Tin94].*

3. Numerical Results

Definitions

In order to get a better understanding of hypersonic flows several different in nature cases were examined. Amongst, there were also validation test cases widely known in literature both two- and three-dimensional as well as comparisons with experimental data and results obtained by other solvers. The compared solutions with the CFD code GALATEA [Lyg13] concern mainly the pressure coefficient distribution as defined in [Abb49, Mun98]

$$C_p = \frac{2\,(p\text{-}p_\infty)}{\rho_\infty \vec{V}_\infty^2} \tag{3.1}$$

where p denotes the local pressure and p_∞, ρ_∞, V_∞^2 the pressure, density and velocity at the free-stream respectively. Furthermore, in flows over aircraft-like geometries, the lift and drag coefficients are used for comparisons. These can be computed as [Abb49, Mun98]

$$C_L = \frac{2L}{\rho_\infty \vec{V}_\infty^2 S} \tag{3.2}$$

$$C_p = \frac{2D}{\rho_\infty \vec{V}_\infty^2 S} \tag{3.3}$$

where S is a characteristic area of the aircraft (usually the mean aerodynamic cord or the fuselage length). The total lift L and drag D forces in GALATEA are evaluated by a single loop over the boundary nodes or faces using the (pressure and viscous) stress tensor (near-field analysis) [Vos10, Vos13]. Whereas, in the DSMC these are calculated as the three-dimensional force and components acting on the surface elements.

This section is continued with the evaluation of the proposed methodology against test cases, considering rarefied flows in the slip regime over complex geometries. All the quantities denoted with the ∞ sign refer to freestream, whereas those with the *e* refer to boundary layer edge values and those with the *w* refer to wall values. For the test cases presented in this chapter the in-house GALATEA CFD code was used for solving the dimensionless Navier-Stokes PDEs [Lyg15, Lyg16]. For the DSMC solutions the code used in all calculations is the open-source SPARTA DSMC kernel developed in Sandia National Laboratories [Gal14].

All flow properties with the subscript symbol of ∞ concern the free-stream properties while the properties having the w subscript symbol refer to wall properties. For the stability analysis the code LiGHT was used developed in University of Liverpool by Dr. Helio Quintanilha Jr. In the cases entitled *Slip effects and stability analysis of a DSMC generated supersonic boundary layer* and *Hypersonic flow around a flat plate at range of* $4.5 \leq M_\infty \leq 9$ the LiGHT code was ran by Dr. Helio Quintanilha Jr. All the rest stability analysis results were produced by Mr. Kamil Dylewicz. In the cases in which GALATEA was used to solve the Navier-Stokes PDEs the code was ran by Dr. Georgios Lygidakis.

Knudsen number was calculated using the classical definition:

$$Kn = \frac{\lambda}{D} \tag{3.4}$$

where λ is the mean free path and D is the characteristic length unless stated otherwise. The mean free path is calculated using the equation:

$$\lambda = \frac{1}{\sqrt{2}\,\pi\, d_{ref}^2\, N_d \left(\frac{T_{ref}}{T}\right)^{\omega - \frac{1}{2}}} \tag{3.5}$$

where d_{ref} is the particle characteristic diameter as mentioned in [Bir94], N_d is the number density, T_{ref} is the characteristic temperature (*273.15 K*), T is the flow temperature and omega is the power law exponent. In all test cases the variable soft sphere (VSS) molecular model has been used as described in [Bir94] and implemented in SPARTA [Gal14]. The code for the analytical calculation of the compressible boundary layer (cBL) was provided by Prof. Vasilios Theofilis. The code used for the dynamic mode decomposition (DMD) is the open-source code PyDMD which implements the DMD method as described by Schmidt [Sch10] and was ran by Mr Kamil Dylewicz.

In simulations where Air is used as the gas it's modelled as 79% N_2 and 21% O_2 unless stated otherwise. In all simulations the Variable Soft Sphere (VSS) molecular model was used. In cases where the Variable Hard Sphere (VHS) model was used the angular scattering parameter (alpha) of VSS was set equal to 1. The two following Tables show the parameters used for the molecular species (Table Species) and the VSS model parameters (Table VSS). Rotational relaxation was considered constant unless stated otherwise.

Table Species: *Species parameters.*

Species	Molecular mass (kg)	Rotational degrees of freedom	Rotational relaxation	Vibrational degrees of freedom	Vibrational relaxation	Vibrational temperature (K)
O_2	5.31×10^{-26}	2	0.2	2	5.58659×10^{-5}	2256
N_2	4.65×10^{-26}	2	0.2	2	1.90114×10^{-5}	3371

Table VSS: *VSS model parameters.*

Species	Diameter (m)	omega	Reference temperature (K)	alpha	Rotational relaxation infinite (Z_{rotinf})
O_2	3.96×10^{-10}	0.77	273.15	1.4	16.5
N_2	4.07×10^{-10}	0.74	273.15	1.6	18.1

3.1 Rarefied flow over a NACA 0012 wing

The first validation test case is a flow over a NACA 0012 airfoil [Fan01, Sho14, All85] at two different angles of attack. The first angle is equal to 0^o (Case *1*) whereas the second is 10^o (Case *2*) [Fan01, Sho14, All85]. The grid utilized for the CFD code comprises of *305,978* nodes, *566,245* tetrahedra and *394,760* prisms the latter located on the solid wall region to allow for effective prediction of the boundary layer region. The Mach number was assumed equal to *2.0*, while the Knudsen and Reynolds numbers are equal to *0.026* and *106* [Sho14] respectively, the latter based on the mean aerodynamic cord, which was re-dimensionalized to become equal to unity due to the dimensionless formulation of the code [Lyg15]. Freestream temperature was set to *161 K*, while the corresponding value on the surface was set to *290 K*. The aforementioned flow conditions are summarized in Table *3.1*.

For the computation of the inviscid fluxes the Roe's approximate Riemann solver along with a second-order spatial accurate scheme, coupled with the Min-mod limiter, was employed; the corresponding viscous fluxes were computed based on the nodal-averaging scheme. Time integration was succeeded via the incorporated explicit scheme (Runge-Kutta method) with a CFL number equal to *0.5*. Both the incorporated first- and second-order spatial accurate slip models were implemented [Bes99]. However, no difference was identified between their results; this lack of difference is attributed to the relatively fine grid utilized. To accelerate the solution procedure on a DELL™ R815 PowerEdge Server with four AMD Opteron™ *6380* sixteen-core processors) the initial grid was decomposed in four sub-domains to be processed in parallel; two coarser levels were constructed for each of them applying the full-coarsening directional agglomeration strategy, in order the incorporated multigrid scheme to be applied [Bes99].

The proposed solver was succeeded with a DSMC approach code, the parallel open-source kernel SPARTA [Gal14]. The encountered computational domain was designed with dimensions *0.38* m and *0.24* m along the x- and y-axis, respectively; its discretization was succeeded with a Cartesian two-dimensional mesh, composed of *1200* cells along x-axis and *800* cells along y-axis. Considering that the mean free path in such test cases is approximately *0.000923 m*, each grid cell was constructed to be more or less *1/3* the size of it, a common practice in such simulations [Bir94]. Furthermore, the grid around the airfoil was generated such as no more than four points, used for airfoil representation (a total number of *1600* was used), to be included at each computational cell; as a result, a smoother discretization was achieved. Figure *3.2* illustrates a close-up view of the utilized computational grid around the NACA0012 airfoil.

The SPARTA code was run on the same to Galatea solver computer system with the flow conditions summarized in Table *3.1*. As far as the simulation parameters are concerned, the number density was set equal to 1.296×10^{21} *particles*$/m^3$, while the time step equal to 3.0×10^{-7} s; the latter value along with the employed grid density ensures that each particle needs approximately three timesteps to cross entirely a grid cell [Bir94]. The simulation began with a transient period of *140,000* steps, producing the initial steady-state solution, while at next samples were taken for additional *40,000* steps, aiming to reduce the statistical scattering error.

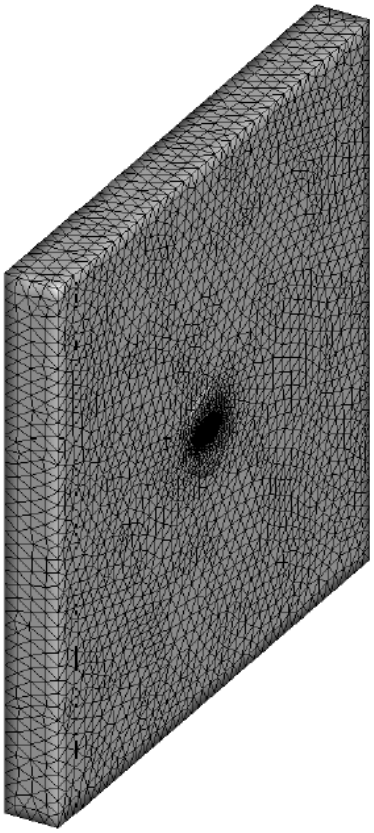

Figure 3.1. *Computational grid used with the Galatea code.*

The aforementioned parameters are outlined in Table *3.2*. Considering that DSMC simulations depend strongly on the employed number of particles, several different numbers of them were tested (between 2×10^6 and 16×10^6) along with the aforementioned grid, as well as with a finer one; the latter was generated by refining each computation cell around the airfoil into *5x5* smaller ones. From this study the optimum number of particles was selected which is of 8×10^6 simulator particles for the whole simulation domain. As far as the grid is concerned, no difference was identified, hence, the initial mesh was selected. The previous parameters defining actually the DoFs (Degrees of Freedom) of the simulation were proved to produce the desired accuracy, avoiding though any excessive requirements for computational load and storage.

In Figure *3.4* the extracted velocity contours around the NACA0012 airfoil by both the Galatea and SPARTA solvers are presented for the first test case (Case *1* - angle of attack 0^o). As one can observe a satisfactory comparison is obtained, especially in the bow shock and stagnation regions, indicating qualitatively the potential of the proposed solver for such simulations. Furthermore, a very good agreement can be observed with the available experimental and numerical results, reported in [All85] and [Fan01, Sho14] respectively. It is pointed out that dimensionless values are included in both the aforementioned figures. Figure *3.5* includes the derived distributions, compared with the one reported in [Sho14]; the distribution of Galatea code simulation was extracted from the mid-span of the wing geometry. Similarly, to Case 1, Figure *3.7* illustrates the extracted velocity contours around the NACA0012 airfoil by both the Galatea and SPARTA codes for Case *2* (angle of attack 10^o). Figure *3.5* shows a comparison between the results obtained from both codes and results found

in literature [Sho14]. Once more, a very good qualitative agreement is achieved between the results of the employed solvers and the results found in literature with the comparison for the distributions of the pressure coefficient Cp around the NACA0012 airfoil, depicted in Figure *3.5*. Figure *3.6* shows a comparison of the results obtained from SPARTA and Galatea in Case *2* where the airfoil is at an angle of attack of 10^o. It is obvious that for both test cases (with angle of attack $0^o$and 10^o) the employed codes produce almost identical results, despite they are based on completely different numerical approaches.

Table 3.1: *Flow parameters (rarefied flow over a NACA 0012 wing).*

Case	M_∞	Re_∞	Kn_∞	$U_\infty\ (m/s)$	***a (deg)***	$\rho_\infty\ (kg/m^3)$	T_∞ ***(K)***	T_w ***(K)***
1	*2.0*	*106*	*0.026*	*506*	*0*	6.026×10^{-5}	*161*	*290*
2	*2.0*	*106*	*0.026*	*506*	*10*	6.026×10^{-5}	*161*	*290*

Table 3.2: *CFD computational parameters (rarefied gas flow over a re-entry capsule geometry).*

CFD parameters	
Grid density	*305,978 nodes* *566,245 tetrahedra* *394,760 prisms*
Number of partitions	*4*
Iterative scheme	*Second order four-stage Runge-Kutta*
CFL	*0.5*
Computational system	*DELL™ R815 Poweredge Server with four AMD Opteron™ 6380 sixteen-core processors*

Table 3.3: *DSMC computational parameters (rarefied gas flow over a re-entry capsule geometry).*

DSMC parameters	
Grid density	*960,000 Cartesian grid cells*
Number of particles	86×10^6
Number density (particles/m³)	1.296×10^{21}
Timestep (s)	3×10^{-7}
Transient period (timesteps)	*140,000*
Sampling period (timesteps)	*40,000*
Number of cores	*60*
Wall-clock time (h)	*6*

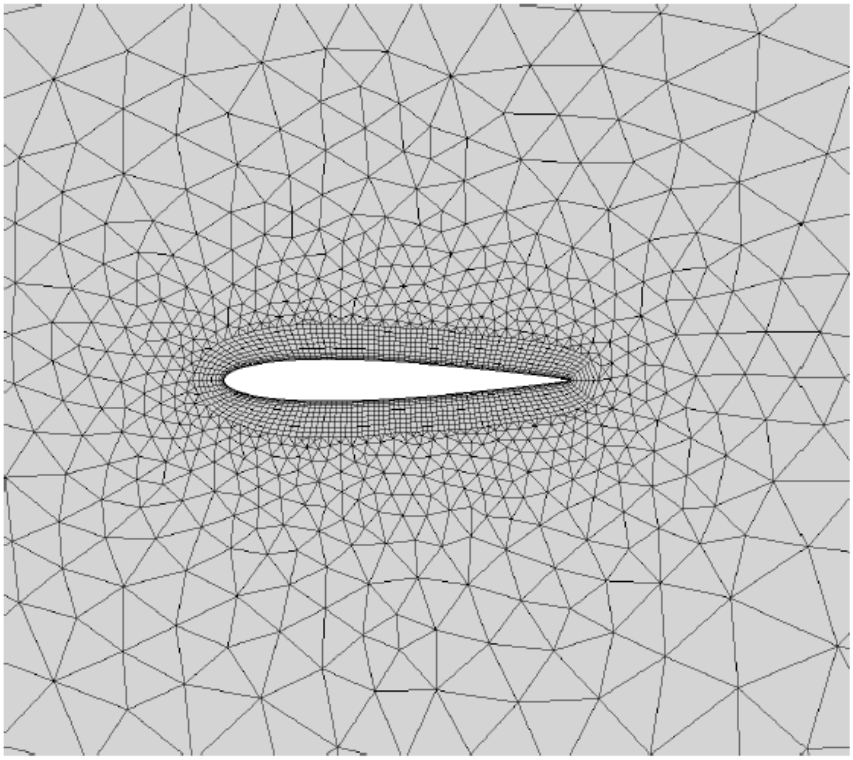

***Figure 3.2**. Density on the symmetry surface of the computational grid used with the Galatea code.*

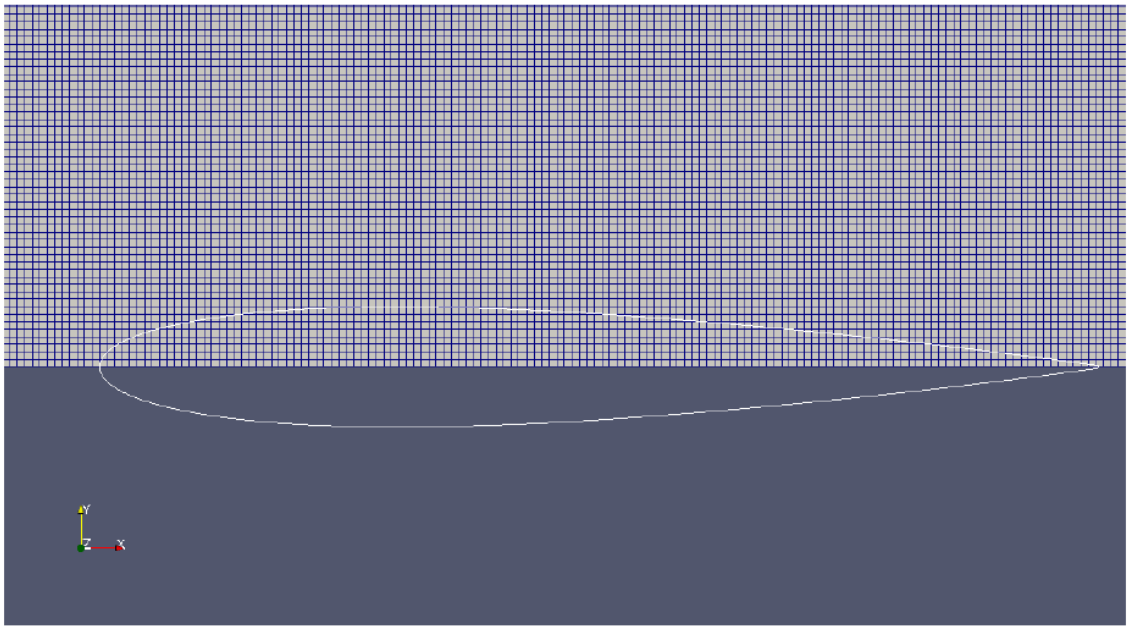

***Figure 3.3**. Computational grid used in SPARTA.*

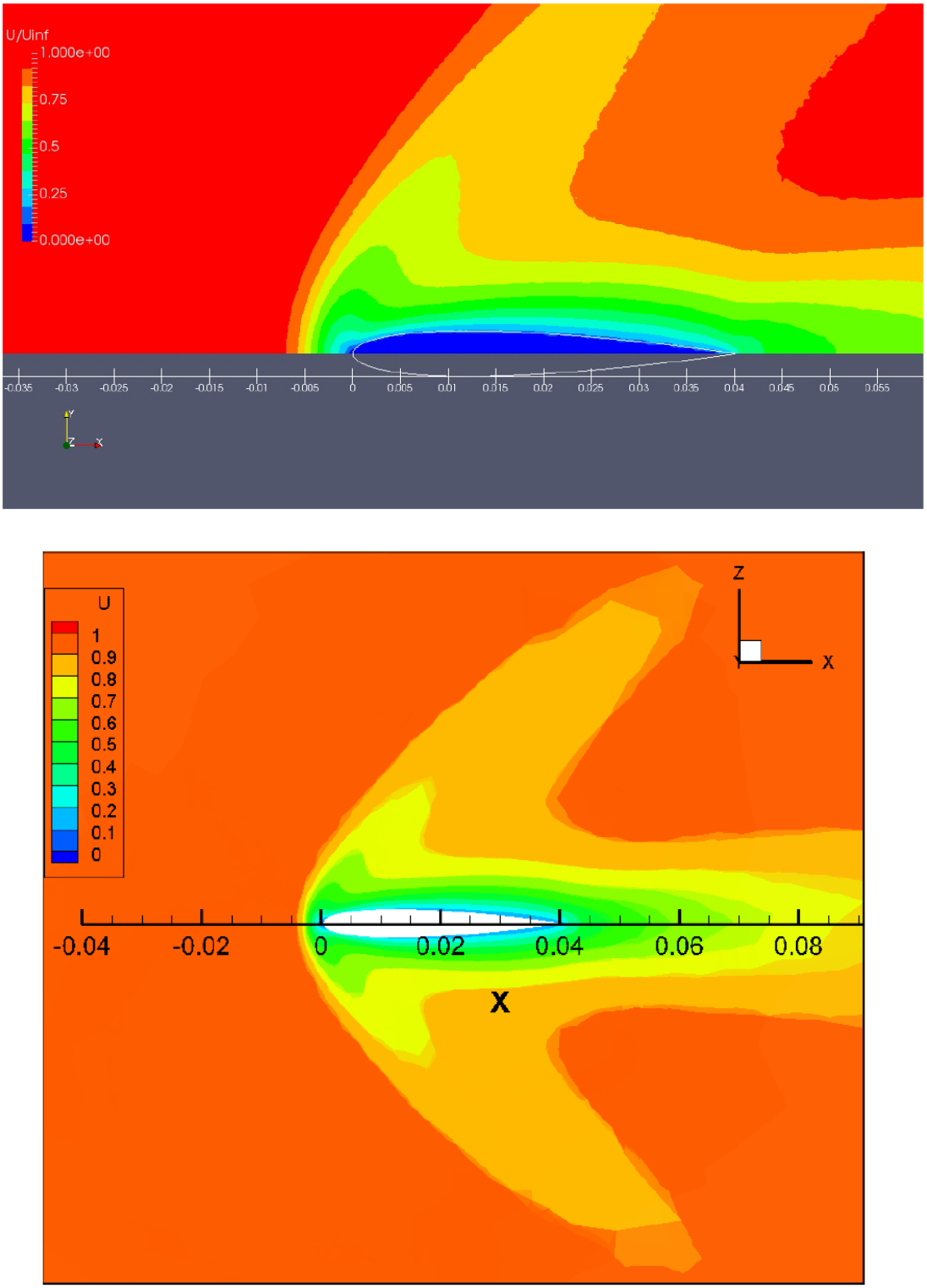

***Figure 3.4**. Velocity contours (Case 1) as obtained from SPARTA (top) and Galatea (bottom).*

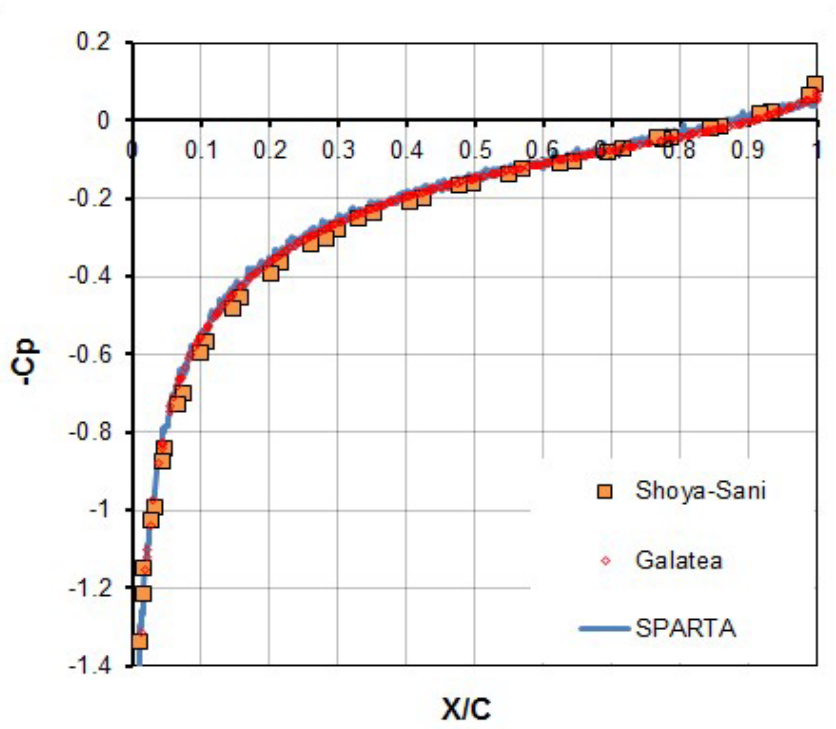

***Figure 3.5**. Distribution of pressure coefficient Cp around the NACA0012 airfoil (Case 1).*

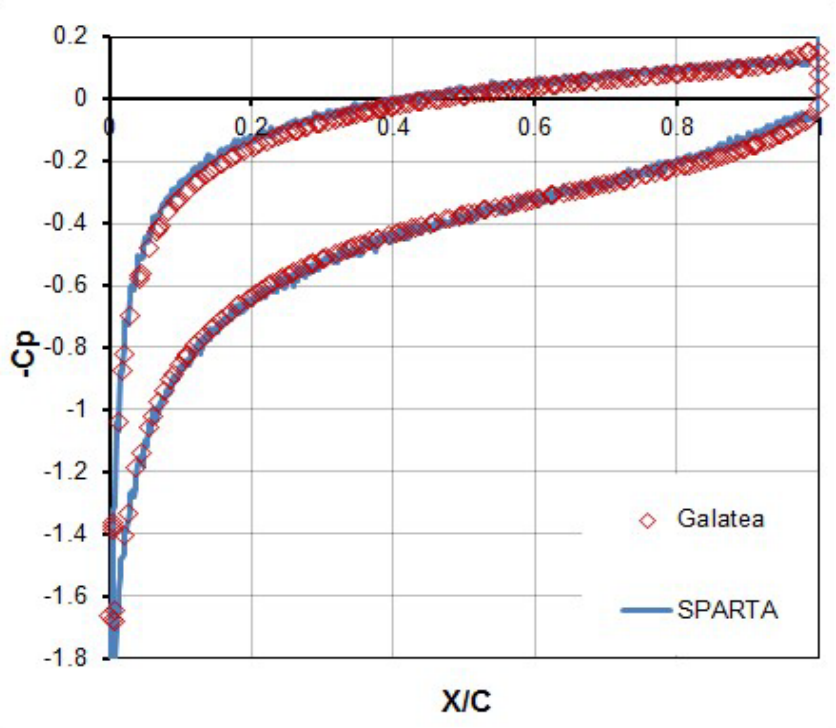

***Figure 3.6**. Distribution of pressure coefficient Cp around the NACA0012 airfoil (Case 2).*

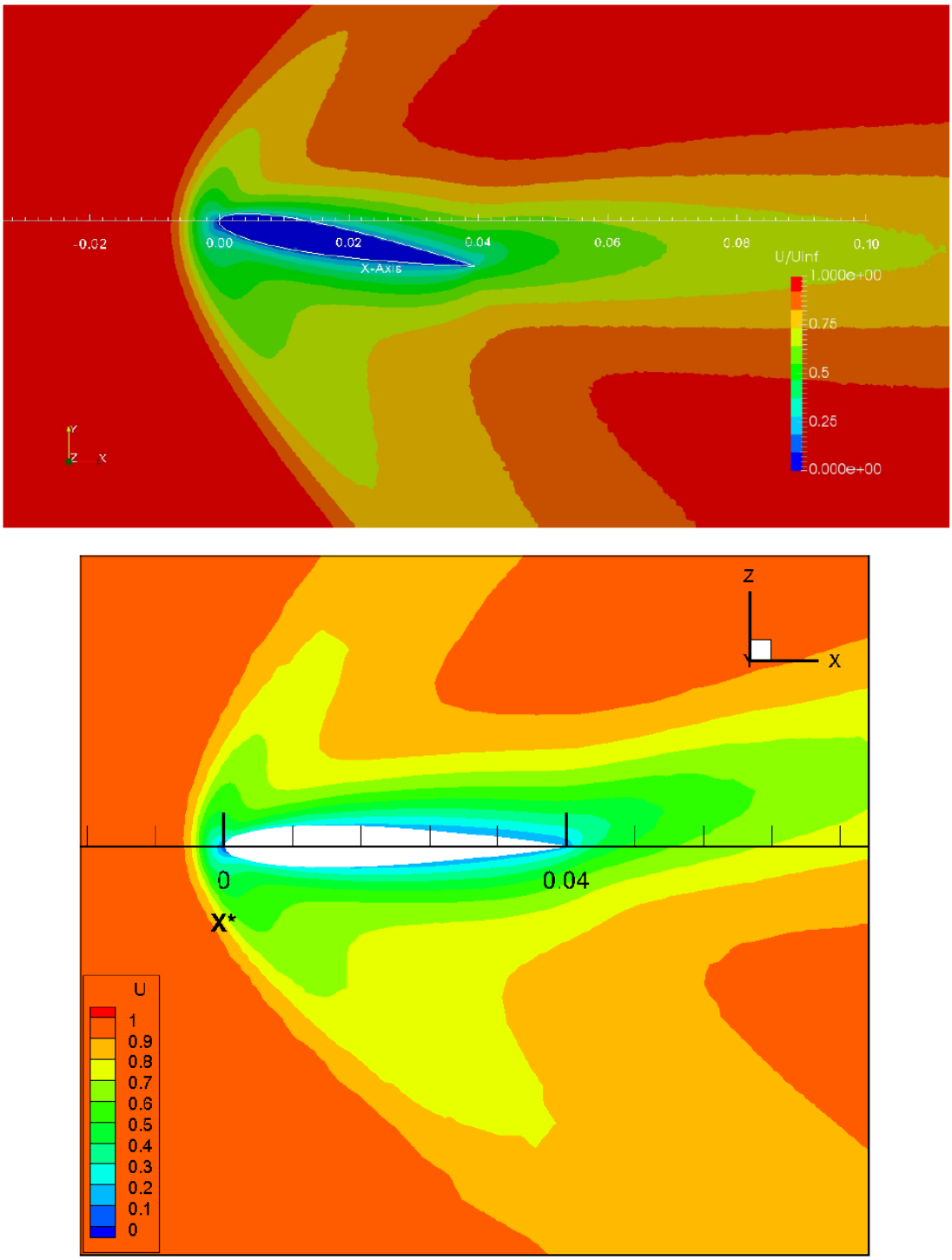

Figure 3.7*. Velocity contours (Case 2) as obtained from SPARTA (top) and Galatea (bottom).*

3.2 Rarefied gas flow over a re-entry space capsule geometry

The second test case is a three-dimensional test case of a Mach *3.2* flow over a space capsule geometry at an angle of attack of 0^o. The examined geometry stands for the blunt portion of a

spaceship returning to Earth after a spaceflight. It resembles the REV (Robotic Enhanced Vehicle) of the DART (Delft Aerospace Reentry Test) demonstrator program [Ott01]. This program began at Delft University of Technology in *2001*, aiming to study the aerodynamic phenomena appearing during the re-entry of space vehicles. An overview of the geometry is shown in Fig. 1. The spherical nose cap has a radius r_n= *345.22* mm, a length L=*1546.63* mm with a cone radius of R=*525* mm. In order to reduce the computational cost only the quarter of the aforementioned configuration was simulated.

For this simulation the flow velocity was set to *850* m/s which results to a Mach number of approximately *3.2*. The freestream temperature was set equal to *168.72* K while the temperature on the surface of the capsule was set to *290* K. The background pressure was set to *0.5* Pa, a value corresponding to an altitude of approximately *90* km. Despite this velocity being relatively small comparing to that of such a space capsule during its re-entry phase, it was assumed to be adequate considering the initial motivation of the study to assess a modified Navier-Stokes solver against a rarefied gas dynamics problem.

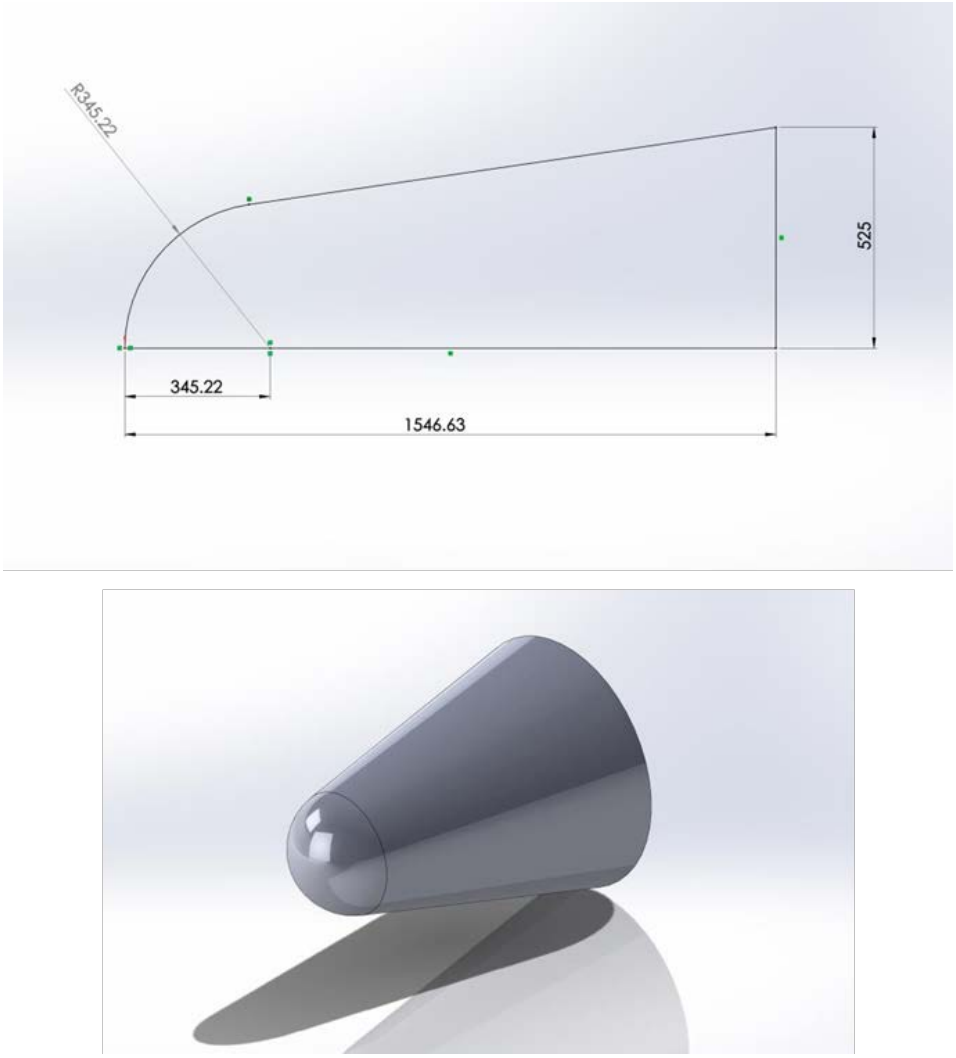

***Figure 3.8**. Capsule geometry details in 2D (top) and 3D (bottom).*

Considering the aforementioned flow data, a hybrid unstructured grid was generated for the CFD solver composed of *4,212,308* nodes, *21,032,650* tetrahedra and *1,168,000* prisms. The

prismatic layers are located on the solid wall region, i.e., close to the surface of the capsule, allowing for accurate prediction of the corresponding flow phenomena [Lyg15, Lyg16]. Figure *3.9* shows the complete computational grid, while Figure *3.10* focuses on the symmetry/capsule surface. In order to use this grid with the dimensionless Galatea solver was re-dimensionalized in order its base's radius to become equal to unity [Lyg15]. For the calculation of the inviscid fluxes the Roe's approximate Riemann solver was employed along with a second-order spatial accurate scheme, coupled with the Van Albada-Van Leer slope limiter [Lyg15, Lyg16]. The nodal-averaging scheme was applied for the computation of the velocity and temperature gradients, and consequently the viscous fluxes. Time integration and iterative approximation of the final steady-state solution was succeeded with the incorporated second-order accurate in time four-stage Runge-Kutta scheme. The CFL number was set equal to *0.5*. To accelerate the iterative procedure the initial grid was divided in eight sub-domains to be processed in parallel [Lyg15] (on a workstation with an AMD FX™ *8350* 8-core processor at 4.00 GHz). Two coarser resolutions were constructed for each of the aforementioned sub- grids, following the incorporated directional agglomeration strategy, in order the corresponding multigrid scheme to accelerate further the solution process [Lyg16].

For the DSMC solution a 2D-axisymmetric computational domain was defined with dimensions *6* m and *2.5* m in x- and r- axis, respectively. Spatial discretization was employed by partitioning of the computational domain to *10,000,000* cells, by constructing a Cartesian grid with *4000* and *2500* cells in $x-$ and $r-$axis, respectively. Regarding the corresponding simulation parameters, the number density was set equal to 2.147×10^{20} particles$/$m^3, whereas the time step was selected equal to 3×10^{-7}s. The time step was defined so that each particle needs approximately five timesteps to cross one cell. The simulation began with a transient period of *100,000* steps, deriving the initial steady-state solution, while samples were taken for additional *60,000* timesteps, aiming to reduce the statistical scattering error. Considering that DSMC methodology relies strongly on the employed number of particles, several different numbers of them were tested (between 10×10^6 and 86×10^6). From these tests the optimum Fnum (real particles per simulator particle) was selected, which subsequently produced a total number of 86×10^6 particles for the whole simulation domain. The aforementioned parameters, defining actually the utilized DoFs (Degrees of Freedom), were revealed to derive the desired accuracy, avoiding yet any excessive computational and memory requirements. The whole parameters used with the SPARTA solver are summarized in Table *3.4*. The DSMC run was carried out on a DELL™ R815 PowerEdge™ server, with four AMD Opteron™ *6380* 16-core processors at *2.50* GHz (*64* cores in total); *60* cores were used for the run, which required approximately *5* days (wall clock).

Figure *3.11* illustrates the pressure coefficient Cp distributions in x and r axis, extracted by both the aforementioned solvers (Galatea and SPARTA). As one can observe, a very satisfactory comparison is obtained. A slight difference in the front area of the capsule geometry can be identified in Figure *3.11* (right), regarding Cp distribution in the r axis. It stems probably from the strong bow shock in front of the capsule. In Figure *3.12* the extracted pressure contours by both solvers are presented. The compared contours appear to be very similar, especially in the bow shock region in front of the capsule. Pressure at the stagnation point was computed approximately equal to *6.8* Pa by both solvers. In Figure *3.13* the extracted (non-dimensional) velocity contours by both solvers are presented. Figure *3.14* contains the axial positions where velocity profiles were extracted; the corresponding profiles are depicted in Figure *3.8*, where a very good agreement between the two solvers is observed. A steeper

velocity transition at the bow shock region is computed by the SPARTA code, compared to the Galatea solver (positions *2*, *3* and *4*, in Figure *3.15*); this is attributed to the relatively low grid density, used by the Galatea solver in the corresponding region (no local grid refinement was applied).

Considering the previously described qualitative and quantitative results, a very satisfactory agreement is clearly identified between the employed solvers, despite the fact that they depend on completely different computational approaches. As a result, the proposed solver's potential to predict effectively such demanding flows is demonstrated.

Table 3.6: *DSMC computational parameters (rarefied gas flow over a re-entry capsule geometry).*

Grid density	*10,000,000 Cartesian grid cells*
Number of particles	86×10^{6}
Number density (particles/m^3)	2.147×10^{20}
Timestep (s)	3×10^{-7}
Transient period (timesteps)	*100,000*
Sampling period (timesteps)	*60,000*
Number of cores	*60*
Wall-clock time (h)	*120*

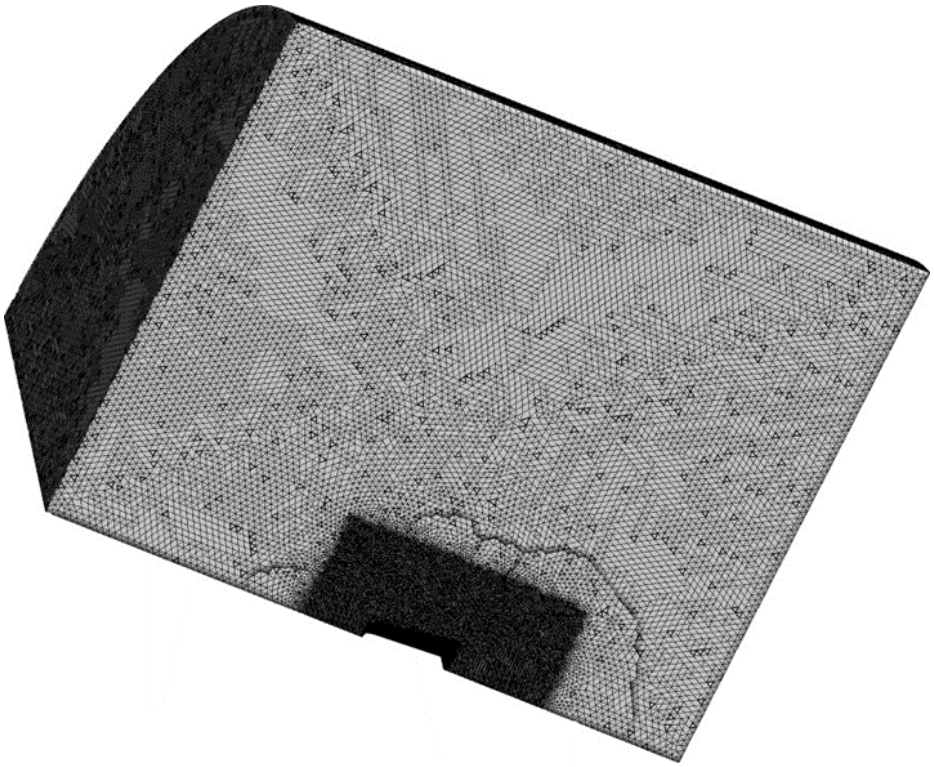

Figure 3.9. *Computational grid used with the Galatea solver.*

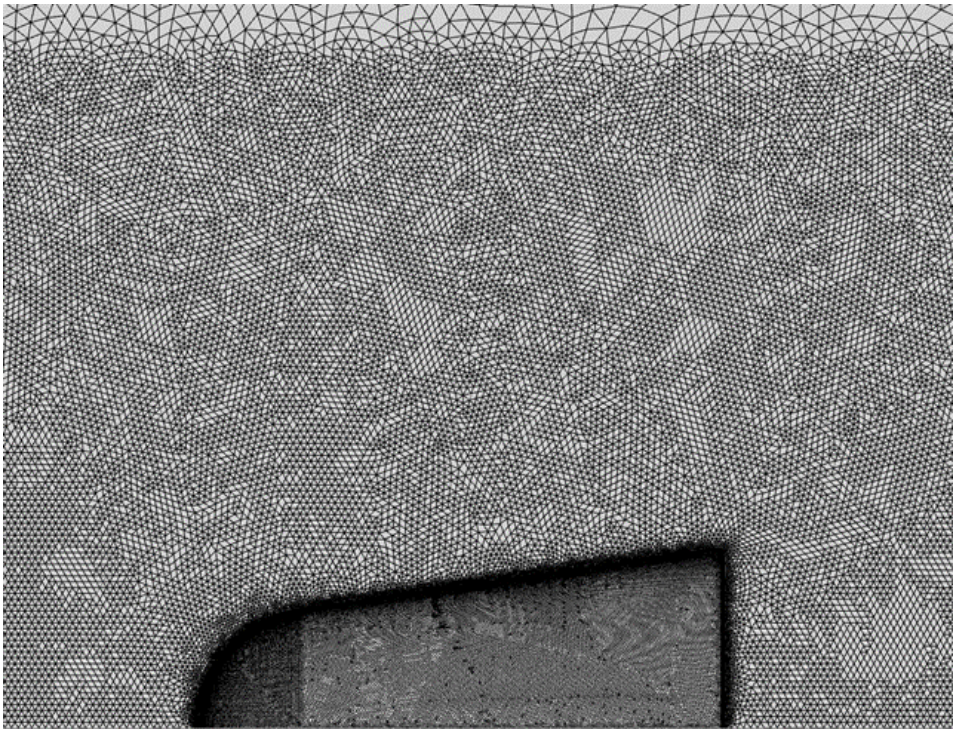

Figure 3.10. *Close-up view of the symmetry/capsule surface of the three-dimensional computational grid.*

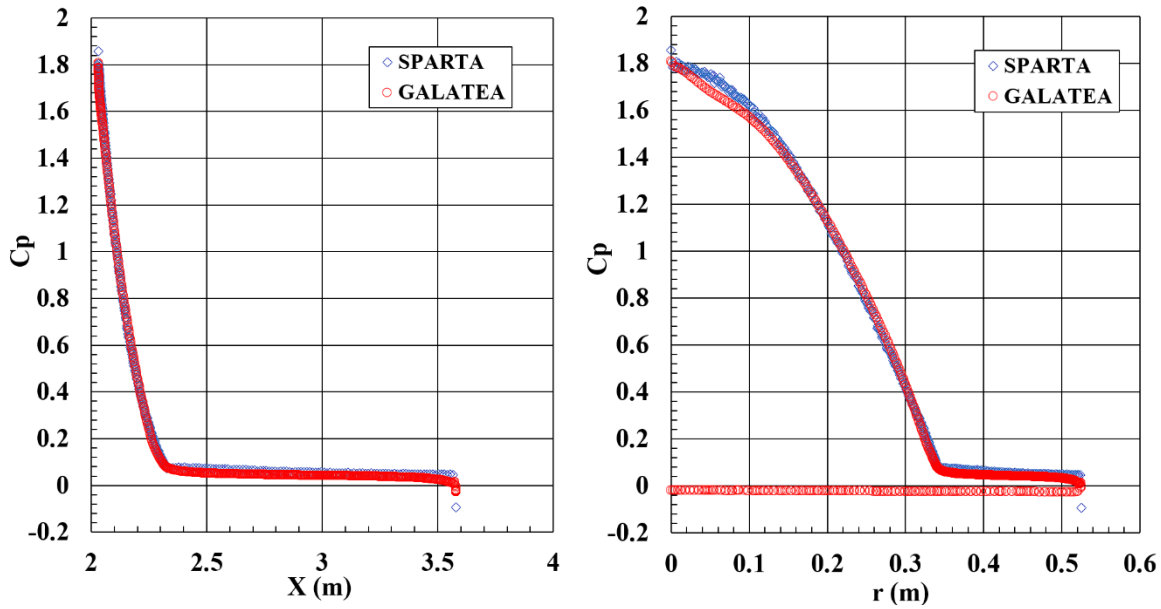

Figure 3.11. *Pressure coefficient distributions at the capsule surface along the x-axis (left) and the r-axis (right).*

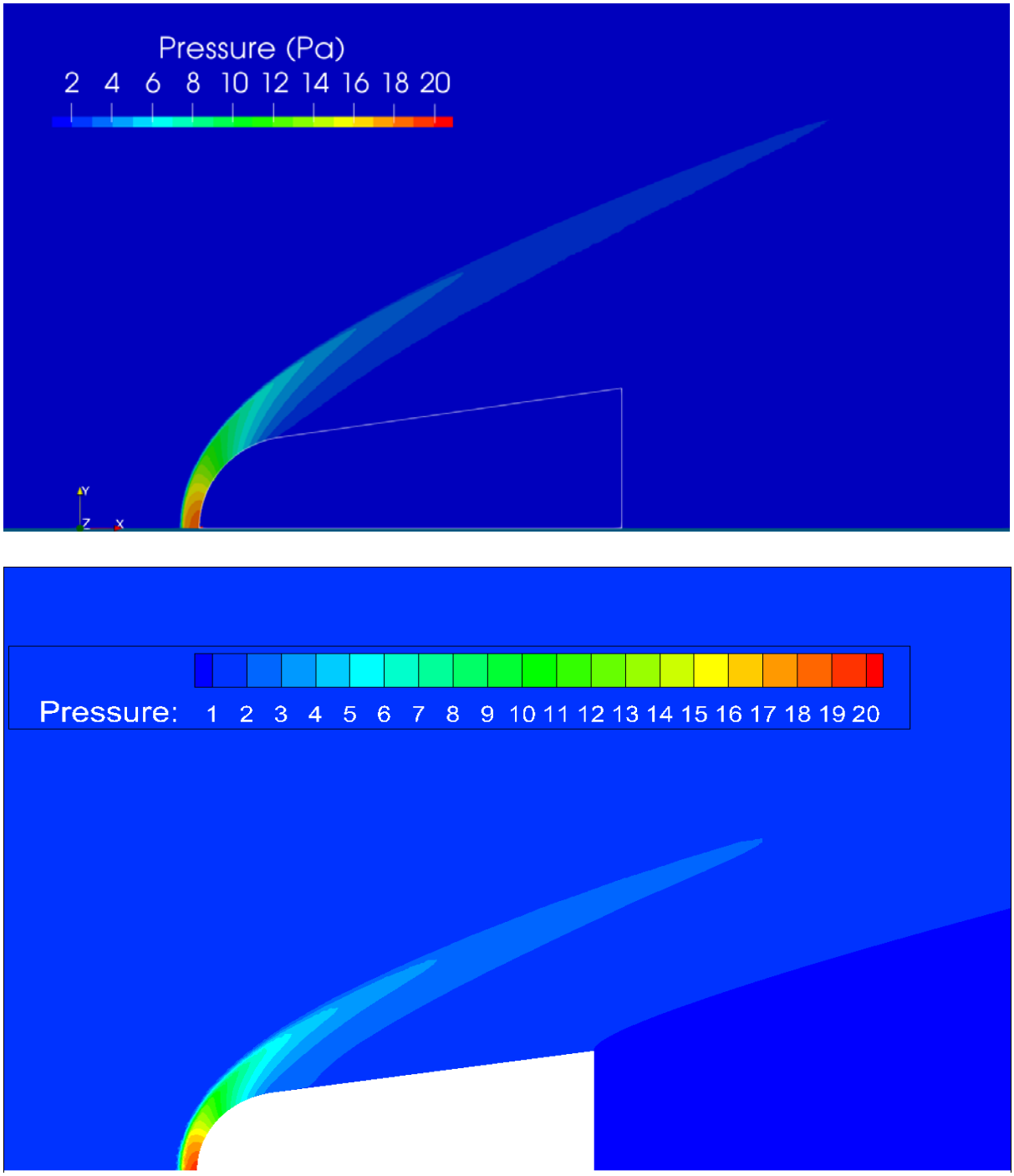

Figure 3.12. *Pressure contours, extracted by the SPARTA software (top) and the Galatea solver (bottom).*

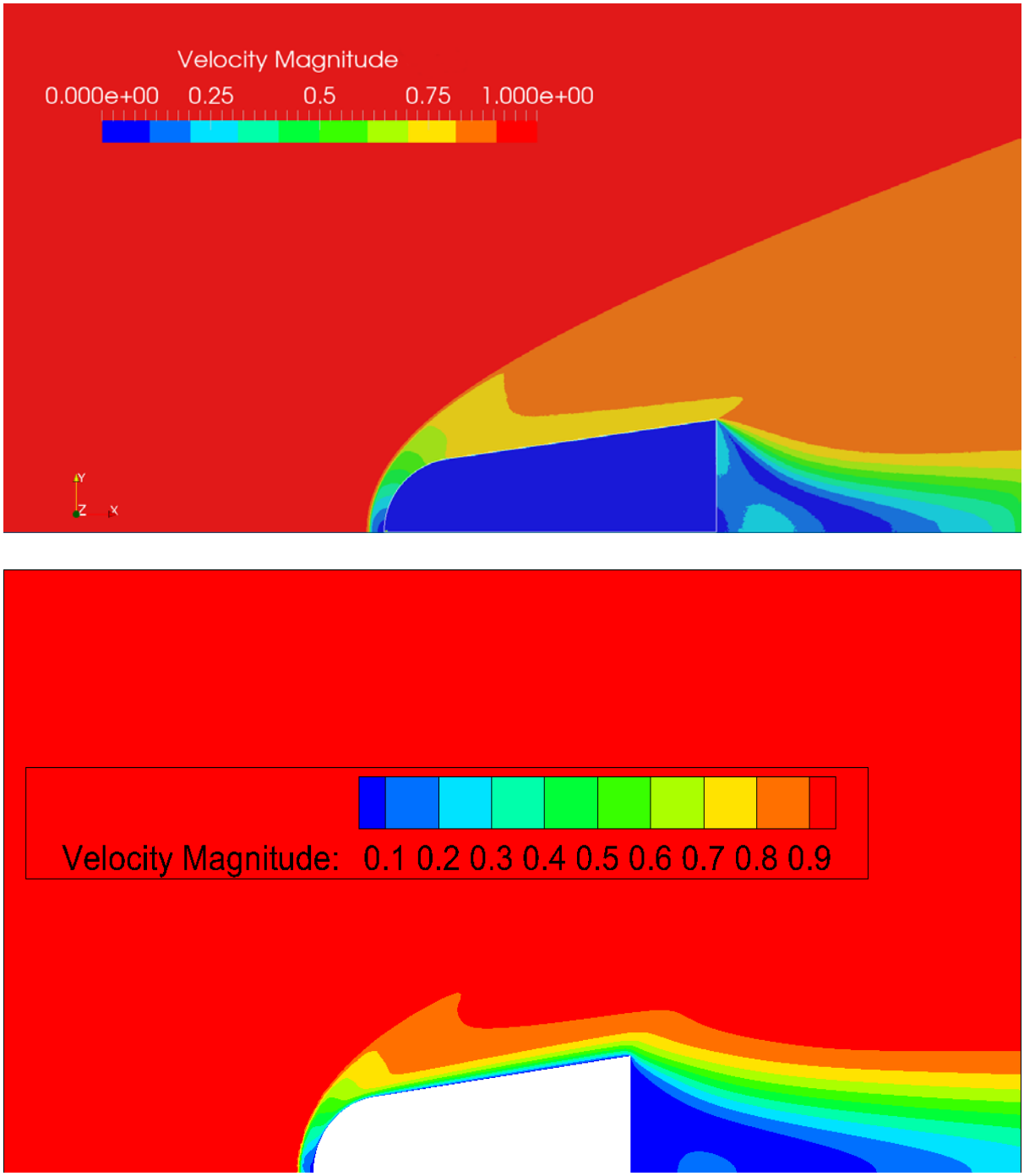

Figure 3.13. *Velocity contours extracted from SPARTA (top) and the Galatea solver (bottom).*

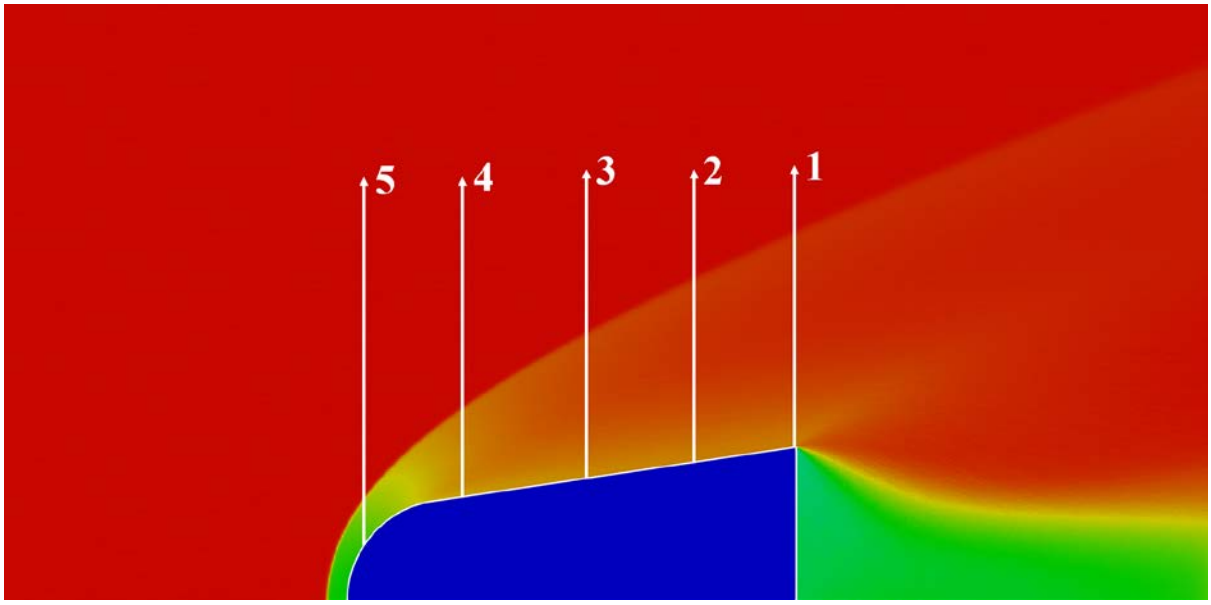

Figure 3.14. *The five axial positions (distance from the cone's base) where velocity profiles were extracted for both solvers (1: x = 0 m; 2: x = 0.355 m; 3: x = 0.71 m; 4: x = 1.065 m; 5: x = 1.42 m).*

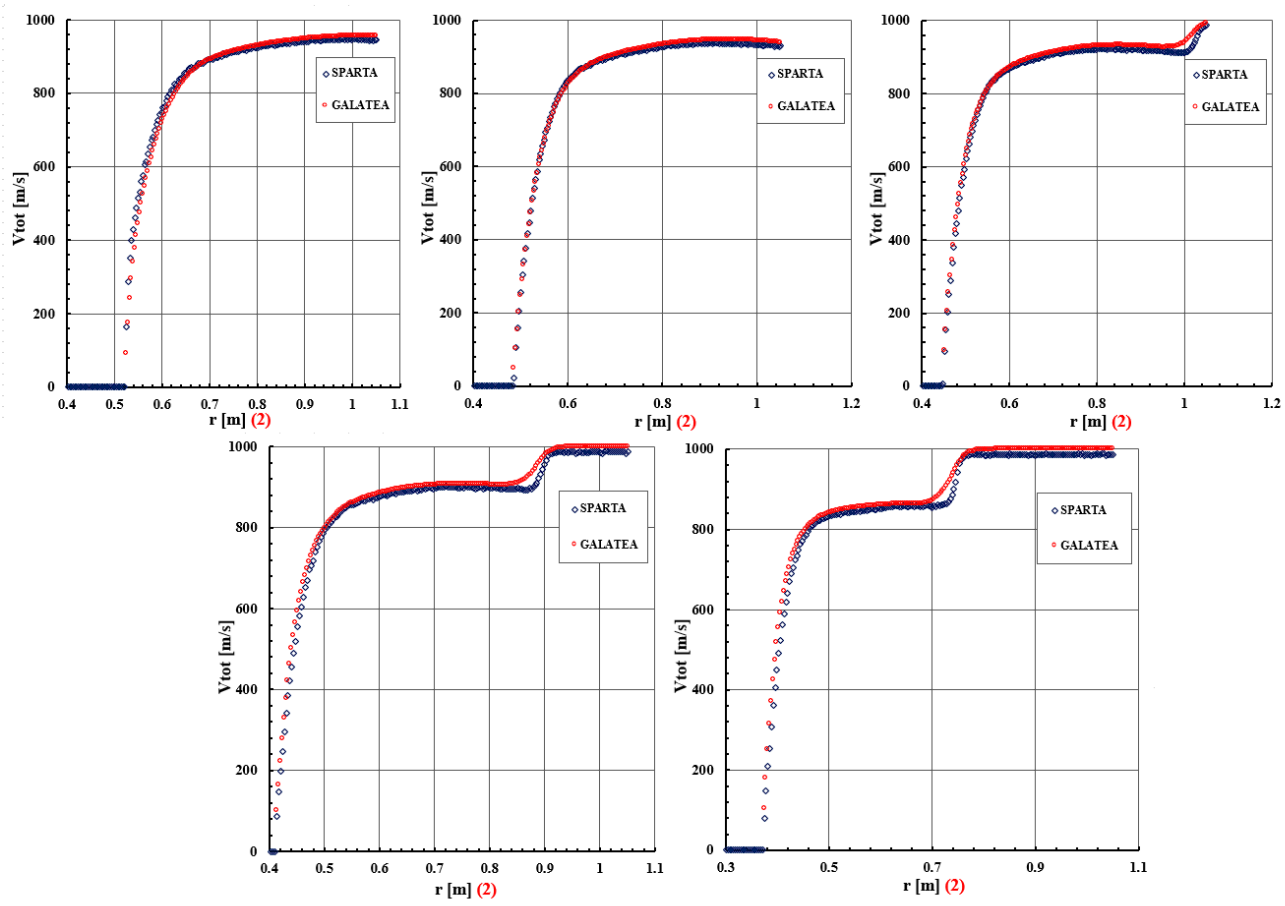

Figure 3.15. *Velocity profiles, extracted for both solvers at the five axial positions of Figure 14.*

3.3 Slip effects and stability analysis of a DSMC generated supersonic boundary layer

The third set (*2*D) of test cases challenges the potential of the DSMC method to produce accurate results that can be later be used for the stability analysis of the flow. In this specific test case, the flow over a two-dimensional flat plate is evaluated. The geometry consists of a flat plate with a blunt leading edge of *0.5* mm radius and a length of *0.15 m* (Case *1*) and a flat plate of a length of 1 m (Case *2*) while the radius remains the same. For Case *1* the flow conditions are the same as in Kumar et al. [Kum11] namely a temperature of *273 K* and a pressure of *48.88* N/m^2. For Case 2 the same conditions were used apart from the Mach number which is increased to *4.5*. In order to accommodate all flow effects a domain of *0.15 m* x *0.1 m* was selected for Case *1* whereas for Case *2* the domain size was set to *1.0 m* x *0.4 m*. The inflow boundary was set to the left side of the domain with uniform flow conditions at the free-stream quantities, u_∞, T_∞ and M_∞ imposed. The right boundary is defined as outflow whereas the upper and lower boundaries are defined as specular reflective. The flat plate surface in both cases is treated as a diffuse reflective isothermal wall with full thermal accommodation and wall temperatures of *273 K* for Case *1* and 290 *K* for Case *2*. The grid density in Case 1 is *6,000,000* cells while for Case 2 is *160,000,000* cells. The Knudsen number based on the Mach number at the edge of the boundary layer and the square root of local Reynolds [Cha61] is calculated as $Kn = M_e/\sqrt{Re_x}$ for both cases. In Case 1 the Mach number at the boundary layer edge was found to be *2.98*, whereas in the second case *4.33*. The flow and computational parameters are summarized in Table *3.7*, Table *3.8* and Table *3.9* respectively. In both test cases the working gas is Argon.

Table 3.7: *Flow parameters (Slip effects and stability analysis of a DSMC generated supersonic boundary layer).*

Case	M_∞	Re_∞*	Kn_∞	U_∞ (m/s)	***Gas***	N_{den} $(\#/m^3)$	T_∞ (K)	T_w (K)
1	*3.0*	*5600*	*0.0392*	*1310*	*Air*	6.297×10^{22}	*273*	*273*
2	*4.5*	*59000*	*0.0018*	*1310*	*Air*	6.297×10^{22}	*245.45*	*290*

*Based on the flat plate length

Table 3.8: *DSMC computational parameters (Case 1)*

Grid density	*6,000,000 Cartesian grid cells*
Number of particles	1.9×10^{6}
Timestep (s)	2.5×10^{-8}
Transient period $(timesteps)$	*80,000*
Sampling period $(timesteps)$	*100,000*
Number of cores	*80*
Wall-clock time (h)	*6*

Table 3.9: *DSMC computational parameters (Case 2)*

Grid density	*160,000,000 Cartesian grid cells*
Number of particles	1.5×10^{8}
Timestep (s)	1.8×10^{-8}
Transient period $(timesteps)$	*300,000*
Sampling period $(timesteps)$	*70,000*
Number of cores	*80*
Wall-clock time (h)	*48*

Table 3.10: *Wall shear* $\frac{du}{dy}(y=0)$ $\left[\frac{1}{s}\right]$ *at three locations on the plate, as extracted from the DSMC simulation (Case 1)*

FD approximation order	***x = 0.05 m***	***x = 0.075 m***	***x = 0.1 m***
2^{nd}	*323250*	*232620*	*214450*
3^{rd}	*346856*	*239640*	*226950*
4^{th}	*368601*	*252495*	*238795*
5^{th}	*390835*	*271279*	*249867*

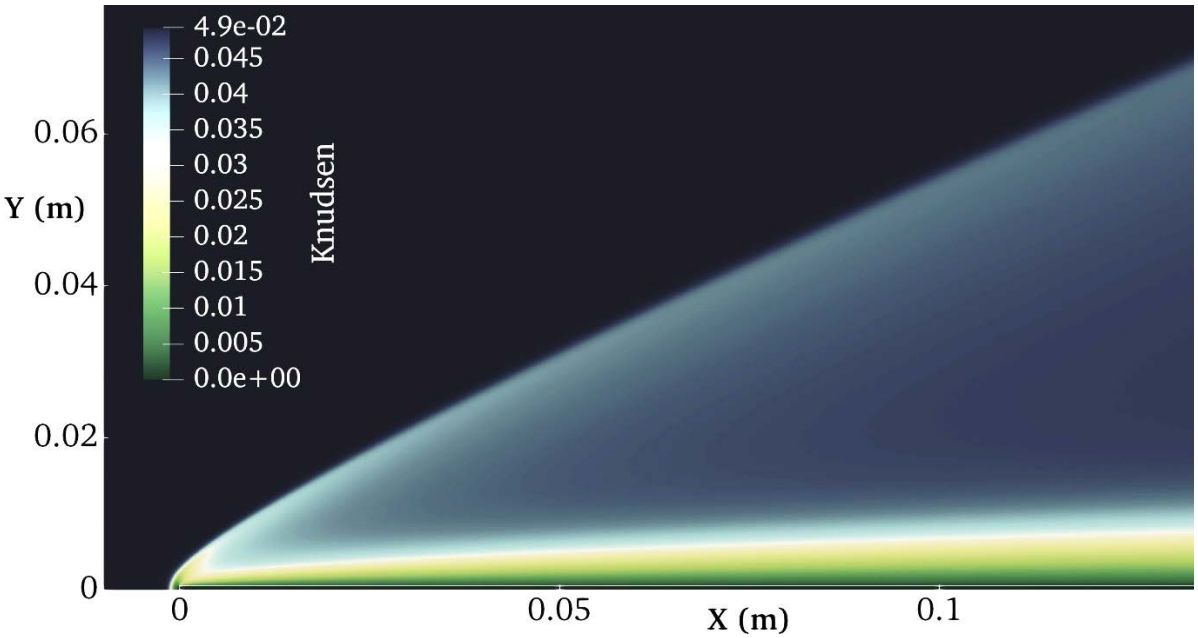

Figure 3.16. *Knudsen number defined as* $Kn = M_e/\sqrt{Re_x}$ *(Case 1).*

Figure *3.16* presents the global Knudsen number (Case 1). It can be seen that its maximum value in the overall domain is Kn < *0.05*, which places this flow well into the slip regime. Figure *3.17* shows the dependence of Knudsen number on the wall normal coordinate, at three streamwise locations, X = *0.05, 0.075* and *0.1 m*. Here, it can be seen that inside the boundary layer *0.04* ≤ Kn ≤ *0.05*, slip walls may be expected. Figure *18* shows the streamwise velocity component and the temperature in the entire field, and it can be clearly seen that slip velocity and temperature jump exist along the plate surface, both of which are decreasing as we

advance toward the end of the plate. In Figure *3.19* the velocity and temperature on the plate surface is shown. Comparisons with the predictions of Kumar et al. [Kum11] at randomly selected streamwise locations along the plate surface are quite satisfactory, e.g. at x = *0.05 m* those authors quote a slip velocity u_{slip}= *30 m/s* and our calculations deliver u_{slip}= *30.86 m/s*.

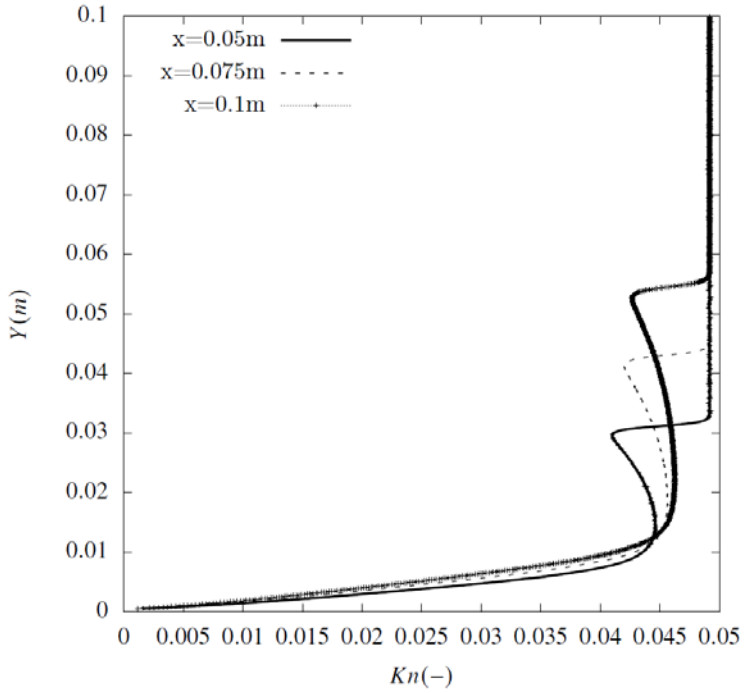

Figure 3.17. *Knudsen number, Kn= $M_e/\sqrt{Re_x}$ (Case 1).*

Turning to comparisons with boundary layer theory, the velocity and thermal boundary layer edge, defined by δ_{99}, can be seen in Figure *3.20* for Case *1*. Figure *3.21* shows the pressure along the x-axis at two different heights from the surface, Y = *0.021 m*, coinciding with the boundary layer edge at the outflow boundary, and Y = *0.05 m*, well outside of the boundary layer. The results of either of these curves suggest that zero pressure gradient conditions have not been obtained in this simulation, although towards the end of the plate the favorable pressure gradient at the edge of the boundary layer is relatively small, dp/dx (y=*0.021* m)= *-50 Pa/m*. This smallness of the streamwise pressure gradient is further corroborated by the results shown in Figure *3.22*, where pressure is presented as a function of Y at three different X locations. Two effects can be seen: firstly, wall pressure tends to converge toward a constant value as X increases, as evidenced by the diminishing differences between the wall pressure values at successive streamwise locations; secondly, pressure across the boundary layer is becoming constant, as required by boundary layer theory. Table *3.10* presents the (dimensional) wall-shear values at the same three x-axis locations discussed in Figure *3.22*; these results are used to generate wall slip velocity and temperature jump conditions according to equations (2.65) and (2.66) in Section *2* and solve the boundary layer equations. Such solutions of the boundary layer equations, subject to slip velocity and temperature jump boundary conditions, have been obtained at a number of flow conditions and Figure *3.23* shows the comparison between the present results and those obtained by [Kum11]. While excellent agreement is obtained for the velocity profiles, a small

discrepancy can be seen in the temperature profiles, which we attribute to the inclusion of the thermal creep term in equation (2.65).

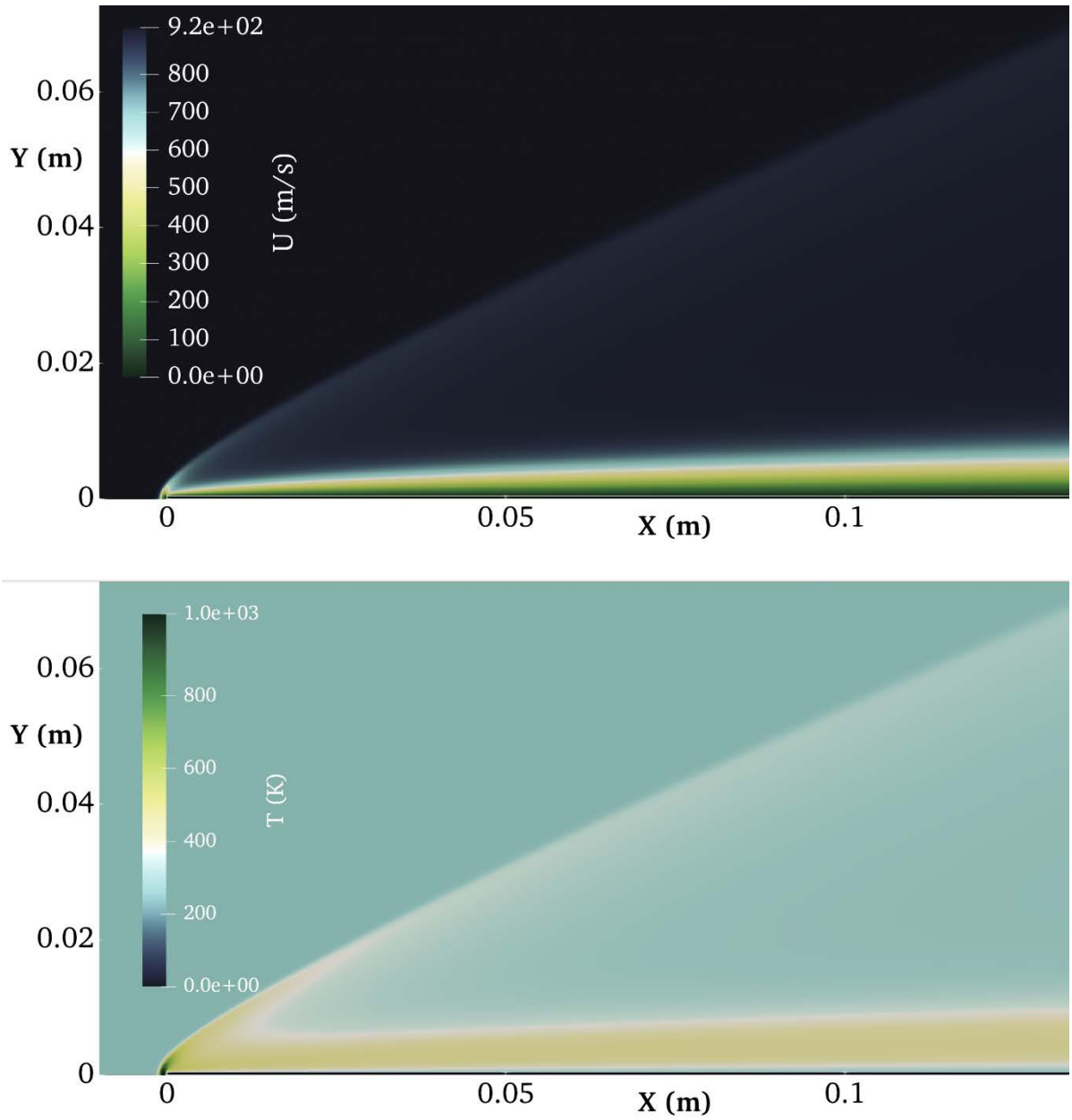

Figure 3.18. *Streamwise velocity (upper) and temperature (lower) fields obtained from the DSMC simulation (Case 1).*

The rather good agreement obtained between DSMC and boundary layer theory at low Reynolds numbers was also observed in the second test case, at an order of magnitude larger Reynolds number. In order to approach zero free-stream pressure gradient conditions, the flat plate length was increased to *1 m*, while the domain height was increased to *0.4 m*. All subsequent DSMC and boundary layer theory comparisons were made at a distance of *0.7 m* from the leading edge of the flat plate. The pressure gradient at that location is shown in Figure *3.23*. In Figure *3.25* very good agreement can also be seen in the streamwise velocity components results obtained by the two methods at the higher Reynolds and Mach number cases. Figure *3.26* shows the result of the temperature across the boundary layer predicted by

the two codes. We can clearly see that in both codes the temperature is matched everywhere except at the boundary layer edge, where the compressible boundary layer theory code predicts a slightly shallower thermal boundary layer. Possible explanations, apart from the underlying pressure gradient, include the different viscosity laws used in the two methods or the exact value of the variable Prandtl number in the DSMC simulations. Figure *3.24* shows the pressure along the boundary layer edge for Case 2. Again, here we see a small pressure gradient as we move downstream the flat plate leading edge.

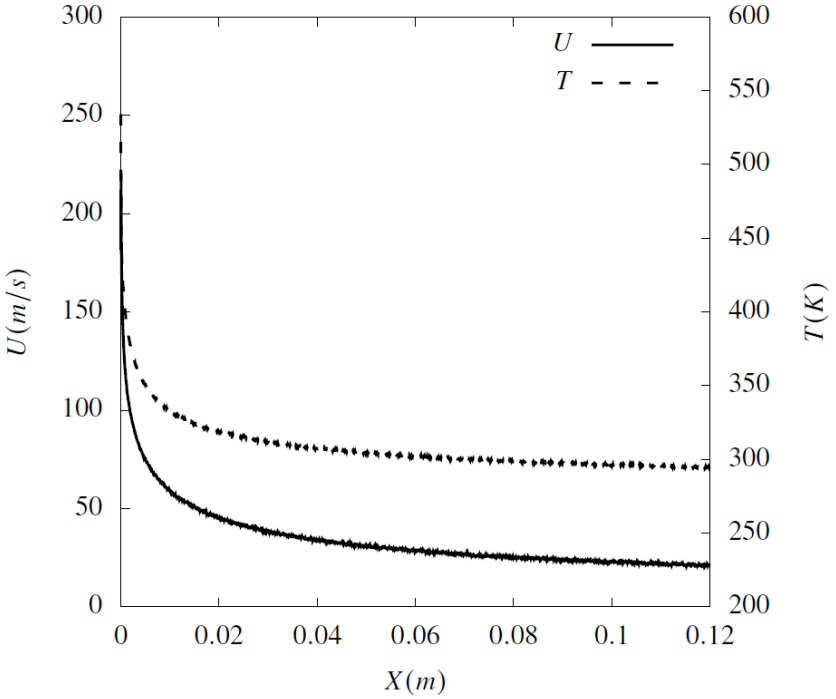

Figure 3.19. *Velocity slip and temperature jump on the flat plate surface (Case 1).*

Moving to stability analysis, the eigenspectra of the two profiles were computed using the LiGHT code and are shown in Fig. *27*. It can be seen that the two spectra are quite close to each other and that, at the analysis conditions chosen, namely edge Mach number $M_e = 4.33$, $\sqrt{Re_x} = 201$, $a = 0.2$ (scaled with the local distance from the leading edge $\left(x/\sqrt{Re_x}\right)$), and $\beta = 0$, no unstable modes exist. Figures *3.28* and *3.29* show the normalized eigenfunctions for velocity and pressure perturbations, respectively. As expected, these figures too evidence the very good agreement over the entire domain. These results point to the fact that, at conditions at which the parameters of the particle-based DSMC method indicate a flow approaching continuum, very good agreement has been obtained in linear instability analysis results of base flows obtained in DSMC and the compressible boundary layer, the latter subject to appropriate velocity slip and temperature jump conditions.

Despite the low pressure and the flow rarefaction generally in this case a good agreement between a double precision boundary layer code and a statistical method (DSMC) can be achieved if the flow is treated carefully. This leads to the conclusion that DSMC informed base flows can be used to stability analysis and produce results with adequate accuracy.

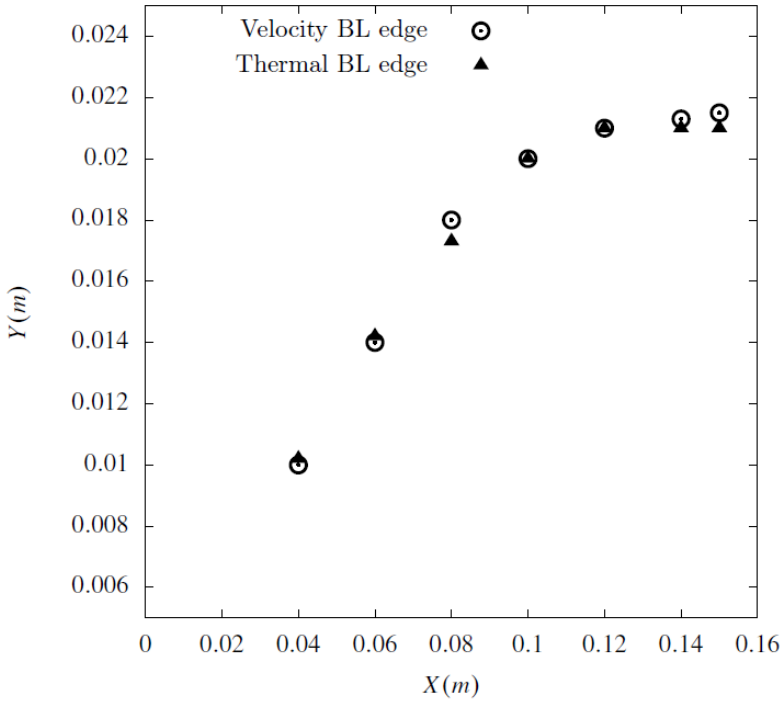

Figure 3.20. *Boundary layer edge (Case 1).*

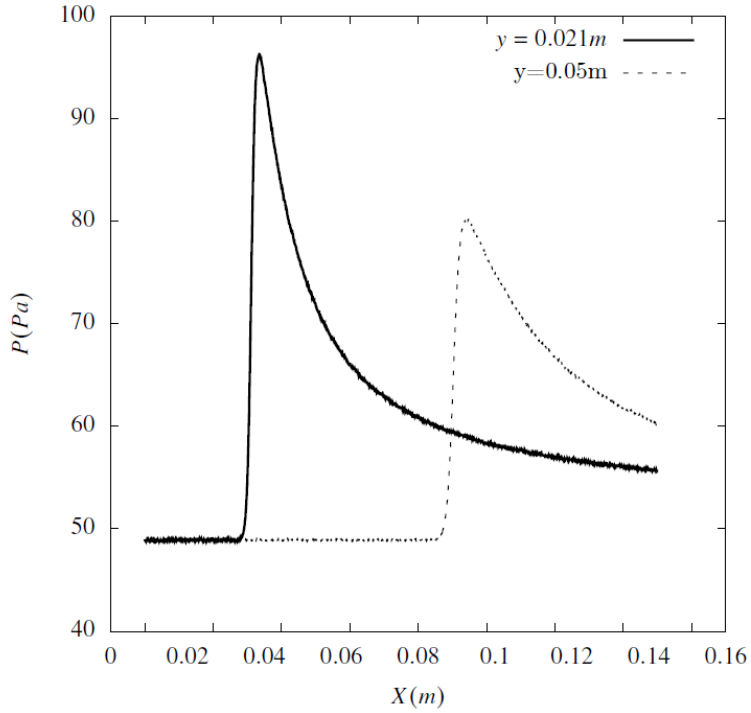

Figure 3.21. *Pressure distribution at the boundary layer edge and outside the boundary layer edge (Case 1).*

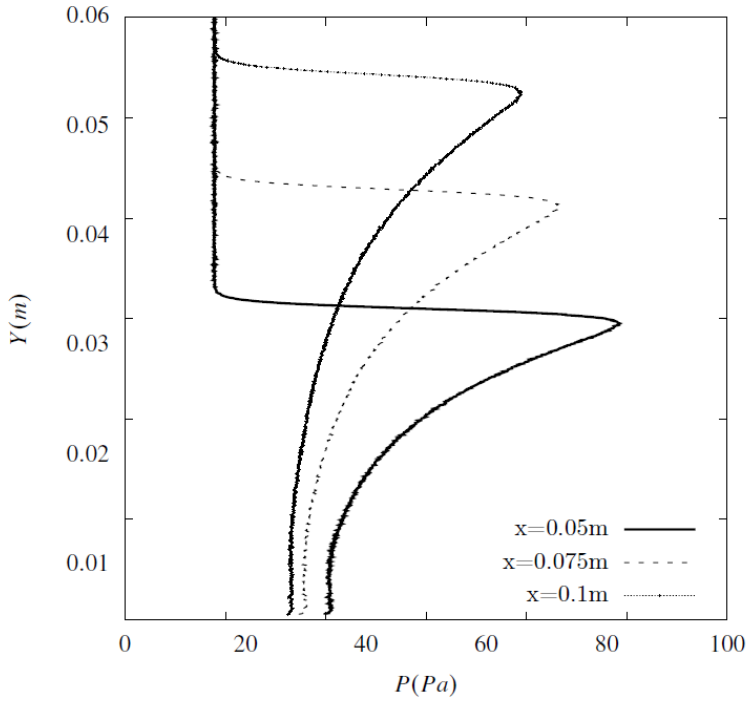

Figure 3.22. *Pressure distribution along the y-axis in 4 locations 0.05 m, 0.075m and 0.1 m from the leading edge (Case 1).*

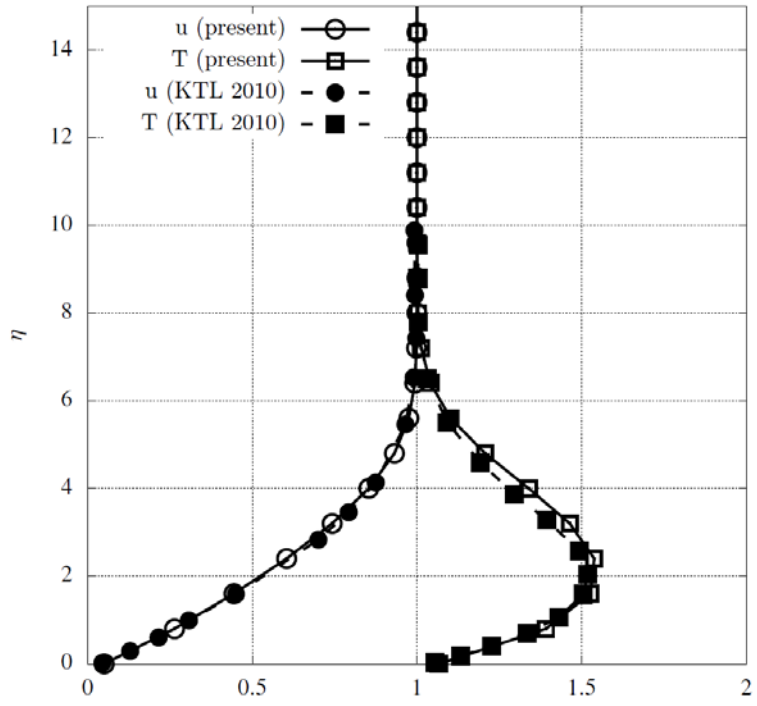

Figure 3.23. *Comparison of present compressible boundary layer analysis with results obtained from [Kum11] (denoted as KTL) (Case 1).*

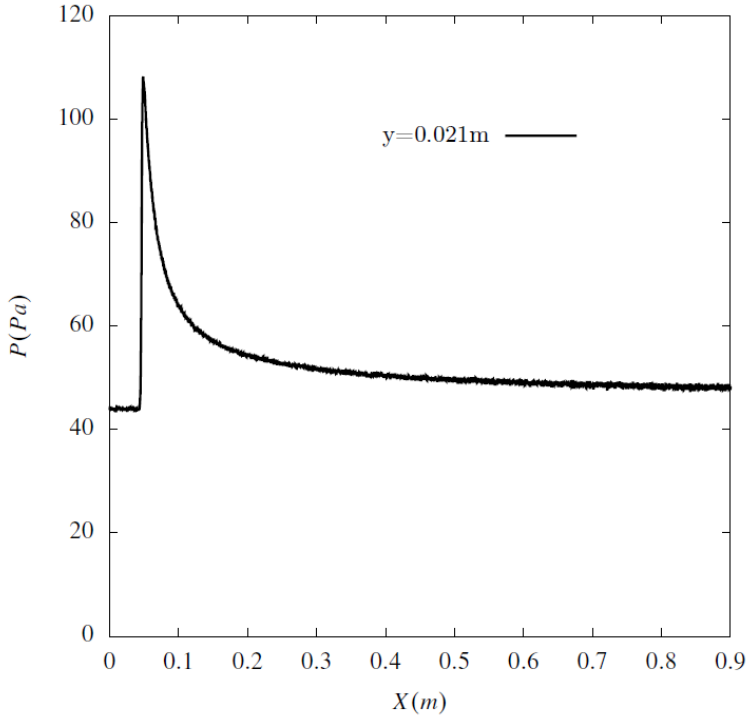

Figure 3.24. *Pressure distribution at the boundary layer (Case 2).*

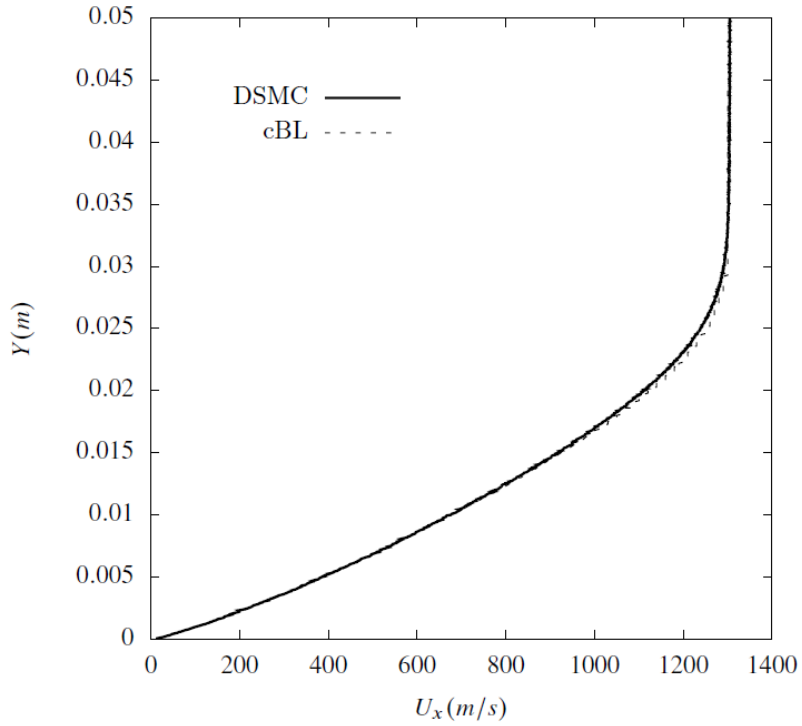

Figure 3.25. *DSMC and compressible boundary layer (cBL) comparison of streamwise velocity at x=0.7 m location (Case 2).*

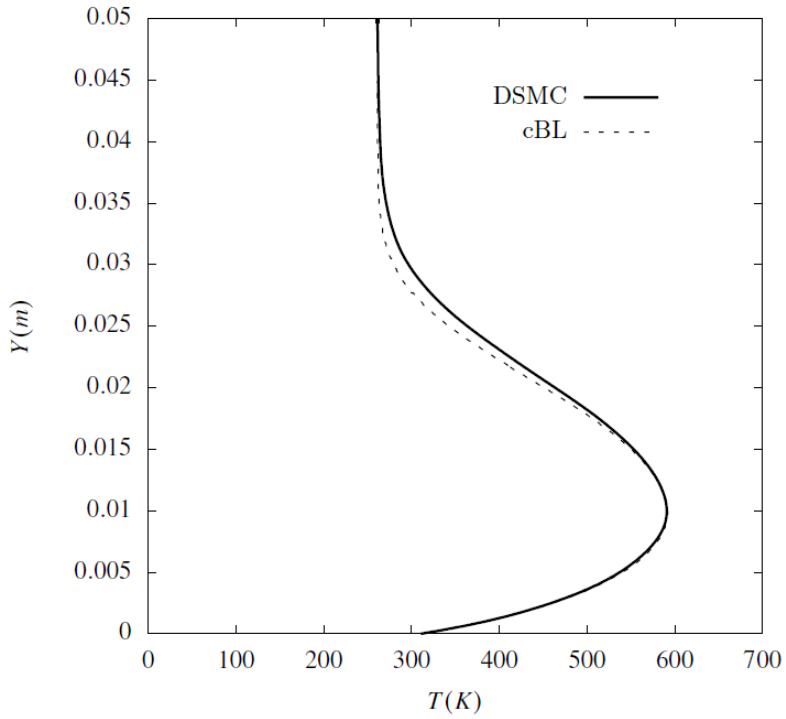

Figure 3.26. *DSMC and compressible boundary layer (cBL) comparison of temperature at x=0.7 m location (Case 2).*

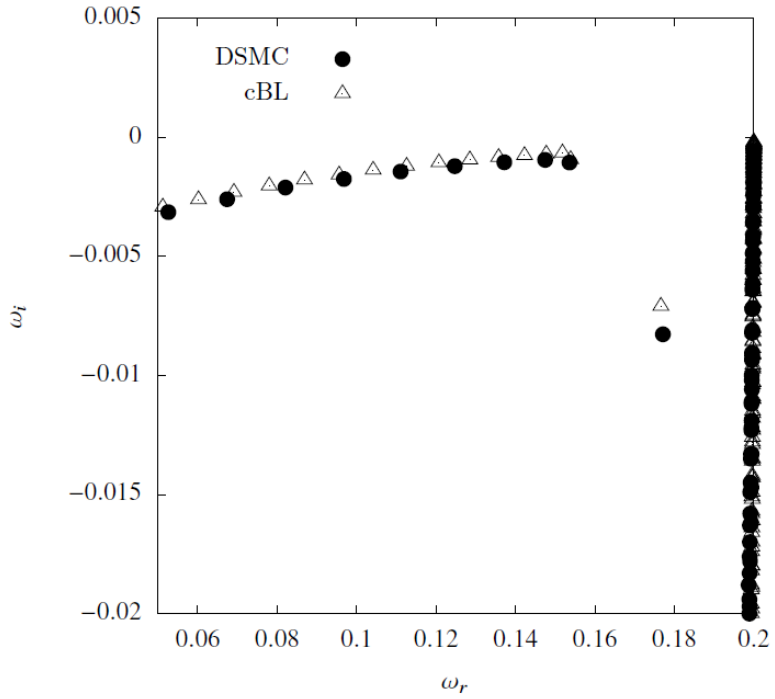

Figure 3.27. *Eigenvalue spectra for the DSMC and cBL base flows for Case 2. The respective discrete modes are ω_{cBL}=0.17611-0.0071i and. ω_{cBL}=0.17728-0.00828i.*

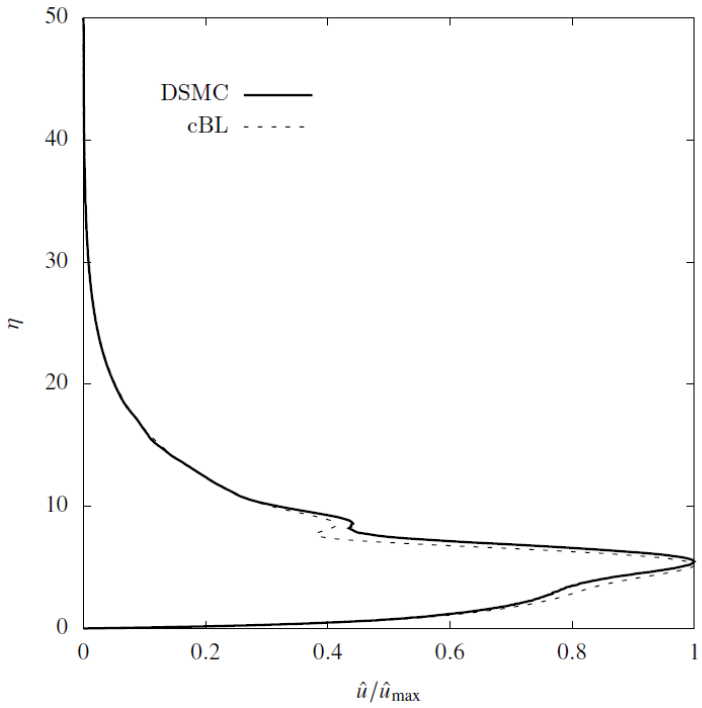

Figure 3.28. *Normalized streamwise disturbance velocity amplitude function $\hat{u}/\hat{u}_{max}(\eta)$ as obtained from analyses of the DSMC signal at x=0.7 m (solid line) and the corresponding compressible zero pressure gradient boundary layer solution (dashed line) at M_e=4.33, Re=$\sqrt{Re_x}$=200.98 and wavenumbers a=0.2 and β=0.*

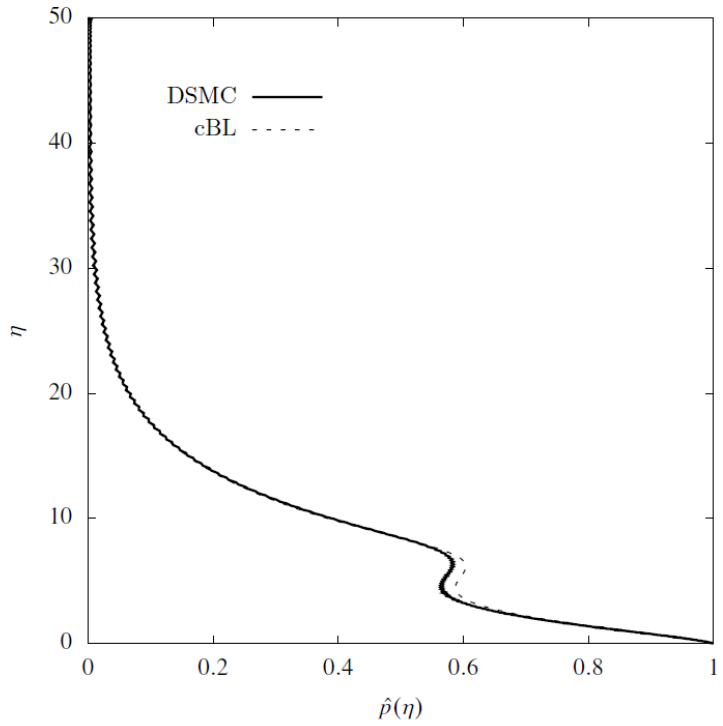

Figure 3.29. *Normalized disturbance pressure amplitude function $\hat{p}(\eta)$ at the same conditions as in Figure 3.28.*

3.4 Hypersonic flow around a flat plate at range of $4.5 \leq M_\infty \leq 9$

In this test Case 1 domain of *1.05 m* by *0.4 m* was used to capture the full flow field in Cases *1* and *2* whereas in Case 3 the domain was *0.105 m* by *0.05 m*. The flat plate has a blunt leading edge of *0.5 mm* radius and is *1 m* in length for Case *1* and Case *2* while in Case *3* the length of the plate was limited to *0.1 m*. To accurately capture the flow characteristics a cell size below the local mean free path was used. This results to a grid for Case *1* and Case *2* of *170,000,000* cells whereas in Case *3* due to the shorter plate and domain the grid was limited to *2,400,000* cells. When the vortex generator was added to Case *3* due to the very high density in that area, in order to reduce the computational cost, specifically in that are the cell size was set equal to two mean free paths. Although the cell size is larger than the local mean free path in that area the near-collision partner scheme was used to ensure collisions accuracy [Gal11, Gal17].

Table 3.11: *Flow parameters (Hypersonic flow around a flat plate at range of $4.5 \leq M_\infty \leq 9$).*

	Case 1 ***Air***	***Case 2*** ***Ar***	***Case 3*** ***N_2***
Mach number (M_∞)	*4.74*	*5.11*	*9.39*
Reynolds number, Re_L (-)	*60,354*	*71,394*	*11,859*
Prandtl number, Pr (-)	*0.72*	*2/3*	*0.72*
Specific gas constant, R ($Jkg^{-1}K^{-1}$)	*287.00*	*208.13*	*296.80*
Ratio of specific heats, γ	*7/5*	*5/3*	*7/5*
Plate length, L (m)	*1.0*	*1.0*	*0.1*
Nose radius, r_n (m)	5×10^{-4}	5×10^{-4}	5×10^{-4}
Freestream velocity, U_∞ (m/s)	*1310*	*1310*	*3000*
Freestream temperature, T_∞ (K)	*190*	*190*	*245*
Freestream density, ρ_∞ kg/m^3	6.04×10^{-4}	8.60×10^{-4}	6.04×10^{-4}
Freestream viscosity, μ_∞ ($N\ s\ m^{-2}$)	1.311×10^{-5}	1.578×10^{-5}	1.528×10^{-5}
Reference viscosity, μ_{ref} ($N\ s\ m^{-2}$)	1.719×10^{-5}	2.117×10^{-5}	1.656×10^{-5}
Reference temperature, T_{ref} (K)	*273*	*273*	*273*
Wall temperature, T_w (K)	*Adiabatic*	*Adiabatic*	*245.45*

According to this collision scheme, a collision partner is selected from within a sphere with radius equal to the distance the particle travels in one timestep. It has been shown that, for cells sizes bigger than the local mean free path and with *30* simulators per cell it produces accurate collisions. The average number of particles per cell for the vortex generator in particular is *270*. In all three cases the inflow is defined left of the flat plate's leading edge and the outflow at the end of the flat plate. The flat plate walls are defined as adiabatic in Case *1* and Case *2* while

in Case *3* are treated as diffuse reflecting with full thermal accommodation. A summary of the flow and computational parameters can be found in Table *3.11* and Table *3.12* respectively. The total number of cells and CPU hours needed for each test case can be found in Table *3.12*. All simulations were run on ARCHER2 supercomputer. Each compute node has dual AMD EPYC™ *7742* processors and *256* GB of RAM.

Table 3.12: *DSMC computational parameters.*

	Case 1 ***Air***	***Case 2*** ***Ar***	***Case 3*** ***N_2***
Knudsen number, Kn	*0.0187*	*0.0212*	*0.0897*
Number of particles, N_p	1.2×10^{9}	1.2×10^{9}	7.2×10^{8}
Timestep, dt (s)	1.8×10^{-8}	1.8×10^{-8}	1.0×10^{-9}
Transient period (timesteps)	*300,000*	*300,000*	*250,000*
Samples	*80,000*	*80,000*	*Instant*
Mean free path, λ (m)	9.11×10^{-5}	8.91×10^{-5}	1.01×10^{-4}
Power law exponent, ω	*0.75*	*0.81*	*0.74*
Number of cells	$\sim 1.7\times10^{8}$	$\sim 1.7\times10^{8}$	$\sim 2.4\times10^{6}$
Wall-clock time (CPU-h)	*75,200*	*75,200*	*37,000*

Furthermore, in this test Case 1 Stack Autoencoder Neural Network (SANN) was used to smooth the DSMC data. An autoencoder is a deep learning neural network that is constructed in a way that it is able to copy its input to its output [Vou18]. In contrast with other neural networks, only one hidden layer is used to represent the input data, such that the autoencoder network be viewed in two parts: the first is an encoder function $h^{*}=f(x)$, which is decoded in the second part, where the reconstruction of the input data is calculated as $r^{*}=g(h^{*})$. Autoencoders can also work with incomplete/undercomplete and sparse data, such as the under sampled DSMC simulation profiles. An undercomplete set is trained such as the input copying task results in the hidden layer capturing useful properties by constraining it to have a smaller dimension than the input. A network that has learnt to represent undercomplete data is able to capture the most important underlying information; in the case of the DSMC simulation profiles, this information is the mean value of the quantities of interest, in which the noise level has been reduced. The learning procedure can be described as minimizing a loss function $L(x, g(f(x)))$, where the L is a loss function penalizing the g(f (x)) or dissimilar to x; as an example an L function can be the mean-squared error. If the decoder is linear and L is the mean squared error then the undercomplete autoencoder learns the principal subspace of the training data as a side effect. It is well known [Kaw84, Sav64] that the choice of an inappropriate smoothing method can cause severe changes to the original data and can lead to false interpretations of the results. The SANN used here is an unsupervised neural network and was fed with the results from Case *1* and Case *2*. Boundary layer profiles were used from different locations of the plate to train the NN. At this point must be mentioned that the quality of the smoothing is determined by that of the simulation itself. More specifically, in order to train the neural network four wall-normal velocity profiles taken at locations x=*0.2 m, 0.3 m, 0.4 m,* and *0.5 m* from the flat plate leading edge and a total of *1200* data points

in each training set were used. After the network was trained, the smoothed wall-normal velocity profile at a single, randomly chosen location x=*0.7* m, was compared with simulation data in order to verify the quality of the neural network training. The result obtained for air at the parameters shown in Table *3.11* and *3.12* are shown in Figure *3.32*.

The temperature used in the simulations is the translational temperature which is the same temperature used in the continuum equations. Nevertheless, during the DSMC simulation translational, rotational and vibrational temperatures are calculated, assuming the correct thermal non-equilibrium, but only the translational temperature, calculated according to [Bir94], is used for the linear stability analysis. Vibrational energy relaxation is neglected in the LST equations and rotational energy relaxation is approximated by the bulk viscosity [Ber98], thus avoiding the need of introducing a rotational temperature. The equations defining the translational temperature have been discussed in detail by Bird [Bir94]. Since DSMC calculations are performed in the slip regime, we obtain relatively low overall temperatures of ~ *800* K in the boundary layer. In the present simulations, rotational and vibrational relaxation numbers were treated as constants. The rotational relaxation number was set to $Z_{rot} = 5$ for both linear stability analysis of hypersonic boundary layers N_2 and O_2, whereas a vibrational relaxation number $Z_{vib} = 52600$ for N_2 and $Z_{vib} = 17900$ for O_2 have been used [Bir94]. Constant values were used because generally Z_{rot} increases with temperature but its variation only becomes significant for temperatures above ~ 1200 K.

To employ the vortex generator (VG) used in Case *3* a pulsating high-density jet was used emanating from the flat plate surface at a specific angle and introducing particles into the flow at a given frequency. Two aspects to be considered are the pulsation frequency, which is chosen in the range of boundary layer response, and the necessity to maintain zero net mass addition in the simulation domain. Both requirements have only been satisfied during a limited period of the simulation, during which comparison data were extracted. As can be seen by the horizontal line in Figure *3.38*, after the VG was eliminated, the flow returned to its unperturbed steady state.

***Table 3.13**: Boundary layer parameters.*

	Case 1 ***Air***	***Case 2*** ***Ar***	***Case 3*** ***N_2***
Mach number, M_e	*4.55*	*4.5*	*6.99*
$Re=\sqrt{Re_x}$, N_p	*214.0*	*213.7*	*78.1*
Streamwise location, x (m)	*0.7*	*0.7*	*0.04*
Slip velocity, u_{slip} (m/s)	*24.28*	*34.89*	*103.62*
Edge velocity, u_e (m/s)	*1301.7*	*1291.5*	*2924.0*
Edge temperature, T_e (K)	*202.9*	*238.41*	*421.00*
Edge density, ρ_e, (kg/m^3)	6.91×10^{-4}	9.59×10^{-4}	1.19×10^{-3}
Edge pressure, P_e, (Pa)	*40.296*	*47.537*	*148.85*
Edge viscosity, μ_e (Nsm^{-2})	1.376×10^{-5}	1.896×10^{-5}	2.282×10^{-5}
Wall temperature, T_w (K)	*887.77*	*1469.66*	*416.73*

The latter has been analyzed with respect to its linear stability. The orifice from which the vortical perturbations are introduced inside the boundary layer by a jet of high-density particles has a diameter $D_o = 1\ mm$, placed at $x_o = 1\ cm$ from the leading edge. The jet pulsates periodically at an excitation frequency $f_e = 277.77\ kHz$ and particles are injected with a velocity magnitude of $U_o = 4000\ m/s$ at an angle of *60* degrees to the plate, at a temperature of T_o =

245.45 K. Each time the jet fires about *105* particles enter the domain and the mass flow rate that passes from a surface with a length of *20* computational cells is $\dot{m}=3.76\times10^{-4}$ *kg/s*. The reduced momentum coefficient, C_μ, and reduced frequency F^+, corresponding to the jet actuation are, respectively, defined [Gre00] as in equations (vale to noumero) and are equal to *0.268* and *0.983* respectively. On account of the rather large jet velocity, U_o, chosen in the simulations, the reduced momentum coefficient is substantially larger than that which was found to be adequate for the excitation of linear perturbations in the boundary layer experiments of [Gre00], while the reduced frequency value is of the same order of magnitude as that found in experiments.

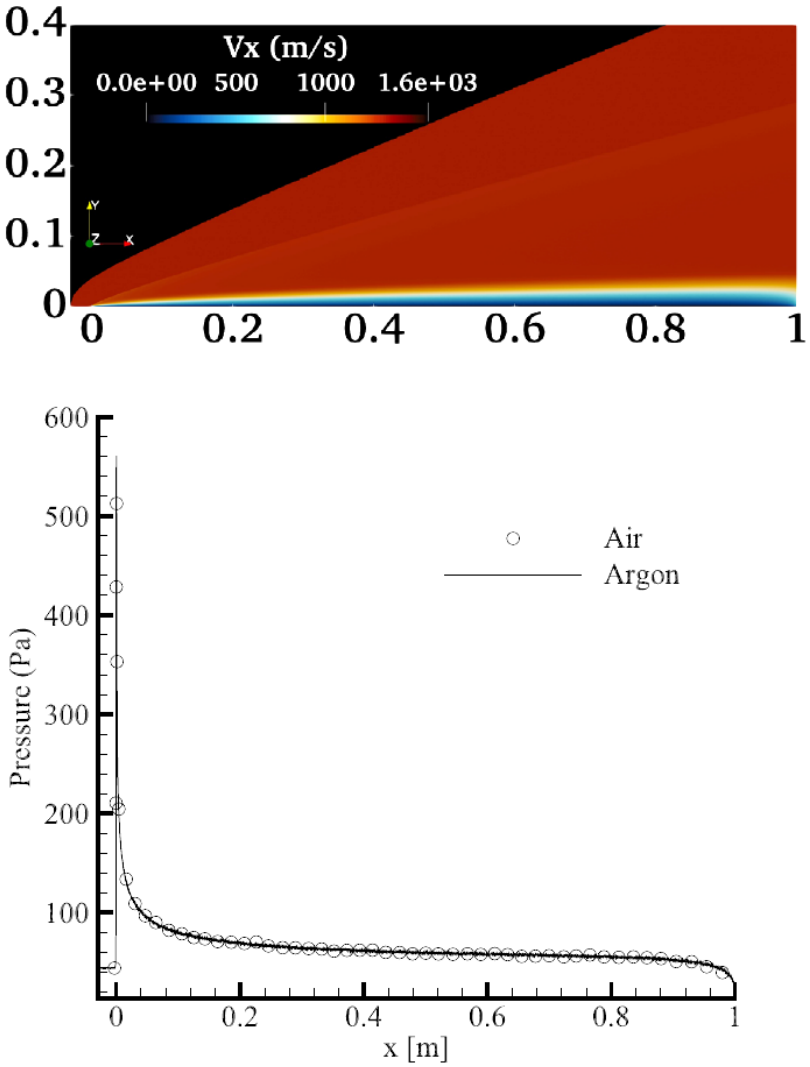

Figure 3.30: *Upper: Streamwise velocity component at steady state in the DSMC simulation for argon. Lower: Pressure along the plate at the boundary layer edge (y = 0.0014m) for argon and air.*

At the start of the simulation, properties of the particle group that is going to be inserted such as number density, velocity components and thermal temperature are defined. At every timestep inside each grid cell that overlaps with one or more emitting surface elements, the number of particles to be added is computed, according to equation (4.22) in [Bir94]. The number of particles to be inserted is based on the molecular flux calculated by this equation

and also from properties like the ratio f_{num} of the injected particles to those in the flow, the overall number density, velocity components and temperature of the injected particles, as well as the fraction of the surface element that overlaps with the corresponding insertion grid cell and the cell orientation with respect to the streaming velocity.

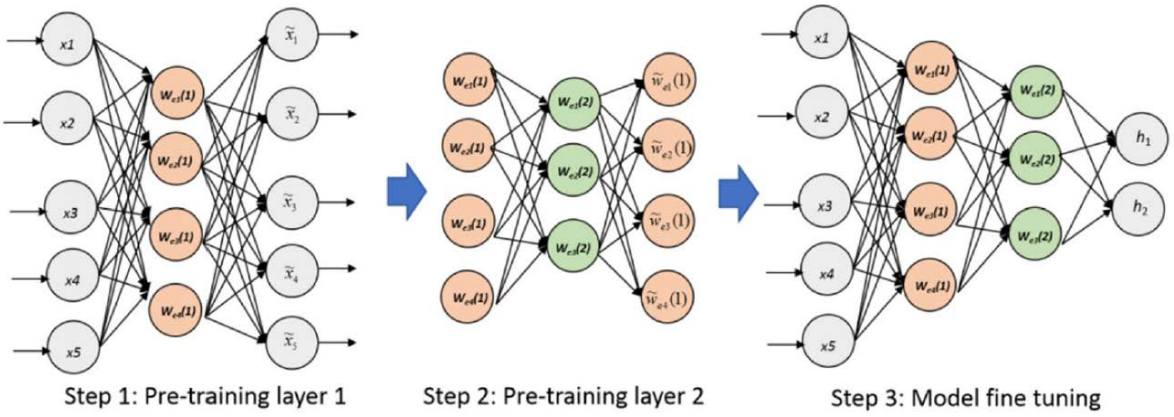

Figure 3.31: *Schematic of the Stack Autoencoder Neural Network used to smooth DSMC simulation data [Pra17].*

Figure *3.33* shows a comparison of velocity and temperature profiles for argon and air at a given location x = *0.7* m along the plate, where $\sqrt{\mathrm{Re}_x} \cong 200$, as obtained by DSMC and the compressible similar zero pressure gradient boundary layer equations. The different properties of the gases result in substantially different boundary layer velocity and (especially) temperature profiles, the wall temperature for Ar being *75%* higher than that of air. When comparing the DSMC and boundary layer predictions, it can be seen that the former is marginally thicker than the latter. The quantitative differences observed are attributed to the mild pressure gradient of the DSMC results at the streamwise location monitored, as well as to the slightly different value of the Prandtl number, which is taken to be constant in the boundary layer approximation.

Eigenspectra pertaining to the DMSC and boundary layer profiles obtained for air in Case 1 and Argon in Case *2* at a given two-dimensional wavenumber $\alpha = 0.2$ are, respectively, shown in Figures *3.34* and *3.35*; the corresponding amplitude functions can be found in Figures *3.36* and *3.37*. In the plots showing the amplitude functions of air, the location of the generalized inflection point (GIP) is also indicated by a dashed horizontal line. Both sets of results show that the linear instability properties of the profiles extracted from the DSMC simulations and those computed in the corresponding boundary layer approximation are qualitatively identical and actually in close quantitative agreement. Only damped eigenvalues have been found at all sets of parameters, as expected from the relatively low values of $\mathrm{Re}=\sqrt{\mathrm{Re}_x}$.

Interestingly, Figure *3.34* also includes the eigenspectra of compressible boundary layer profiles in which the classic no-slip boundary condition is imposed, as well as that calculated from the neural network smoothing. The least damped discrete mode corresponding to the no-slip boundary layer profile is less stable than that pertaining to the profile in which the slip and temperature jump boundary conditions have been imposed. The implication is that imposition of the no-slip boundary condition in the base flow profile leads to theoretical prediction of earlier boundary layer transition. On the other hand, the least damped discrete eigenvalue

pertaining to the smoothed data is marginally more stable than that of the raw DSMC profiles. As can be seen in the results of Figure *3.34*, the least damped discrete boundary layer mode is *25%* more stable than its counterpart based on the Navier–Stokes equations. This is attributed to the stabilizing effect of the pressure gradient visible in Figure *3.30* and is analogous in magnitude to the effect that slip has on the stability of the base flow.

The acoustic branches pertaining to all four base flow profiles are practically identical, as are (rather surprisingly), the frequencies of the leading discrete modes of the raw DSMC profile and that of the boundary layer subject to slip velocity and temperature jump boundary conditions. The quantitative differences between the damping rates of air and argon may be attributed again to the nonzero pressure gradient present in the DSMC results, seen in Figure *3.30* (lower); consequently, DSMC profiles are found to be stronger damped than their boundary layer counterparts. These results also demonstrate that imposition of the no-slip boundary condition on the base flow profiles leads to prediction of less damped/more unstable leading discrete eigenmodes compared to those found when the slip boundary condition is imposed.

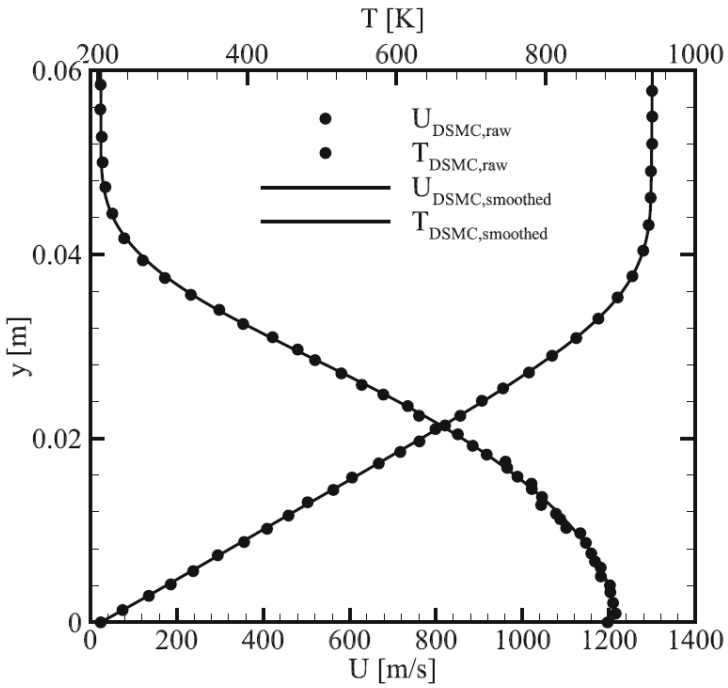

Figure 3.32: *Comparison of raw DSMC data and the smoothed profiles at x = 0.7m, obtained by the neural network for air at the parameters of Tables 3.11 and 3.12.*

A qualitative image of the perturbations generated can be seen in Figure *3.39*. In the bottom image of this figure, two white lines are marked, one inside in the boundary layer at a distance *0.001* m from the plate surface, and another one close to the shock, at a distance *4.4* mm from the flat plate and at an angle $\varphi=13.19^{o}$ to the plate. On these lines, unsteady flow data are extracted. In Figure *3.38* (upper), the evolution in time of the total number of particles in the simulation is shown. Immediately after the jet firing has started at t = *0*, an increase in the number of particles can be seen, as expected due to the addition of new particles in the simulation domain and a steady state is reached after $t \approx 0.2$ *ms*. As the injection of particles continues, a new periodic state is arrived at around $t \approx 0.54$ *ms*, as shown in the inset figure, in which a zero-net-mass state, in which the number of particles entering and exiting the

simulation domain is the same, has been established. At around t ≈ *0.67 ms*, the injection of particles ceases and the flow returns to its previously established steady state, as evidenced, for example, by the streamwise velocity profile at x = *0.05* m, shown before ("pre") and after ("post") the action of the vortex generator in the lower part of Figure *3.38* (Lower).

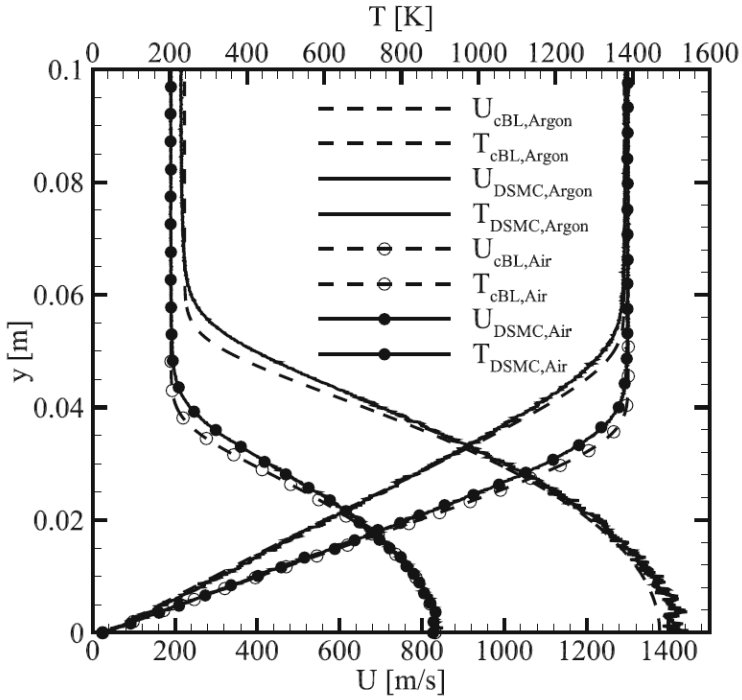

Figure 3.33: *Velocity and temperature profiles obtained by DSMC in argon and air (solid) at x= 0.7m and comparison with corresponding boundary layer solutions (dashed). The velocity slip computed in DSMC and calculated by equations. (number) is shown in Table 3.13.*

Figure *3.40* presents the wall-normal component of the velocity as a function of the streamwise spatial coordinate at a height of *1.5* mm, at two successive timesteps, t_1 = *0.5549* ms and t_2 = *0.5569* ms, shortly after the zero-net-mass injection conditions shown in Figure *3.38* (left) had been established. This quasi-periodic signal, as well as others extracted at different heights within the boundary layer, but not shown here for brevity, can be seen to decay exponentially with x along the downstream spatial direction. In order to compare the characteristics of this signal with the theoretical result of the least damped linear instability, an exponential curve fit was constructed, in the form $y=Ae^{\sigma x}+C$ with A=*508.86*, σ=*-40.32* and C=*25.60*. The curves resulting from damping rates with an error bar of ±*10%* are also indicated in the figure.

The steady laminar boundary layer profile at x = *0.04* m was subsequently analyzed at the parameters shown in Table *3.13*. Figures *3.12* and *3.13*, respectively, present the eigenspectrum and the eigenfunctions of the leading damped modes of this flow, as predicted by solution of the eigenvalue problem pertaining to the DSMC profile; the respective dimensionless and dimensional results are shown in Table *3.4*. Figure *3.42* presents the amplitude functions of the least damped flow perturbation, denoted as Mode *1*, alongside the second in significance linear perturbation at these parameters, denoted as Mode *2* and identified as the compressible analog of a Tollmien–Schlichting (TS) wave. Interesting as it may be, the fact that a TS wave exists

in the eigenspectrum of the steady laminar DSMC profile is less significant than the ability of the kinetic theory to capture as damped periodic oscillation the leading eigenmode of the underlying steady boundary layer profile. The dimensional value of the damping rate obtained in the stability analysis is used as σ to construct the curve-fit equation plotted in Figure *3.40*, where an error bar corresponding to *±10%* deviation from the value of σ used is also indicated. The results leave little doubt that the damped oscillation generated by the action of the pulsating jet is that captured as Mode 1 in the linear stability analysis of the steady laminar DSMC profile.

Figure *3.43* presents the wall-normal velocity component inside the boundary layer, already shown in Figure *3.40*, alongside the value of the same quantity along the oblique line shown in Figure *3.39* in the shock. It can clearly be seen that the oscillation inside the boundary layer is synchronized with the footprint of the shock oscillation. In order to quantify the oscillations, the two signals are Fourier transformed and the result is shown in the lower part of Figure *3.43*. It can be seen that the wavenumber of the oscillation inside the boundary layer, given by the equation below,

$$\frac{1}{L_x} = \frac{a}{2\pi L_{ref}} \approx 100 \frac{1}{m}$$

can also be found in the signal measured below the shock, although the peak wavenumber of the shock oscillation is slightly displaced toward lower values; in other words, the waves propagating along the shock are found to have slightly larger wavelengths than those inside the boundary layer. Additionally, it is interesting to note that the lower wavenumber content of the shock oscillation is consistently higher than that inside the boundary layer. The dimensional frequency of the leading damped mode inside the boundary layer can be computed from the dimensionless result for ω_r *by*

$$f = \omega_r \frac{u_e}{2\pi L_{ref}} \approx 288.66\ kHz$$

and is found to be within *4%* of the jet oscillation frequency.

It may be argued that these results are not surprising due to the Knudsen number regime at which the present analysis is performed. But it's very reassuring to be able to recover instability results that are closely related to their Navier–Stokes counterparts and only show relatively small quantitative differences due to pressure gradient and slip. Thermal non-equilibrium effects are not expected at these temperatures. However, thermal non-equilibrium will become increasingly important as temperatures increase. This effect can be captured in the DSMC base flow. Linear stability analysis of these effects will require extending the system of stability equations solved to accordingly account for non-equilibrium thermal effects. As far as prediction of frequency response of the system is concerned, it's not surprising that the boundary layer and shock system oscillate at the imposed frequency. What makes the results of Figure *3.40* very interesting is that the decay of the amplitude of this oscillation downstream is exactly predicted by linear stability analysis of the steady-state profile of the boundary layer in the absence of an excitation. We are unaware of the response of this system in the transition or the free molecular regimes. The present analysis builds confidence in applying DSMC-based stability analysis tools to explore these regimes.

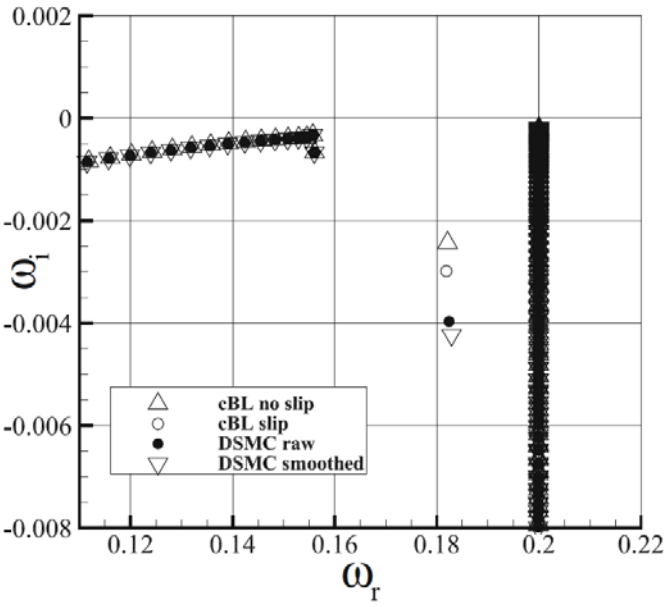

Figure 3.34: *Eigenvalue spectra of raw and smoothed DSMC data, compared with compressible boundary layer (cBL) spectra under slip and no-slip boundary conditions on the base flow at the parameters of Case 1. The discrete eigenvalue obtained on the profiles including velocity slip and temperature jump for the boundary layer is* ω_{BL} *= 0.181859-0.00298i, while that corresponding to the raw DSMC data is* ω_{DSMC}*=0.182390-0.00396i.*

Table 3.14*: LST parameters and results.*

	Case 1 Air	***Case 2 Ar***	***Case 3 N_2***
Length scale, L_{ref} (mm)	*3.269*	*3.276*	*0.511*
Streamwise wavenumber, α (-)	*0.20*	*0.20*	*0.20*
Spanwise wavenumber, β (-)	*0*	*0*	*0*
cBL, ω_r (-)	*0.1818*	*0.1846*	*-*
DSMC, ω_r (-)	*0.1824*	*0.1850*	*0.3169*
cBL, ω_i (-)	*-0.0029*	*-0.0021*	*-*
DSMC, ω_i (-)	*-0.0039*	*-0.0039*	*-0.0206*
cBL dimensional frequency, f (kHz)	*11.523*	*11.586*	*-*
DSMC dimensional frequency, f (kHz)	*11.557*	*11.610*	*288.640*
cBL amplification rate, (1/m)	*-0.91*	*-0.61*	*-*
DSMC amplification rate, (1/m)	*-1.21*	*-1.21*	*-40.32*

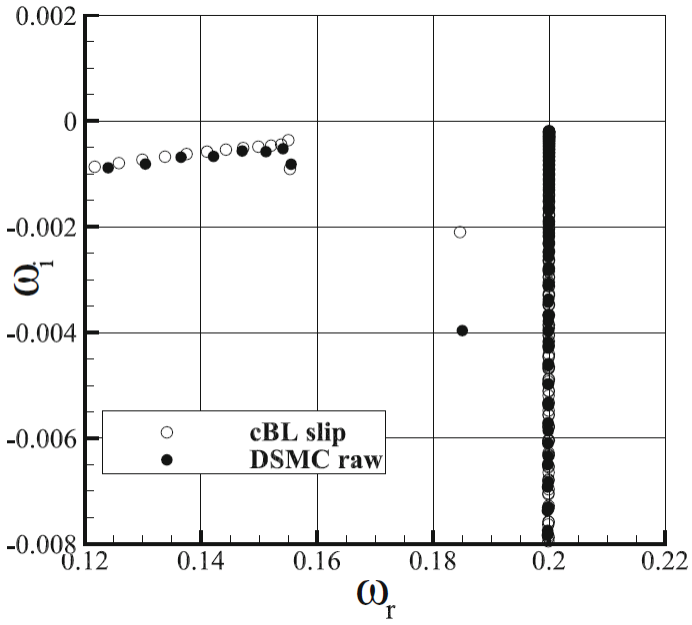

Figure 3.35: *Eigenvalue spectra of DSMC and compressible boundary layer (cBL) profiles for argon at the parameters of Case 2. The respective discrete eigenvalues are* ω_{BL}*=0.18651-0.00209i and* ω_{DSMC}*=0.185048-0.00396i.*

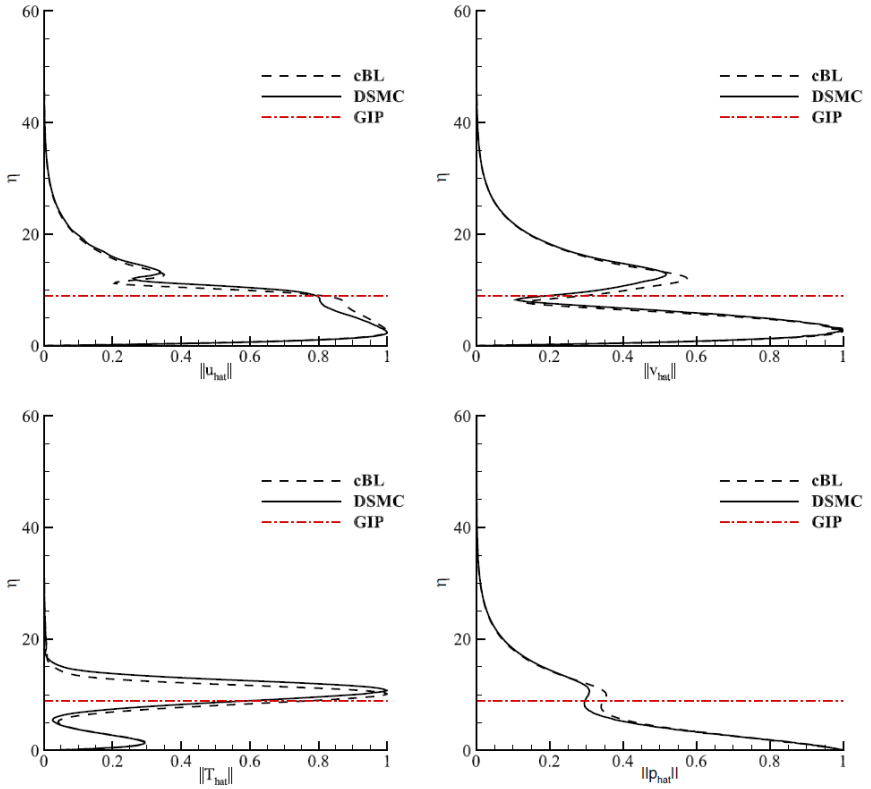

Figure 3.36: *Normalized amplitude functions of linear perturbations in air, at the parameters of Figure 3.34. The location of the generalized inflection point (GIP) is indicated by a horizontal line.*

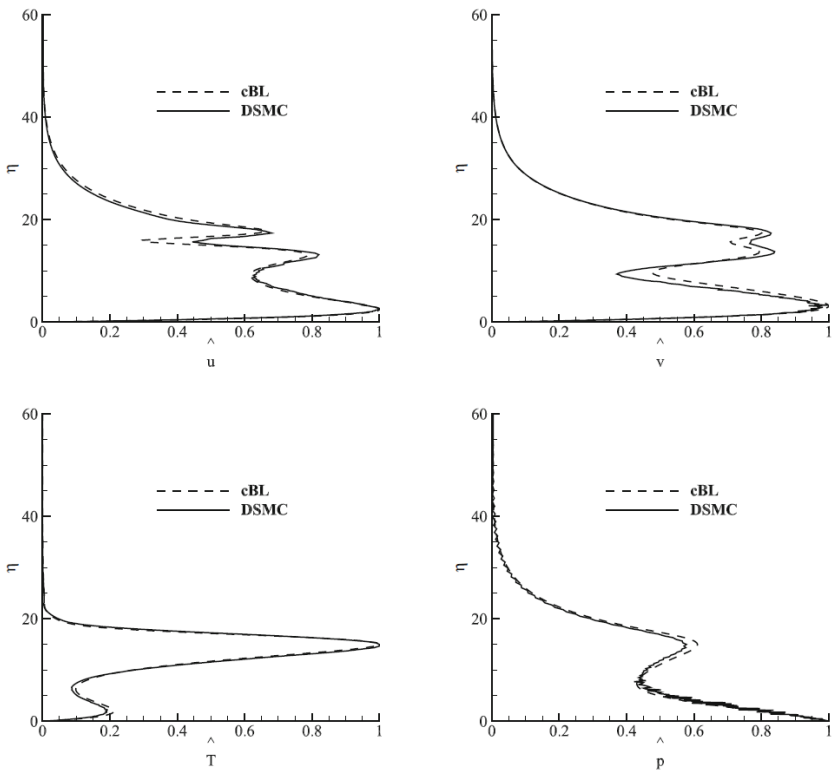

Figure 3.37: *Normalized amplitude functions of linear perturbations in argon, at the parameters of Figure 3.35.*

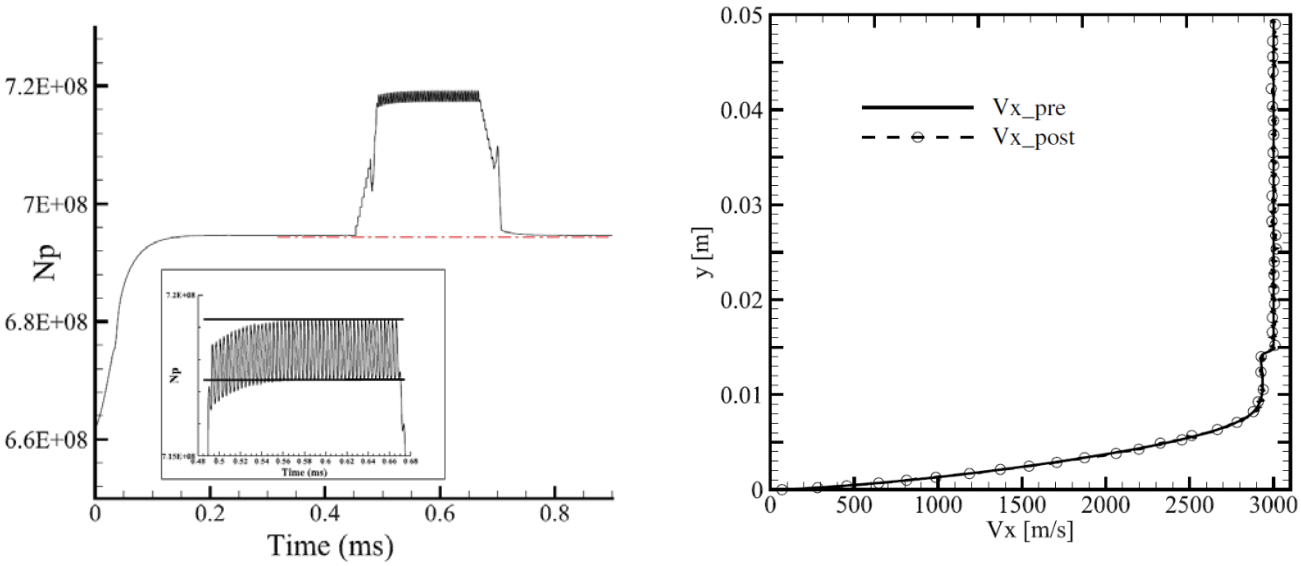

Figure 3.38: Left: *Total number of particles in the simulation as a function of time. The inset shows a magnified view of mass-neutral oscillations generated.* ***Right:*** *Wall-normal velocity component, sampled at steady state at x = 0.05 m, and instantaneous velocity obtained at t = 0.75 ms, after the jet stops emitting; the location of the shock is clearly visible at y ≈ 0.015 m.*

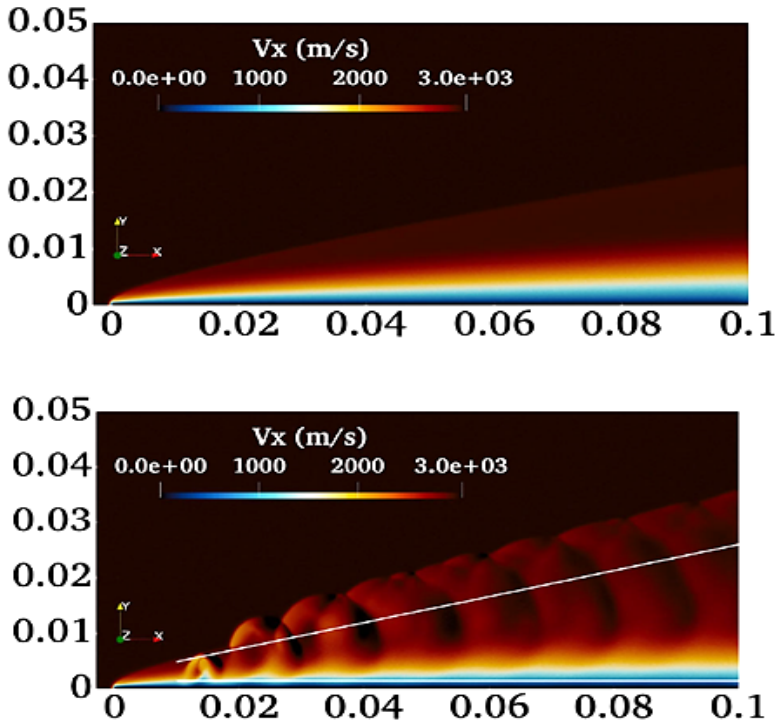

Figure 3.39: *Comparison of steady state (upper) and disturbed velocity field (lower). The white lines show the measurements positions close to the shock and in the boundary layer. The measurements close to the shock were taken along a 13.19^{o} angle line.*

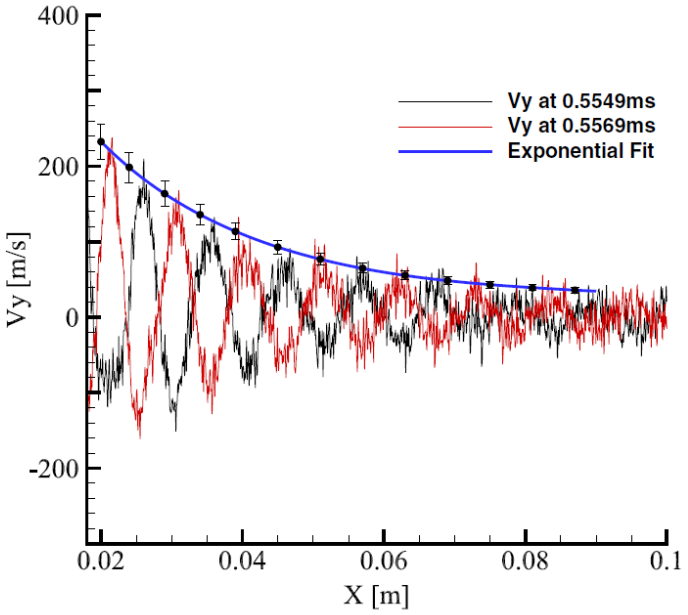

Figure 3.40: *Wall-normal velocity component inside the boundary layer and at a height of 0.0015 m from the wall, as a function streamwise coordinate; black and red indicate raw data at two successive time steps. Also shown an exponential curve of the form $y=Ae^{\sigma x}+C$ with A=508.86, σ=-40.32 and C=25.60. On the curve fit a ±10% error bar in the dumping rate σ has been marked.*

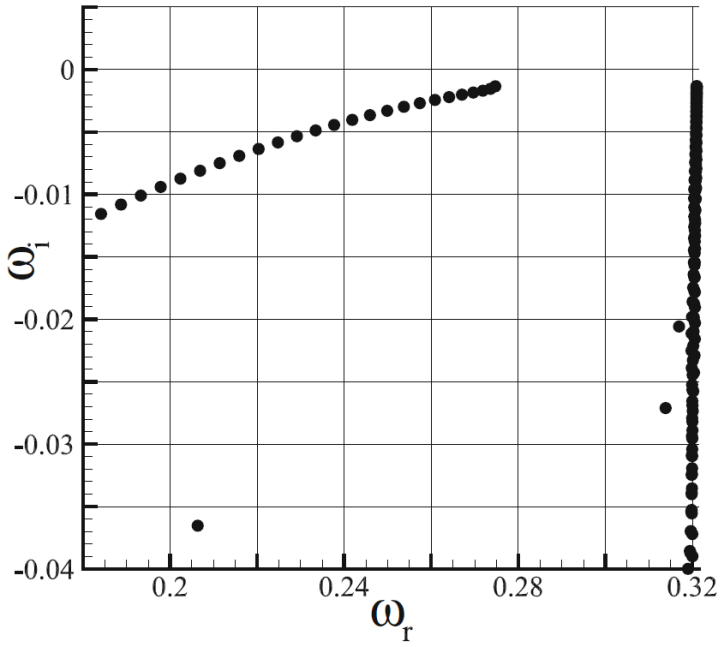

Figure 3.41: *Eigenvalue spectrum of the DSMC profile of nitrogen flow at M_e=6.99, $\sqrt{Re_x}$=78.1 and wavenumbers α=0.321 and β=0.*

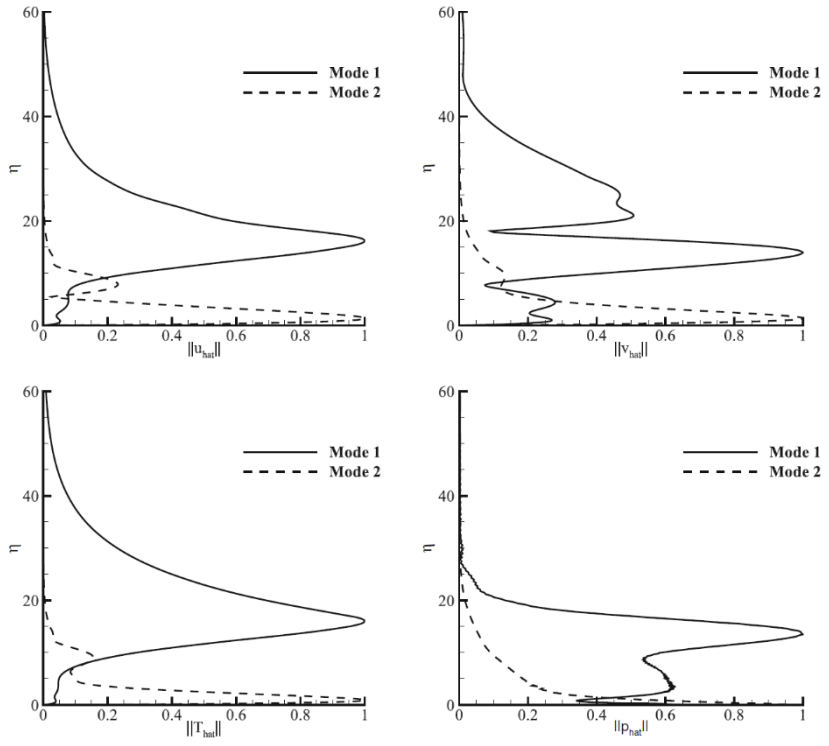

Figure 3.42: *Normalized disturbance amplitude functions corresponding to the leading discrete damped mode shown in Figure 3.41. Dashed lines represent the amplitude functions of the second in significance Mode 2.*

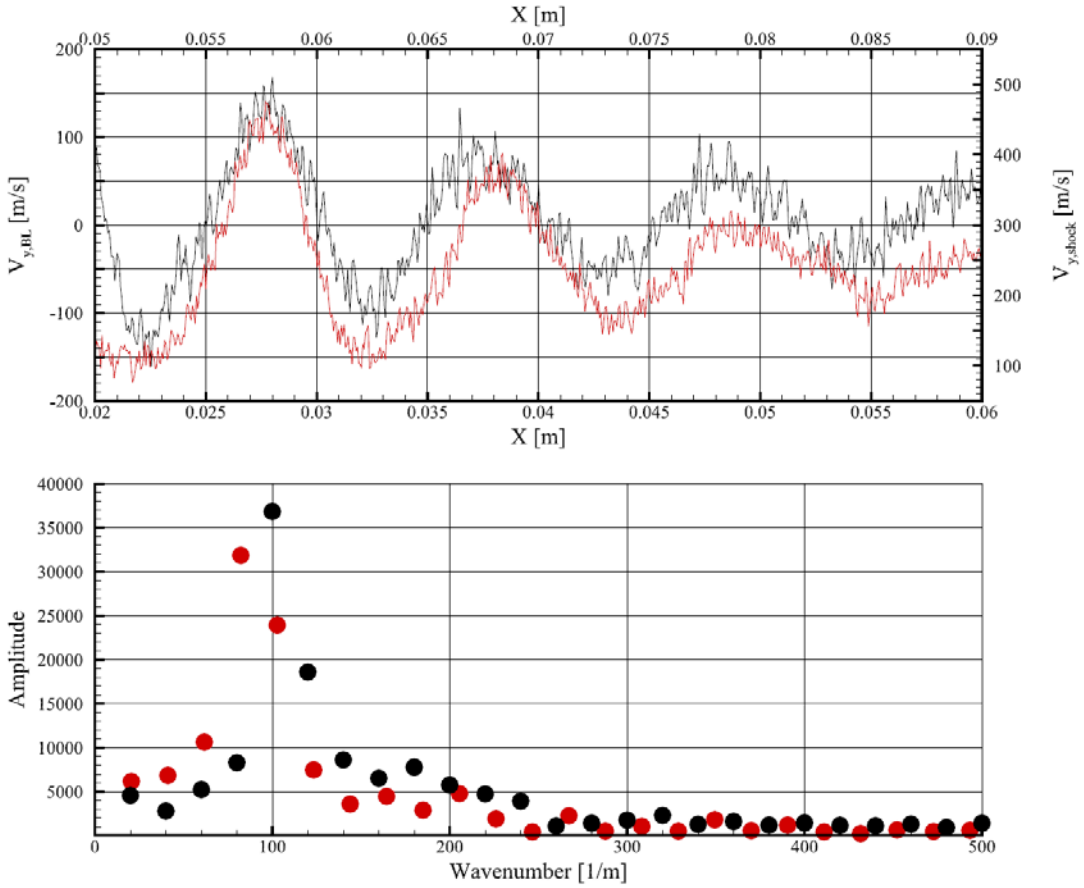

Figure 3.43: *Upper: Streamwise disturbance amplitude as extracted from the DSMC signal in the boundary layer (black) and in the shock (red). Lower: Fourier decomposition of two signals using the same color code.*

3.5 Investigation of the Instabilities of Hypersonic Flow over a Blunt Geometries

This test case extends the previous work done concerning the analysis of linear stability of a planar compressible semi-infinite flat plate boundary layer flow. In the previous test cases the flow was considered two-dimensional while in this case the flow is axisymmetric. The geometry used is a *7*-degree half angle blunt cone at Mach *5.9*. Two cases with this flow were examined, each at an order of magnitude different Knudsen number (and free stream pressure) from the next, are examined. In the first case, corresponding to free-stream pressure of *100* Pa, the Knudsen number is at the border of slip flow, Kn ~ O (*0.007*), whereas in the second case, with a free stream pressure of 1000 *Pa*, the Knudsen number Kn ~ O (*0.0007*) is such that the flow is at the limit of the slip regime. The respective Reynolds numbers based on the nose radius are *1359* and *13590*. Both cases are also computed by Direct Numerical Simulation (DNS). The flow conditions as well as the DSMC computational parameters for this set of test cases can be found in Table *3.15* and Table *3.16* respectively.

For all test cases the flow gas was air containing a mixture of *79% N_2* and *21% O_2*. The DNS methodology was employed to a low-pressure environment in the first test case thus

discrepancies are expected for these parameters. The geometry used in all the test cases is a 7-degree blunt cone with a length of *0.047 m* and a nose radius of *1.524 mm*. In the DSMC simulations an adapted grid was used with an adaption criterion based on the local Knudsen number to be greater than one. This ensures that the size of the computational cells to be less or equal to the mean free path of the flow. As evidenced from Table *3.16* the mean free path for Case *1* is 1.04×10^{-5} *m* and for Case *2* is 1.04×10^{-6} *m.* Finally, to accommodate all the effects of the flow, a domain of *0.048 m* x *0.055 m* was used. The inflow boundary is defined at the left side of the computational domain; uniform flow at the free-stream quantities, U_∞, T_∞ and P_∞ are imposed at this boundary. The right boundary is defined as outflow, the lower boundary is the axis of symmetry and in the upper boundary a specular reflection boundary condition was applied. The entire flow field mesh was generated using a uniform Cartesian grid. On the cone's surface an isothermal wall with full thermal accommodation and a wall temperature of *300* K was imposed. Gas molecules are assumed to reflect diffusely from the wall, according to the Maxwellian distribution at T_w. To validate and compare the flow parameters 3 different locations were chosen as it can be seen in Figure *3.44*. The first measuring location is across the stagnation point the second is at an angle of *135*-degrees and the last one is at the shoulder of the cone's nose. In Figures *3.45* and *3.46* the velocity magnitude, the temperature and the pressure can be seen for both cases. As evidenced in Case *1* the shock layer is much thicker than the one in Case *2*. This difference is attributed due to the more rarefied environment of Case *1*. Furthermore, the pressure at the stagnation points for both cases is ≈ 40 times higher than the one in the free-stream.

Comparisons of DSMC with DNS velocity and temperature can be seen in Figures *3.47, 48, 49* and *50*. Generally a very good agreement is observed between the two methods for both test cases examined. In Figure *3.47* the velocity along x-axis for the first test case can be seen. For the first location (across the stagnation line) close to the surface there is very good agreement between the 2 methods. DNS predicts a U_x velocity on the surface of *0.10555 m/s* whereas the DSMC predicts *0.096019 m/s*. Differences can be seen close and at the shock location. The very good agreement at this particular location can be attributed to the fact that the pressure is very high in that area so the velocity slip is quite small and DNS can perform better under these conditions. DSMC predicts a shock at the same location as DNS but $\approx 30\%$ thicker. In the second location there is an excellent agreement between the two methods.

Table 3.15: *Flow parameters (Investigation of the Instabilities of Hypersonic Flow over a Blunt Geometries).*

Case	***Free stream pressure, P_∞ (Pa)***	***Re_∞****	***U_∞ (m/s)***	***Gas***	***N_{den} $(\#/m^3)$***	***T_∞ (K)***	***T_w (K)***
1	*100*	*1359*	*1038.15*	*Air*	9.43833×10^{22}	*76.74*	*300*
2	*1000*	*1350*	*1038.15*	*Air*	9.43833×10^{22}	*76.74*	*300*

*Based on the cone radius

A slight disagreement can be seen in the prediction of the slip velocity on the wall as DSMC predicts a higher slip velocity than DNS. On the other hand, shock location and thickness are in perfect agreement. In the last location on the shoulder of the cone there is excellent agreement everywhere apart from the shock thickness. Again, a thicker shock in

that location is predicted by DSMC. As far the second test case is concerned it can be evidenced from Figure *3.49* that there is an excellent agreement in the shock location, thickness and slip velocity. This perfect agreement was expected because for this test case with an order of magnitude higher pressure than the previous case there are no rarefaction effects. The shock thickness is very small (infinitesimally small maybe) and the slip velocity is very close to zero.

Table 3.16: *DSMC computational parameters.*

	Case 1	***Case 2***
Knudsen number, Kn	*0.0068*	*0.0006*
Number of particles, N_p	1.65×10^{8}	1.25×10^{9}
Timestep, dt (s)	1.0×10^{-9}	1.0×10^{-10}
Transient period (timesteps)	*60,000*	*600,000*
Samples	*100,000*	*100,000*
Mean free path, λ (m)	1.04×10^{-5}	1.04×10^{-6}
Power law exponent, ω	*0.75*	*0.81*
Mach number, Ma_∞	*5.92*	*5.92*

As far as the temperature comparison is concerned there is a general good agreement apart from the area close and inside the shock. For first test case it is evidenced from Figure *3.48* that in the location across the stagnation point DSMC and DNS have an excellent agreement close to the surface. Moving towards the shock DNS is unable to analyze the temperature close and inside the shock. This happens because DNS treats the shock as a discontinuity. Both methods predict the shock at the same location while DSMC as previous mentioned and is evident also in Figure *3.48* predicts a thicker shock.

For the other two locations a general good agreement is achieved. For the second test case where the pressure is an order of magnitude higher, and the shock is stronger and thinner than the first test Case 2oth methods agree quite well as it can be seen in Figure *3.50*. In the first location both methods have a slight disagreement in the temperature around the shock area whereas very good agreement can be observed in the other two locations. Even with this thinner shock DSMC can capture the temperature rise inside the shock whereas DNS seems to smooth out the temperature spike inside the shock. In Figure *3.51* the surface properties for both test cases can be seen. In both test cases the pressure on the surface for the location near the stagnation point is ≈ 45 times higher than the free-stream pressure. As expected, the pressure drops as we move away from the stagnation point. The temperature in the first case has a spike near the shoulder of the cone whereas in the second case is doesn't change much as we move along the surface. This can happen because of rarefaction effects occurring in the *100 Pa* test case. Finally, the slip velocity increases from 0 to ≈ 100 *m/s* and ≈ 50 *m/s* for the first and second test case respectively. This happens because of the major pressure drop occurring as we move away from the stagnation point but then after right after the shoulder the flow stabilizes across the rest of the surface.

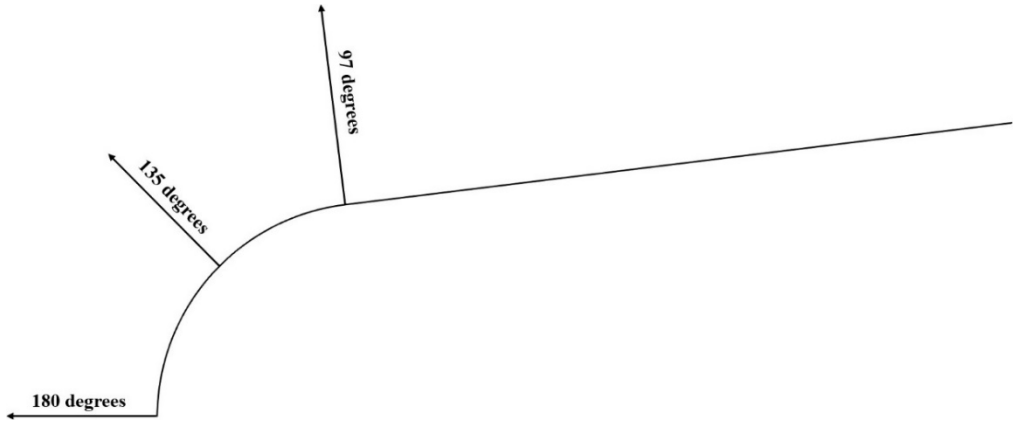

Figure 3.44: *Locations at which flow properties are extracted in the vicinity of the cone nose.*

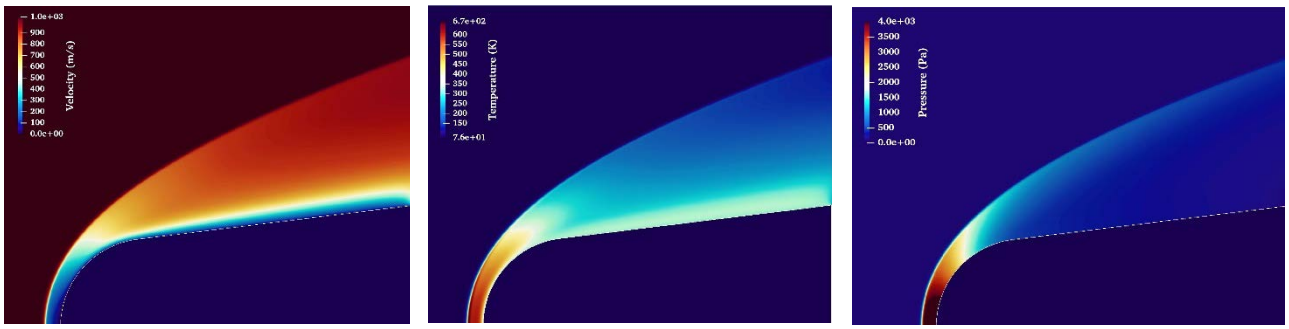

Figure 3.45: *Velocity (left), temperature (middle) and pressure (right) fields, as calculated from the DSMC at 100 Pa.*

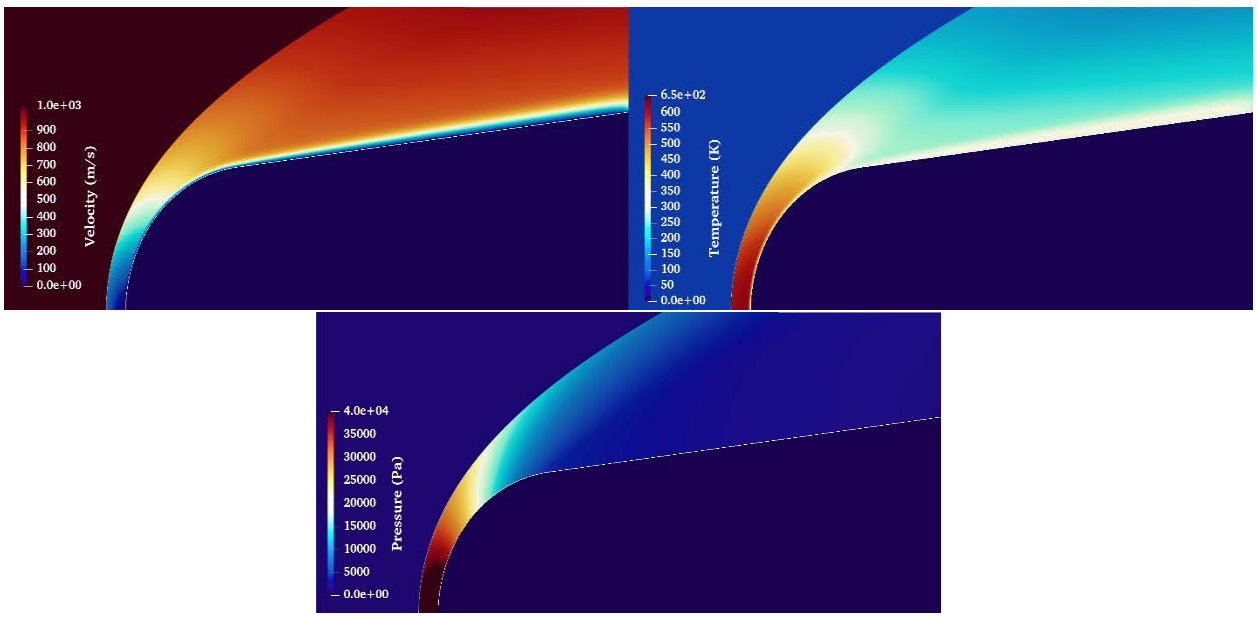

Figure 3.46: *Velocity (left), temperature (right) and pressure (bottom) fields, as calculated from the DSMC at 1000 Pa.*

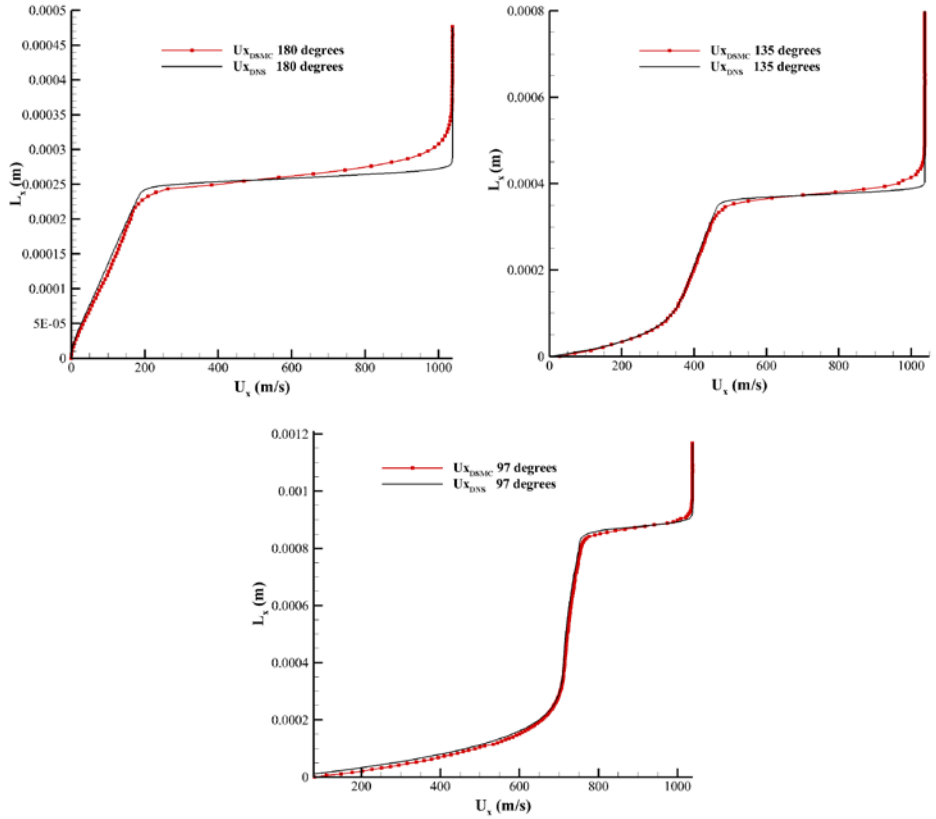

Figure 3.47: *Comparison of velocity profiles obtained by DSMC and DNS at the three locations shown in Figure 3.44, at a pressure of 100 Pa.*

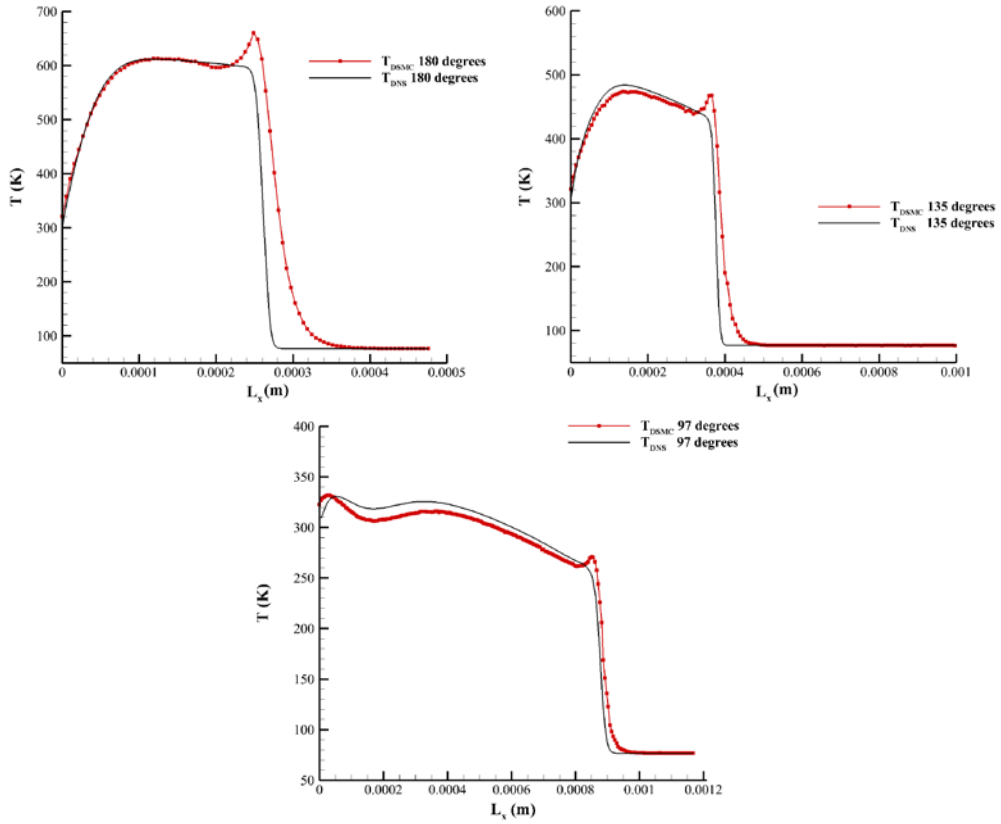

Figure 3.48: *Temperature comparison of DSMC and DNS at the three locations shown in Figure 3.44 at a pressure of 100 Pa.*

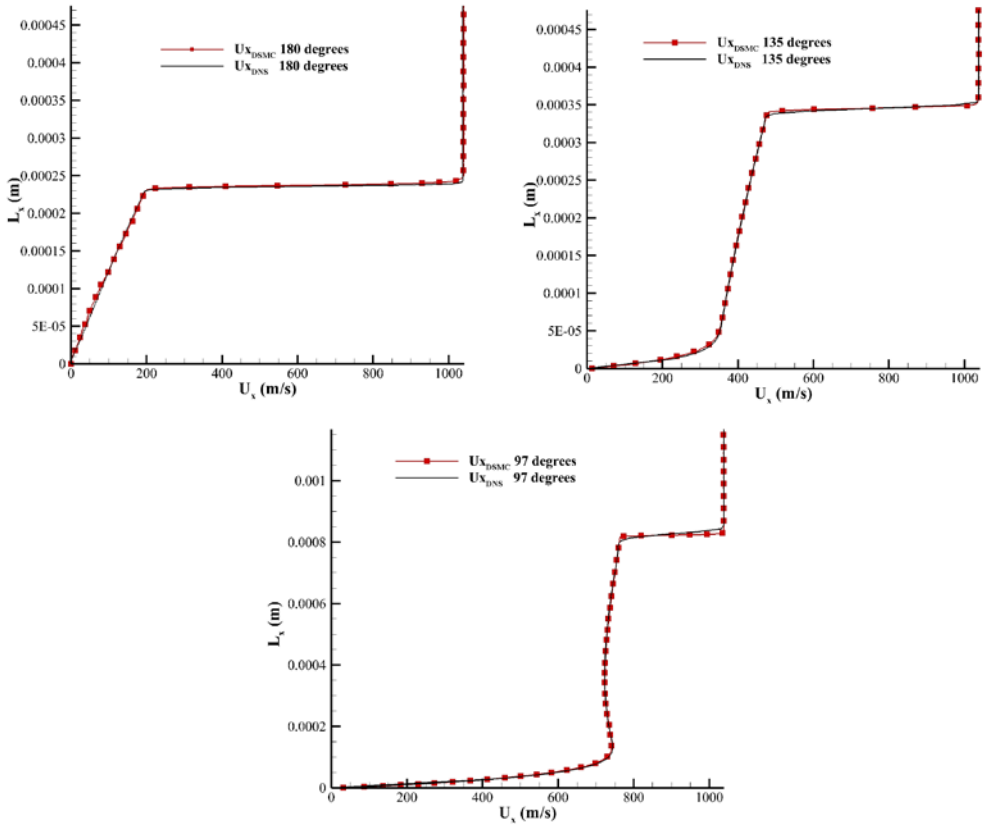

Figure 3.49: *Comparison of velocity profiles obtained by DSMC and DNS at the three locations shown in Figure 3.44 at a pressure of 1000 Pa.*

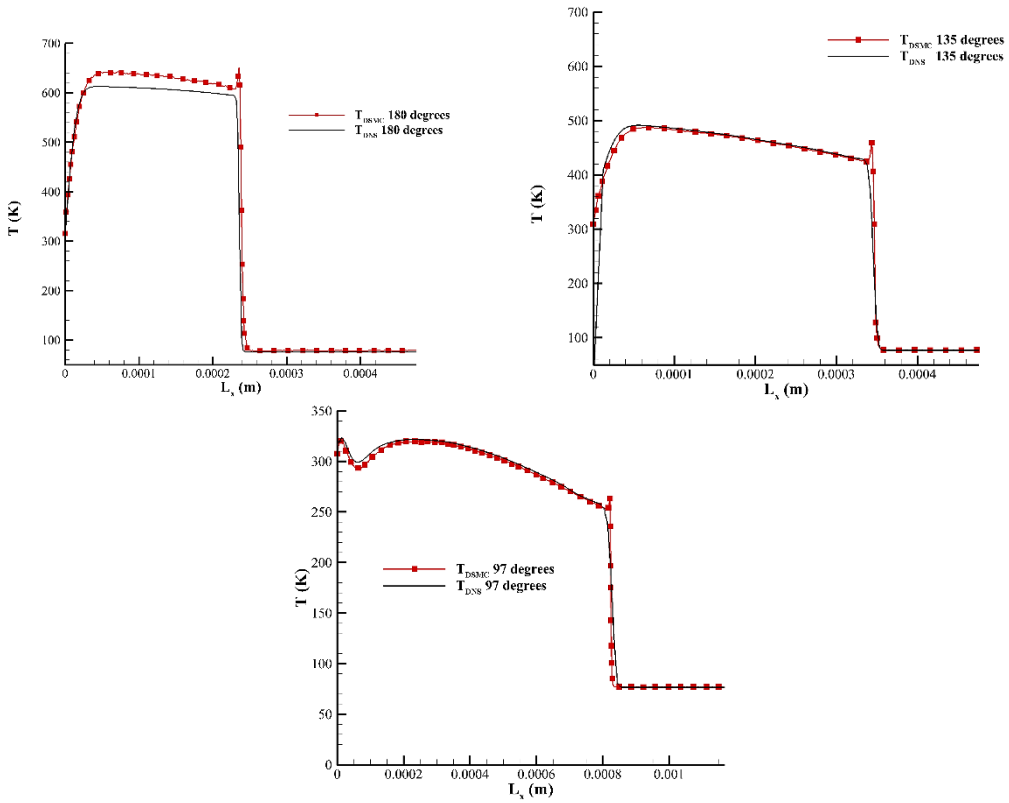

Figure 3.50*: Temperature comparison of DSMC and DNS at the three locations shown in Figure 3.44, at a pressure of 1000Pa.*

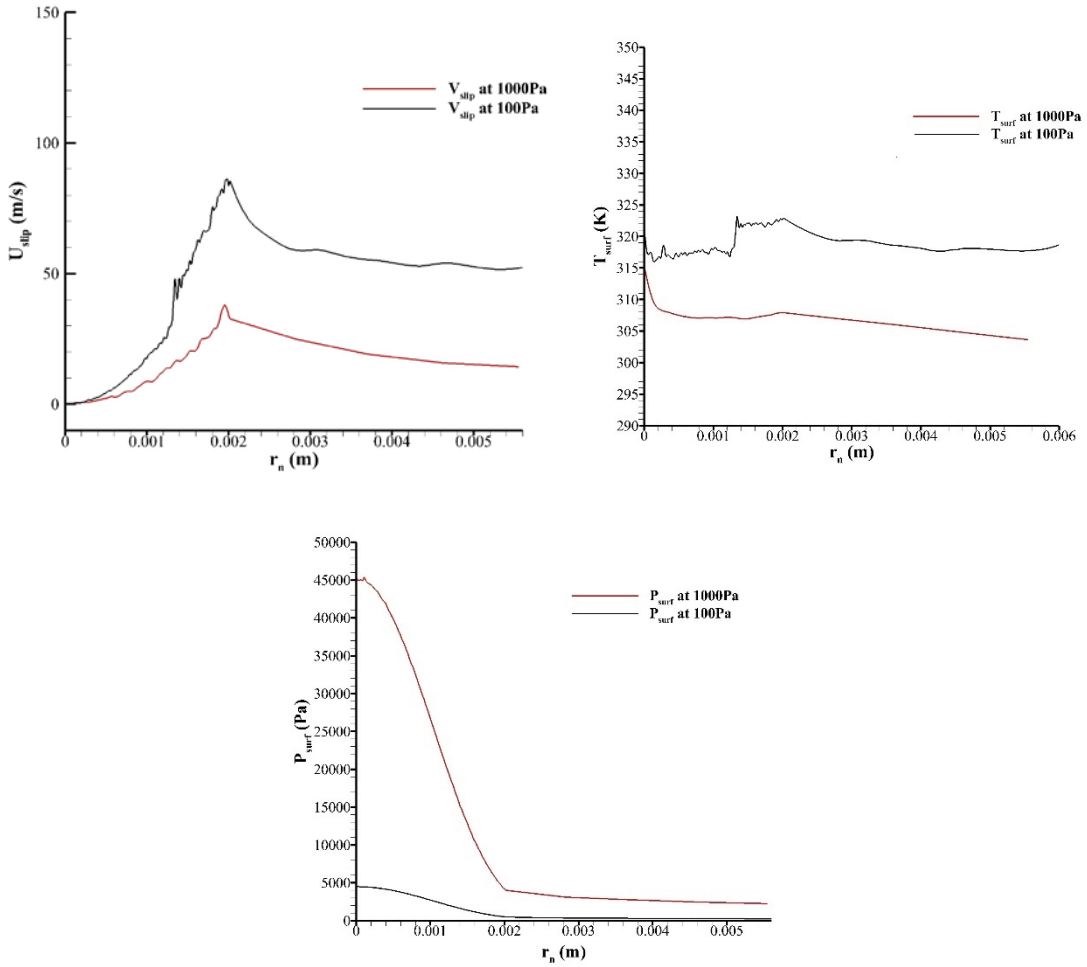

Figure 3.51: *Comparison of velocity slip, surface temperature and surface pressure, as calculated from DSMC at 100 Pa (black line) and 1000 pa (red line).*

3.6 Hypersonic flow over a complex suborbital vehicle

The sixth test case is a fully three-dimensional (3D) test case. The geometry used was provided by Thomas Frevillier. The vehicle was designed by his team (Azim UTBM) and won the Airbus Group Prize during the 2014 Student Aerospace Challenge. The length of the vehicle is *12.8* m, while its wingspan is approximately *8* m with curved wingtips. Figure *3.52* includes three different of the geometry. For this test case half configuration was simulated to account for computational efficiency. In order for this geometry to be used with the *Galatea* [Lyg15, Lyg16] solver it had to be re-dimensionalized, in order the mean aerodynamic cord to become unity. The mean aerodynamic cord and consequently the required for the N-S simulation reference length was set to *6.0578 m*. To be able to validate our velocity slip and temperature boundary conditions implementation two test cases were examined whose differences focus on the values of the free-stream velocity and angle of attack. The first one called thereafter Case *1*, the angle of attack was set to *0º*, while the free-stream velocity was assumed *700* m/s. The same values were used for the second test case, called thereafter Case *2*, were *40º* and *1400* m/s respectively. The Mach and Reynolds

numbers (the latter based on the mean aerodynamic cord) were computed equal to *2.693* and *273.207* respectively for Case *1*; for Case *2* the corresponding values were *5.386* and *424.414*. In both cases the Knudsen number was assumed equal to *0.01634* (slip flow regime). The free-stream temperature was set equal to *168.721 K* while the corresponding temperature on the shuttle surface was set to *290 K*. The background pressure was assumed equal to *2.8* Pa, a value corresponding to an altitude of *120* km. The flow conditions for both test cases are summarized in Table *3.17*. The velocity values are relatively small comparing to this of a shuttle during the re-entry phase, nevertheless, they were assumed adequate, considering our motivation to assess *Galatea* solver against rarefied gas dynamics problems.

Considering the flow conditions, a hybrid unstructured grid was constructed for the N-S solver, composed of *2,265,392* nodes, *10,618,201* tetrahedra, *906,706* prisms and *561* pyramids. The prismatic elements were located on the solid wall regions such as the fuselage and the wings of the vehicle, to allow for the effective prediction of the boundary layer. Figure *3.53* illustrates the employed computational grid while Figure *3.54* depicts its density on the symmetry (top) and the vehicle (bottom) surfaces.

Table 3.17: *Flow parameters (Hypersonic flow over a complex suborbital vehicle).*

	Case 1	***Case 2***
Mach number, Ma_∞	*2.693*	*5.386*
Reynolds, Re_∞	*213.207*	*426.414*
Freestream velocity, U_∞ (m/s)	*700*	*1400*
Knudsen number, (Kn)*	*0.01634*	*0.01634*
Angle of attack, α (degrees)	*0*	*40*
Freestream density, ρ_∞ (kg/m^3)	5.77×10^{-7}	5.77×10^{-7}
Freestream temperature, T_∞ (K)	*168.721*	*168.721*
Wall temperature, T_w (K)	*290*	*290*
Gas	*Air*	*Air*

***Based on the vehicle's length**

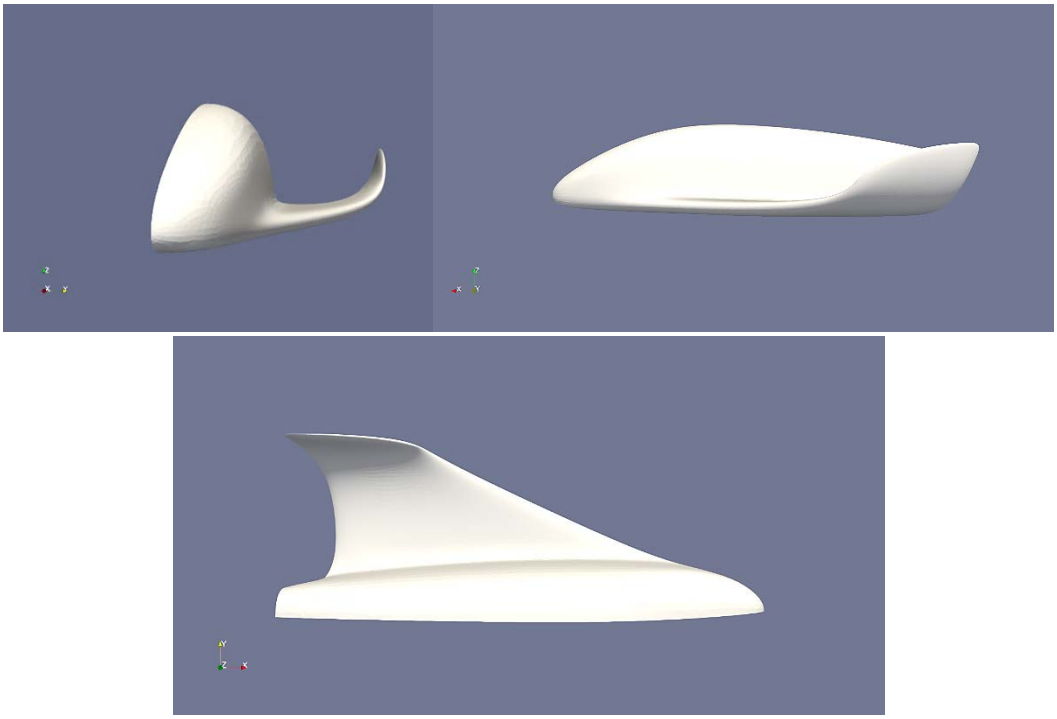

Figure 3.52: *Vehicle geometry overview. Front view (top left), side view (top right) and top view (bottom).*

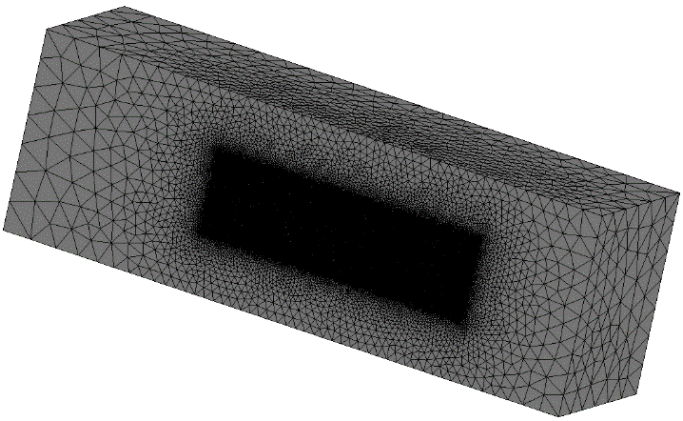

Figure 3.53: *Overview of the computational grid used in Galatea solver.*

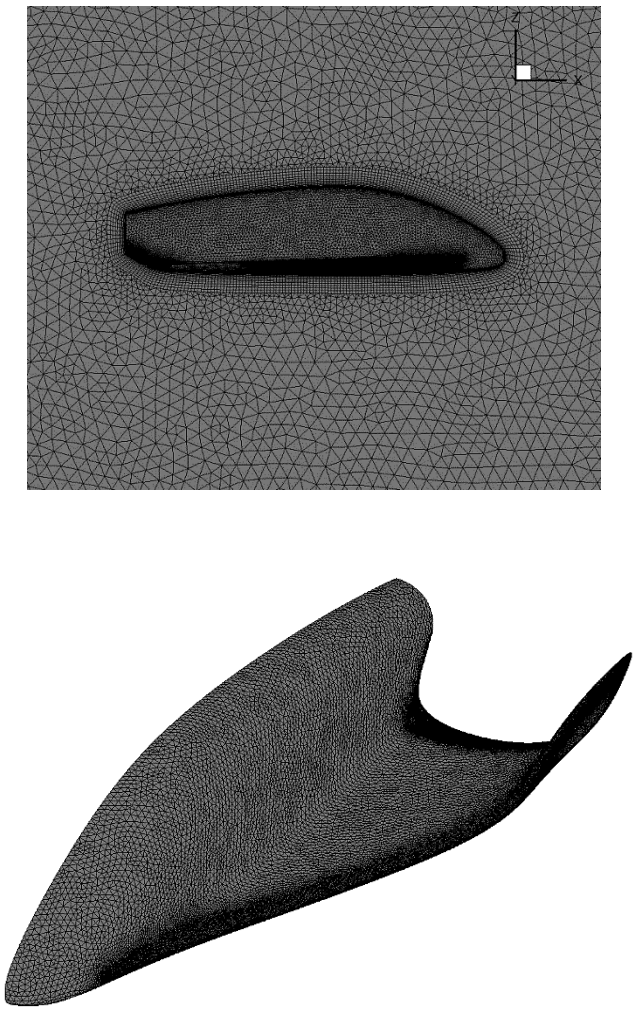

Figure 3.54: *Grid density on the symmetry (top) and shuttle (bottom) surfaces of the computational grid used with the Galatea solver.*

For the *Galatea* solver the calculation of the inviscid fluxes the Roe's approximate Riemann solver was employed along with a second-order spatial accurate scheme, coupled with the Van Albada-Van Leer slope limiter. The nodal-averaging scheme was applied for the computation of the velocity and temperature gradients, and consequently the viscous fluxes. Time integration and iterative approximation of the final steady-state solution was succeeded with the incorporated second-order accurate in time four-stage Runge-Kutta scheme. The CFL number was set equal to *0.5*. In Case *1* (Mach number *2.693* and angle of attack *0º*) both the incorporated first- and second-order accurate slip models were implemented [Bes99, Kar02]. To accelerate the solution procedure (on a DELL™ R*815* Poweredge Server with four AMD Opteron™ 6380 sixteen-core processors) the initial grid was divided in eight sub-domains to be processed in parallel. Moreover, two coarser resolutions were constructed for each partition applying the full-coarsening directional agglomeration strategy; further acceleration was succeeded via the incorporated multigrid scheme. For this test case due to the absence of any experimental or computational data, the assessment of Galatea in terms of accuracy was performed with the SPARTA DSMC code. For its implementation a computational domain with dimensions *50 m*, *10 m*, and *42 m* in x-, y- and z-axis, respectively, was designed. Spatial discretization was succeeded by

dividing the domain in approximately *21,000,000* cells, by employing a Cartesian grid with *500*, *120* and *420* cells in x-, y- and z-axis, respectively.

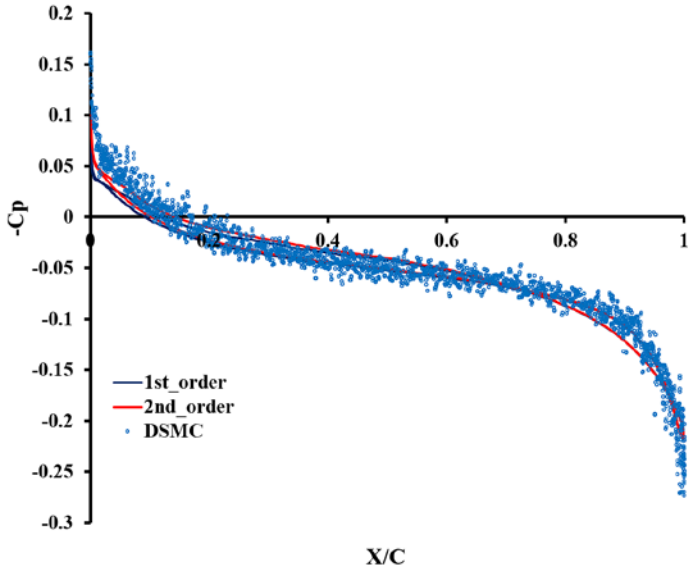

Figure 3.55. *Pressure coefficient distribution at wing spanwise section Y=1.21156 m (Case 1).*

For the DSMC solver as seen in Table *3.18* the number density was set to 1.22×10^{19} $(\#/m^3)$, while the time step was selected equal to 3.5×10^{-5} *s* for Case *1* and 1.42×10^{-5} *s* for Case *2*. The time steps were defined so that are smaller than the mean collision time and each particle requires approximately five-time steps to cross each cell. The simulation began with a transient period of *25,000* steps, deriving the initial steady-state solution, while after that samples were taken for additional *120,000* steps, aiming to reduce the statistical scattering error. Considering that DSMC methodology depends strongly on the used number of particles, several tests were performed and from these tests the optimum F_{num} of $6.3\times10^{17}$was selected, which subsequently produced a total number of 4.21×10^{8}particles for the whole simulation domain. The parameters, defining actually the employed DoFs (Degrees of Freedom), were revealed to derive the desired accuracy, avoiding yet any excessive computational and memory requirements. In order to enhance accuracy near the surfaces a cell volume grid weighting scheme was used in the DSMC code. This mechanism induces every grid cell to contain roughly the same number of particles (even if cells are of varying size or closed to surfaces), to minimize the total number of particles used in a simulation while preserving accurate time and spatial averages of flow quantities.

Table 3.18: *DSMC computational parameters.*

	Case 1	***Case 2***
Number density, Nd_∞ $(\#/m^3)$	1.22×10^{19}	1.22×10^{19}
Timestep (s)	3.5×10^{-5}	1.42×10^{-5}
Transient period	*25,000*	*25,000*
Sample period	*120,000*	*120,000*

Number of particles (#)	4.21×10^{8}	4.21×10^{8}

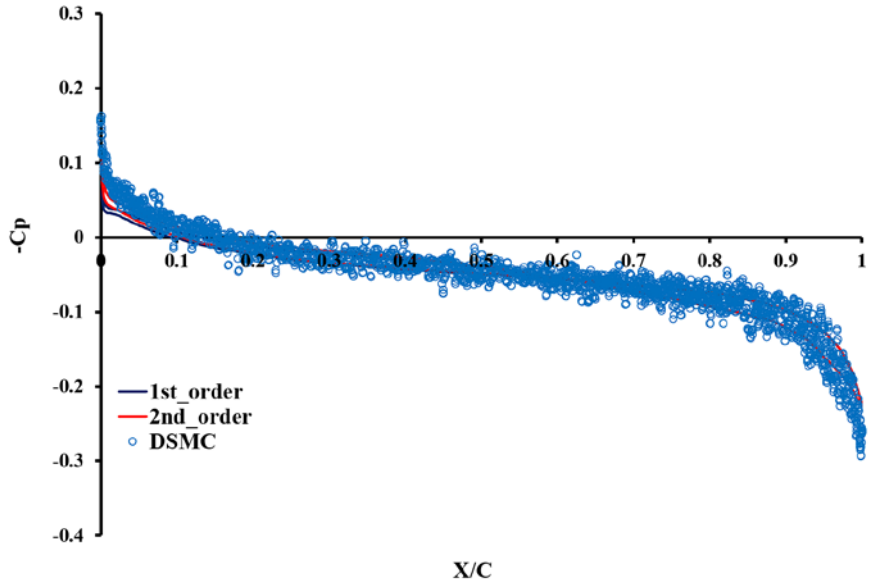

Figure 3.56. *Pressure coefficient distribution at wing spanwise section Y=1.51445 m (Case 1).*

Due to the big three-dimensional domain and the high computational cost of the DSMC method it should pointed out that for this test case, SPARTA required approximately six times more wall clock computational time than *Galatea*. More specifically the DSMC solution required about *145* hours using *64* cores, while the N-S solution required only *24* hours in *8* cores at the same computer system. Figures *3.61* and *3.62* illustrate the dimensionless velocity magnitude contours on the symmetry plane, extracted with the *Galatea* and SPARTA solver respectively, for Case *1*. As observed, a satisfactory agreement is achieved, particularly in the bow shock region at the front of the vehicle. *Galatea* predicts a shock angle of 36^{o} (without grid adaption), while SPARTA predicts a shock angle of 34.5^{o}. This results in a 4.25% difference in shock angle prediction between the two methods. Besides the qualitative comparison, quantitative comparisons have also been performed. Figures *3.55* to *3.60* contain the pressure coefficient distributions, extracted by the two solvers at six different wing spanwise sections, namely, Y=*1.21156 m, 1.51445 m, 2.42312 m, 3.0289 m, 3.63468 m* and *4.24046 m*. The results include the distributions derived by the incorporated second-order accurate slip model of Beskok and Karniadakis as well. It is quite obvious that the employed solvers produced very close results, despite the fact that they are based on completely different computational approaches. Though no significant differences are identified between the first- and second-order accurate slip models, the latter one appears to derive results about 30% ~~(quantify)~~ closer to those of the DSMC approach in the leading-edge region Therefore, in Case *2* only the second-order model was implemented.

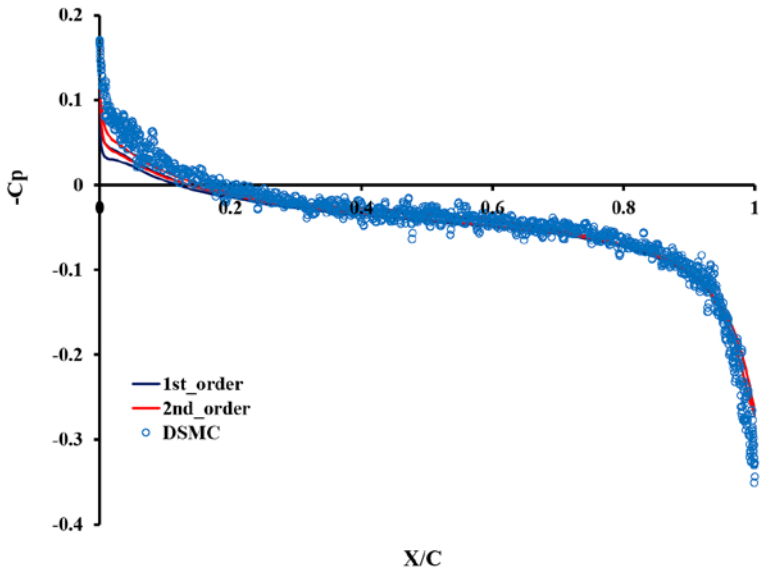

Figure 3.57. *Pressure coefficient distribution at wing spanwise section Y=2.42312 m (Case 1).*

In Figures *3.63* and *3.64* the dimensionless velocity magnitude contours on the symmetry plane, derived by the aforementioned N-S and DSMC solvers respectively, for Case *2* is shown. At this point should be highlighted that the *40º* angle of attack was succeeded with a corresponding rotation of the far field flow direction in case of the Galatea code; in case of the SPARTA code a respective revolution of the whole surface grid was performed for easiness reasons. Once more, the derived qualitative results appear to be very close. The same holds for Figures *3.65* to *3.69* containing the produced pressure coefficient distributions at six different wing spanwise sections (Galatea was used only with the second-order accurate slip model as aforementioned in this test case). As a result, the capability of the Galatea solver to predict such complex rarefied gas flows in terms of accuracy is clearly demonstrated. In the DSMC data there is some noise in the negative coefficient of pressure area. Since the vehicle is at an angle of attack this accounts for the wing's upper surface. This happens due to the lack of particles hitting the upper surface of the wing. If the number of particles was higher this effect would have been avoided but a higher number of particles in this particular test case would exceed the available system memory. Thus, the number of particles used in the simulation had to be limited in order for the test case to fit in the available system's memory.

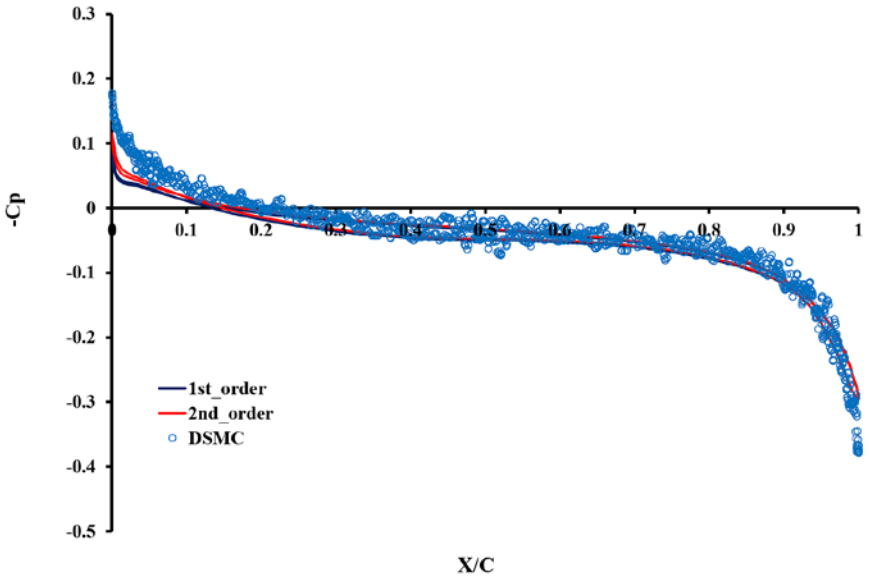

Figure 3.58. *Pressure coefficient distribution at wing spanwise section Y=3.0289 m (Case 1).*

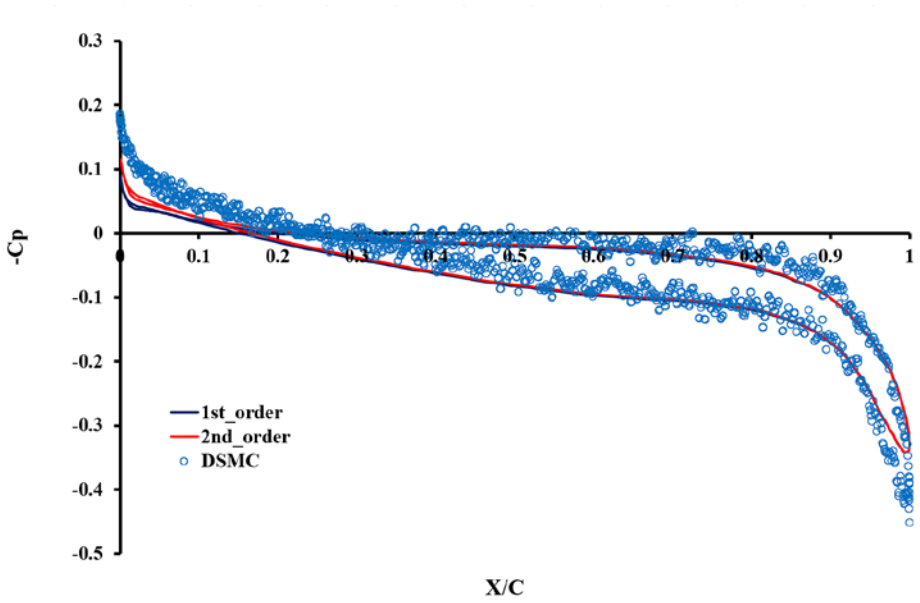

Figure 3.59. *Pressure coefficient distribution at wing spanwise section Y=3.63468 m (Case 1).*

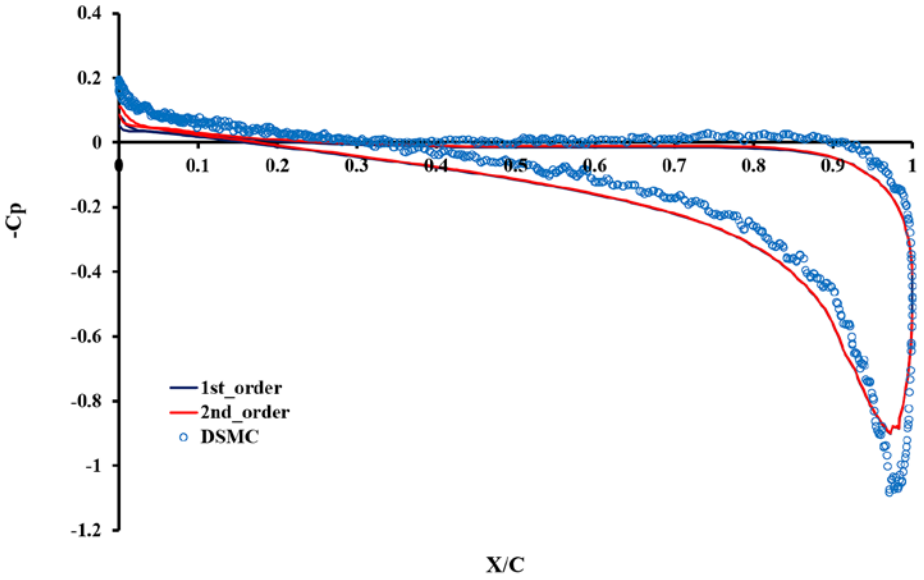

Figure 3.60. *Pressure coefficient distribution at wing spanwise section Y=4.24046 m (Case 1).*

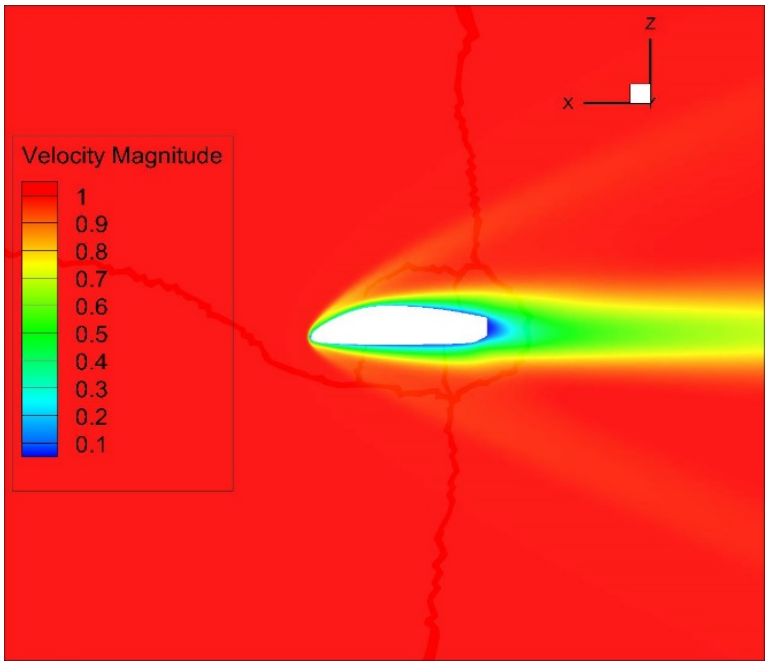

Figure 3.61. *Dimensionless velocity magnitude contours on the symmetry plane, extracted with the Galatea solver (Case 1).*

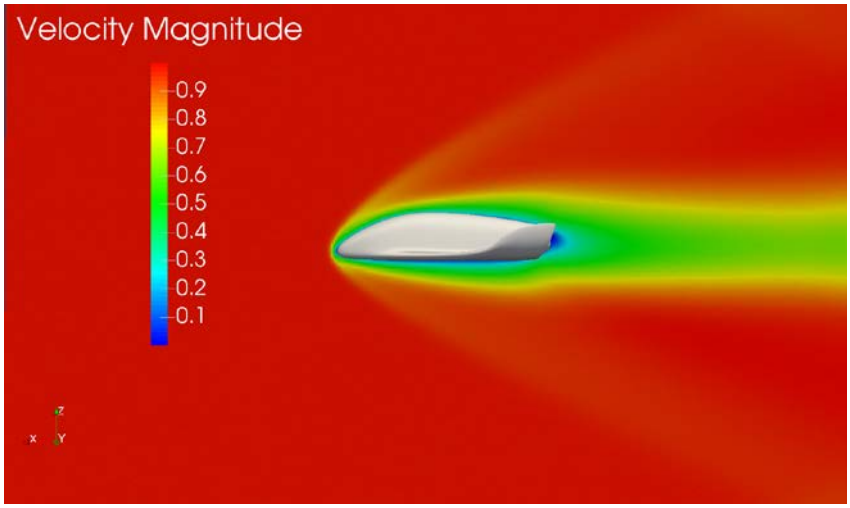

Figure 3.62. *Dimensionless velocity magnitude contours on the symmetry plane, extracted with the SPARTA solver (Case 1).*

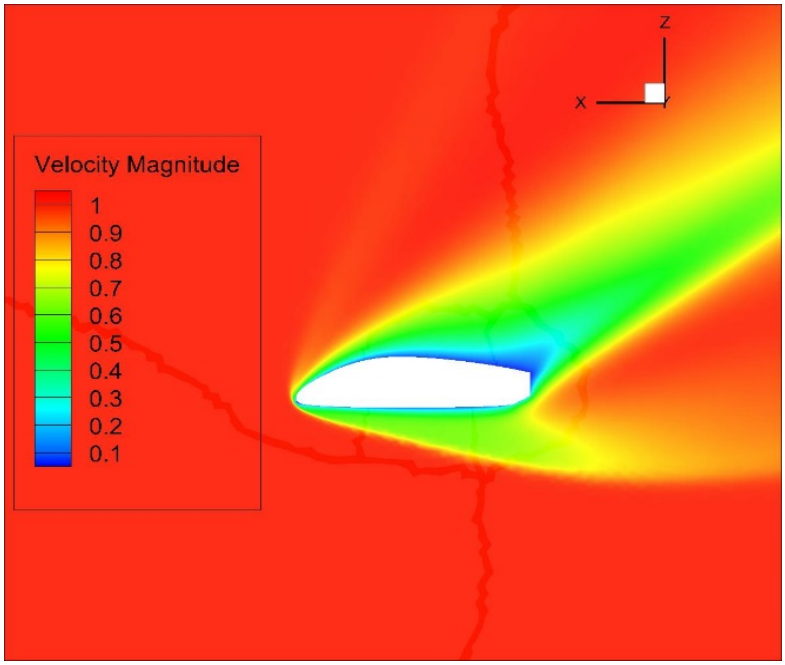

Figure 3.63. *Dimensionless velocity magnitude contours on the symmetry plane, extracted with the Galatea solver (Case 2).*

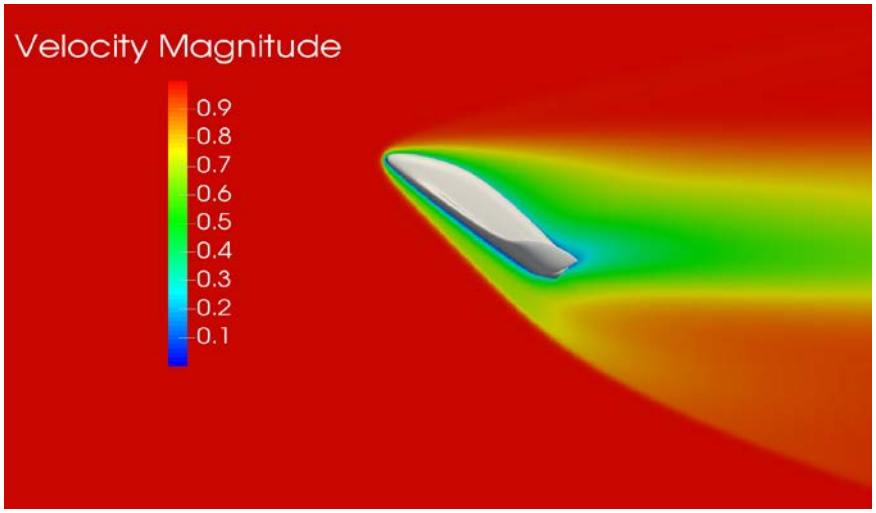

Figure 3.64. *Dimensionless velocity magnitude contours on the symmetry plane, extracted with the SPARTA solver (Case 2).*

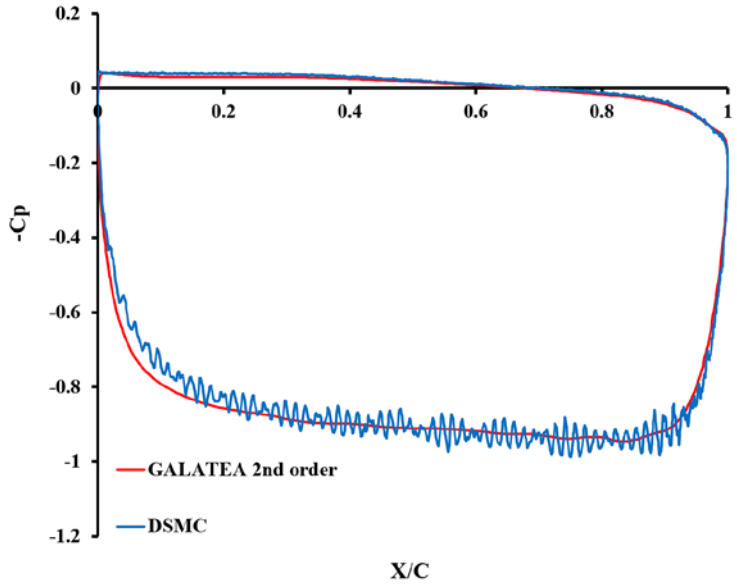

Figure 3.65. *Pressure coefficient distribution at wing spanwise section Y=1.21156 m (Case 2).*

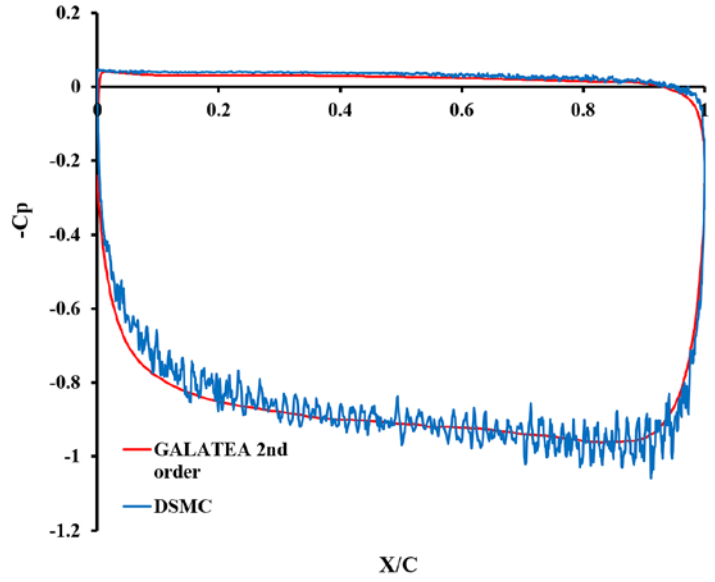

Figure 3.66. *Pressure coefficient distribution at wing spanwise section Y=1.51445 m (Case 2).*

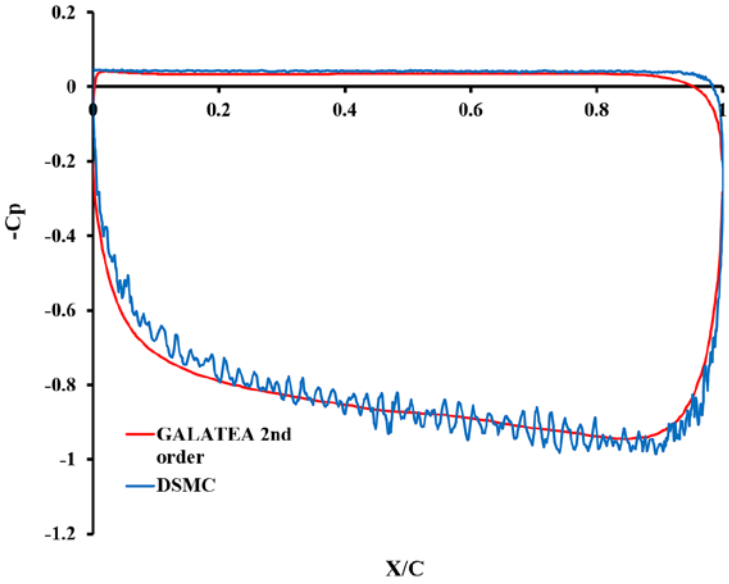

Figure 3.67. *Pressure coefficient distribution at wing spanwise section Y=1.2.42312 m (Case 2).*

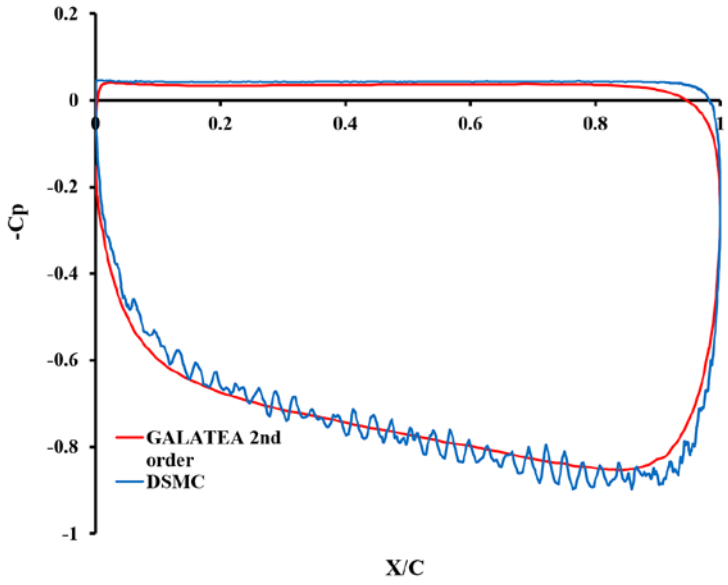

Figure 3.68. *Pressure coefficient distribution at wing spanwise section Y=3.0289 m (Case 2).*

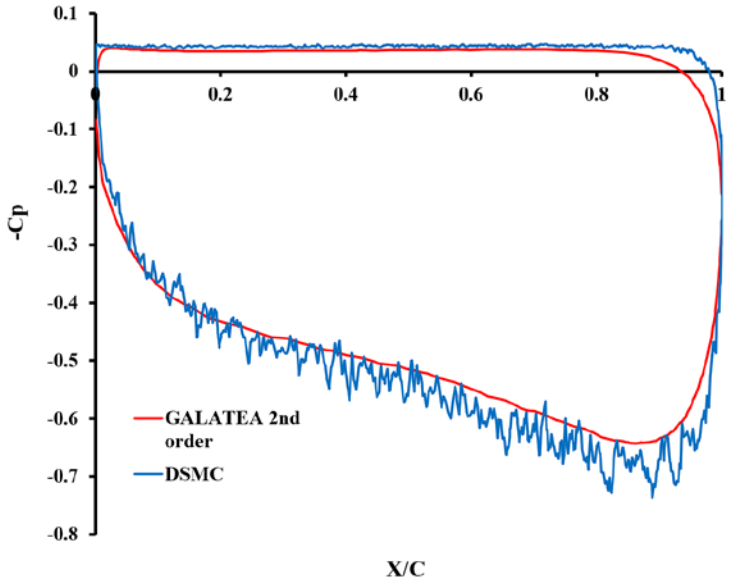

Figure 3.69. *Pressure coefficient distribution at wing spanwise section Y=3.63468 m (Case 2).*

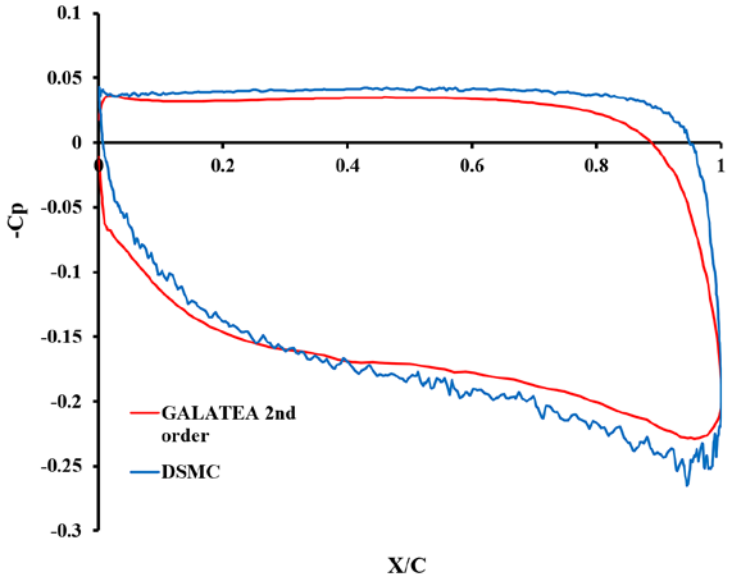

Figure 3.68. *Pressure coefficient distribution at wing spanwise section Y=4.24046 m (Case 2).*

3.7 Hypersonic flow over a complex suborbital vehicle with stability analysis

After simulating this geometry with N-S using the velocity slip and temperature jump boundary conditions described above the case was rerun with a different set of flow conditions this time closer to re-entry conditions and an effort has been made to extract more data and perform a stability analysis based on the new DSMC that obtained. The gas mixture used for this variation is again a *79%* N_2 and *21%* O_2. The surface of the vehicle was modelled as diffuse reflecting with full thermal accommodation at *300* K. The flow conditions chosen for this simulation occur at 100 km altitude. The velocity selected is the typical velocity for that altitude according to [Viv20, Zup14, Pez16]. The rest parameters regarding the conditions at that altitude were taken from the US Standard Atmosphere *1976* model. The simulation conditions are summarized in Table *3.19* and the parameters for the DSMC simulation can be found in Table *3.20*. In order to accommodate all the flow effects the simulation domain in this run was set to *36* m long, *13* m in width and *35* m in height. The inflow boundary is defined at the left of the shuttle and at a distance of about *14* m from the nose whereas the outflow is defined about *22* m downstream of the nose. After running several tests this size was adequate to capture the fully developed flow field as well as a good fraction of the wake. The inter-particle collisions are modelled using the Variable Soft Sphere (VSS) model with default parameters as described in [Bir94]. In order to reduce the computational cost and further enhance the simulation accuracy the a near-neighbor collision partner selection scheme was used as described in [Gal11] where collision partners are selected within a sphere with radius equal to the distance the particle travels in one timestep. The shuttle was set at a *30º* angle of attack. Typical values for this altitude range

are between *35-45* degrees as mentioned [Bla94] but for this specific test case after discussions with the Azim UTBM team, which designed the vehicle, as it's entering not from outer space but from low earth orbit an angle of *30º* seemed more reasonable. The resources for the simulations discussed here were provided by the Archer2 supercomputer. For the production runs *1024* nodes were used for *12* hours whereas for the visualization *10* nodes were used to visualize the flow field. In this particular test case chemical reactions were neglected. In total twelve probes were used in order to capture flow characteristics in specific regions of flow field. More specifically, three probes are located along the lower part of the fuselage, another three at the wake, three more along the wing leading edge, one probe is close to the wingtip and two other probes are close to the leading-edge shock.

Table 3.19: *Flow parameters (Hypersonic flow over a complex suborbital vehicle with stability analysis.*

Mach number, Ma_∞	*16*
Reynolds, Re_∞	*66,690*
Freestream velocity, U_∞ (m/s)	*4500*
Knudsen number, (Kn)*	*0.00836*
Angle of attack, α (degrees)	*30*
Freestream density, ρ_∞ (kg/m^3)	*4.97×10^{-7}*
Freestream temperature, T_∞ (K)	*196*
Wall temperature, T_w (K)	*300*
Gas	*Air*

****Based on the vehicle's length***

Table 3.20: *DSMC computational parameters (Hypersonic flow over a complex suborbital vehicle with stability analysis.*

Number density, Nd_∞ (#/m^3)	*1.19×10^{19}*
Timestep (s)	*1.0×10^{-8}*
Transient period	*25,000*
Sample period	*120,000*
Number of particles (#)	*6.6×10^{9}*
Number of cells	*$\approx15\times10^{8}$*
Wall-clock time (CPU hours)	*1,572,864*

In Figure *3.69* we can see the streamwise velocity and in Figure *3.70* the Q-criterion on the symmetry plane can be seen. As seen in Figure *3.70* strong vortexes arise above the nose propagating downstream and then dumped, while under the nose, we can evidence the generation of weaker vortexes interacting with the shock. Due to this interaction inside the shock and at the interaction point, strain disturbances generated and propagated inside the shock downstream. To further enhance this observation a cut was made in the flow-field with a plane at the angle (Plane *1*) and normal (Plane *2*) to the shock as seen in Figure *3.71*. The result of this cut can be seen in Figure *3.72* where the disturbances are propagating downstream within the shock region and then dumped. Moreover, the vorticity magnitude inside the shock region is shown in Figure *3.73*. As shown in Figure *3.74* along Lines *1* and *2* information about the generated vortexes are extracted. Line *1* is right under the fuselage whereas Line *2* is inside

the shock. Figure *3.75* shows the spatial evolution of the vortices. Both vortices and strain disturbances are debilitated. After analyzing the evolution of Q-criterion over time it was found that the vortexes produced above the nose and the vortexes produced under the fuselage have the same frequency of *2.5* kHz.

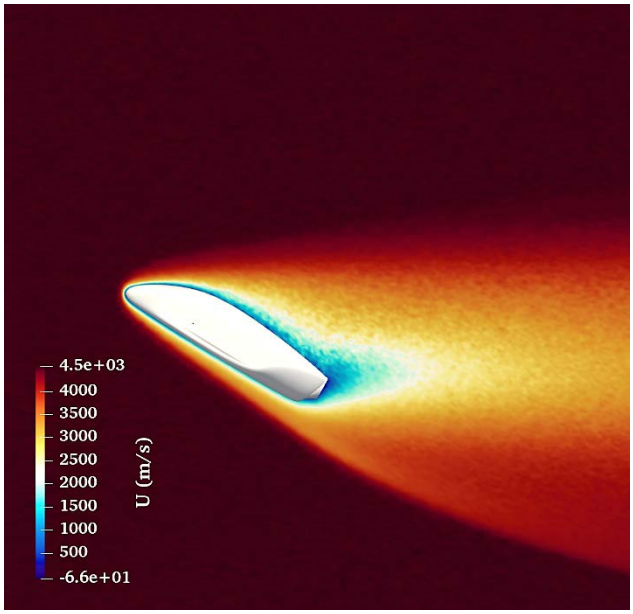

Figure 3.69. *Snapshot of the streamwise velocity.*

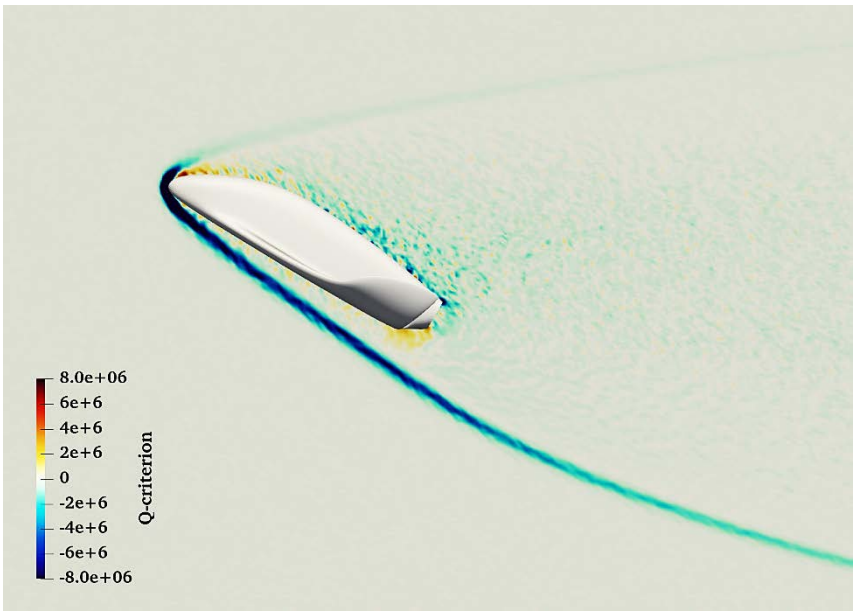

Figure 3.70*. Q-criterion visualized on the symmetry plane.*

In order to further understand the aforementioned oscillations, the Strouhal number inside the shock was calculated with the reference length set equal to the length of the examined vehicle. By using the frequency and as velocity the average velocity magnitude inside the shock

the Strouhal number was calculated as *7.8539*. A Strouhal number above unity means that viscosity dominates the fluid flow, resulting in a collective movement of the fluid. This outcome is backed up by the negative Q-criterion values inside the shock which mean that this area is dominated by viscous stresses.

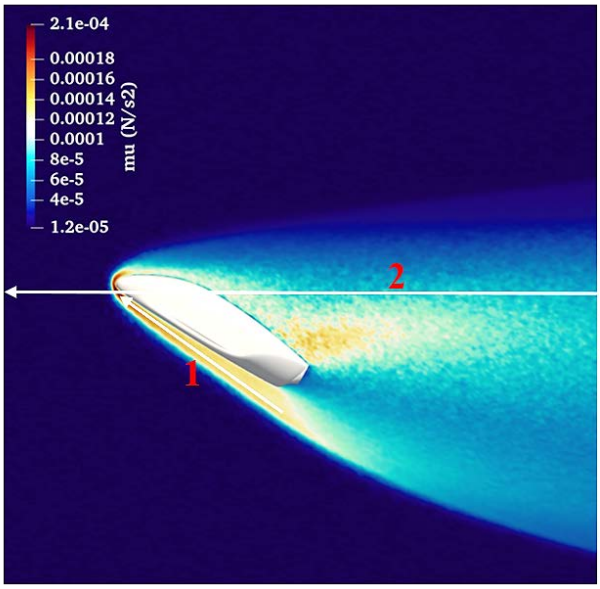

***Figure 3.71**. Viscosity around the vehicle and two plane locations used for data acquisition.*

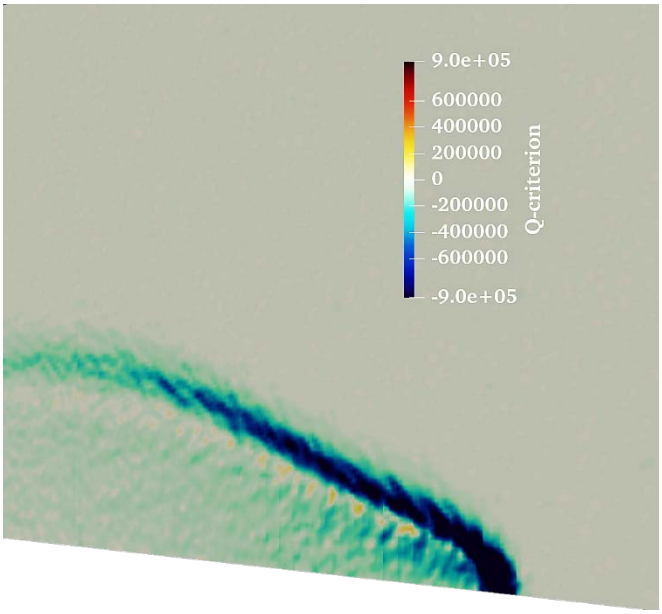

***Figure 3.72**. Q-criterion inside the shock region.*

As discussed earlier and as shown by other researchers [Saw21, Saw22] boundary layers and shock layers can be subjected to coupling. That's the reason for placing probes close to the shock layer as well as in the boundary layer below the vehicle. The last flow feature that is under investigation using probes is the vehicle's wake. From investigations carried out in the

past found in literature [Beh71, Tay64, Mur69] it is known that wakes can exhibit highly unstable behavior and contain reach topological structures of the instabilities.

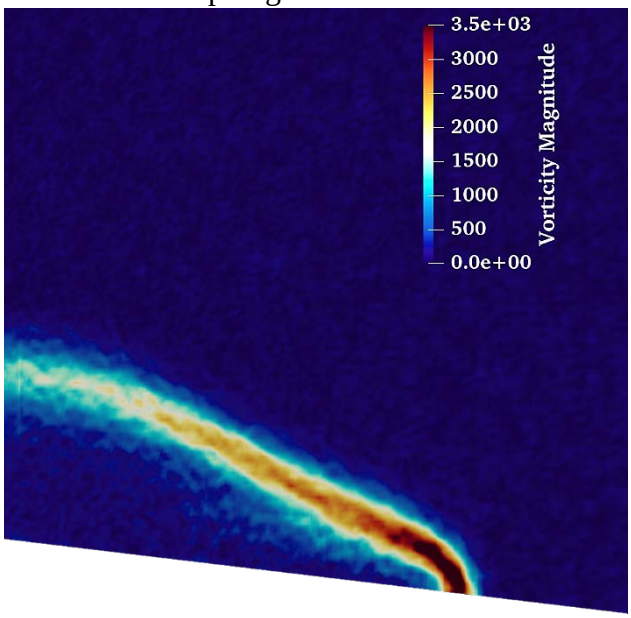

***Figure 3.73**. Vorticity magnitude inside the shock region.*

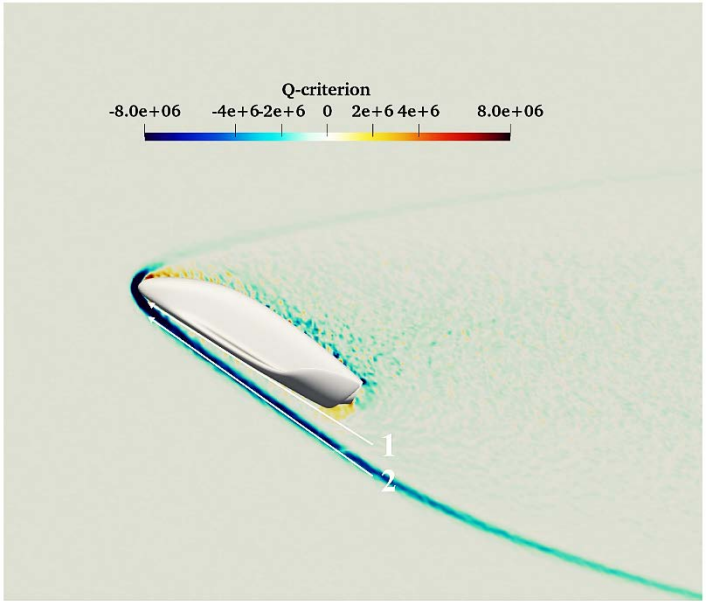

***Figure 3.74**. Lines used to extract vortex data.*

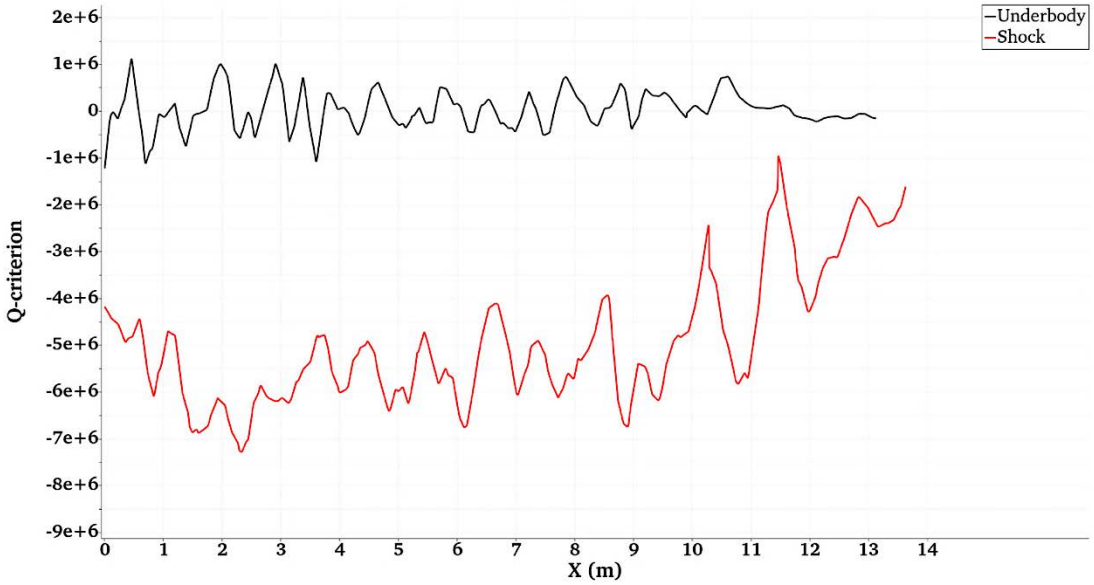

***Figure 3.75**. Q-criterion snapshot at 11.5 ms.*

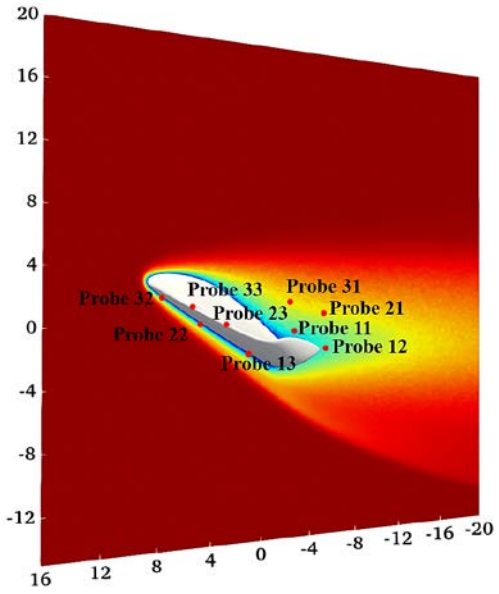

(a)

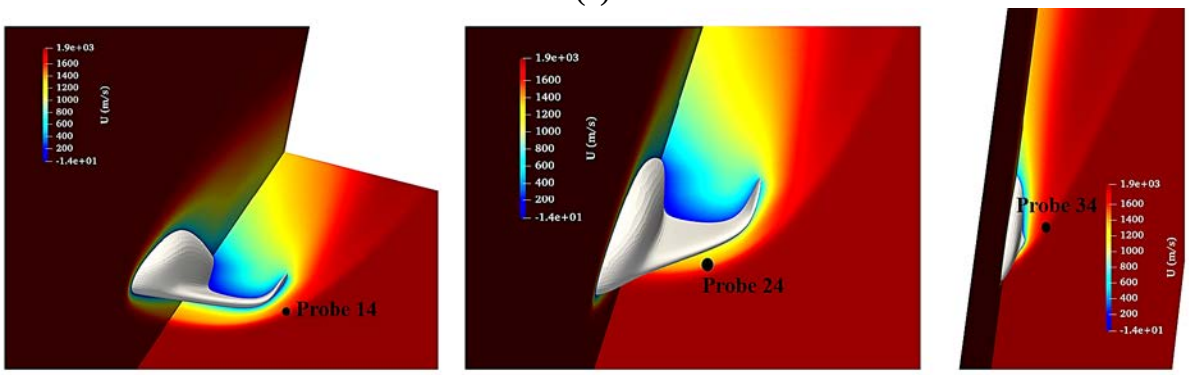

(b)

***Figure 3.76**. (a)Probe locations, (b) probe locations in the shock.*

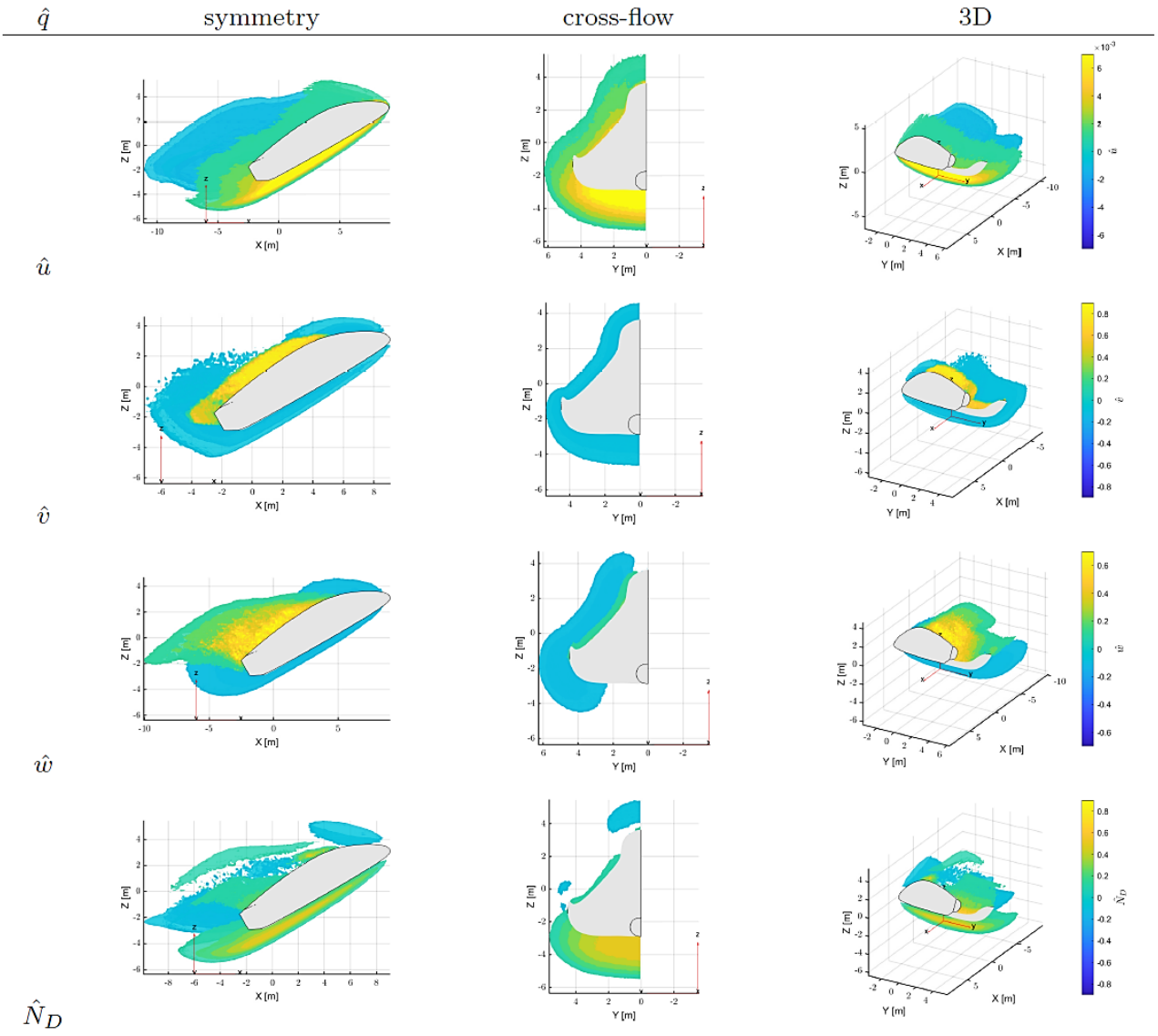

Figure 3.77*. Underwing mode (Mode I).*

In order to monitor flow convergence relative residuals of number density and streamwise velocity have been obtained from the probe data and shown in Figures *3.80* and *3.81* respectively. Each color in these figures represents one of the three probes at each location. Two regions of interest are highlighted in the figures in grey with reference numbers. These have been chosen as mentioned before based on the linear decay of the temporal signal. More specifically, Figures *3.80*a and *3.81*a show consistently that the linear decay in the region of the shock (Probe *14*, Probe *24*, Probe *34*) is strongly dumped in comparison with the other probed locations and it takes approximately *4-5 ms* to reach an established flow. In the area below the fuselage (Probe *13*, Probe *22*, Probe *32*) in Figures *3.80b* and *3.81b* is evidenced more distinct linear decay than the one in the shock layer. This can be associated to disturbances decaying in the boundary and entropy layers formed over the geometry of the vehicle. The decay rates for this region appear to be smaller than the ones in the shock as the flow is established between *7 ms* and *8 ms*. The characteristics of wake's least stable global mode differ significantly from the two previously discussed. In Figures *3.80*c and *81*c is evidenced

that mode 1 does not exist (no linear decay) in the wake. On the other hand, the second mode, is clear and very distinct with small damping as it takes about *11 ms* for the flow to establish.

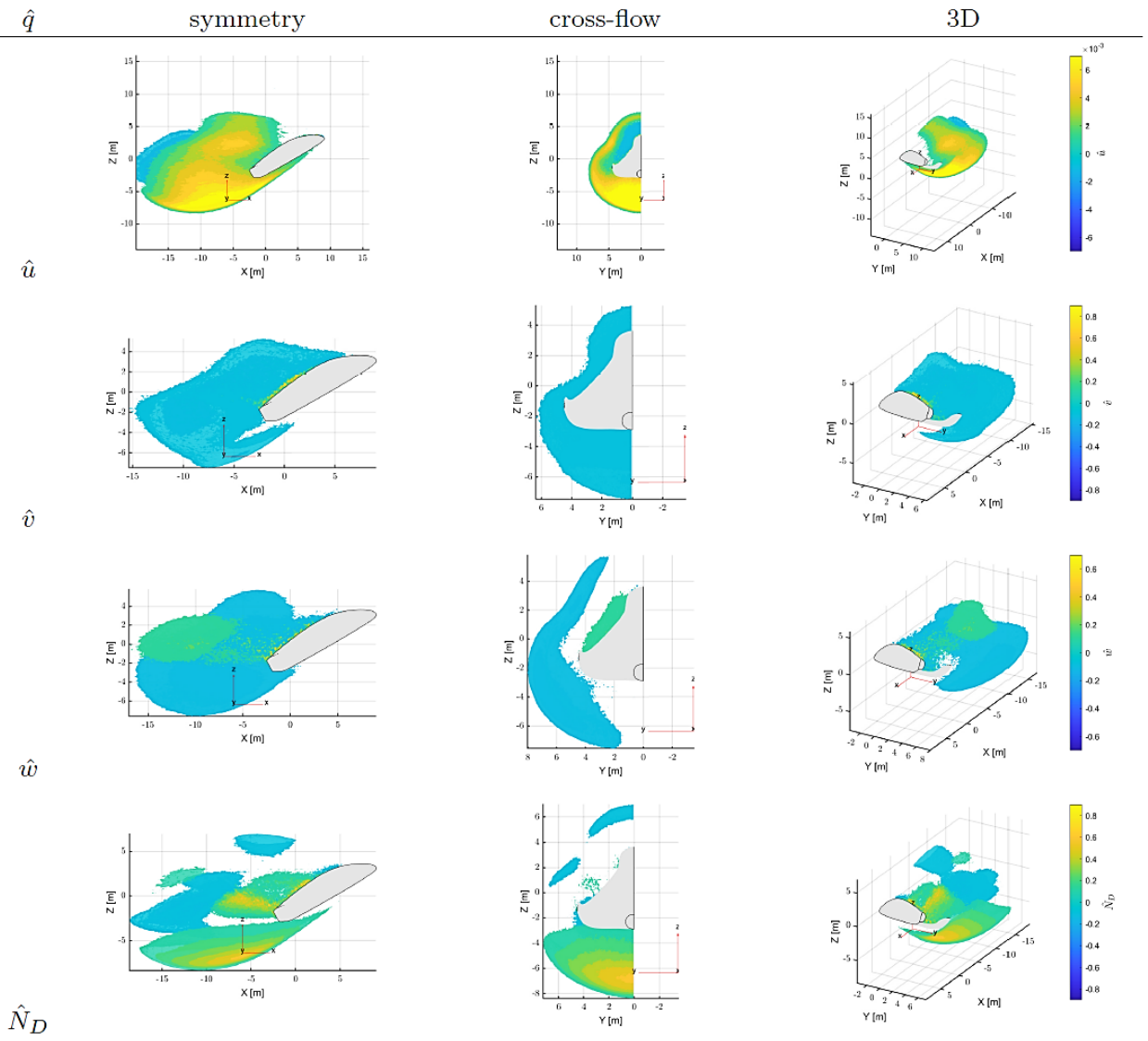

***Figure 3.78**. Wake mode (Mode II).*

For this reason, the first mode is referred to as the underwing mode in order to emphasize its special proximity to the vehicle itself. These localized effects of this relatively short-lived perturbation are confirmed by the eigenmodes shown in Figure *3.77*. The mode is better visible in the three-dimensional perturbation plot of number density ($\widehat{N_d}$) and streamwise velocity ($\hat{u}$). Mode I has a conical like shape and it exists under the fuselage and a part of it as can be seen from the figures in the middle exists above the wing area. It starts at about *2.5* m away from the nose and ends at a distance of about *3* m from the end of the vehicle, slightly extending into the wake. The second mode (Mode II) as seen in Figure *3.78* exists solely in the wake region and is referred to as the wake mode. This mode starts from a location of about *8* m from the nose and protrudes into the wake region of the vehicle. Its shape is more complicated than Mode I as it tries to circle around most of the vehicle's wake region. Figure *3.82* shows a representation of Mode I and Mode II using streamlines to further understand the shape and the location of these modes.

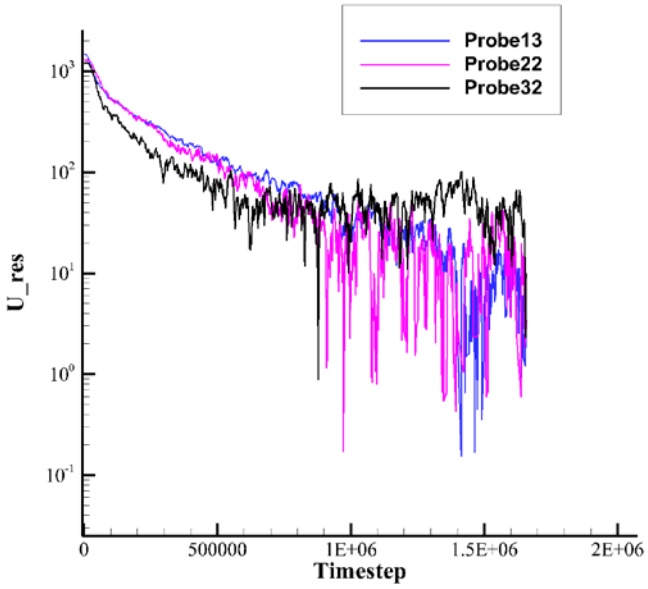

***Figure 3.79**. Residual of the streamwise velocity for three probes at the underside of the vehicle.*

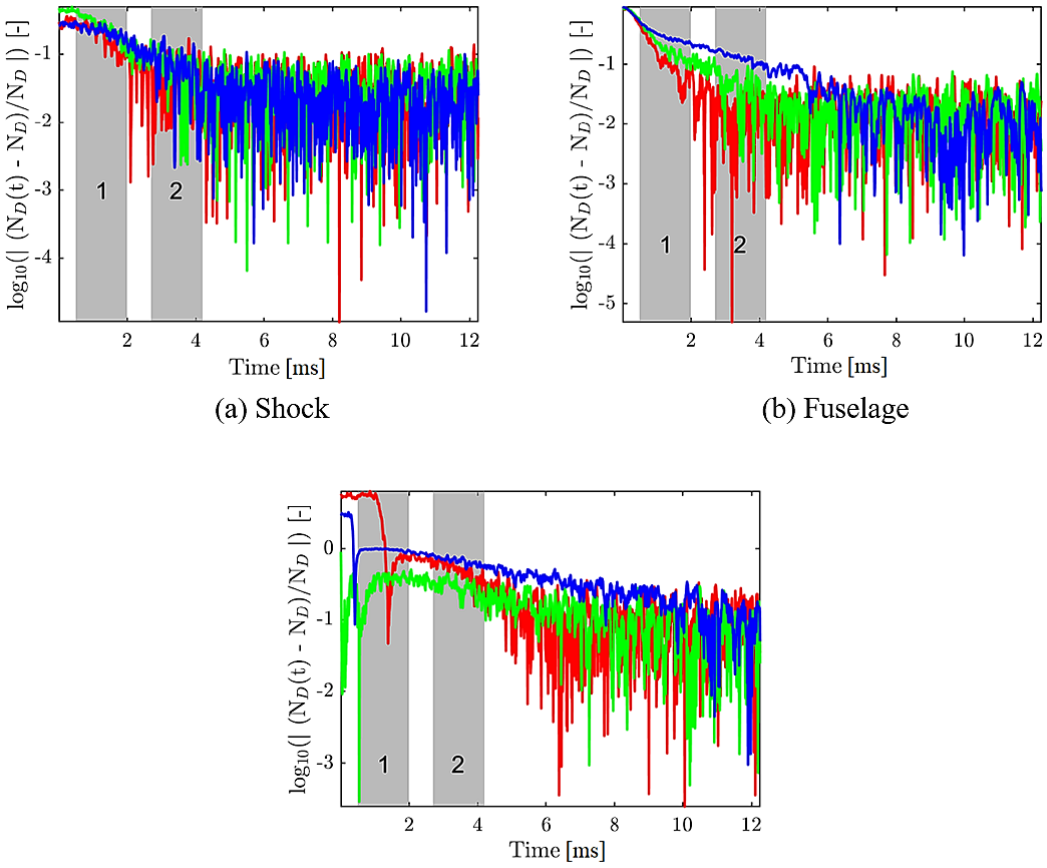

***Figure 3.80**. Number density residuals for three probe groups.*

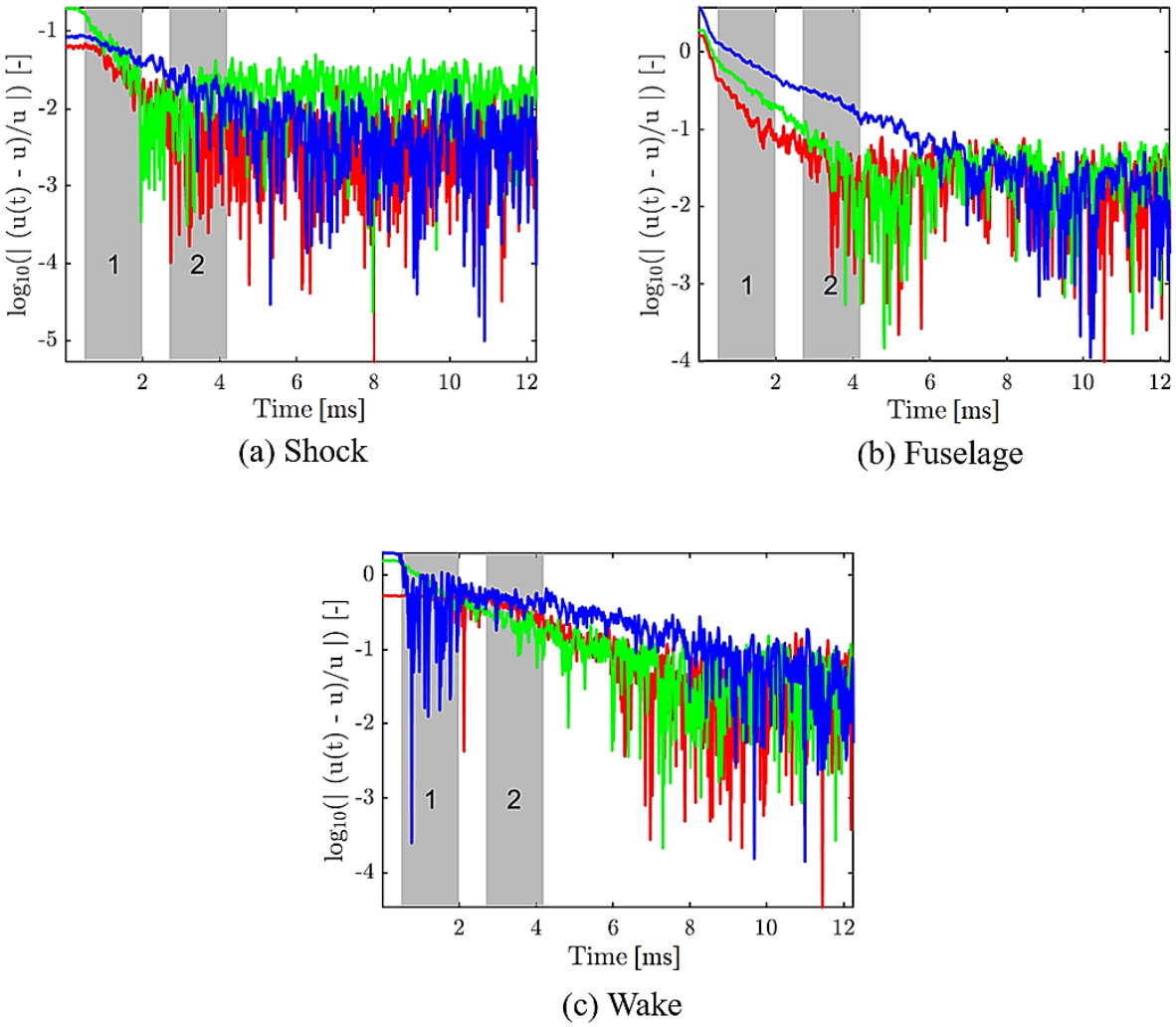

***Figure 3.81**. Streamwise velocity residuals for three probe groups.*

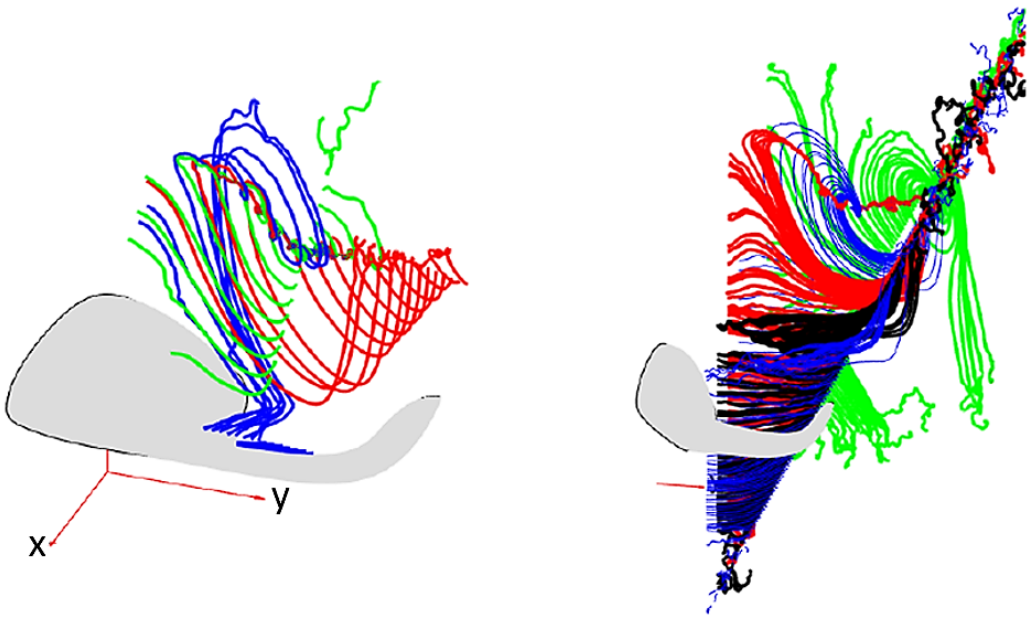

***Figure 3.82**. Streamlines of the disturbances computed using the residuals algorithm Mode I (left) and Mode II (right).*

In Figure *3.82* we can see the streamlines of Mode I (left) and Mode II (right) computed by the residuals algorithm (RA). Both figures are plotted using the streamlines of the streamwise velocity perturbation. Mode I although it mainly exists below the vehicle and only a part of it exists below and above the wing area as shown in Figure *3.77*, in Figure *3.82* (left) we can see that the part that exists above the wing creates a massive stationary vortex above the vehicle, whereas Mode II which exists in the wake creates an interacting complicated vortex system in the wake area of the vehicle and at a distance of about *11* meters from the back of the vehicle. Furthermore, a few small size vortexes are created at a height of *6* meters above the wingtip. These vortexes exist due to the curvature and the presence of the wingtip.

Figure *3.83* shows an overview of the Q-criterion colored by the velocity magnitude below the vehicle. The transparent grey contour is the shock generated by the vehicle. As seen, hairpin vortices start to form right below the nose and the leading edges and propagate downstream. Moving downstream we see that vorticity increases (since the Q-criterion increases) and then they blend into the wake flow at the back of the vehicle. As aforementioned the vortices close to the nose interact with the shock creating strain disturbances inside the shock that stay within the shock limits and decay downstream. A better view of this physical effect can be seen in Figure *3.74* where a cut is made at the symmetry plane and the strain disturbances inside the shock can be seen.

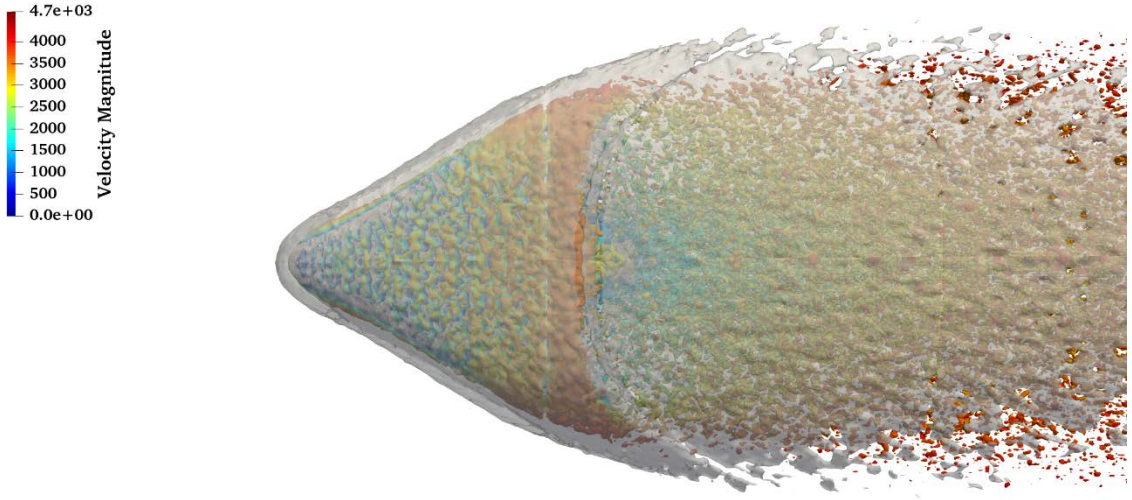

***Figure 3.83**. Q-criterion colored by velocity magnitude.*

3.8 Hypersonic flow over a flat plate with a roughness element

The seventh case is comprised of a two-dimensional and a three-dimensional flow over a roughness element. Before defining the geometry of the roughness element, the two-dimensional flat plate without the roughness element has been solved. After that, the boundary layer thickness and properties are measured at the location of the roughness element and then the roughness element geometrical characteristics can be defined. In this test case the roughness element location was selected based on the critical Reynolds number (Re_{kk}) which according to [Red02] a number of *250* and above gives a good probability for transition to happen.

According to [Red02] Re_{kk} should not be taken into account as a guarantee for transition. Other aspects such as the examined geometry and the flow conditions play also an important role. Sometimes it happens that for a specific Re_{kk} transition happens but when geometry is changed even with the same flow conditions there is no transition [Red02]. Schneider has also studied experimentally transition due to surface roughness and showed that different geometries can cause transition at different locations [Sch08]. In comparison with the earlier studies the Reynolds number in our conditions seems to be low but the Re_{kk} is *249* which gives a good probability for transition to happen. The flow conditions for this case and the simulation parameters can be seen in Table *3.20* and *3.21* respectively.

Table 3.20: *Flow parameters (Hypersonic flow over a flat plate with a roughness element).*

Mach number, Ma_∞	*6*
Reynolds, Re_∞	*18,693.5*
Critical Reynolds, Re_{kk}	*249*
Freestream velocity, U_∞ (m/s)	*1916*
Knudsen number, (Kn)*	*0.01*
Angle of attack, α (degrees)	*0*
Freestream density, ρ_∞ (kg/m^3)	9.95×10^{-4}
Freestream temperature, T_∞ (K)	*245.45*
Wall temperature, T_w (K)	*300*
Gas	*Air*

****Based on the flat plate nose radius***

Table 3.21: *DSMC computational parameters (Hypersonic flow over a flat plate with a roughness element).*

Number density, Nd_∞ (#/m^3)	2.14×10^{22}
Timestep (s)	5.0×10^{-9}
Transient period	*70,000*
Sample period	*40,000*
Number of particles (#)	29.0×10^{9}
Number of cells	$\approx2.25\times10^{8}$
Wall-clock time (CPU hours)	*570,486*

The flat plate geometry and the roughness element geometry as well can be seen in Figure *3.83*. The flat plate used has a length of *0.15* m and a width of *0.09* m with a *2* mm blunt leading edge and a width of *0.09* m. A cylindrical roughness element was selected with a height and diameter of *0.006* m. The roughness element has a distance of *0.1* m from the leading edge. As aforementioned this location was picked due to the boundary layer thickness and the flow properties at that location. The roughness element is fully immersed into the boundary layer. The simulation domain used is *0.16* m in length, *0.09* m wide and has a height of *0.1* m in order to accommodate the leading-edge shock and all flow phenomena. The solution of the two-dimensional flow field is shown in Figure *3.85*.

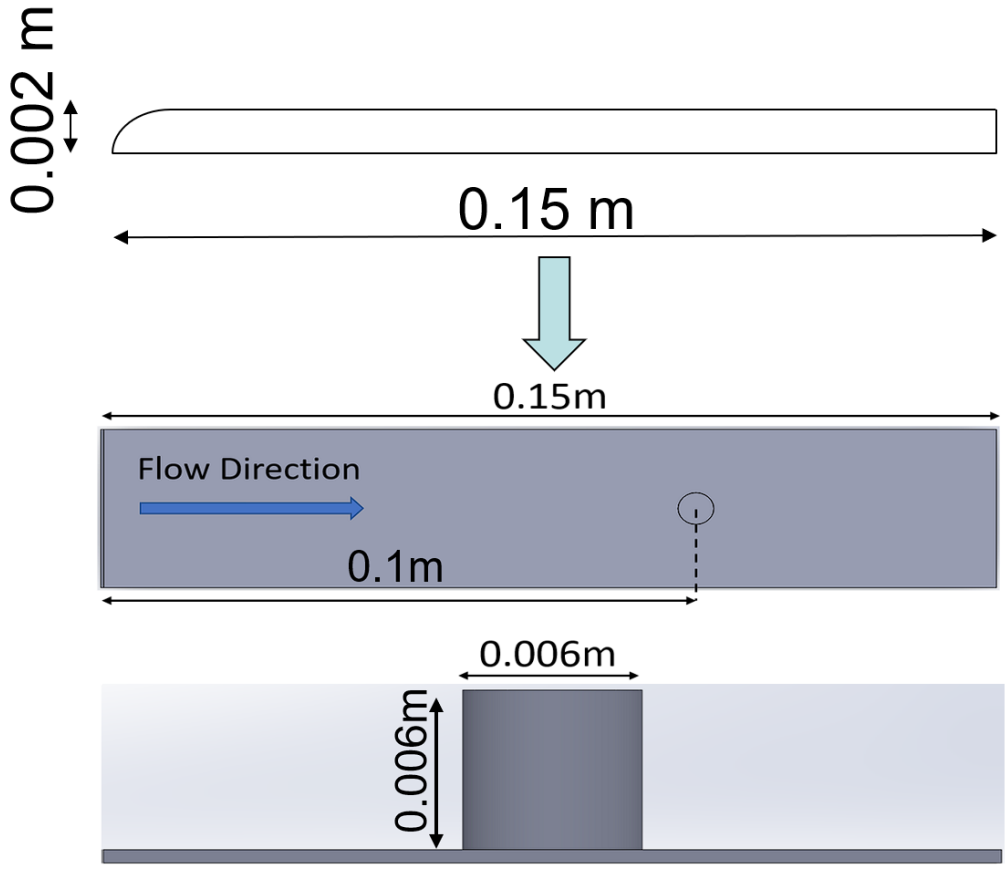

***Figure 3.84**. Flat plate and roughness element geometry.*

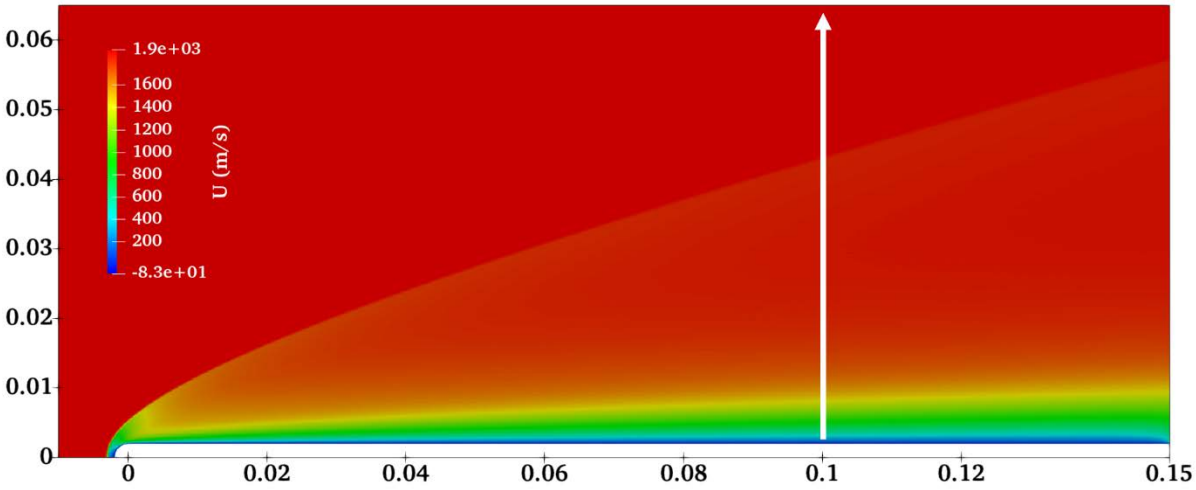

***Figure 3.85**. Streamwise velocity of the two-dimensional flat plate without the roughness element. White line shows the direction along flow properties was measured.*

In Figure *3.86* the flow properties at the roughness element location are shown along the line shown in Figure *3.85*. The boundary layer thickness was calculated based on the δ_{99} assumption and is equal to *0.026* m. Apart from the boundary layer, in Figure *3.86* the shock location can be seen as well on the same plot. After the solution of the two-dimensional flow field was obtained the roughness element geometry was decided. As mentioned earlier in this

case the roughness element is cylindrical and a height and diameter of *6* mm were selected which according to the two-dimensional calculation allow for the roughness element to be fully inside the boundary layer. The three-dimensional geometry of the flat plate and the roughness element were designed in CAD software.

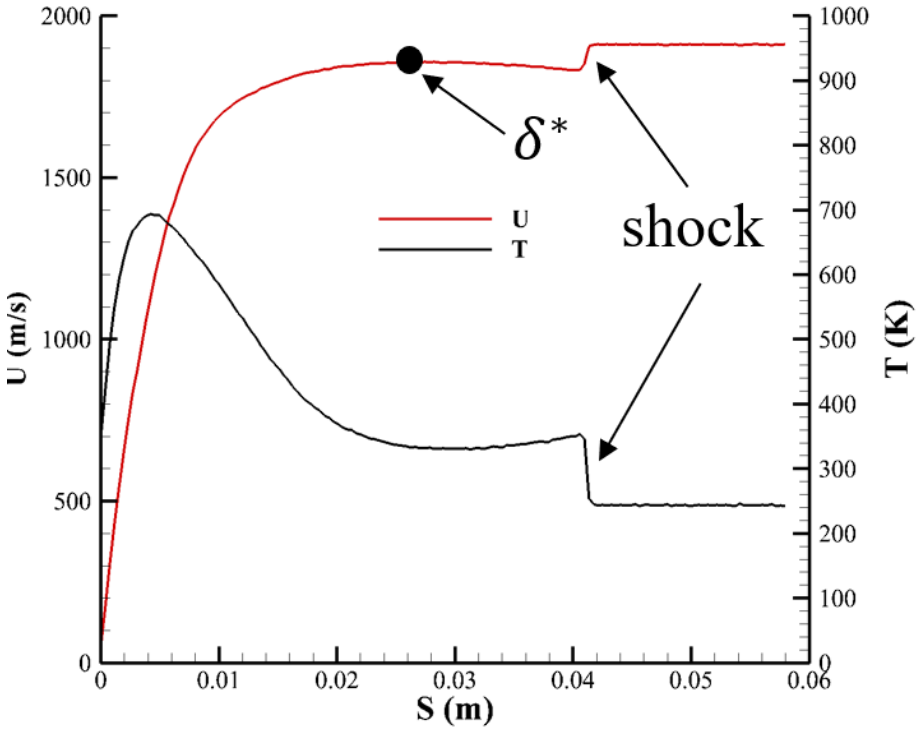

Figure 3.86*. Flow stream-wise velocity and temperature at the location of the roughness element.*

Before running the three-dimensional case a two-dimensional equivalent of the 3d domain was run in order to have an insight of any two-dimensional flow effects before running the three-dimensional case and in order to compare the 2d flow with the 3d flow. In Figure *3.87* the stream-wise velocity for the two-dimensional test case can be seen and Figure *3.88* shows an overview of the velocity magnitude streamlines. As seen in Figure *3.87* although the roughness element is well inside the boundary layer a secondary oblique shock occurs at its location and is parallel to the leading-edge shock. By plotting the velocity magnitude in Figure *3.88* two big vortices are revealed, one in front and one in the back of the roughness. After evidencing the interesting secondary shock structure revealed in the two-dimensional calculation a fully three-dimensional simulation of the flow-field was conducted.

Figure *3.89* shows an overview of the streamwise velocity of the three-dimensional flow field and the shock structures as well. In the *3*d calculation the shape of the second shock was identified. As seen in the parallel and the crossflow plane the second shock is a conical shock emanating from the roughness element. The vortex at the front of the roughness was identified as well but in the 3d calculation the size is very different from the one in the *2*d calculation. In *3*d the vortex is smaller in size and it goes around the roughness element. Figures *3.90, 3.91, 3.92* show a close-up view of the vortex in front of the roughness element. As evidenced the flow recirculates at the base of the roughness element creating a vortex core which goes around

the geometry and extending downstream. As seen in Figure *3.91* the existence of a horseshoe vortex in front of the roughness element is shown and two necklace vortices as well, one left and one right of the examined geometry. The necklace vortices propagate downstream and then decay to the wake flow. After obtaining the solution of the three-dimensional flow field three planes were extracted from the behind the roughness element and more specifically at *0.105* m, *0.11* m and *0.13* m from the leading edge.

These planes revealed a complex flow structure at the back of the roughness element moving downstream. These structures can be seen in detail in Figure *3.92* along with all the physical effects of the flow. As evidenced in Figure *3.93* by plotting the vorticity of the streamwise velocity component, this structure comprises by two pairs of counter-rotating vortices, two at the bottom and two on top. Moving downstream although these vortices grow, they become weaker as shown in Figure *3.94*. The size of the vortices is determined by the angle of the conical shock as they grow up to the conical shock and cannot surpass it. Due to the existence of this complex vortex system a stability analysis was conducted on the plane at a distance of *0.105* m from the leading edge.

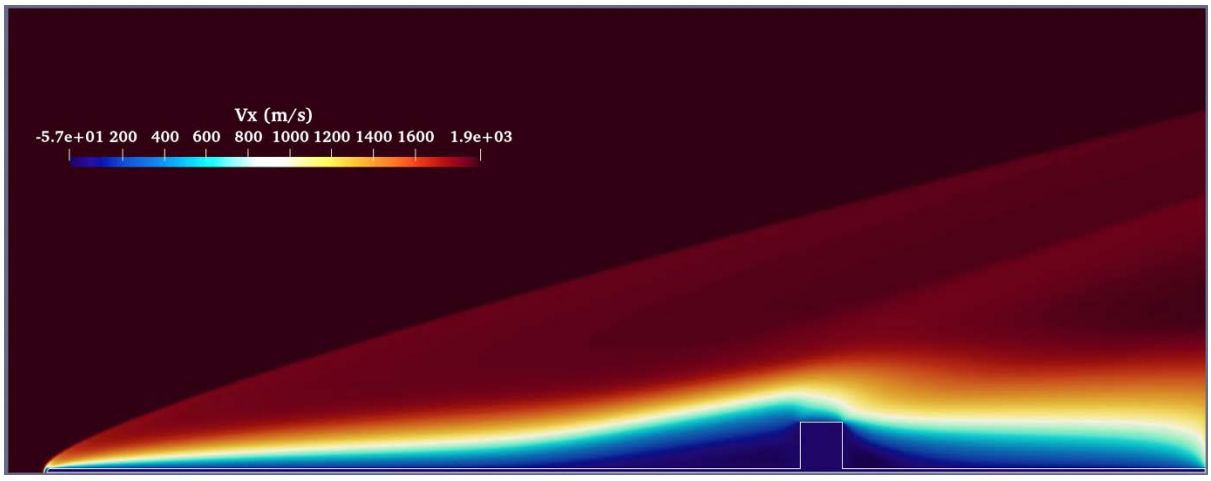

***Figure 87**. Streamwise velocity of the two-dimensional test case.*

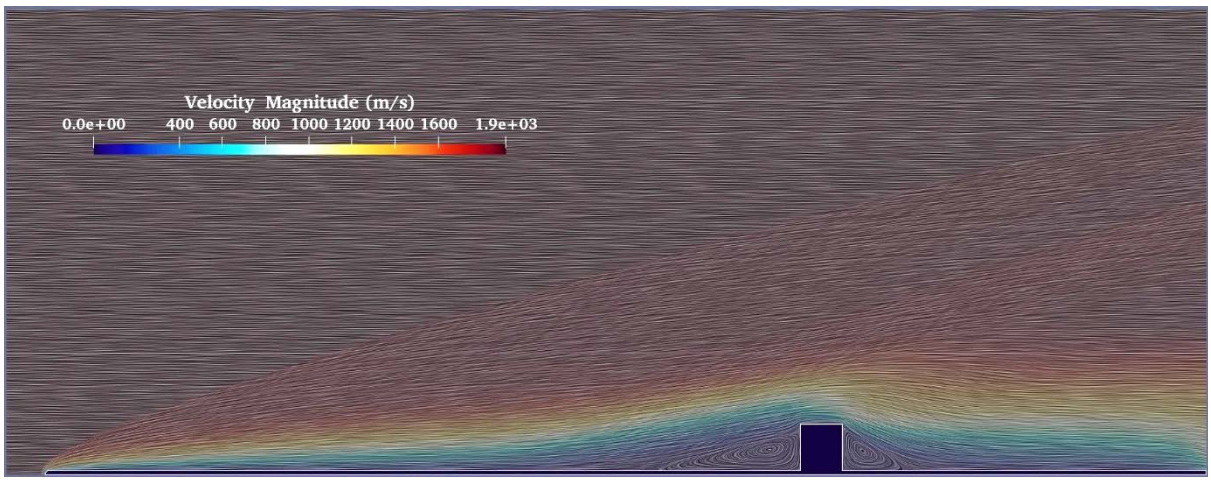

***Figure 3.88**. Velocity magnitude streamlines of the two-dimensional test case.*

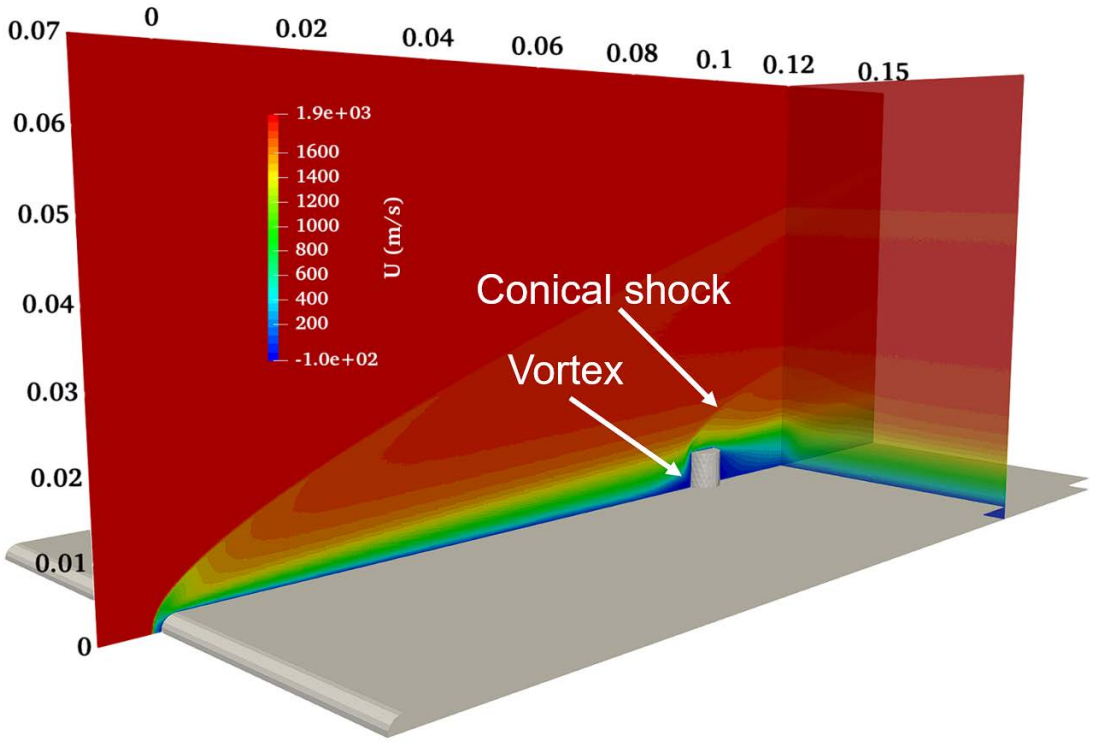

***Figure 3.89**. Streamwise velocity and shock structures of the three-dimensional test case.*

***Figure 3.90**. Vortex core streamlines at the base of the roughness element.*

In order to conduct a stability analysis a high-resolution base flow is needed. In order for this test case to increase the resolution and limit the computational cost a plane at a distance of *0.07* m from the leading edge was used from data obtained from the full three-dimensional field. By using this procedure, the computational domain was limited to half of its length and height. Then, the flow data gathered from the full field were interpolated to the new domain inflow. In order to examine the validity of this implementation the flow properties of the

previous domain at that location were compared with the properties of the new domain. Figure *3.95* shows a comparison of the full three-dimensional domain and the interpolated data of the new domain. An excellent agreement between the two domains can be seen. Furthermore, the shock also has been properly interpolated and represented in the new domain. In order to further enhance the flow resolution about *100* particles per cell were used yielding a total of *30* billion particles.

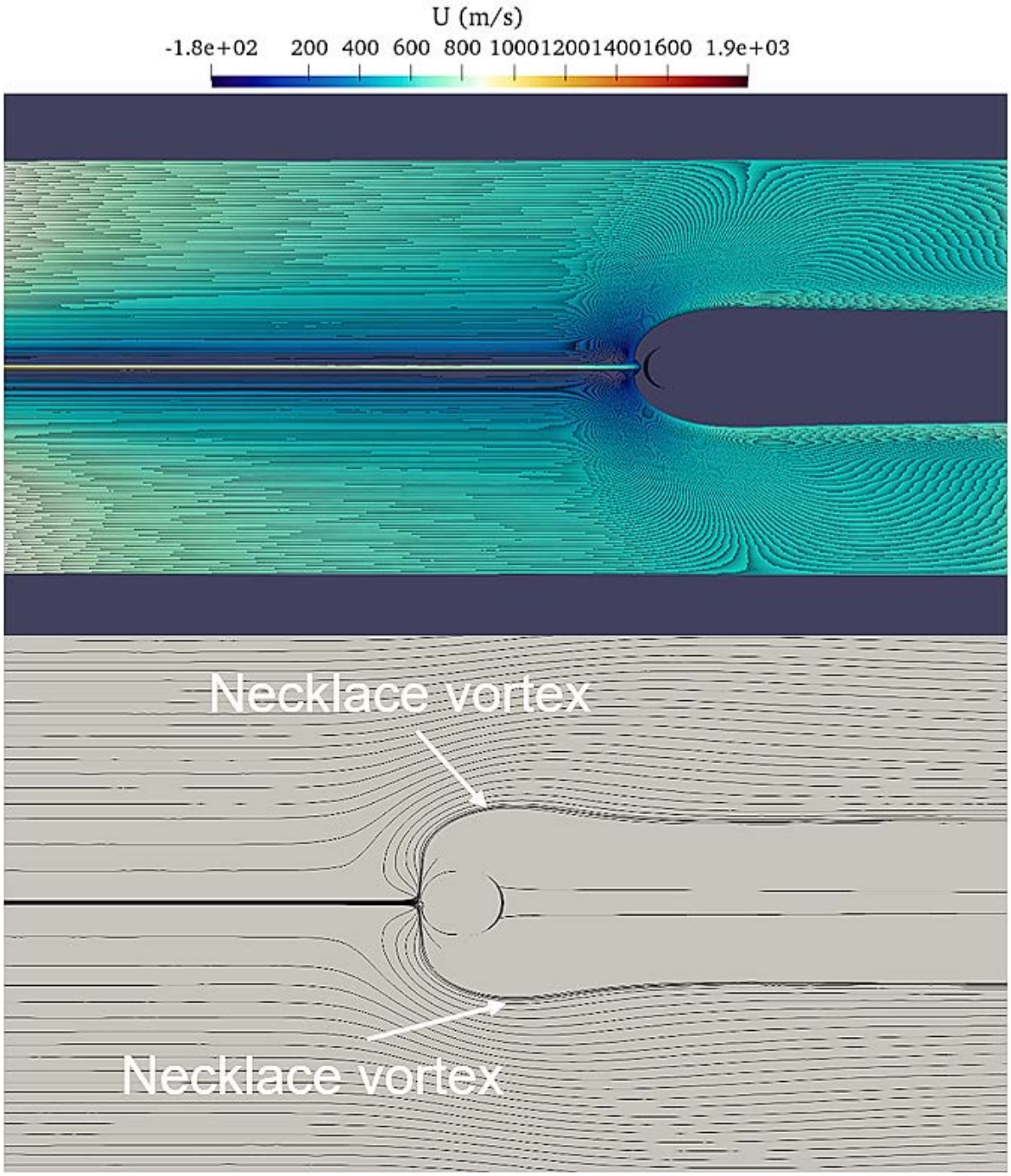

Figure 3.91. *Top view of the necklace vortex around the roughness element. Colored streamlines (top) and black streamlines (bottom).*

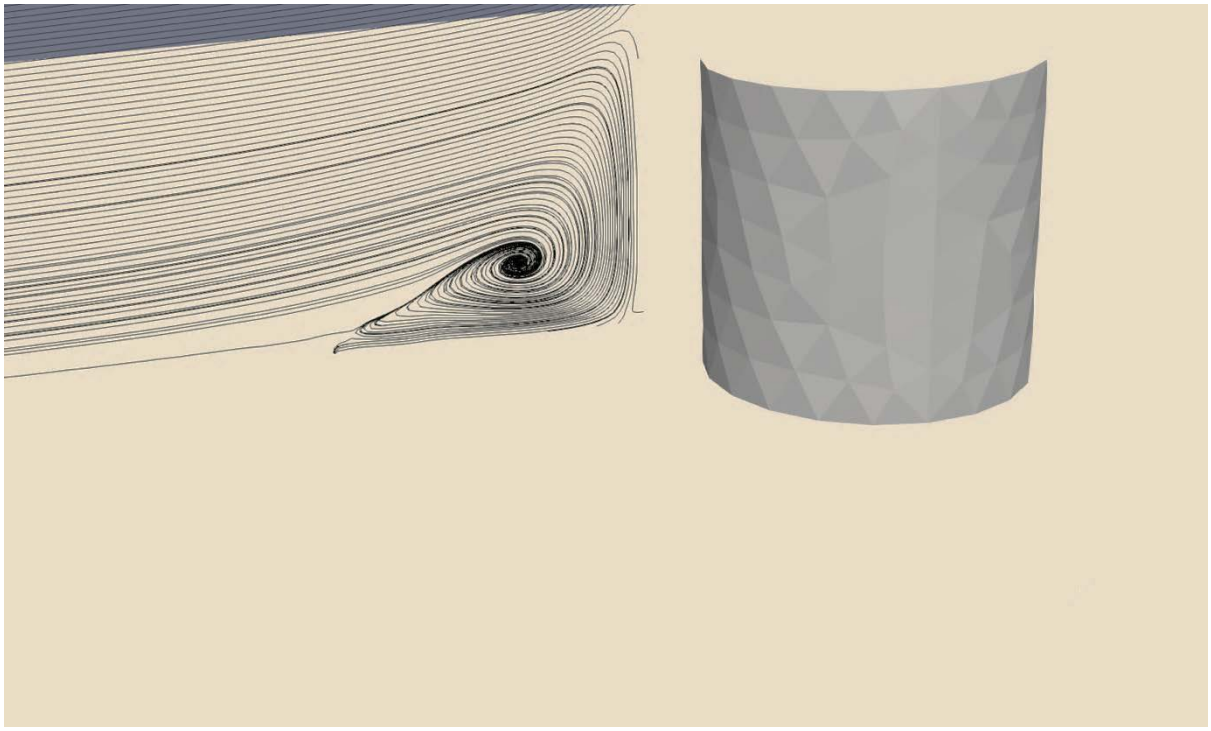

***Figure 3.91**. Streamlines of the vortex core in front of the roughness element.*

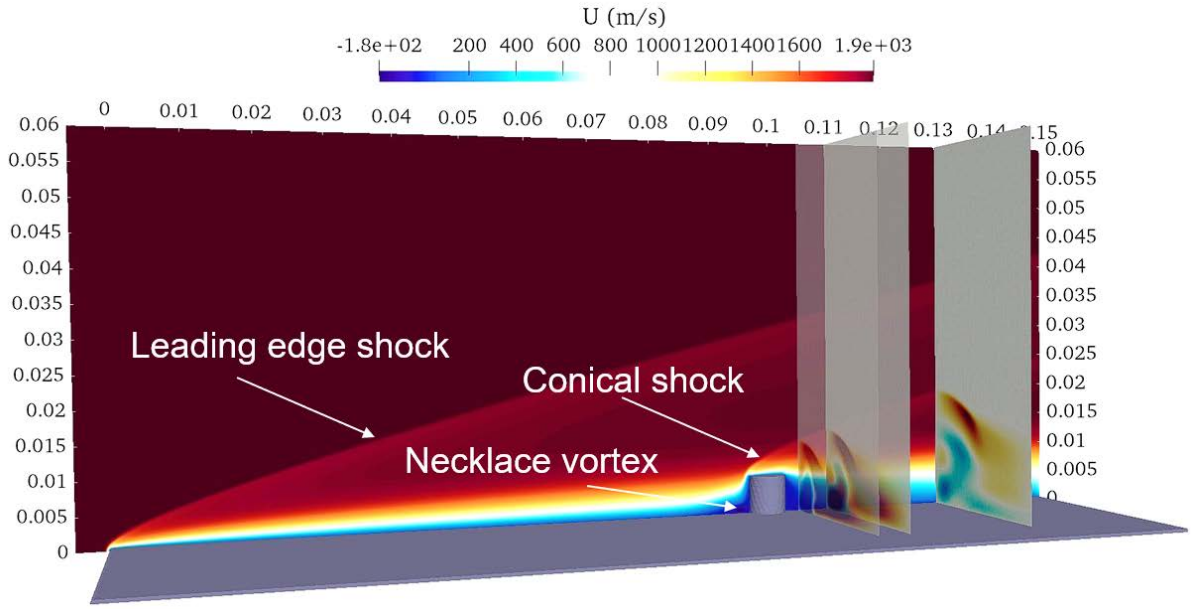

***Figure 3.92**. Planes at x=0.105m, x=0.11m and x=0.13m from the leading edge.*

Before starting the stability analysis, the convergence of the flow was checked by using data gathered from a probe at the back and at the same height of the roughness element. The residuals obtained by analyzing the number density and streamwise velocity time series captured by the probe and shown in Figure *3.96.* As seen in the flow residuals there is a linear decay time window for both velocity and number density between timestep *25000* and *45000* and the number density residual reveals clearly a damped stationary mode. For the stability analysis of this particular case *100* snapshots were used from the linear decay regime.

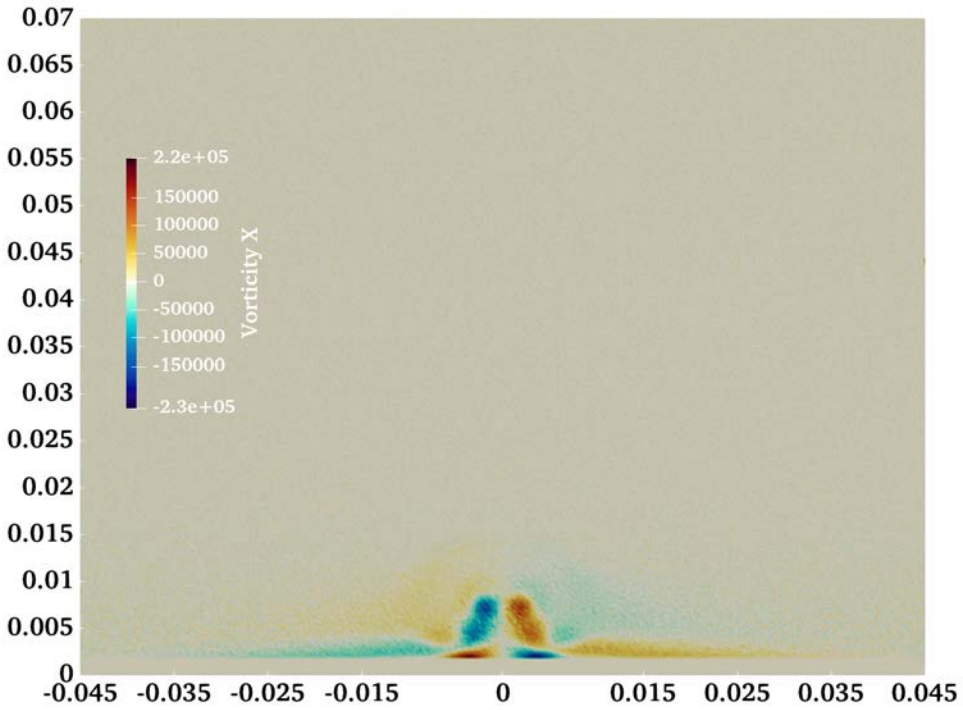

***Figure 3.93**. Vorticity of the streamwise velocity component at x=0.105m from the leading edge.*

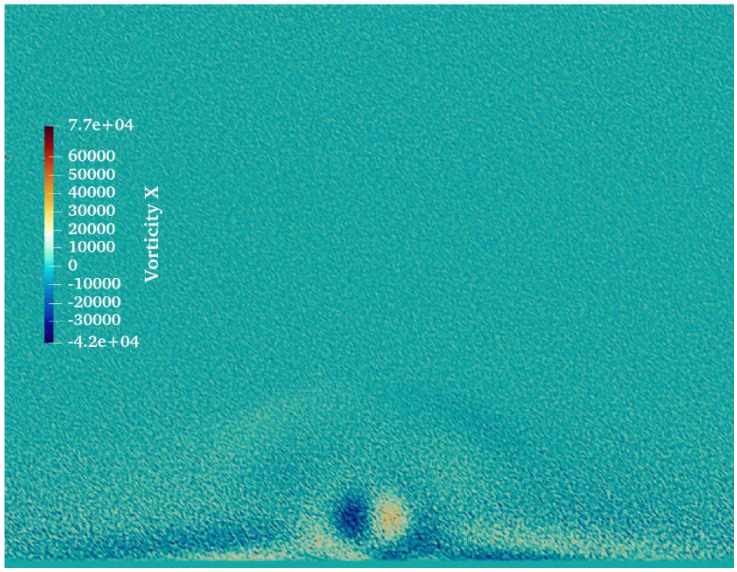

***Figure 3.94**. Vorticity of the streamwise velocity component at x=0.13m from the leading edge.*

In order to perform our stability analysis two different methods were used and compared side by side. The first method is the Residuals Algorithm (RA) as described in [The00] and the second method implemented is the Dynamic Mode Decomposition (DMD) first introduced by Schmidt [Sch10]. More specifically, in this work the term *residuals algorithm* is used to describe the method of recovering an amplification rate and amplitude functions of least-damped global flow eigenmode directly from a numerical simulation. On the other hand, the DMD methodology decomposes temporally resolved data into a set of dynamic modes

associated with a specific frequency and growth or damping rate. DMD can be regarded as a combination of Proper Orthogonal Decomposition (POD) and discrete Fourier transform [Row09, Chen12]. Modal analysis of the flow, including DMD, is thoroughly described by [Tai17]. Good agreement between RA and DMD, that is to be discussed next, indicates that 100 snapshots were sufficient to converge the least-stable global eigenmode with dynamic mode decomposition.

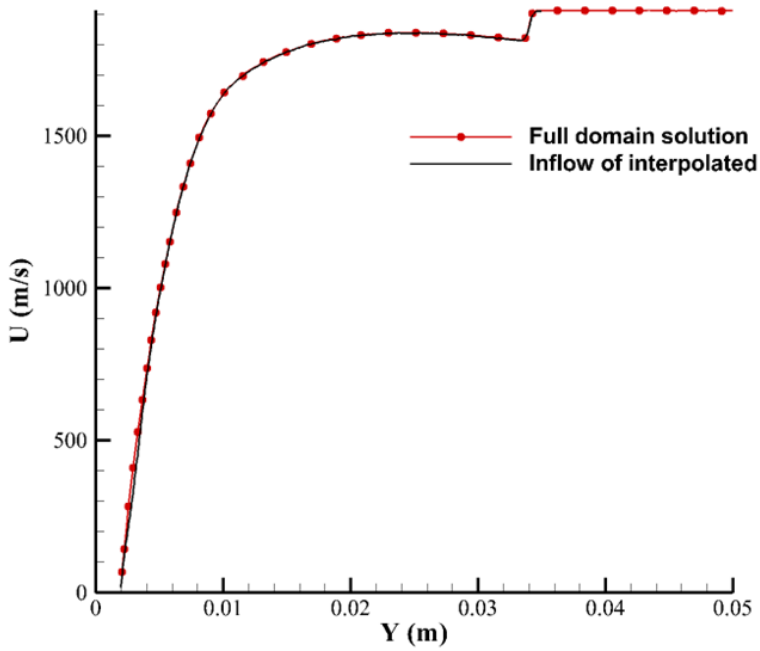

Figure 3.95*. Comparison of data interpolation from the full three-dimensional domain to the reduced domain used for the stability analysis.*

As aforementioned, the three-dimensional nature of the flow is shown in Figure *3.92*, in which three y-z (cross-flow) planes are included, at x = *0.105*, *0.1105* and *0.*13 m from the leading edge of the flat plate. The Residuals Algorithm and dynamic mode decomposition have been applied to the most downstream plane. For easier manipulation of the CAD geometry, it was necessary to use non-dimensional units to describe the geometry. Thus, the roughness element diameter (D) was used to un-dimensionalize the geometry (Figure *3.97*). As evidenced in Figure *3.98*, a mushroom-like structure arises at the back of the roughness element. This structure is bounded by the curved shock created due to the roughness element geometry. Based on our non-dimensional geometry a crossflow plane was extracted from DSMC base flow at *5*D behind the center of the roughness element.

The boundary layer parameters for that location can be seen in Table *3.22*. In order to further reduce the computational cost of the analysis, stability calculations were performed only on velocity components and number density. Dynamic mode decomposition and residuals algorithm are both data-driven techniques meaning that the stability properties of the flow can be inferred directly from the non-linear simulation (DSMC) without explicitly relying on any governing equations (e.g., Linearized Navier-Stokes equations).

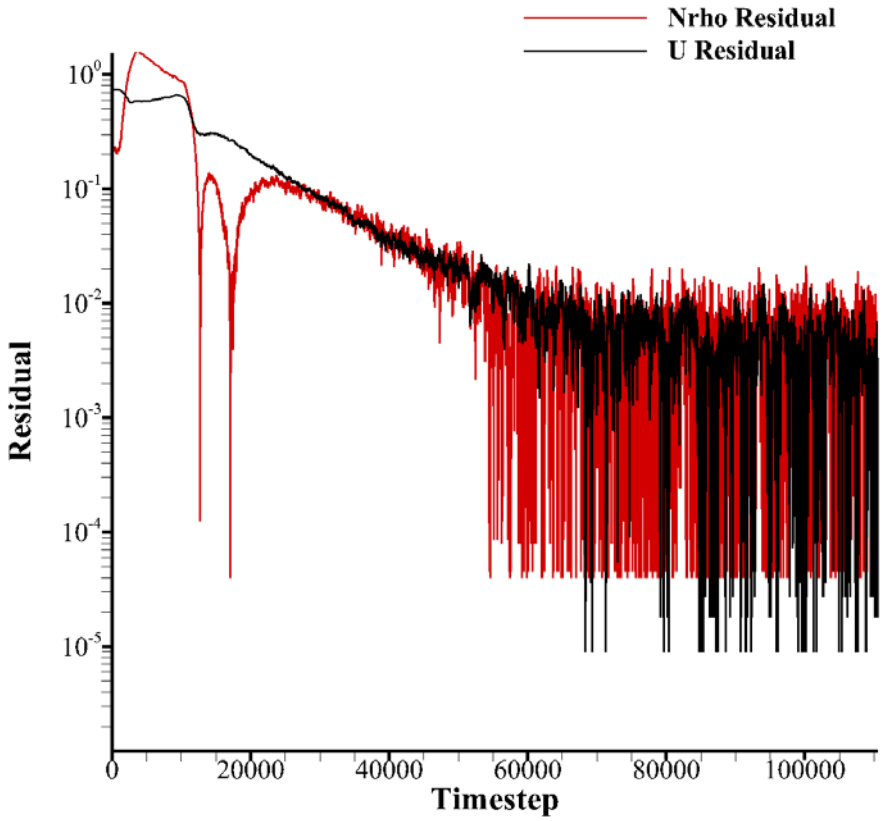

***Figure 3.96**. Number density, streamwise velocity and temperature residuals obtained from two probes.*

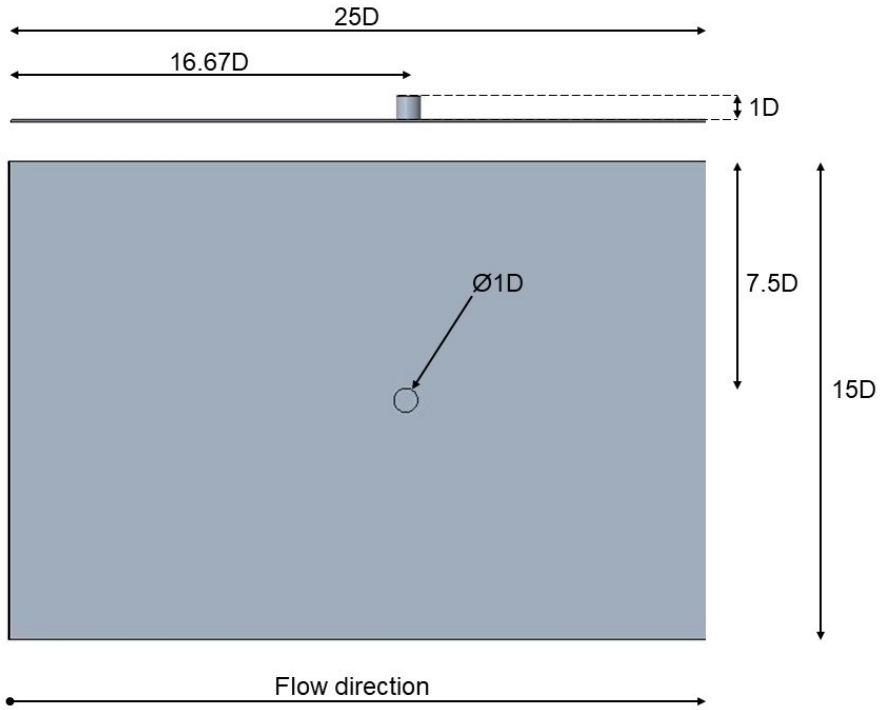

***Figure 3.97**. Non-dimensional CAD geometry used in stability analysis.*

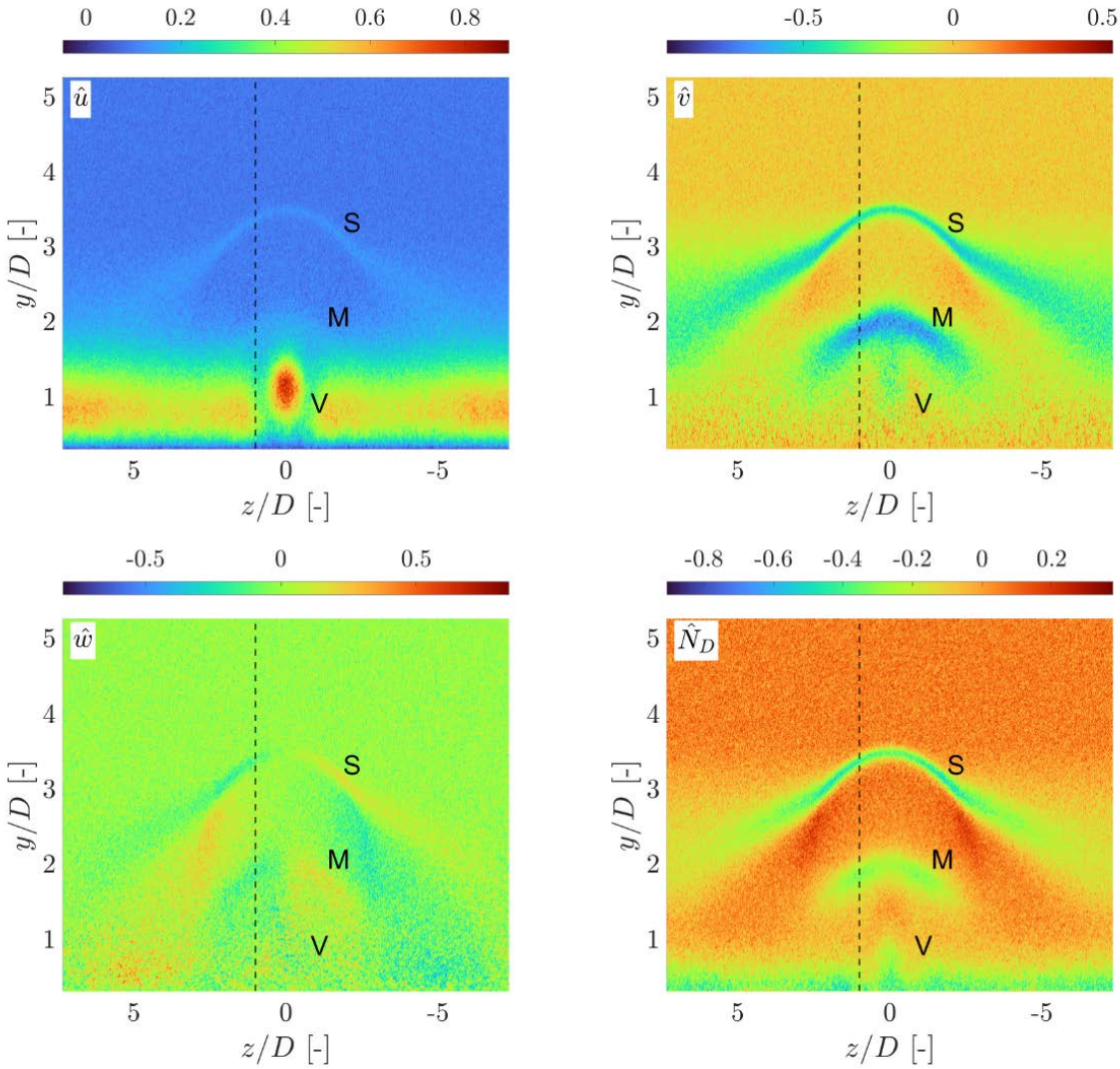

***Figure 3.98**. Least-stable global flow eigenmode, $\hat{q}$, obtained from dynamic mode decomposition at x = 0.13m from the leading edge, with figures representing stream-wise velocity component perturbation (top left), wall-normal velocity component perturbation (top right), cross-flow velocity component perturbation (bottom-left) and number density perturbation (bottom right). Black dotted lines represent locations of the cuts in Figure 3.99 and letters refer to structures of interest; shock layer (S), mushroom-like structure (M) and vortex (V). All modes are self-normalized.*

Figure *3.98* shows the least-stable global flow eigenmode computed using dynamic mode decomposition. The velocity components are normalized by $\widehat{u_{max}}$ while number density is self-normalized. In the figure, three main structures can be identified contributing to mode's shape; a shock layer (S), a separated shear layer with a mushroom-like structure (M) and a vortex (V). Contribution of the shock layer to the least stable global flow eigenmode can be seen in all eigenfunctions presented with the structure peaking near $z/D \pm 2$. Similarly, the vortex contribution to the mode is present in all eigenflowfields but clearly peaks in $\hat{u}$ velocity component while number density shows the lift-up of the boundary layer due to the horseshoe vortex at $z/D \pm 1$. The mushroom-like structure is very faint in $\hat{u}$ and $\hat{w}$ velocity components while being prominent in $\hat{v}$ which can be attributed to the vertical displacement of the flow.

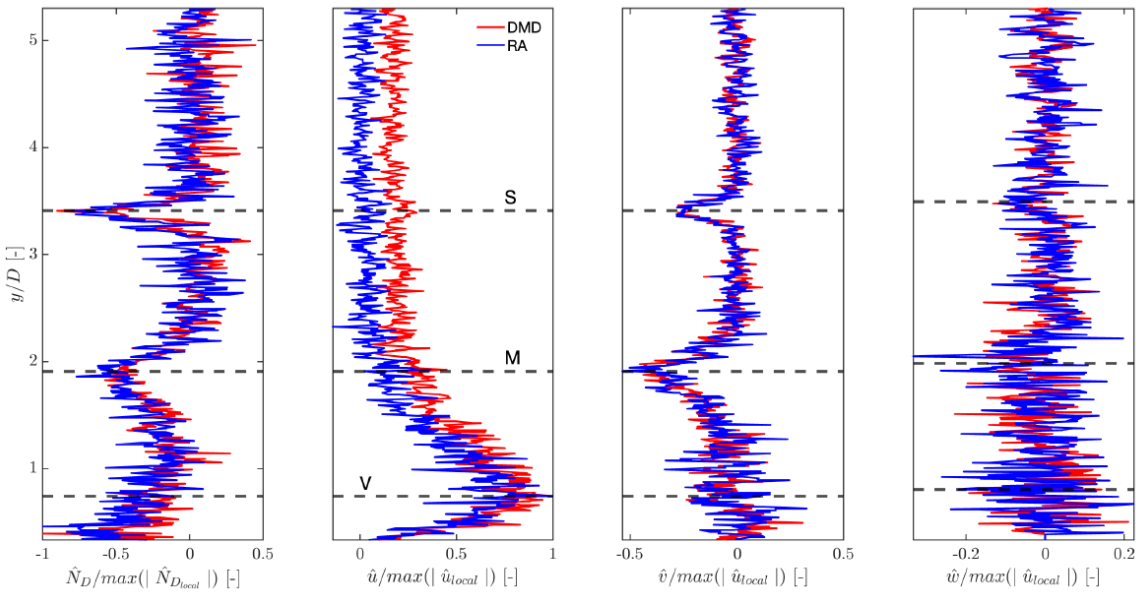

***Figure 3.99**. Number density, streamwise velocity and temperature residuals obtained from two probes.*

***Table 3.22:** Boundary layer parameters at 5D behind the center of roughness element*

Specific gas constant, R, $(Jkg^{-1}K^{-1})$	*296.8*
Ratio of specific gas heats, γ (-)	*7/5*
Reference viscosity, μ_{ref}, (Nsm^{-2})	*1.656×10^{-5}*
Reference temperature, T_{ref}, (K)	*273*
Power law exponent, $\bar{\omega}$, (-)	*0.74*
Mach number, M_e, (-)	*5.14*
Re= $\sqrt{Re_x}$, [-]	*101.52*
Streamwise location, x, (m)	*0.13*
Slip velocity, u_{slip}, (m/s)	*51.98*
Edge velocity, u_e, (m/s)	*1847.7*
Edge temperature, T_e, (K)	*310.10*
Edge density, ρ_e, (kg/m^3)	*1.49×10^{-3}*
Edge pressure, P_e, (Pa)	*144.96*
Edge viscosity, μ_{ref}, (Nsm^{-2})	*1.819×10^{-5}*
Wall temperature, T_w, (K)	*300*

To get a better understanding of the relative contributions of different structures to the global mode, a cut through the 2D plot is taken at $\approx 1D$ off the roughness element center shown with black dotted line in Figure *3.98* and the results are plotted in Figure *3.99* where cuts obtained with dynamic mode decomposition and residuals algorithm are overlapped for validation purposes. Both methods produce the same results (within inherent DSMC fluctuations) and

have a good agreement for all compared properties apart from the stream-wise velocity perturbation $\hat{u}$. DMD is sensitive to the number of snapshots acquired in order to converge. Although *100* time-accurate snapshots of the flow field were used seems that were not enough for DMD in order to capture accurately the dynamics of the stream-wise velocity in comparison with RA. Horizontal color lines refer to locations of previously identified two-dimensional structures (as per Figure *3.98*). Number density is self-normalized by the maximum value at that location, while velocity components are normalized by local maximum value of $\hat{u}$.

Figure *3.99* shows that the vortical structure (V) behind the roughness elements significantly contributes to linear perturbation of stream-wise velocity component, $\hat{u}$ and has small relative influence on the eigenfunctions of remaining velocity components and number density. On the other hand, the amplitude function of $\hat{u}$ does not display significant traces of shock layer (S) nor the mushroom structure (M). Linear perturbation of the wall-normal velocity component, $\hat{v}$, is dominated by the M-structure and followed in significance by contributions of shock layer with contribution of $\hat{v}/\hat{u}_{\text{max, local}} \approx 50\%$ at that location. Interestingly, eigenfunction of $\hat{w}$ does not display any significant effects from V, S nor M structures. Finally, for the number density, the shock layer has the highest magnitude with the mushroom-like structure still being significant but of secondary importance with the contribution of only $\approx 80\%$ with respect to the shock layer. Even though the vortex has a moderate contribution to this eigenfunction, the lift-up of the boundary layer seems to play an important role near the wall with O^1 effect.

Sawant *et al.* [Saw21] have shown, also using kinetic methods, that shock waves exhibit low-frequency fluctuations that may contribute to laminar-turbulent transition. Furthermore, in our previous work [Klo21, Klo22] we have used DSMC and linear stability analysis of the compressible boundary layer on a semi-infinite two-dimensional flat plate at supersonic and hypersonic conditions and demonstrated the synchronization of instabilities of the shock layer with linear perturbations that decay inside the boundary layer. Very recently, Sawant *et al.* [Saw22] demonstrated, on a fully three-dimensional configuration, synchronization of shock layer with laminar separation bubble instabilities in hypersonic flow. Therefore, these findings about shock layer significant contribution to the least-stable global flow eigenmode may be consistent with existing literature. Moreover, present findings suggest that transition on this geometry, and chosen conditions, may occur on account of a complex mechanism that couples shock layer, detached shear layer (mushroom-like structure), horseshoe vortex and macroscopic fluctuations.

Since the solution of the three-dimensional solution has been obtained with adequate resolution by using the DSMC it was deemed appropriate to examine the velocities distribution functions inside the shocks. DSMC is not bounded by the solution of PDEs so with an appropriate grid the internal structures of shocks can be resolved. In our case the leading-edge shock and the curved shock emanating from the roughness element have been examined by placing probes inside these shocks. Figures *3.100* and *3.101* show the location of the probes inside the leading-edge shock and inside the curved shock created by the roughness element respectively. In addition, in the same Figures the velocity magnitude distribution functions for each probe are presented, along with the corresponding Maxwellian velocity distribution at each location. The Maxwellian velocity distribution is computed using the average translational temperature obtained by each probe. For probes P7, P6, P1 and P5 located in the roughness element shock, the respective temperatures are *621.86 K*, *913.16 K*, *1256.62 K* and 957.92 K. For the probes LE1, LE2 and LE3 situated inside the leading-edge shock the temperatures are *537.15 K*, *1248.82 K* and *1861.29 K* respectively. All distribution functions

are normalized to unity. We can clearly see in Figure *3.100* that for all three probes in the leading-edge shock the velocity magnitude distribution function clearly shifts away from the corresponding Maxwellian. As moving further downstream inside the shock (probes LE2 and LE3) the velocity distribution function approaches the bimodal distribution.

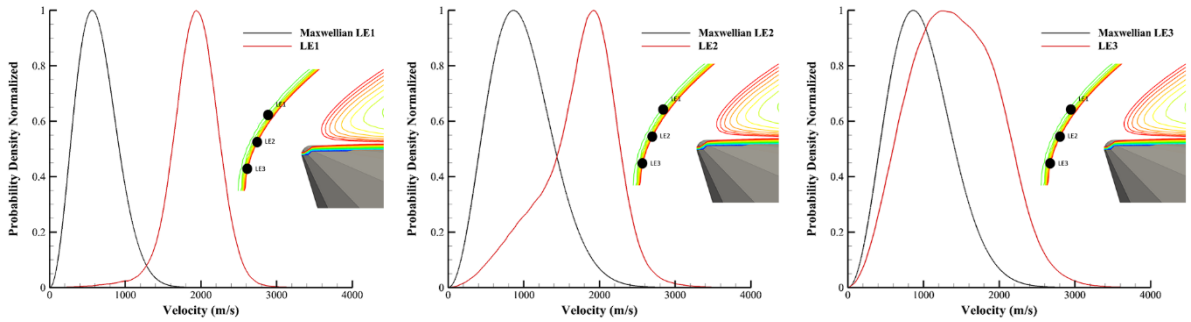

***Figure 3.100**. Velocity magnitude distribution function along with probe locations inside the leading-edge shock.*

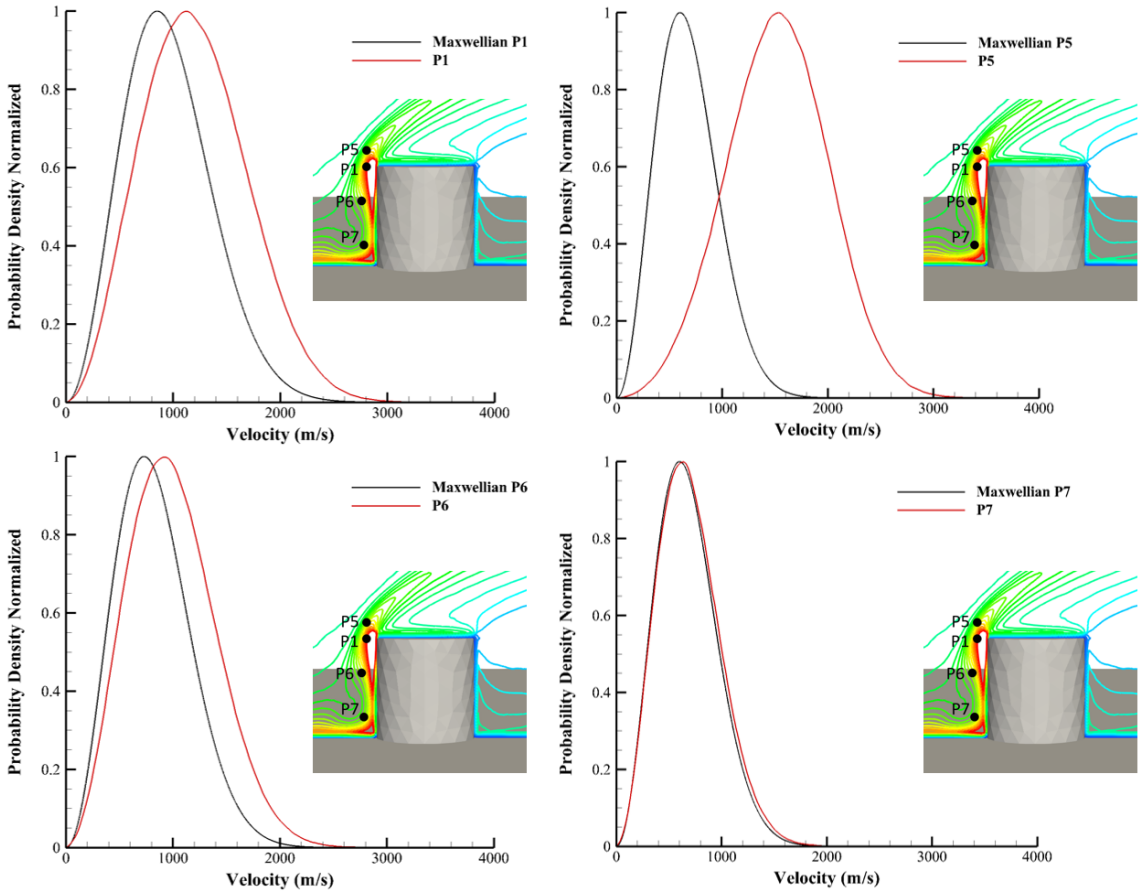

***Figure 3.101**. Velocity magnitude distribution function along with probe locations inside and outside the curved shock emanating from the roughness element.*

An analogous behavior is not evidenced in Figure *3.101* for the probes around the shock in the roughness element location. It can be noted that as the distance from the curved shock increases the velocity distribution has very good agreement with the Maxwellian distribution (P7), however in close proximity to the shock (P5) the velocity probability density appears to

differ from the Maxwellian distribution. This shift of the velocity magnitude from the Maxwellian distribution leads to the conclusion that the flow in the shock and in the area close to the shock is not in equilibrium. Furthermore, as seen in [Tum18] close to the shock there's bi-modality in the velocity distribution. For the area around the roughness element, we don't evidence that. In an attempt to explain this behavior, the velocity in the shock location was measured and was found to be equal to Mach *1*. This fact leads to the conclusion that the shock is not strong enough at the location of the probes in order to see any bimodal distribution of the velocities.

Since in this group of roughness element test cases the curved shock is parallel to the leading-edge shock there is no shock-shock interaction. In order to generate a shock-shock interaction a new geometry has been generated and the same roughness element has moved closer to the leading edge. More specifically the distance between the leading edge of the plate and the roughness element center has now become *1* cm. This geometry will cause the shock generated from the roughness element, now protruding well outside the boundary layer, to interact with the leading-edge shock. This configuration has been run with chemical and without chemical reactions and in *2D* mode. Figure *3.101* shows an overview of the new geometry configuration with the probe locations and Figure *3.102* shows the steady state of the streamwise velocity flow with chemical reactions. To capture physical flow effects or fluctuations within the flow a configuration of seven probes were places in the simulation domain in the locations shown in Figure *3.101*. To amplify the chemical reactions in the flow and close to the surface, flow velocity was increased to Mach *10* and surface temperature was increased from *300* K to *1500* K. The DSMC parameters remained the same as in Table *3.21*. The new flow field properties can be seen in Table *3.23* and the chemical reactions used and along with their respective parameters can be seen in Table *3.24.* The model for implementing the chemical reactions in this case is the Total Collision Energy (TCE) as implemented by [Bir94] and the reactions rates are the ones used in [Gim19, Kar23]. As seen in Figure *3.102* in this configuration, in steady state the shock has a very different shape than in the previous configuration (Figure *3.92*).

Table 3.23: *Flow parameters (Hypersonic flow over a flat plate with a roughness element 1cm from the leading edge).*

Mach number, Ma_∞	*10*
Reynolds, Re_∞	*31,031.21*
Freestream velocity, U_∞ (m/s)	*1916*
Knudsen number, (Kn)*	*0.01*
Angle of attack, α (degrees)	*0*
Freestream density, ρ_∞ (kg/m^3)	9.95×10^{-4}
Freestream temperature, T_∞ (K)	*244.12*
Wall temperature, T_w (K)	*1500*
Gas	*Air*

****Based on the flat plate nose radius***

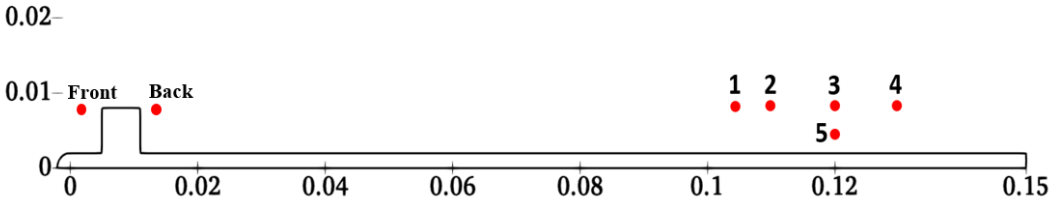

***Figure 3.101**. New geometry with the center of the roughness move to 1cm from the leading-edge. Probe locations are also shown.*

The leading-edge shock is at a very shallow angle in reference to the roughness element and the vortex in front of the roughness element almost reached the leading edge of the plate as shown in Figure *103*. Furthermore, an expansion wave is formed at x=*0.04* m position and extends to the end of the domain. To get a better insight of this flow the data from the probes have been analyzed and are presented next. The exact coordinates of all probe locations are shown in Table *3.24.* As evidenced in Figure *3.103* all five probes capture a natural oscillation in the density of the flow, even probe *5* which is located inside the boundary layer which persists even after *1* million timesteps.

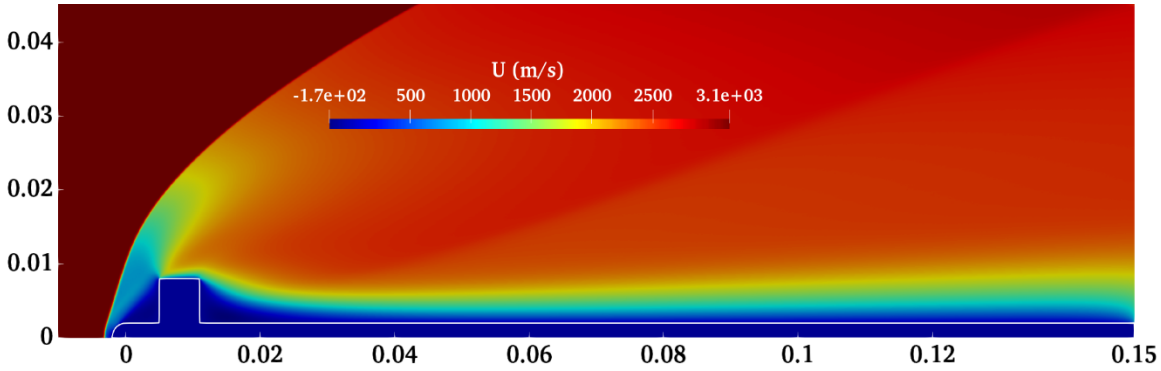

***Figure 3.102**. Steady state of the streamwise velocity domain with chemical reactions.*

***Table 3.23:** Chemical reaction parameters (Hypersonic flow over a flat plate with a roughness element 1cm from the leading edge).*

Reaction	***A*, $m^3/_s$**	***E_a (J)***	***b***	***DOF***
$N_2+O_2 \rightarrow N_2+O+O$	1.198×10^{-11}	8.197×10^{-19}	-1.0	1.0
$O_2+O_2 \rightarrow O_2+O+O$	5.393×10^{-11}	8.197×10^{-19}	-1.0	1.0
$N_2+O \rightarrow NO+N$	4.000×10^{-17}	5.288×10^{-19}	0.25	1.0
$NO+N \rightarrow N_2+O$	8.890×10^{-18}	0.0	0.25	0.0

$NO+O \rightarrow O_2+N$	5.279×10^{-21}	2.719×10^{-19}	*1.0*	*0.0*
$N_2+NO \rightarrow N_2+N+O$	6.590×10^{-10}	10.43×10^{-19}	*-1.5*	*1.0*

Figure *3.104* reveals that the streamwise velocity is fluctuating as well in the shock layer and in the boundary layer as well. In order to calculate the frequency of these oscillations an FFT was performed on the probe data and a frequency of *34.20* kHz has been computed. Moreover, to verify is this oscillation comes from the interaction between the two shocks the data from probes Front and Back have also been examined. Figure *3.105* shows the data gathered from both probes. Probes Front and Back capture the same oscillation as the other probes. Especially probe Front being closer to the shock captures a more amplified oscillation than the other ones. This leads us to conclude that in this specific case the roughness element acts as a media to reduce the oscillation amplification. To verify this observation an FFT has been conducted to the data from probes Front, Back and Probe 1 and shown in Figure *3.106*. FFT verified that the frequency of the oscillations captured by the Front probe are the same frequency as the oscillations at the rest of the probes, whereas the oscillation at the Front probe location is ≈*28.8* times more amplified than in the rest probes. Comparing this result with the no chemistry simulation we can see in Figure *3.107* the same oscillation occurs at the same frequency but after about *400,000* timesteps decays and after another *200,000* timesteps dies out.

This leads us to conclude that the inclusion of chemistry has a massive impact in the flow as it alters the equilibrium. Although this is two-dimensional shock the measured oscillation frequency is very close to the one measured by Sawant *et al.* in [Saw21]. As shown before the particle distribution functions differ from the Maxwellian inside the shock and close to the shock area. Thus, these oscillations can be attributed to the difference in the particle distribution functions in the nonequilibrium zone of the shock versus the equilibrium regime in the absence of chemical reactions

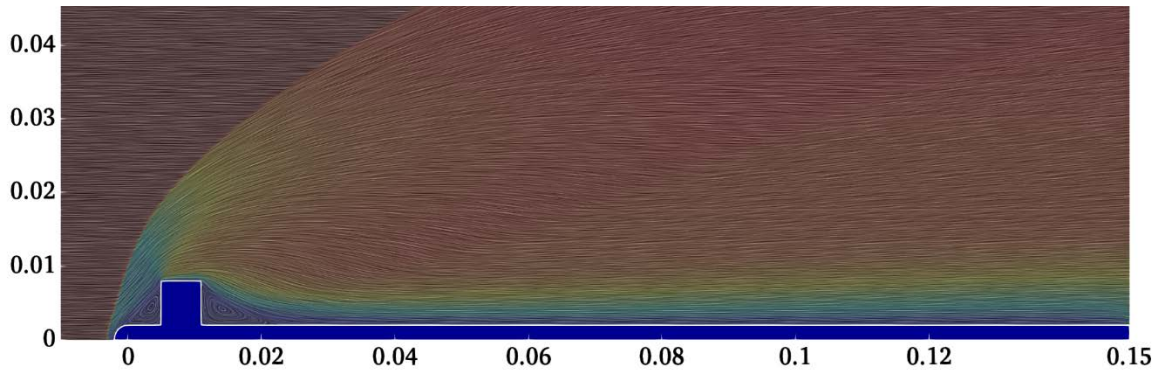

***Figure 3.102**. Velocity magnitude oil lines.*

***Table 3.23:** Probe coordinates (Hypersonic flow over a flat plate*

with a roughness element 1cm from the leading edge).

Probe	*X*	*Y*
1	*0.105*	*0.008*
2	*0.11*	*0.008*
3	*0.12*	*0.008*
4	*0.13*	*0.008*
5	*0.12*	*0.004*
Front	*0.003*	*0.008*
Back	*0.013*	*0.008*

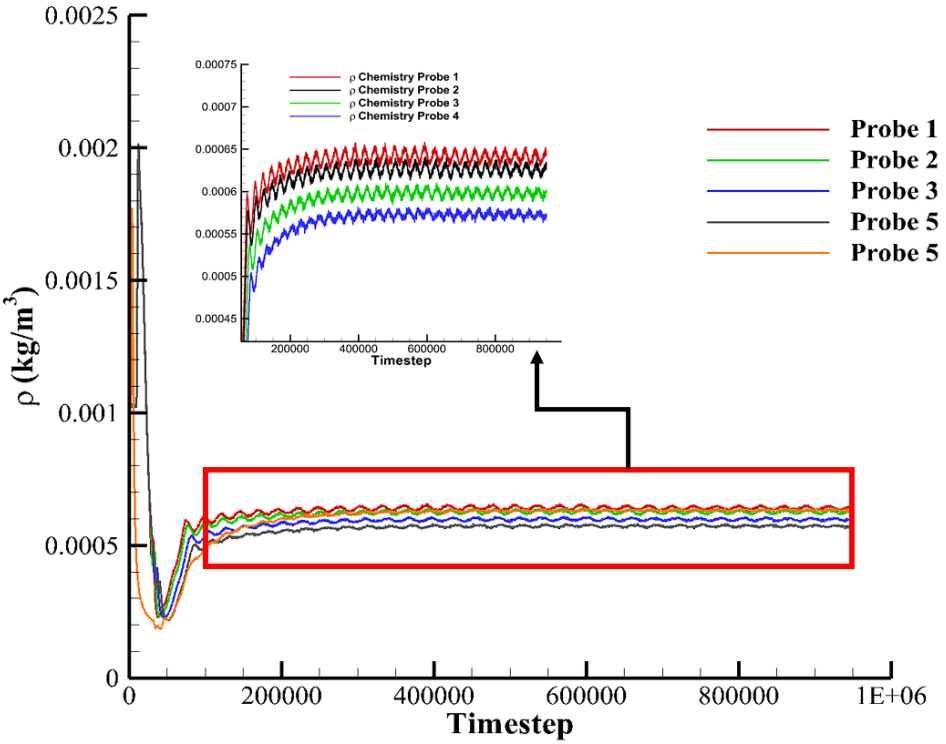

Figure 3.103*. Flow density fluctuations captured by the five probes at the back of the roughness element.*

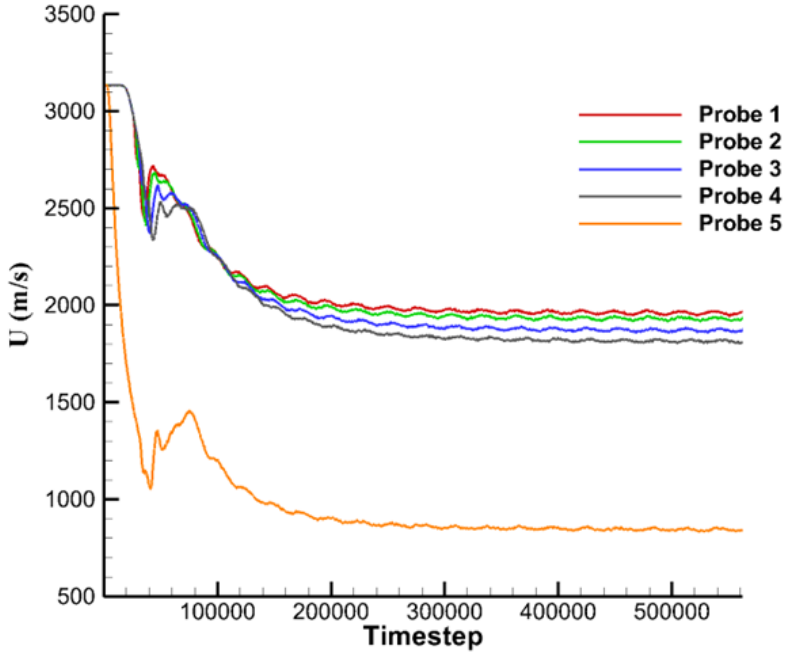

***Figure 3.104**. Flow streamwise velocity fluctuations captured by the five probes at the back of the roughness element.*

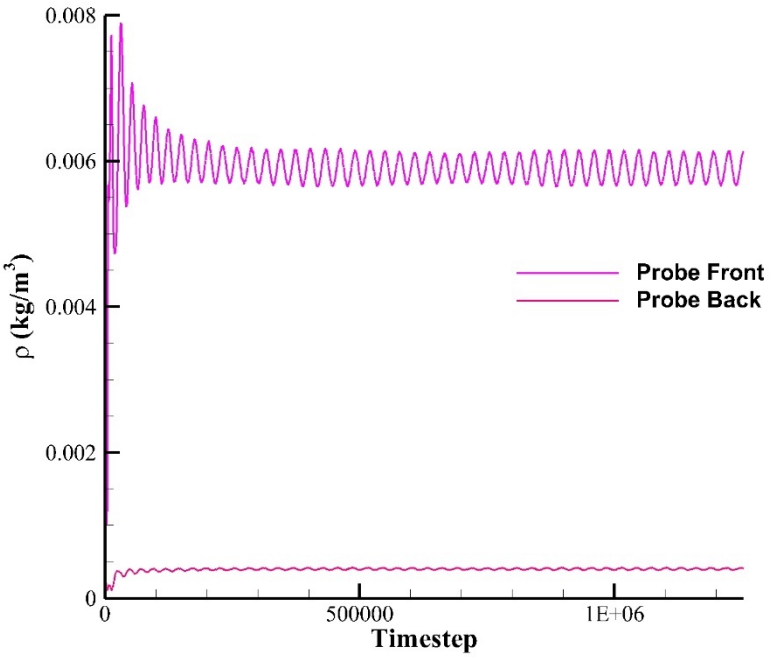

***Figure 3.105**. Flow density fluctuations captured by the probes Front and Back at the back of the roughness element.*

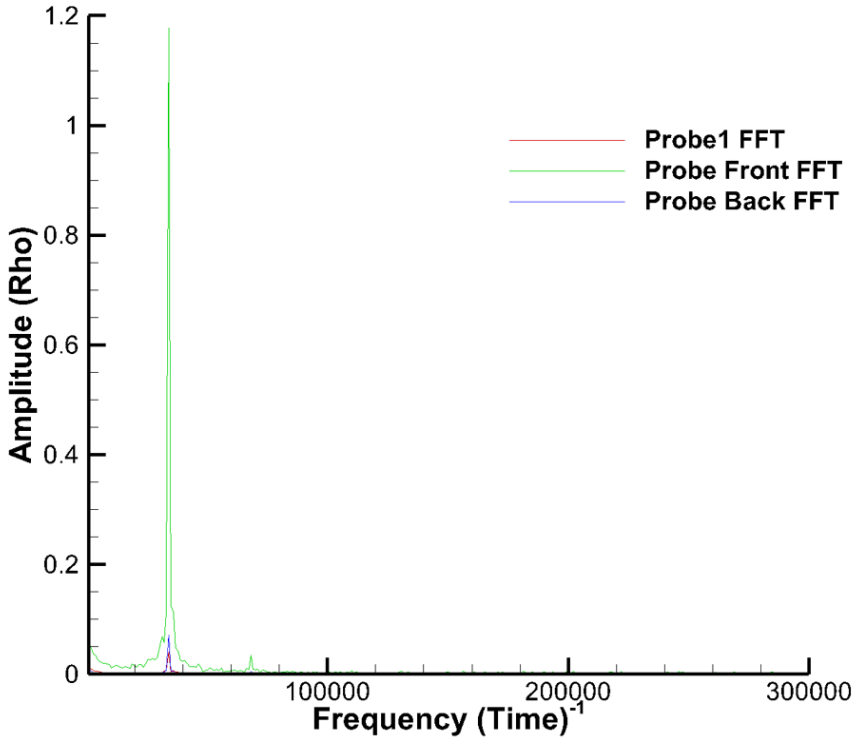

***Figure 3.106**. FFT of the data from probe 1, Front and Back.*

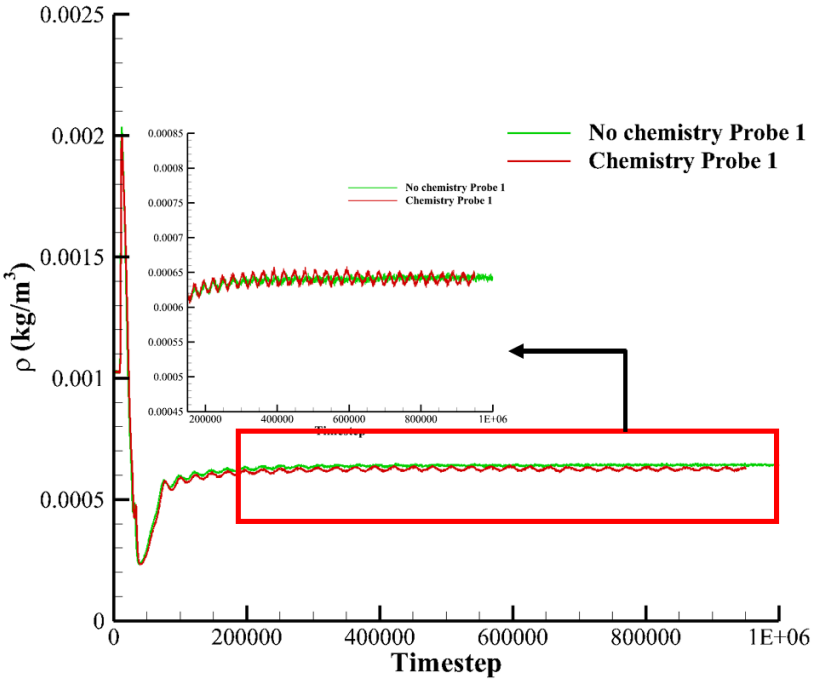

***Figure 3.107**. Comparison of density oscillation with and without chemistry.*

3.9 Hypersonic flow over a cone with a swept fin

The eighth case is a full three-dimensional simulation of a flow over a cone with a swept fin. This case was run in collaboration with Ms. Madeline Peck from the Purdue University. The geometry used was based on an experimental geometry used by many researchers to study boundary-layer transition on the surface of the cone and the fin [Tur18, Tur19, Mul19]. An overview of the aforementioned geometry is shown in Figure *3.108*. The fin is *40.64* cm in length, *9.5 cm* in height, it has a *1 mm* hemispherical nose-tip and half-angle of 7º [Tur18a, Tur21]. The fin starts at a location of *10.16* cm from the leading edge and is swept at 65º. The presence of the fin at the top of the cone introduces a complex shock interaction system, between the leading-edge shock and the shock induced due to the fin. Due to large pressure gradients introduced by the geometry a series of vortices are generated between the cone and the fin. Very little attention has been given to the base of the fin. In this region the shock generated by the fin results in a shock-boundary layer interaction [Pec23]. In order to enhance our understanding on this interaction the boundary layer and the shock layer has to be resolved.

Two geometry configurations were examined. The very high pressure used in the experiment yield an enormous computational cost for the full three-dimensional case for the DSMC. Thus, a set of parameters, different from the experiment parameters, was decided that could allow for a three-dimensional DSMC calculation while maintaining to some degree the structures observed in the higher-pressure test cases. In harmony with the previous statement of the fin was also modified in order to promote an interaction in the lower pressure environment. The swept of the fin used in the three-dimensional simulations is 75º instead of 65º. The simulation parameters for the axisymmetric and the three-dimensional configurations can be found in Table *3.24* and *3.25* respectively. The experimental conditions allowed for a two-dimensional configuration [Tur18a, Tur21]. Comparisons in the experiment conditions were made with simulations run with the Navier-Stokes Data Parallel Line Relaxation code (DPLR) by Dr. Madeline Peck. In DPLR simulations a no-slip boundary condition was used on the surface. The axisymmetric simulation domain is *0.01 m* in length and *0.0025 m* in height and a grid with *161,600,000* cells and 4.5×10^{9} particles were required to capture all flow physics accurately. The DSMC parameters for the axisymmetric and the three-dimensional case can be seen in Tables *3.26* and *3.27* respectively.

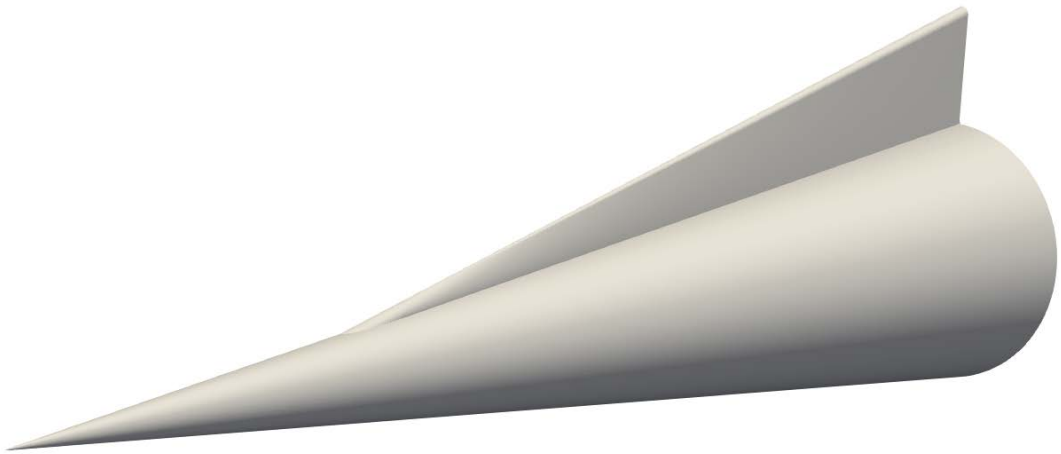

***Figure 3.108**. Cone with a swept fin geometry.*

***Table 3.24:** Flow parameters for the 2D-axisymmetric case (Hypersonic flow over a cone with a swept fin).*

Mach number, Ma_∞	*6*
Reynolds, Re_∞ (1/m)	6.3×10^{6}
Freestream velocity, U_∞ (m/s)	*870*
Knudsen number, (Kn)*	*0.0018*
Angle of attack, α (degrees)	*0*
Freestream density, ρ_∞ (kg/m^3)	2.40×10^{-2}
Freestream pressure, p_∞ (Pa)	*348.6*
Freestream temperature, T_∞ (K)	*50.61*
Wall temperature, T_w (K)	*300*
Gas	N_2

***Based on the cone nose radius**

Due to the elevated pressure, the full three-dimensional simulation of the cone was impossible to compute. To account for that, and to reduce the computational cost of the DSMC the full three-dimensional geometry was first run using DPLR. Then, for the DSMC, a three-dimensional domain around the start of the fin was setup and the inflow boundary conditions for that location were taken from the DPLR solution. A plane was extracted from the three-dimensional solution of DPLR and then the data points of that plane were interpolated to the DSMC grid using the inverse-distance method. An overview of the domain used for the DSMC can be seen in Figure 3.*109*. As seen, the DSMC computational domain is a fraction of the domain used in DPLR (Figure *3.110*). More specifically, the volume of the three-dimensional DSMC domain is *60* times smaller than the one used in DPLR. As mentioned earlier, although the pressure was reduced in the three-dimensional simulation to be feasible, despite that, this domain required 5.62×10^{8} computational cells and about 4.8×10^{10} particles. In order for this simulation to be feasible *22%* of the UK national supercomputer ARCHER2 was acquired for *23,5* hours.

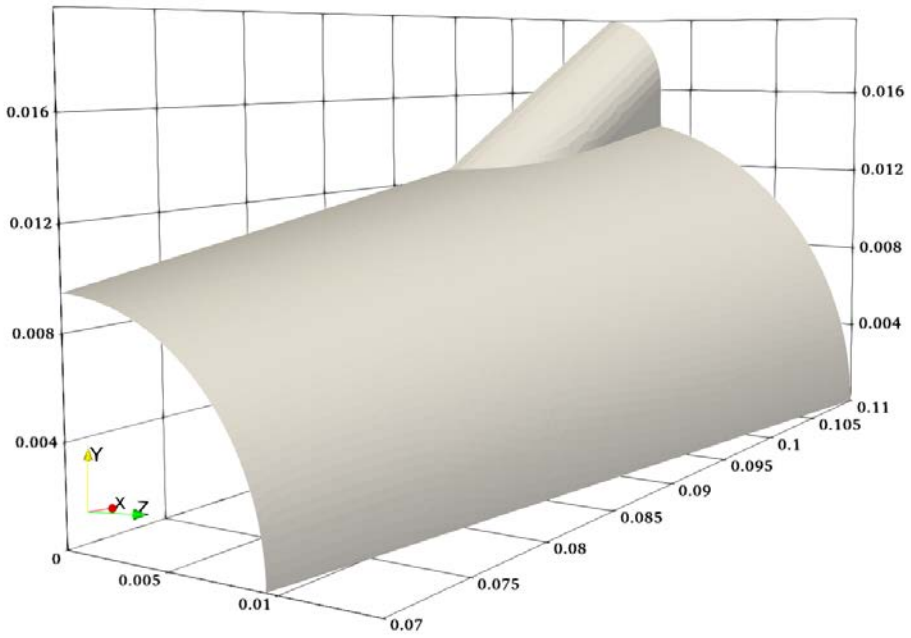

Figure 3.109. *DSMC computational domain for the three-dimensional fincone case.*

Table 3.25: *Flow parameters for the 3D case (Hypersonic flow over a cone with a swept fin).*

Mach number, Ma_∞	*6*
Reynolds, Re_∞ (1/m)	*1.37×10^{6}*
Freestream velocity, U_∞ (m/s)	*855*
Knudsen number, (Kn)*	*0.162*
Angle of attack, α (degrees)	*0*
Freestream density, ρ_∞ (kg/m^3)	*4.99×10^{-3}*
Freestream pressure, p_∞ (Pa)	*75*
Freestream temperature, T_∞ (K)	*50.61*
Wall temperature, T_w (K)	*300*
Gas	*Air*

***Based on the cone nose radius**

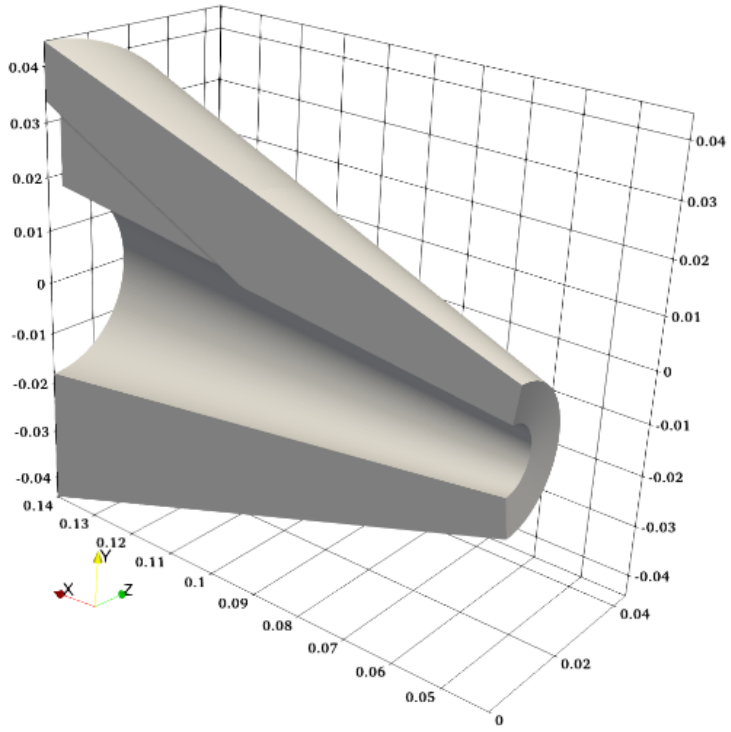

***Figure 3.110**. DPLR computational domain for the three-dimensional fincone case.*

***Table 3.26:** DSMC computational parameters for the 2D axisymmetric case (Hypersonic flow over a cone with a swept fin).*

Number density, Nd_∞ (#/m^3)	*4.99×10^{23}*
Timestep (s)	*2.0×10^{-9}*
Transient period	*150,000*
Sample period	*300,000*
Number of particles (#)	*4.5×10^{9}*
Number of cells	*1.616×10^{8}*
Wall-clock time (CPU hours)	*405,623*

***Table 3.27:** DSMC computational parameters for the 3D case (Hypersonic flow over a cone with a swept fin).*

Number density, Nd_∞ (#/m^3)	*1.08×10^{23}*
Timestep (s)	*2.0×10^{-9}*
Transient period	*70,000*
Sample period	*150,000*
Number of particles (#)	*4.5×10^{10}*
Number of cells	*5.625×10^{8}*
Wall-clock time (CPU hours)	*3,927,040*

Starting with the comparisons for the axisymmetric case first, a very good agreement in the Mach number contours shock position and boundary-layer thickness can be seen in Figure *3.111* meaning the effects of velocity slip on the surface and temperature jump conditions are minimal in this area. In order to verify the visual result exact boundary layer profiles were extracted from the axial location *x=0.008 m* are shown in Figure *3.112*. A more close-up view of these profiles focused on the boundary layer location is shown in Figure *3.113*. Generally, the agreement between the two methods is very good. In Figure *3.113* some near-wall discrepancies can be seen probably resulting from the no-slip and no-temperature jump boundary conditions used in DPLR.

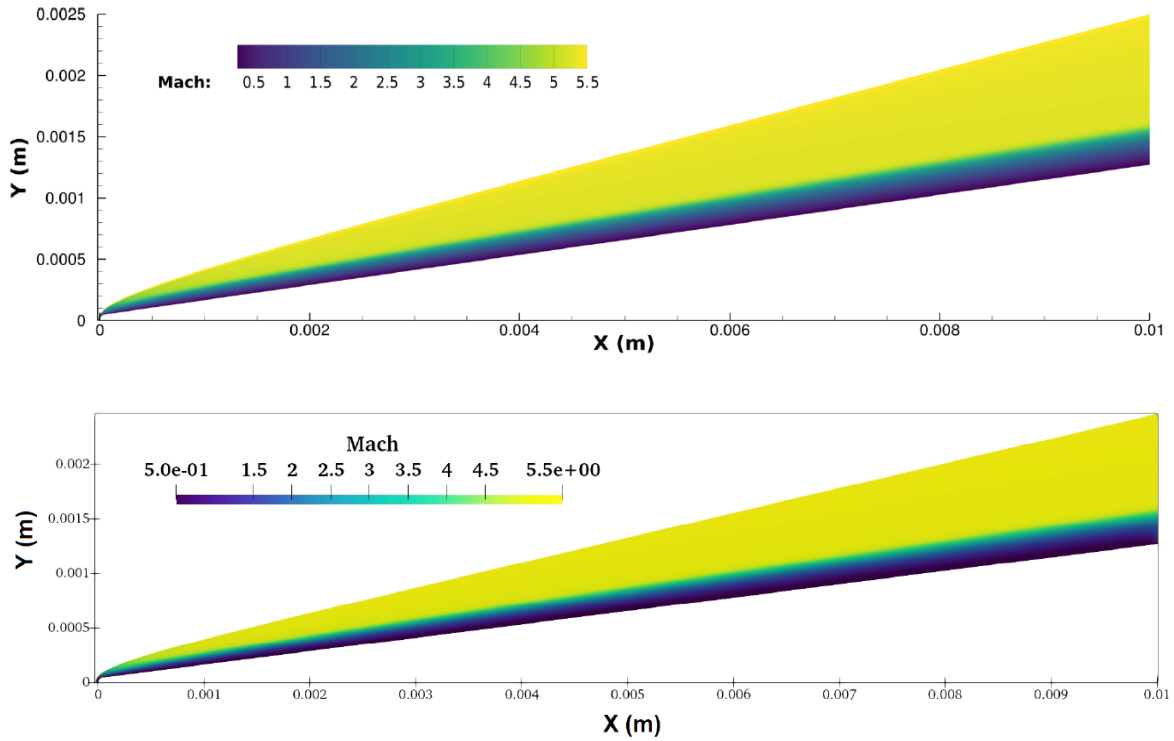

Figure 3.111. *DPLR Mach number (top) and DSMC Mach number (bottom).*

The excellent agreement between the DSMC and Navier-Stokes simulations along the whole flow field from the boundary till the shock indicates that the error introduced by the near-wall discrepancies is localized. Furthermore, the error near the wall is very small compared to the freestream values. After obtaining this very good agreement in the two-dimensional high pressure axisymmetric case the lower pressure three-dimensional test case was ran.

Even though the pressure was lowered in the three-dimensional case, due to the extremely high computational cost it was not feasible to run the full three-dimensional configuration of the cone. Thus, a small portion of the full domain, around the fin area was chosen and can be seen in Figure *3.109*. For this small domain more than half a billion computational cells were required to capture the flow effects accurately. To limit the statistical noise a minimum number of *50* particles per cell was utilized and *150,000* samples were taken to calculate the flow macro-properties. The inflow plane was taken from the DPLR simulation at the same conditions and interpolated to the DSMC grid. The whole simulation was run using *166,400*

MPI processes which is more than *22%* of the UK Archer2 National Supercomputer for *23.6* hours.

To compare the results between the two solvers a fixed location was chosen in which the vortex created on the surface of the cone is present and not close to the DSMC outflow in order to avoid any fluctuations caused due to the particles deletion after they exit the simulation domain. This location for the SPARTA domain is *0.035* m from the outflow and the analogous location in DPLR domain is *0.065 m* from the inflow boundary. A comparison of the three velocity components can is shown in Figure *3.114*. As seen, all velocity components agree very well to the boundary layer, the shock position, the shear layer and the vortex size. Excellent agreement is also evidenced in Figure *3.115* for density temperature and the Mach number.

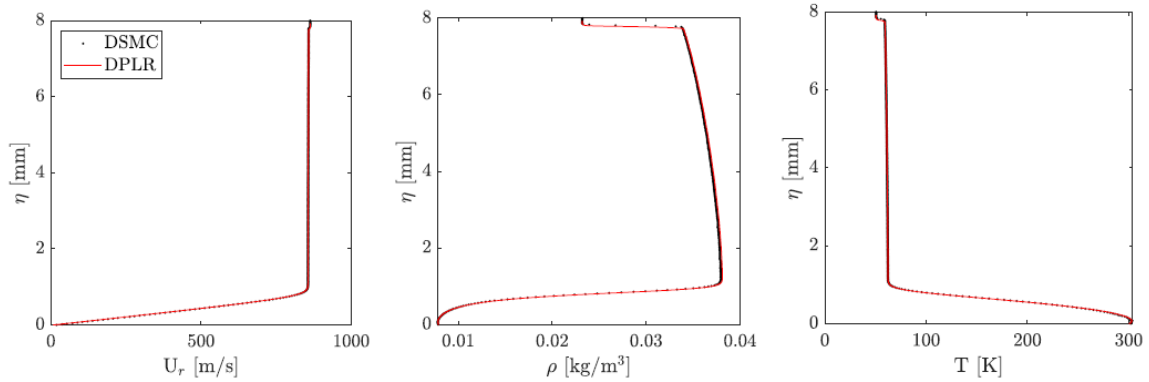

***Figure 3.112**. Wall normal profiles at x=0.08 m.*

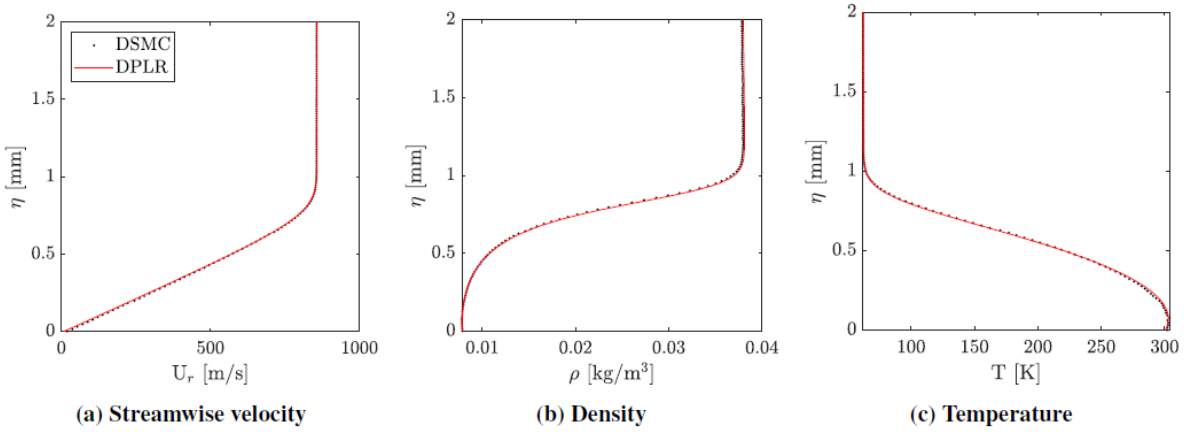

***Figure 3.113**. Boundary layer profiles at x=0.08 m.*

Visually a difference between the two methods can be seen in the contours of the *W* velocity component, density and temperature. It is present in the DSMC results in the middle of the shear layer. This flow feature looks like a very weak shock or a flow disturbance smoothed out in the DPLR result. In order to shed some light, the vorticity magnitude has also been plotted in Figure *3.116*. Horizontal and vertical lines seen in Figure *3.116* are an artifact of the visualization software and not the solution. This slight disturbance is still present in the vorticity magnitude of the DSMC result although as seen in Figure *3.116* some flow characteristics are indeed smoothed out in the Navier-Stokes solution. DSMC captures a high vorticity number inside the shock and at an angle of 45-degrees in relation to the cone's surface,

whereas in the Navier-Stokes only a fraction of that vorticity is captured and is the same across the whole shock. Also, in the vorticity plot of the DSMC solution small vortices can be seen emanating from the fin shock and moving sideways towards the boundary layer and the cone's surfaces. These vortices reveal an area of non-equilibrium between the fin's boundary layer and fin's shock.

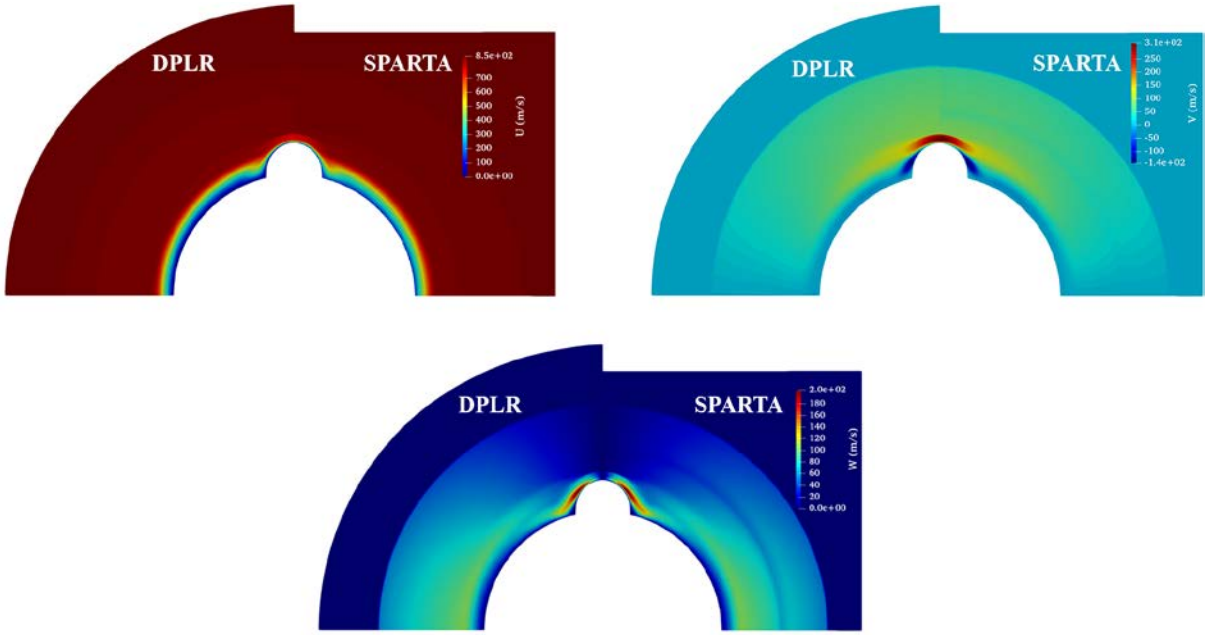

***Figure 3.114**. Comparison between SPARTA and DPLR of the three velocity components at a location of 0.035 m from SPARTA inflow.*

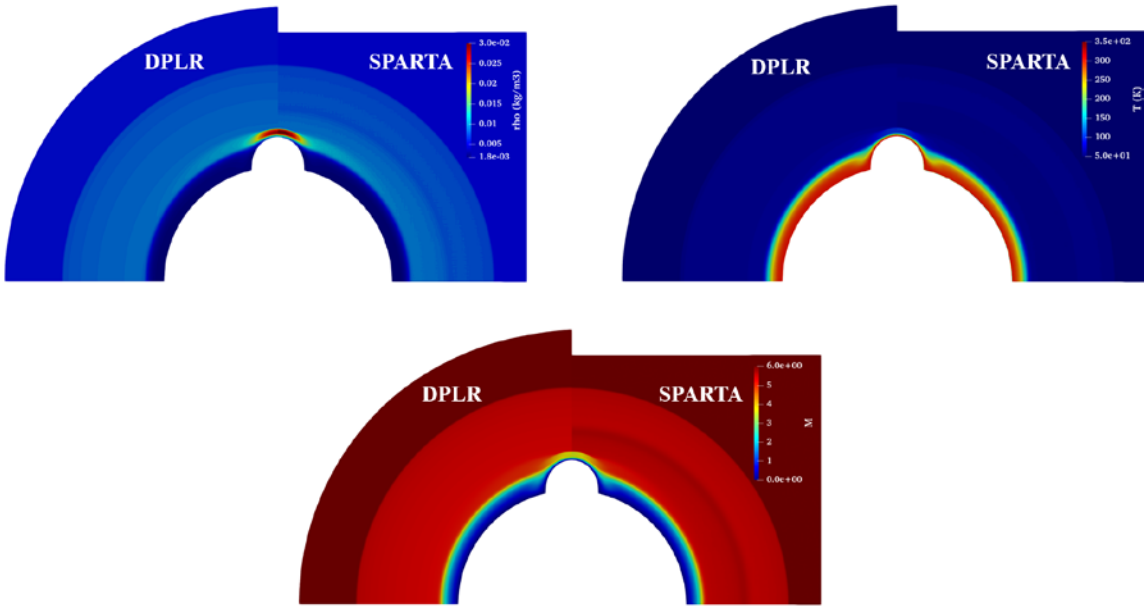

***Figure 3.115**. Comparison between SPARTA and DPLR of density, temperature and Mach number at a location of 0.035 m from SPARTA inflow.*

Apart from visual comparisons, profiles of the examined flow field have been extracted along three different locations shown in Figure *3.117*. The lines named *Side* and *Vortex Location* are taken normal to the cone's surface while the line *Fin Shock* is parallel to the vertical domain boundaries. The three velocity components, density and temperature for all data locations are plotted in Figures *3.118-3.120* respectively. For all the examined flow properties the line plots reveal an excellent agreement. The flow disturbance, as seen in Figure *3.118*, is more prominent to the *V* and *W* velocity components and it is shown by a sudden change "shock-like" change in these velocity components. In addition, it can be seen in the density profiles for all data locations and in the temperature profile of the *Fin Shock* line. Since there is excellent agreement across the whole flow profile this disturbance seems to be localized and doesn't affect the entire flow field.

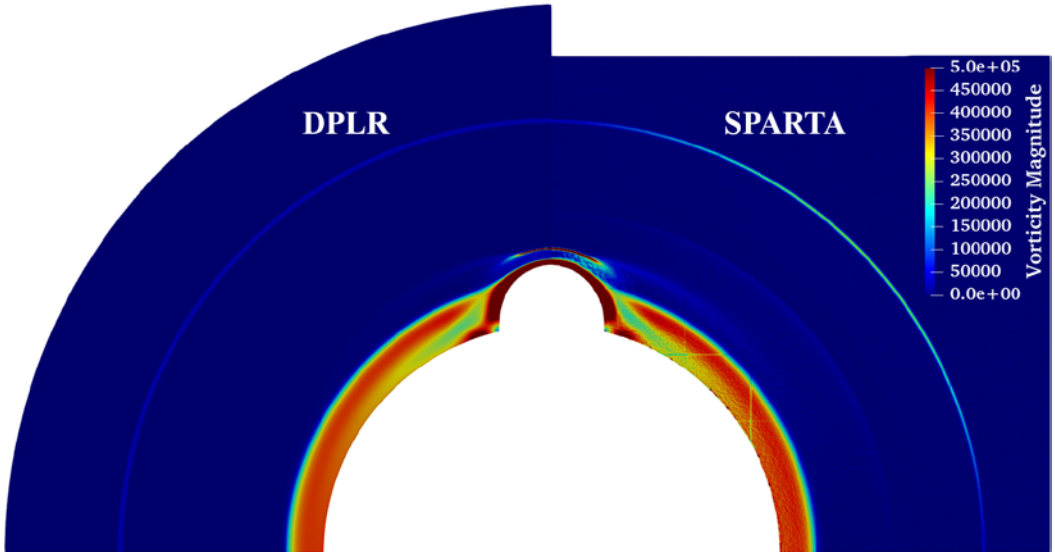

***Figure 3.116**. Comparison between SPARTA and DPLR of vorticity magnitude at a location of 0.035 m from SPARTA inflow.*

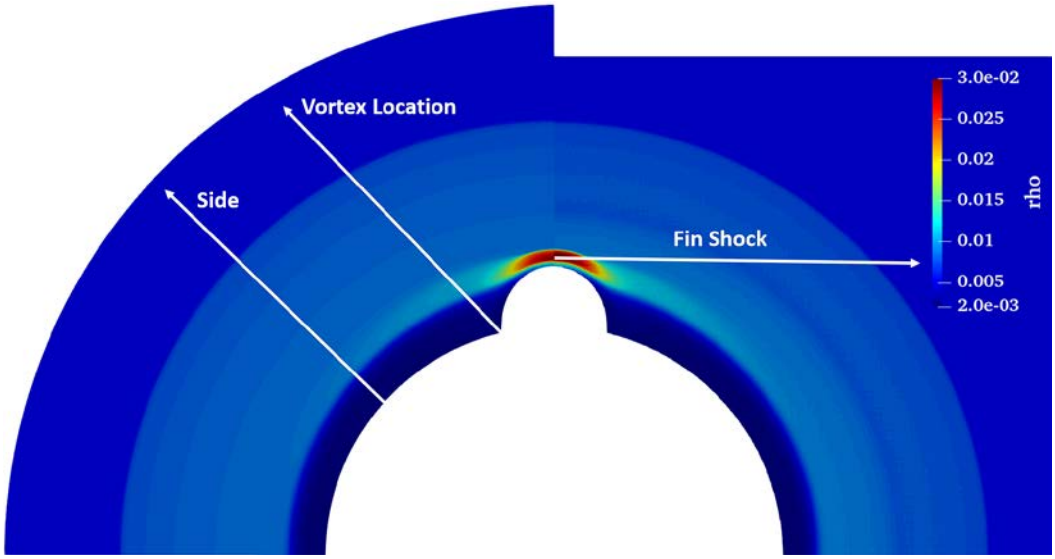

***Figure 3.117**. Data extraction lines.*

In conclusion, this case demonstrates the ability of DSMC to fully analyze all physical effects occurring in a hypersonic flow. Despite the high computational cost, the method can provide a valuable insight of physical phenomena that cannot be analyzed by the classical Navier-Stokes approach. Furthermore, as evidenced the accuracy of the method is comparable to the Navier-Stokes approach and can offer significant advantages at the very small flow scales such as velocity distributions of the gas particles across the entire domain and non-equilibrium phenomena can be simulated without the use of approximation models. In this particular test case chemistry was not used and it was assumed that no chemical reactions are happening in the flow. In our future work this case will be revisited and chemical reactions will be taken into account in order to compare the impact of chemistry in this particular flow configuration.

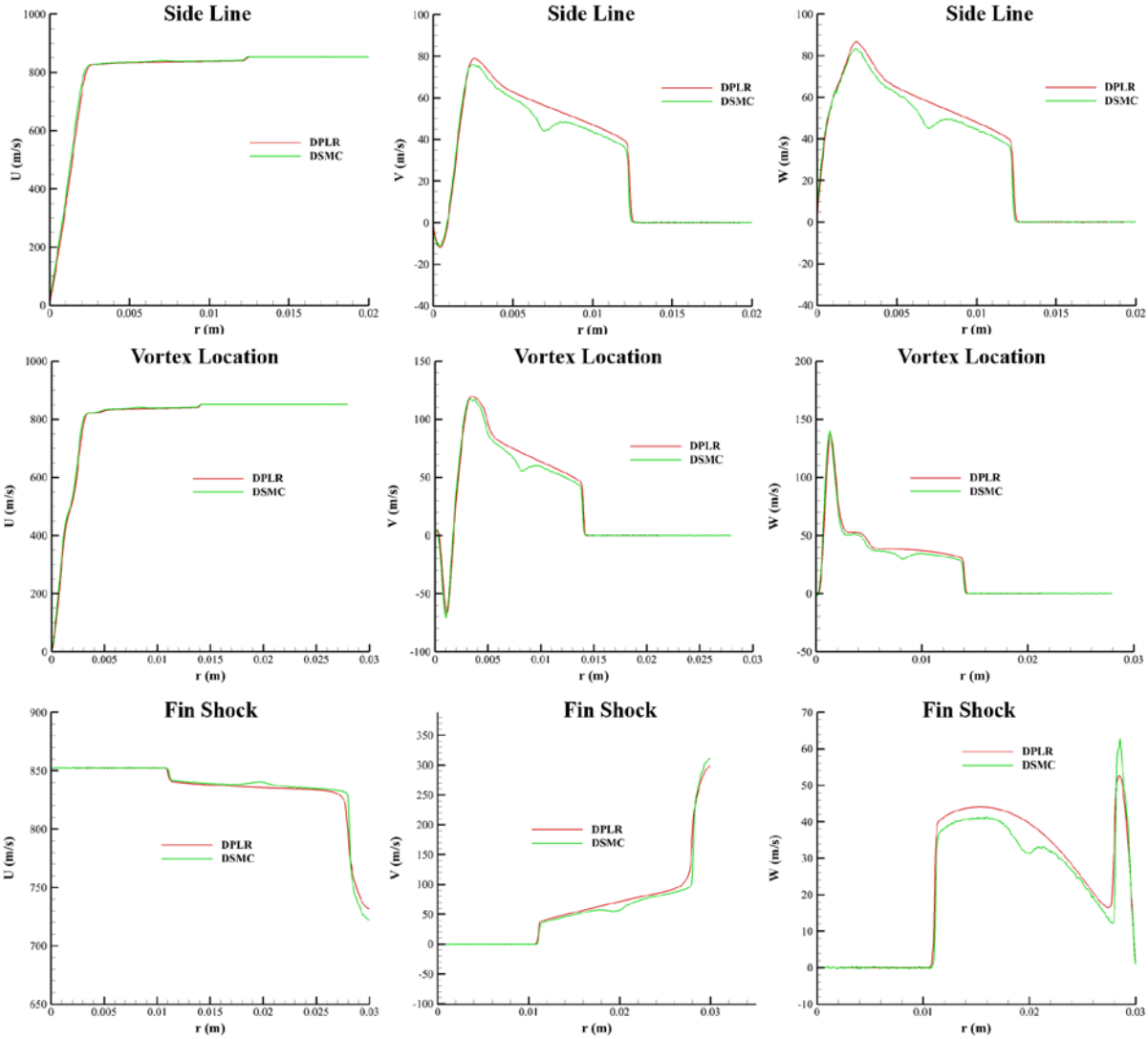

***Figure 3.118**. Velocity components across all three data extraction lines.*

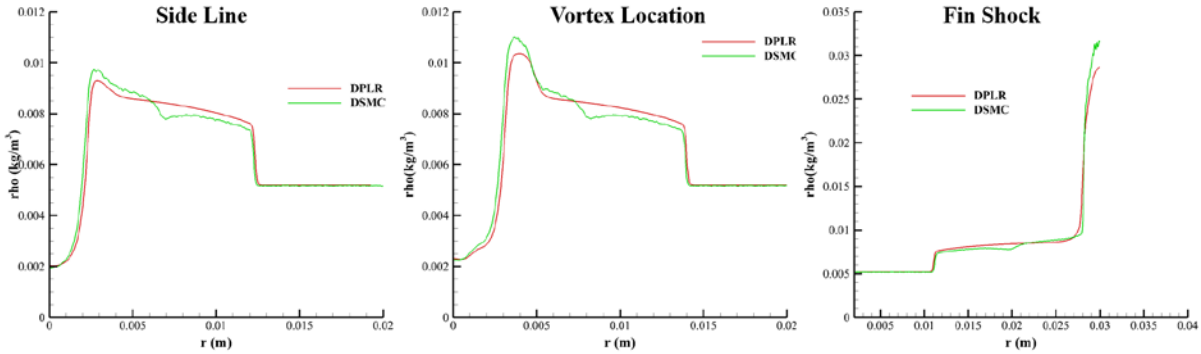

***Figure 3.119**. Density profiles across all three data extraction lines.*

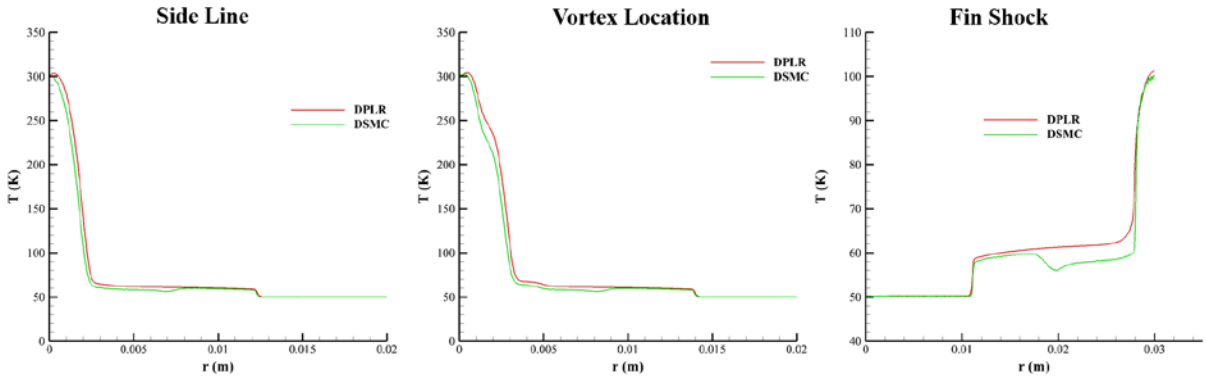

***Figure 3.120**. Temperature profiles across all three data extraction lines.*

3.10 Hypersonic flow over a Mach 7 waverider

In this case an effort has been made to design a Mach 7 waverider using the osculating cone method described in section *2.3.5*. As aforementioned, to design a functional waverider configuration a base flow field must be first generated. In this case the initial base flow field was generated by a 7^o half-cone with a length of *2 m* and a blunted nose with a radius of *1 cm*. The full three-dimensional configuration of the cone was simulated. The flow conditions represent the conditions occurring at an altitude of *90 km* and were taken from the US standard atmosphere model. To capture the flow effects accurately a grid of *91,832,000* cells was used with an additional level of refinement close to the surface. The flow conditions along with the DSMC simulation parameters can be seen in Tables *3.28* and *3.29* respectively. A three-dimensional representation of the geometry of the cone used to produce the initial flow field can be seen in Figure *3.121*. After the computation of the initial three-dimensional flow field the planar streamlines around the cone were extracted in order to identify the shock boundaries.

The calculated field streamlines can be seen in Figure *3.122*. The shock boundaries in the side and top plane (Figures *3.122 (middle)* and *3.1.122 (top)*) can be identified by the bending of the flow streamlines whereas in the rear plane at the back of the cone the shock layer is clearly visible in the streamwise velocity flow field. After extracting the flow data, the flow planes are imported to CAD (Computer Aided Design) in order to design the three-dimensional

shape of the waverider. After importing the planes, starting from the end of the initial cone shown in Figure *3.122 (bottom)* curves that are tangent to the circular shock shape are drawn, resulting to the first section of the waverider. The first section can be seen in Figure *3.123*. As mentioned in section *2.3*.5 to obtain a realistic configuration, the leading edges must be blunted and not sharp.

Table 3.28: *Flow parameters (Hypersonic flow Mach 7 waverider).*

Mach number, Ma_∞	*7*
Reynolds, Re_∞ (1/m)	*1.37×10^{6}*
Freestream velocity, U_∞ (m/s)	*1965*
Knudsen number, (Kn)*	*0.621*
Angle of attack, α (degrees)	*0*
Freestream density, ρ_∞ (kg/m^3)	*9.62×10^{-6}*
Freestream pressure, p_∞ (Pa)	*0.55*
Freestream temperature, T_∞ (K)	*196*
Wall temperature, T_w (K)	*300*
Gas	*Air*

****Based on the cone nose radius***

Table 3.29: *DSMC computational parameters (Hypersonic flow Mach 7 waverider).*

Number density, Nd_∞ (#/m^3)	*2.00×10^{20}*
Timestep (s)	*3.0×10^{-7}*
Transient period	*80,000*
Sample period	*100,000*
Number of particles (#)	*8.0×10^{9}*
Number of cells	*9.83×10^{7}*
Wall-clock time (CPU hours)	*184,320*

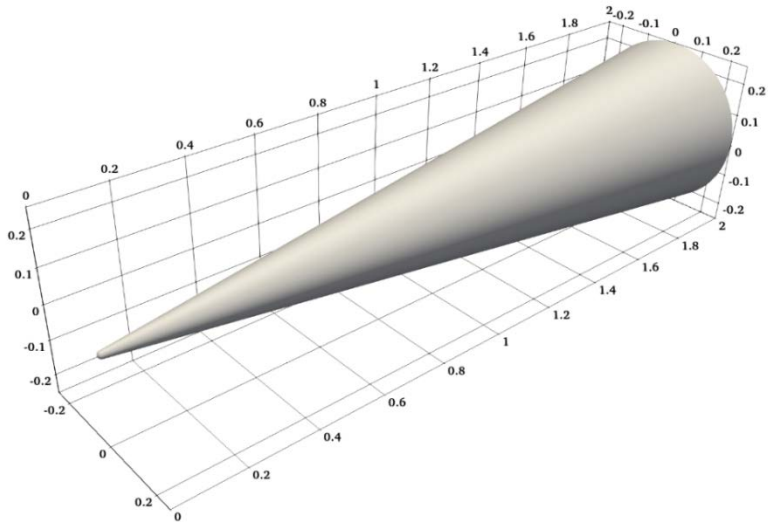

Figure 3.121*. 7-degree half cone used in the calculation of the initial flow field.*

To control the bluntness of the leading edges a four-point Bezier curve was used to generate the leading-edge shape. Moving downstream to the flow field one section of the waverider is designed every *30 cm*. Figure *3.1.24* shows an overview of these sections. For cleanness, not all sections are visible. Finally, when all sections are designed a loft operation with tangency constraints is imposed to generate the waverider surfaces. To reduce the design complexity and to take advantage of the symmetry of the flow field, only half of the final geometry is designed and then mirrored around the symmetry plane. Before starting the three-dimensional simulation, the surface of the waverider was meshed in order to be used in the SPARTA solver. As seen in Figure *3.125* attention has been given to the surface close to the leading edge, the nose and the compression part of the lower surface of the vehicle so that the grid transitions smoothly as we approach the surface's change in curvature.

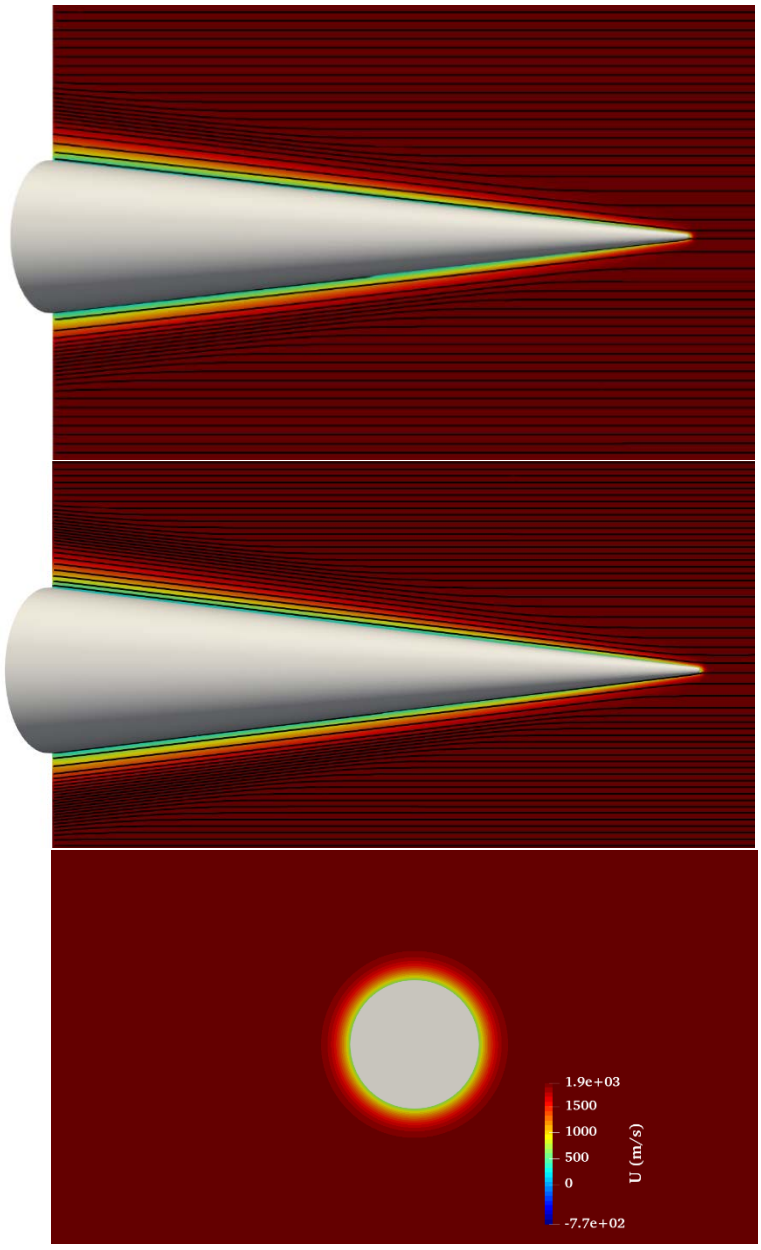

***Figure 3.122**. Streamlines of the three-dimensional flow field around the cone. Side view (top), top view (middle), rear view (bottom).*

To identify if the shock is properly attached to the leading edge of the vehicle the pressure and the Q-criterion contours have been plotted in Figures *3.126* and *3.127* respectively. Pressure contours in Figure *3.126* show an increase of pressure around the leading edge which is the result of the attached shock. This is also verified also by the Q-criterion contours in Figure *3.127* where below the leading edge a negative value of Q-criterion is found which is evident of a shock existing in that area. In Figure 47 also the surface of the waverider is colored by the pressure exerted on the vehicle surface. Higher values of pressure are evidenced around the leading edges and the nose, which verifies the existence of an attached shock wave in these regions.

Apart from the three-dimensional contours, Q-criterion, is also plotted in the plane of symmetry in Figure *3.128* and on a vertical plane normal to the back section of the waverider in Figure *3.129*. As verified, the Q-criterion is again negative around the nose and the leading edges. Figure *3.129* shows clearly that the shockwave is attached to the leading edges of the vehicle. Figures *3.130* and *3.131* show the streamwise velocity and the temperature field respectively around the vehicle. For the flow conditions used in this work a maximum temperature of 1400 K is identified in front of the nose. In this case due to the low temperature and the rarefaction of the flow chemical reactions were not enabled. In Figures *3.132* to *3.135* flow field properties are shown on a plane parallel to the waverider and the surface of the vehicle is colored by surface pressure. Figure *3.132* shows the pressure on the aforementioned plane. Taking into account that the free-stream pressure is *0.55 Pa* a temperature rise of one order of magnitude around the nose is evidenced. The pressure around the leading edges is increased as well, about four times higher than the free-stream pressure. The very high pressures in the nose and the leading-edge regions are exerted due to the shock attachment in these surfaces. Figure *3.133* shows the streamwise velocity on the same plane. Here, its evidenced again the shock adhering to the leading-edge and the nose of the vehicle. As seen in Figure *3.134* the temperature around the leading edges is *800 K* which is about four times higher than the free-stream temperature of *196 K*. Q-criterion on the same plane as before is shown in Figure *3.135* and shows the full field of the attached shock.

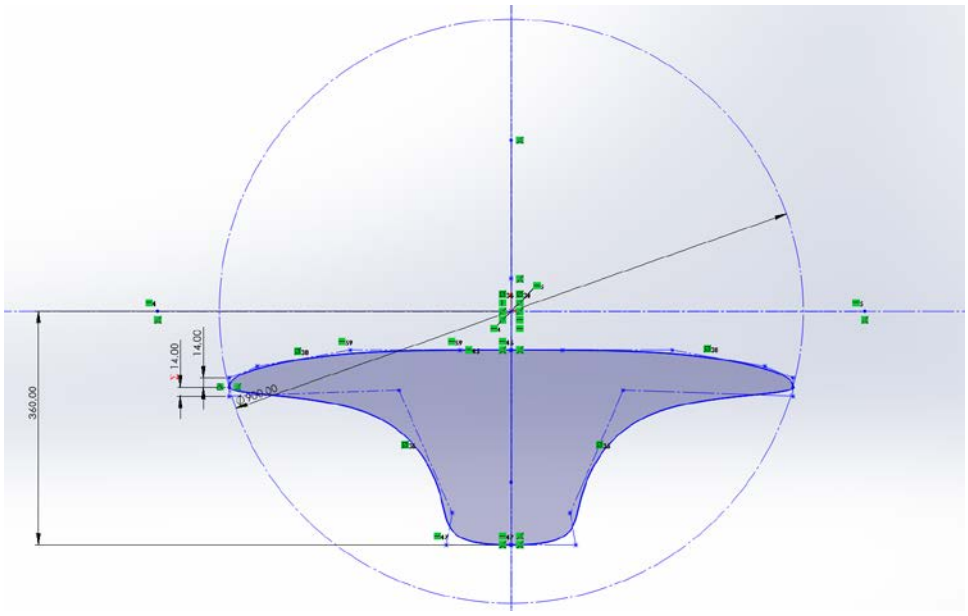

***Figure 3.123**. First section of the waverider (units in mm).*

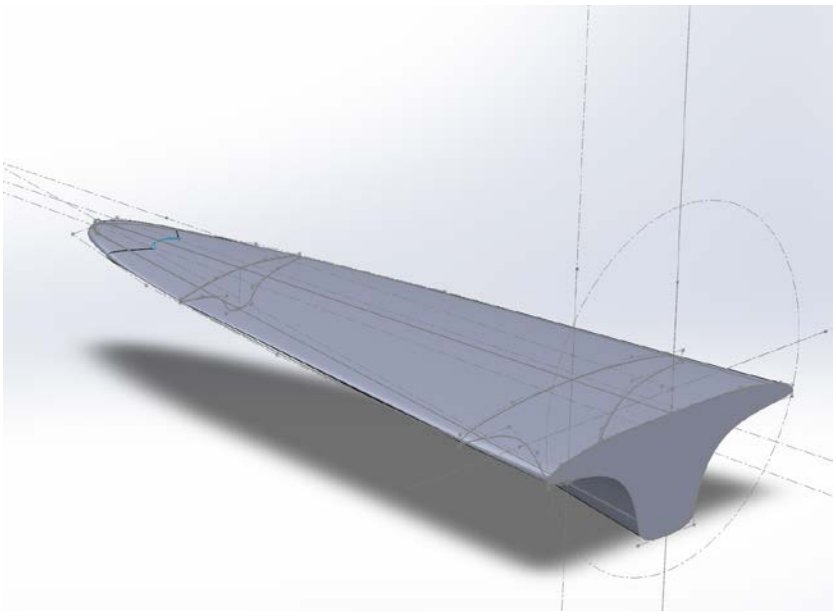

***Figure 3.124**. Final waverider geometry.*

Furthermore, in Figure *3.127* the altering positive and negative values of Q-criterion around the leading edge reveal a vortex on the top part of the leading-edge surface. The extend of this vortex can be seen in Figure *3.136* where the vorticity magnitude at the back of the vehicle is plotted. On the plane two vortices exist, one left and one right, at the tip of the back section of the vehicle. Viewing the vehicle in the symmetry plane in Figure *3.128* the Q-criterion shows that these vortices are created due to flow separation at that point. The vortices separate from the surface and then damped into the vehicle's wake region.

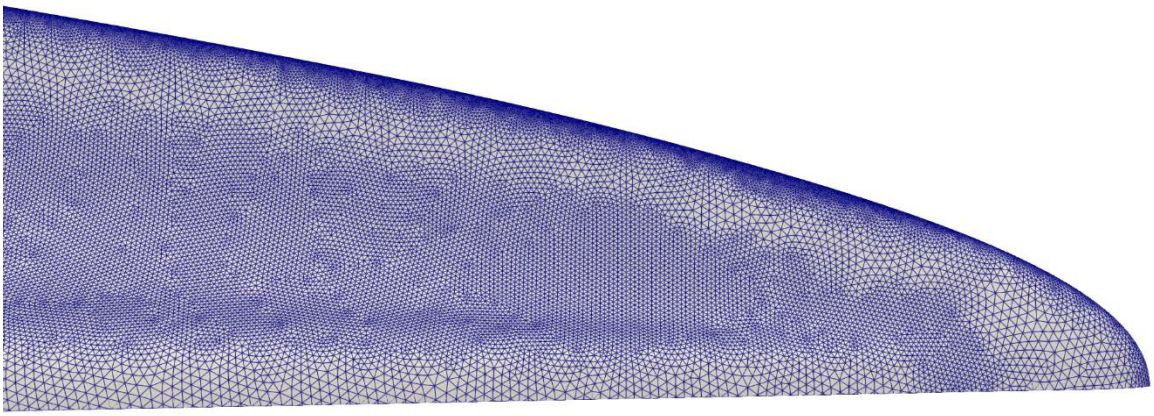

***Figure 3.125**. Portion of meshed waverider surface.*

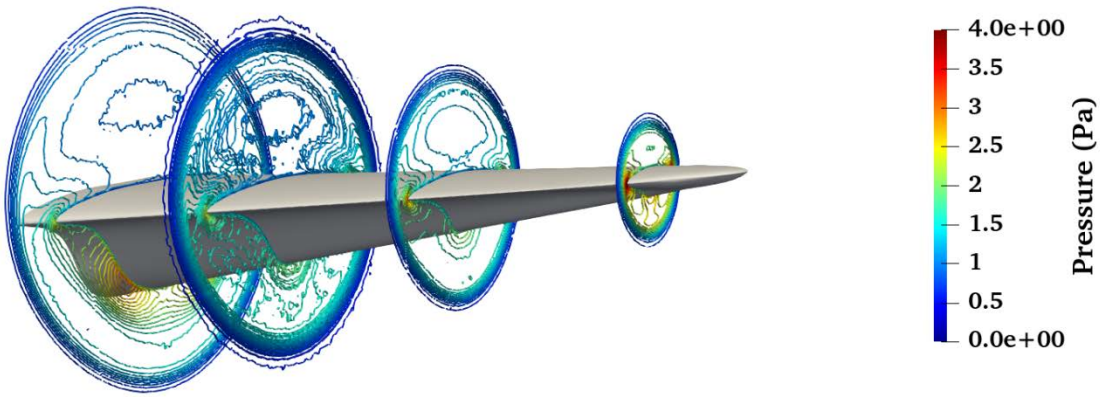

***Figure 3.126**. Pressure contours around the vehicle.*

Due to the complexity of the vehicle surface introducing complex flow effects, the three-dimensional iso-surfaces of the Q-criterion around the vehicle are plotted in order to identify the three-dimensional shape of the shock and the vortices. Figure *3.137* shows the three-dimensional Q-criterion contours around the vehicle colored by vorticity magnitude. The transparent grey contours correspond to the three-dimensional outer shape of the shock. A part of the shockwave close to the compression surface can also be seen. In Figure *3.138* the same contours are plotted but this time colored by the velocity magnitude. As seen in Figure *3.138* about 30 cm after the nose, where the compression surface is steeper, the vortices separate from the flow and continue downstream to the higher-pressure area towards the back side of the vehicle. Due to the angle of the compression surface towards the end of the vehicle a pressure rise is evidenced and the flow slows down about 1000 m/s within a few centimeters. In order to validate the vehicles performance, the L/D ratio was calculated using the pressure exerted on the surface.

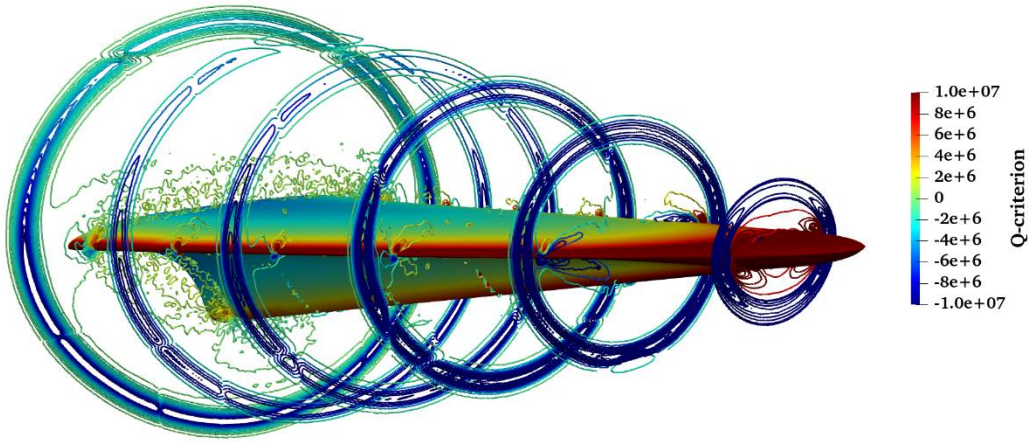

***Figure 3.127**. Q-criterion contours around the vehicle*
(Surface is colored by pressure).

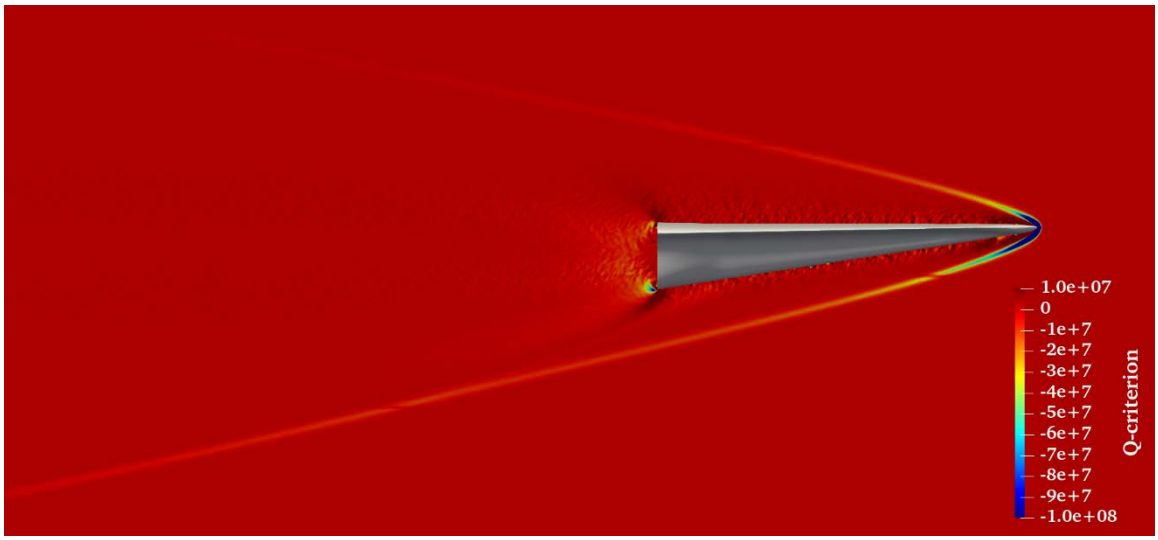

***Figure 3.128**. Q-criterion contours in the plane of symmetry.*

To calculate lift and drag the shear stresses and the pressure three-dimensional components have been calculated. From the calculation the lift and drag forces in each surface cell have been computed. The lift and drag at each surface cell can be seen in Figure *1.139*. From that figure we can also see that the maximum drag is concentrated at the tip of the nose whereas the area below the nose generates also a large amount of lift. By integrating the values of all cells, the total lift and drag have been calculated and the ration L/D is equal to *2.18*. According to open literature this value if typical for a waverider flying at 0^o angle of attack [Hua11]. A value of L/D of above *2.0* yields a good vehicle performance for the design condition selected. Only one angle of attack was examined in this case, according to [Hua11] a slightly positive angle of attack can increase the L/D ration, thus performance, two to three times. In the open literature, waveriders are usually analyzed between *25 km* and *40* km and in *90 km*, used in this work. This fact has an impact to lift generation on the surface by the fluid, thus in this design the compression surface is larger than a conventional compression surface seen in waveriders flying in lower altitudes.

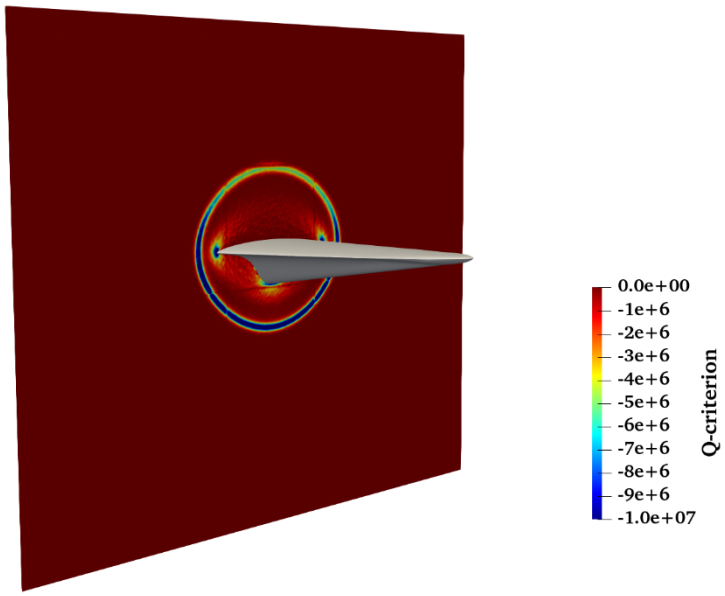

***Figure 3.129**. Q-criterion contours on a vertical plane normal to the first section of the vehicle.*

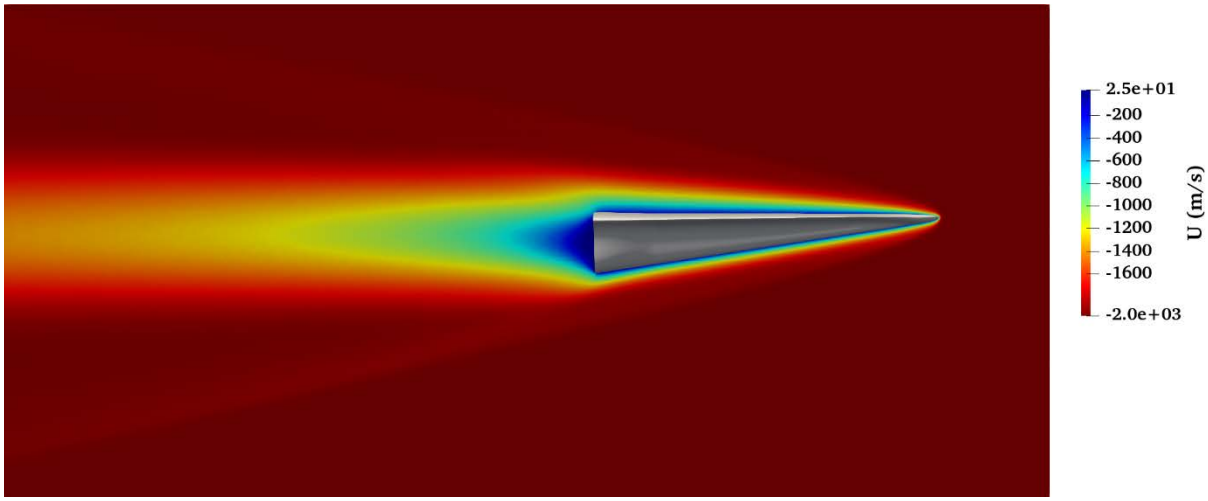

***Figure 3.130**. Streamwise velocity on the symmetry plane.*

In conclusion, in this case an effort to design a high altitude waverider is presented and analyzed at a zero angle of attack. The waverider yields good performance in the design condition due to the high L/D ratio. The simulation revealed lots of interesting physical phenomena occurring close to the vehicle. For waveriders presented in open literature the L/D ratio is typically over *3.0* and sometimes over *4.0*, in comparison to these values this vehicle's performance might seem poor at first glance. It must be noted though that these waveriders are simulated at much lower altitudes where air is denser, a fact that, has a major impact on the L/D ratio.

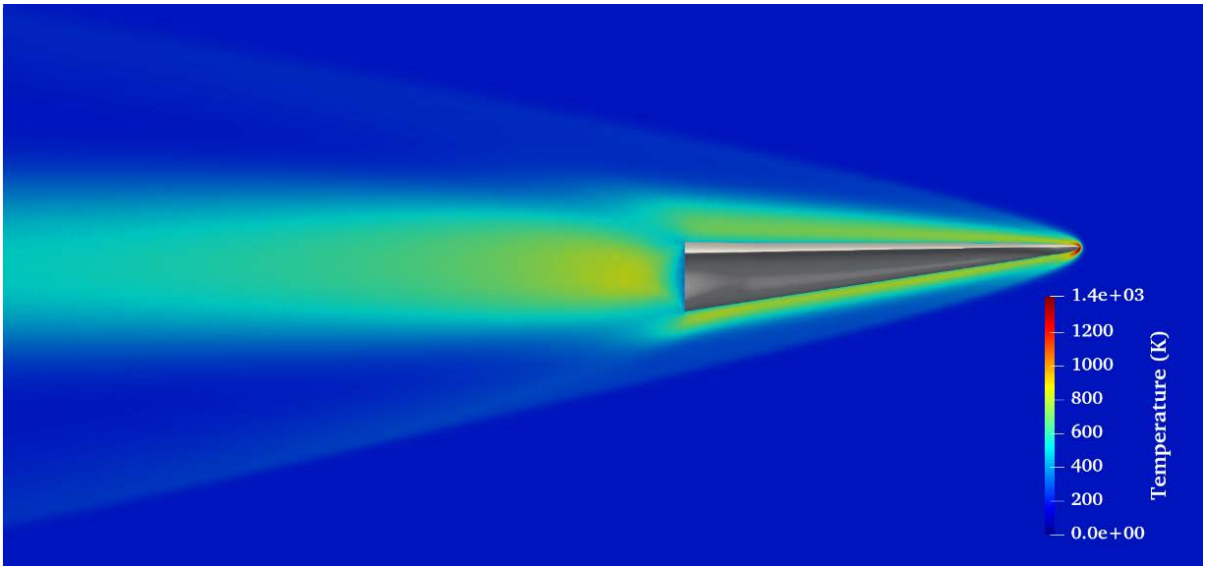

***Figure 3.131**. Temperature field on the symmetry plane.*

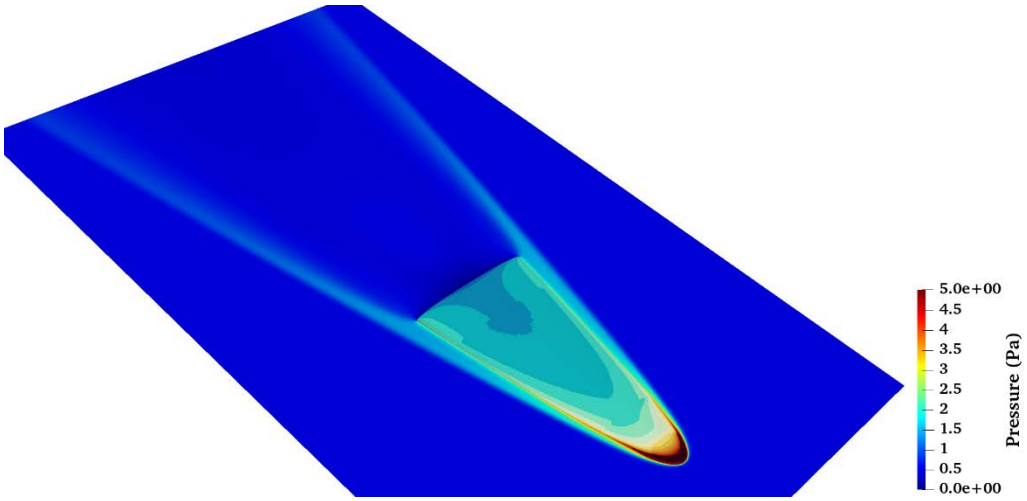

***Figure 3.132**. Pressure on a plane parallel to the vehicle (Surface is colored by the surface pressure).*

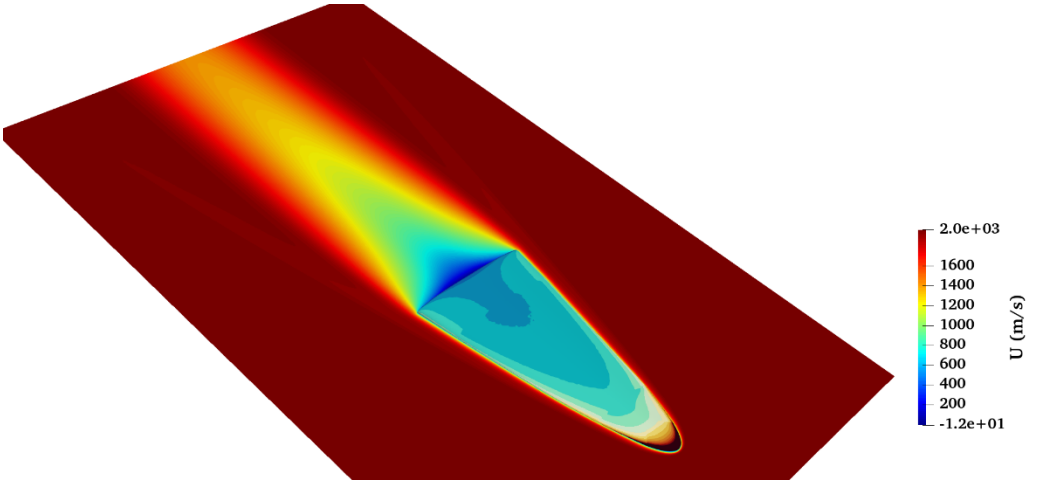

***Figure 3.133**. Streamwise velocity on a plane parallel to the vehicle (Surface is colored by the surface pressure).*

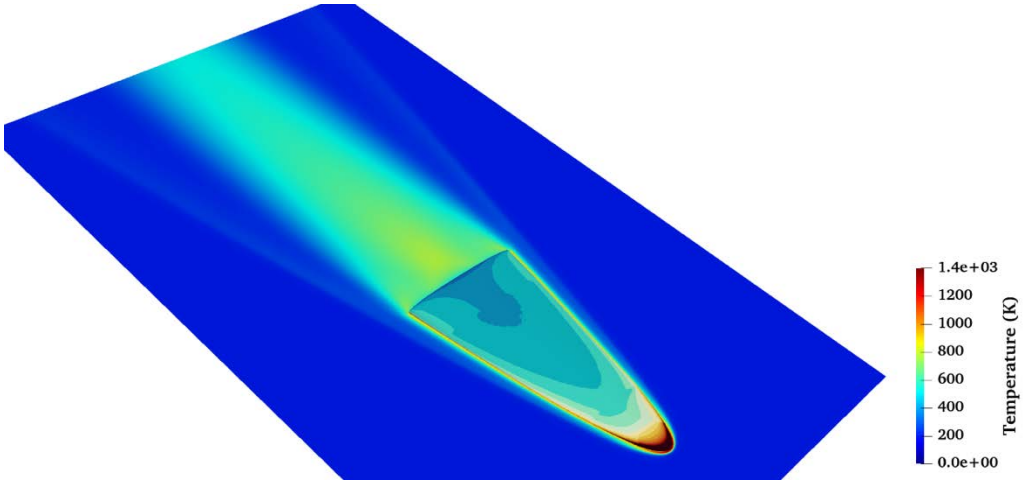

***Figure 3.134**. Temperature on a plane parallel to the vehicle (Surface is colored by the surface pressure).*

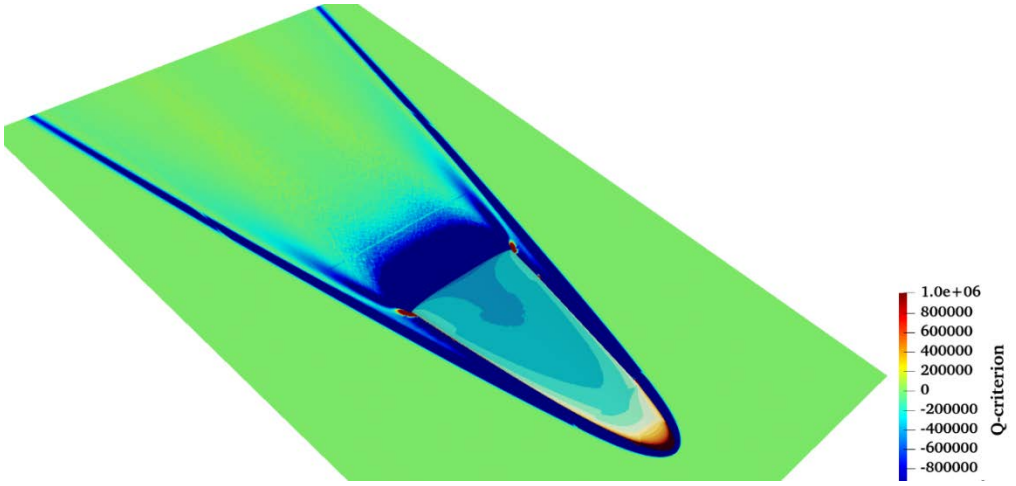

***Figure 3.135**. Q-criterion on a plane parallel to the vehicle (Surface is colored by the surface pressure).*

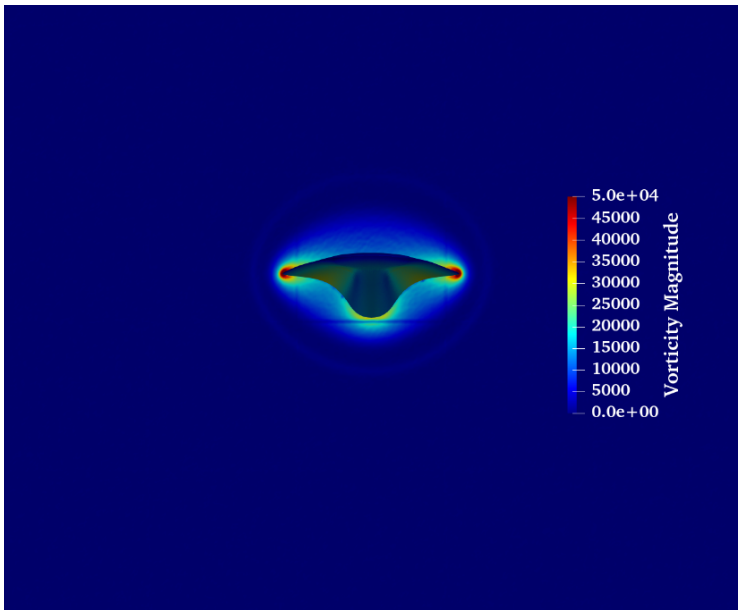

***Figure 3.136**. Vorticity magnitude on a plane normal to the vehicle's first section (Surface is colored by the lifting force).*

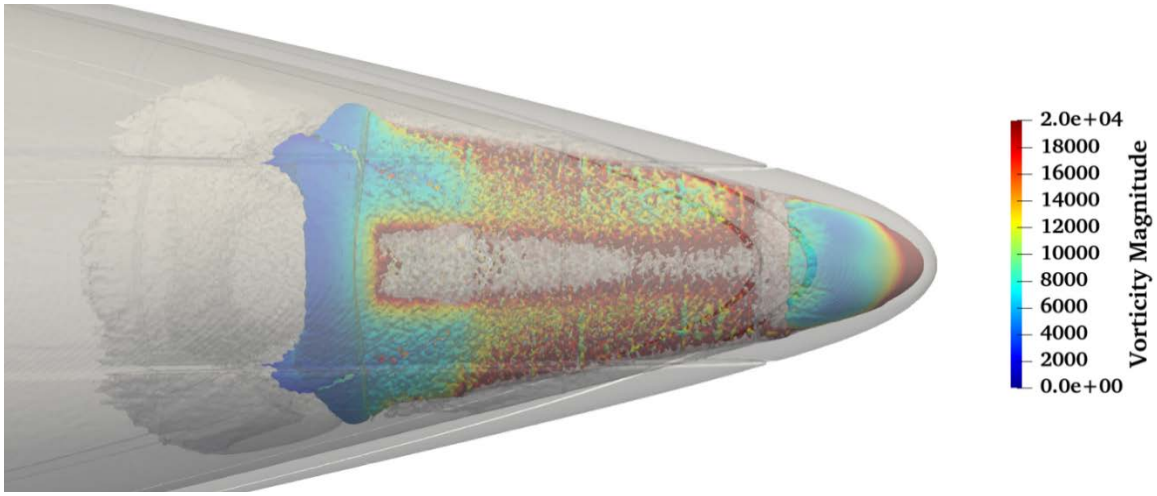

***Figure 3.137**. Three-dimensional Q-criterion contours colored by vorticity magnitude.*

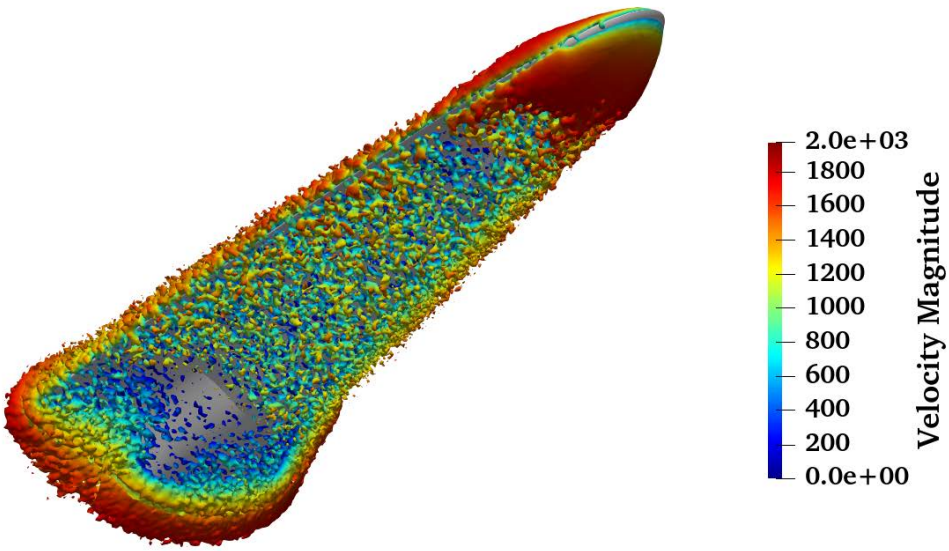

***Figure 3.138**. Overview of the three-dimensional Q-criterion contours around the vehicle colored by velocity magnitude.*

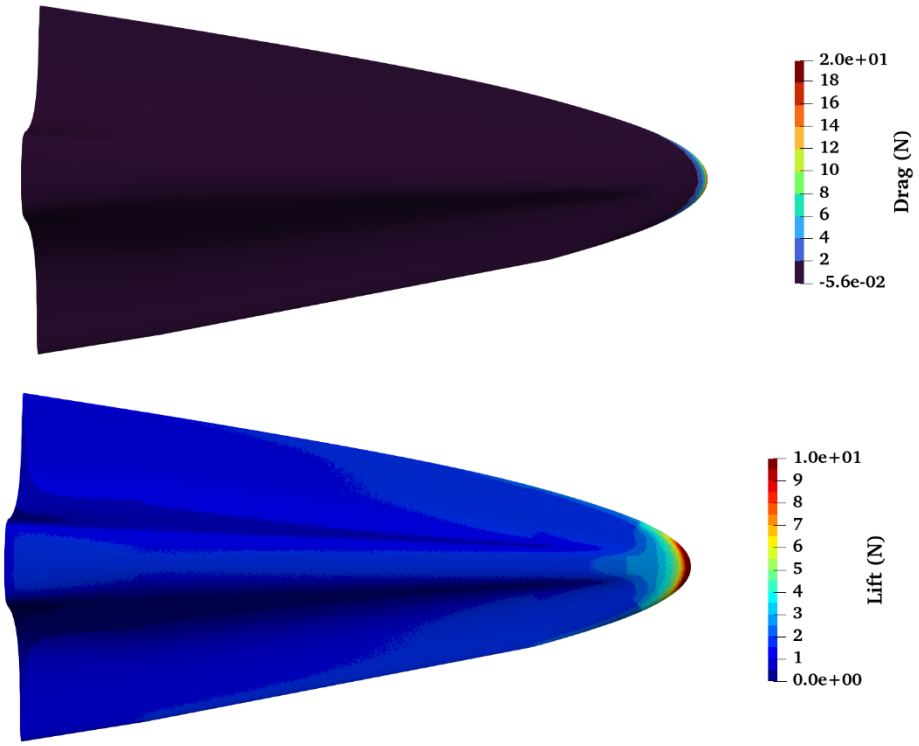

***Figure 3.139**. Overview of the lift (bottom) and drag (top) exerted on the waverider's surface.*

“Intentionally left blank”

4. Conclusions

4.1 Summary

In this thesis a two-fold objective has been reported. Firstly, the simulation of low-density high altitude hypersonic flows with a modified version of the in-house developed N-S solver *Galatea* and comparison of the solutions obtained from the DSMC method and secondly analysis of hypersonic base flows using linear stability analysis theory (LST) has been reported. Comparisons also have been made between chemically reacting and non-chemically reacting flows. For the representation of the computational domains for the *Galatea* solver, three-dimensional unstructured grids have been used, whereas cartesian grids with different levels of refinement are employed for the SPARTA DSMC solver. The unstructured grids have tetrahedral, prismatic and pyramidical elements mainly to resolve effectively the severe anisotropy of boundary layers in viscous flows. The Cartesian grids on the other hand, have mainly cubical elements and triangular prismatic elements in locations where the surfaces cut the computational grid.

In the numerical results for the rarefied gas cases obtained with the *Galatea* solver the RANS PDE's implementation of the code was used without any turbulence models and the results were compared against those obtained by the DSMC method which is the dominant method for solving rarefied gas flows. From all the implemented slope limiters in *Galatea* solver the Van Albada-Van Leer and Min-Mod were used as both yielded the most accurate results by limiting sufficiently numerical diffusion and because of their smoothing abilities. As aforementioned in section *2* the Navier-Stokes equations cannot simulate rarefied gas flows without appropriate boundary conditions. Velocity slip and temperature jump boundary conditions [Bes96, Bes99, Kar02], first order and second order accurate, were implemented to *Galatea* in order to enhance the solver's ability to simulate rarefied gas flows. It was shown that the code was able to simulate flows with Knudsen numbers well into the slip regime. In the cases examined in this work, no significant difference was evidenced between the first order and second order accurate methods. This can be attributed to the very fine grids used in the simulations. Very good agreement has been shown between the solutions obtained from the modified Navier-Stokes implementation and the DSMC method and experimental results, whenever the latter when available. In order to simulate complex geometries a normalization coefficient had to be introduced in the implemented models to allow to reduce residual oscillations during the initial timesteps and to allow for the gradual increase of the velocity slip and temperature jump values.

Furthermore, the ability of the DSMC method to produce high quality flows suitable for stability analysis has also been reported. Stability analysis requires at least eight-digits convergence in order to produce an accurate result. Despite the fact that DSMC is a stochastic statistical method for the simulation of rarefied gas flows, in this work, has been reported that with a careful treatment of the grid and the simulation parameters DSMC can provide, although not eight-digit convergence, highly resolved base flows for stability analysis comparable to those obtained by solving the N-S equations. The boundary layer has been fully resolved and perturbations inside the boundary layer have been measured and found to match those predicted by the LST theory.

In the first case presented a simple hypersonic flow over a NACA 0012 wing at 0^o and 10^o angle of attack is calculated. The flow was simulated with *Galatea* first and the results obtained

are compared with those obtained from SPARTA and the DSMC method and are also compared against experimental results found in the open literature and obtained by Shoja-Seni. In this case the second order accurate model used didn't produce better results than the first order. In addition, the implemented normalization scheme [Fer13] was revealed a considerable enhancement, as the Dirichlet-type of the slip/jump boundary conditions was found to cause excessive oscillations without it, especially during the initial steps of the iterative solution procedure.

To investigate our implementation in more complex geometries a complex re-entry vehicle geometry was selected, designed by the Azim UTBM team. In this case improved accuracy on solid surfaces is obtained with the second-order accurate slip scheme of Beskok and Karniadakis [Bes99, Kar02]. In particular, two test cases have been examined, with their differences focusing on the employed Mach numbers and angles of attack. Due to the absence of any experimental or computational data for this test case, the assessment of *Galatea* solver in terms of accuracy was performed with a the DSMC solver SPARTA. Both solvers produced very close results, despite they are based on two completely different computational approaches. Though no significant differences are identified between the first- and second-order accurate slip models, the latter one appeared to be slightly more accurate, especially in the leading-edge region. The same geometry but at a larger Mach number and a different angle of attack (30^o instead of 40^o) was ran using the DSMC method. By extracting three-dimensional snapshots of the full flow field and using a data-driven stability analysis technique, two flow modes have been revealed. The first mode part of it relies below the vehicle and another part over the wing. The second is located in the wake. The part of the first mode located above the wing creates a massive stationary vortex above the vehicle while the second mode creates an interacting complicated vortex system within the wake.

Before running three-dimensional simulations, the ability of the DSMC to provide highly resolved flows was checked by analyzing two-dimensional flows over flat plates. To this end simulations of flat plates in different Mach numbers have been presented and the results obtained were compared against an analytical solution of the boundary layer. Good agreement has been obtained not only for the boundary layer properties and thicknesses but also for the amplitude functions. DSMC was able to capture very accurately the amplitude functions of velocity and pressure and also the flow spectra. The generalized inflection point of the DSMC implementation was identical to the one calculated in the analytical solution. In addition, smoothing of the DSMC data by a Stack Autoencoder Neural Network (SANN) has been demonstrated. The neural network smoothing didn't alter the eigenvalue spectra; thus, it is proven that smoothing of DSMC data using SANN networks can provide data for a reliable stability analysis.

Apart from the two-dimensional simulations the ability of DSMC and the solver SPARTA used herein to provide highly resolved three-dimensional results is also demonstrated. A three-dimensional non-reacting flow over a cylindrical roughness element was first the first to be studied to that end. This specific geometry was selected due to complex physical phenomena occurring due to the present of a roughness element in a hypersonic flow. The simulation of this case revealed two shocks in the flow field. One due to the leading-edge of the flat plate and a second conical shock was found. The presence of the conical shock is attributed to the roughness element. Stability analysis conducted in a plane behind the roughness element revealed a complicated flow structure comprising of the shock layer, a separated shear layer with a mushroom-like structure and a vortex. Contribution of the shock layer to the least stable

global flow eigenmode was seen in all eigenfunctions. The vortex contribution was seen in all eigenflowfields as well but was clearly picking in the $\hat{u}$ velocity component eigenfunction while the number density shows the lift-up of the boundary layer due to the horseshoe vortex. The mushroom-like structure was very faint in the $\hat{u}$ and $\hat{w}$ velocity components while being very prominent in the $\hat{v}$ component. Further analysis of this structure using two different data-driven techniques was employed in order to confirm the aforementioned conclusions but also revealed that a discrepancy between the DMD and the Residuals Algorithm (RA) in the streamwise velocity U. This discrepancy can be attributed to the fact that DMD is sensitive to the number of snapshots acquired in order to converge. In this case although *100* time-accurate snapshots have been used in the DMD analysis we conclude that more were needed in order to capture the dynamics of the streamwise velocity accurately in comparison with the RA.

Enabling chemical reactions for the aforementioned flow and moving the roughness element closer to the leading-edge of the flat plate, in order to enforce a shock-shock interaction revealed interesting physical phenomena occurring in the flow field. Chemistry caused a sustainable flow oscillation not only around the roughness element area but also downstream. This means that the flow oscillation beginning in front of the roughness element, propagates further downstream. By examining the probe data, it was found that the amplitude of the oscillation in front of the roughness element is about *20* times larger than the amplitude downstream. This verifies that the source of the oscillation is located within the interaction region of the two shocks. Although the oscillation decreases in amplitude downstream it's still maintained. By applying FFT to the probe data the frequency of the oscillation was measured and found to be equal to *34.20 kHz*, both in front and downstream of the roughness element.

Due to the inability of N-S equations to fully analyze the internal structure of a shock, DSMC was applied to a portion of a cone with a swept fin in order to quantify any physical phenomena not captured by an N-S solver. To that end, the inflow plane taken from the solution of the flow field with an N-S solver was used to initialize DSMC at the area of interest. Despite the fact that the inflow was provided by another method, SPARTA was able to calculate the flow field accurately. Through the whole flow field excellent agreement was found between the two methods. Although the computational field of the DSMC was much smaller than the one used in the N-S solution, due to the high pressure and the flow three-dimensionality more than *20%* of the UK national supercomputer was required for this calculation. The same geometry was also run in a 2d axisymmetric configuration with pressure about 4 times more than the pressure used in the three-dimensional configuration. Again, very good agreement in the extracted flow profiles was evidenced.

Finally, an attempt has been made in this work to design a Mach 7 waverider. The well documented in open literature method of the osculating cones was used in order to extract the geometry profile of the waverider. Firstly, the three-dimensional flow field around a 7-degree cone with a blunt leading edge was calculated. Secondly, by extracting the flow streamlines in different planes the exact shock profile and location was found. Thirdly, by using the streamline data the profiles of the waverider surfaces were designed. After simulating the calculated waverider geometry the lift/drag ratio was calculated and was equal to *2.18*. A lift/drag of *2.18* seems to be small with lift/drag ratios found in open literature, but in the case studied in this work the flow conditions were set equal to the conditions occurring at *90 km* altitude where air is very rarefied, while the waveriders found in literature are simulated with flow conditions occurring at *25-40 km* altitudes. Despite this fact, a lift/drag of *2.18* demonstrates that the vehicle is capable of flying at the examined rarefied conditions. A close examination of the

simulation data also revealed that for the on-design conditions examined the shock wave is fully attached at the tip and the leading-edges of the vehicle.

4.2 Contributions

Considering similar studies available in the literature, the following original contributions have been introduced in this thesis:

- **An enhancement of an in-house developed three-dimensional N-S solver with velocity slip and temperature jump boundary conditions.** At the time of modifying the aforementioned solver only two-dimensional analytical implementations of the velocity slip and temperature jump boundary conditions described were found in the literature. A three-dimensional implementation was not straightforward due to numerical difficulties introduced by the complex geometries examined. A methodology of how to counter this shortcoming has been presented and results were compared with those obtained from the DSMC method. A very good has been evidenced for all simulated cases.

- **The ability of the DSMC method to provide high quality flows for stability analysis has been demonstrated.** A notable contribution of this thesis concerns the capability of DSMC to provide base flows for stability analysis. Despite the statistical nature of DSMC and the underlying statistical fluctuations it has been shown in this work that the method is capable to produce highly accurate base flows for stability analysis. Different approaches on how to limit the statistical noise documented and comparisons have been made with smoothed and unsmoothed data. To the authors knowledge, it's also the first time the ability of a Stack Autoencoder Neural Network to smooth flow data is presented. Base flows provided by the DSMC method were also used in data-driven stability analysis methods and revealed interesting physical phenomena for the geometries examined in this thesis.

- **Velocity distribution functions inside shocks were documented.** Due to the ability of the DSMC to fully analyze the internal structure of shock waves, velocity distribution functions of the particles inside shocks were calculated. It was found that inside a shock wave or in highly non-equilibrium areas the fluid particles don't follow the well-known Maxwellian distribution but their velocities approach a bimodal distribution.
- **Shock-shock interaction with and without chemistry and the resulting flow oscillations have been quantified.** A Mach *10* flow around a roughness element has been studied and was shown that by taking into account the chemical reactions occurring at the examined conditions flow oscillations originating from a shock-shock interaction can be maintained and propagate downstream. The dominant frequency of the oscillation was measured by applying FFT to the simulation data

and was found to be close with the frequency of oscillations inside shocks found in the literature [Saw21].

- **The influence of a cylindrical roughness element in a Mach 6 flow was investigated.** The influence of a cylindrical roughness element embedded in the boundary layer of a hypersonic Mach 6 flow was studied. In this test case several flow planes behind the roughness element were extracted and a structure comprising of 2 vortex pairs was revealed behind the roughness element. Furthermore, for the examined flow conditions a curved shock was generated from the roughness element although it was inside the boundary layer. The aforementioned flow structure was growing downstream and its growth was defined by the shock location at each examined flow plane. Stability analysis was conducted to the plane closer to the roughness element and the different parts of the structure were analyzed and their contribution to the flow eigenfunctions was quantified.

- **Data-driven stability analysis techniques are applied to three-dimensional DSMC data.** By using a complex re-entry vehicle geometry and flow conditions occurring at *90 km* altitude DMD has been applied to three-dimensional DSMC data. The data were collected during a DSMC run, but were not averaged, and then fed to a DMD code in order to reveal any underlying three-dimensional structures that could lead to transition. The results were also analyzed using the residuals algorithm and compared with the DMD method. It was found that in that flow two modes existed one below the surface of the vehicle and one in the wake of the vehicle.

- **A Mach 7 waverider has been designed and simulated in highly rarefied flow conditions.** In this thesis the design methodology of a Mach 7 waverider operating at *90 km* altitude has been presented. Unlike other waverider configurations found in literature this specific waverider was designed for high altitude flight in rarefied atmosphere. Despite the rarefied environment the proposed geometry has a lift to drag ratio of *2.18* which is similar to waveriders designed for lower altitudes and dense environments.

4.3 Future work

Besides the previously described work, future extension of the presented cases includes the following:

- Examine different shapes of roughness elements and quantifying the impact each different shape has to the flow.

- Examine the impact of the location of the roughness element and the shock-shock interactions of the flow field.

- Compare different chemical models and quantifying the impact each chemical model has to the stability of the flow.

- Study the impact of chemistry to the flow stability in different geometry configurations such as cylinders and spheres.

- Simulate the proposed waverider configuration in off-design conditions and examine the ability of the vehicle to fly at velocities that are different than the ones taken into account during the design phase.

- Coupling the geometries of waveriders designed at different conditions to a single vehicle geometry and study the aerodynamic characteristics of the hybrid vehicle.

“Intentionally left blank”

5. References

[Abb49] Abbott I.H., and Doenhoff A.E., Theory of wing sections, *Dover Publications Inc*, New York, 1949.

[All85] Allegre J., Raffin M., and Lengrand J.C., Experimental flow fields around NACA0012 airfoils located in subsonic and supersonic rarefied air streams, *M.O. Bristeau et al. (eds.), Numerical Simulation of Compressible Navier-Stokes Flows*, pp. 5968, 1985.

[And06] Anderson J.J., Hypersonic and high temperature gas dynamics", Second Edition: *AIAA*, 2006.

[And77] Anderson J.J. and Bonhaus D.L., HYENA—a computer program for hypersonic viscous flow calculations, *AIAA Journal*, vol. 15(5), pp. 711-717, 1977.

[And94] Anderson W.K., and Bonhaus D.L., An Implicit Algorithm for Computing Turbulent Flows on Unstructured Grids, Computers & Fluids, vol. 23, pp. 1-21, 1994.

[Bar89] Baeza A., Castro C., Palacios F. and Zuazua E., 2D Euler Shape Design on Non-Regular Flows Using Adjoint Rankine-Hugoniot Relations, *AIAA Journal*, vol. 47, pp. 552-562, 2009.

[Bar92] Barth T.J., Aspects of unstructured grids and finite-volume solvers for the Euler and Navier-Stokes equations, *Proceedings of the AGARD-FDP-VKI special course at VKI*, AGARD-R-787, pp. 6.1-6.61, Rhode-Saint-Genese 2-6 March 1992.

[Bag90] Baganoff D., and McDonald J.D., A collision-selection rule for a particle simulation method suited to vector computers, *Physics of fluids*, pp.1248-1259, July 1990.

[Bes15] Beskok A. and Karniadakis G.E., A model for flows in channels, pipes, and ducts at micro and nano scales, *Microscale Thermophysical Engineering*, vol. 3, pp. 43-77, 1999.

[Bes96] Beskok A., Karniadakis G.E., and Trimmer W., Rarefaction and compressibility effects in gas microflows, *Journal of Fluids Engineering*, vol 118(3), pp 448–456, 1996.

[Bes99] Beskok A., and Karniadakis G.E., A model for flows in channels, pipes and ducts at micro and nano scales, *Microscale Thermophysical Engineering*, vol. 3, pp. 43-77, 1999.

[Beh71] Behrens W., and Ko DR., Experimental stability studies in wakes of two-dimensional slender bodies at hypersonic speeds, *AIAA Journal*, 9(5), pp 851-857, 1971.

[Ber98] Bertolotti F.P., The influence of rotational and vibrational energy relaxation on boundary-layer stability, *Journal of Fluid Mechanics*, vol 372, pp 93–118, 1998.

[Bha54] Bhatnagar P. L., Gross E. P., and Krook M., A model for collision processes in gases. I. Small amplitude processes in charged and neutral one-component systems, *Physical review*, vol. 94(3), pp. 511, 1954.

[Bir05] Bird G.A., The DS2V/3B program suite for DSMC calculations, *AIP Conference Proceedings,* vol. 762. pp. 541-546, 2005.

[Bir09] Bird G.A., Gallis M.A., Torczynski J.R., Rader D.J., Accuracy and efficiency of the sophisticated direct simulation Monte Carlo algorithm, *Physics of fluids,* vol. 21(1), 2009.

[Bir63] Bird G. A., Approach to translational equilibrium in a rarefied gas. *Physics of Fluids*, vol. 6(11), pp. 1518-1529, 1963.

[Bir76] Bird G.A., Molecular gas dynamics, *Oxford University Press,* Oxford UK, 1976.

[Bir94] Bird G.A., Molecular gas dynamics and the direct simulation of gas flows, *Clarendon Press*, Oxford, 1994.

[Bir13] Bird G.A., The DSMC method, version 1.2; 2013. ISBN: 9781492112907.

[Bla01] Blazek J., Computational Fluid Dynamics: Principles and Applications, *Kidlington: Elsevier Science*, 2001.

[Bla03] Blankson I. M., and Schneider S., Hypersonic Engine Using MHD Energy Bypass with a Conventional Turbojet, *AIAA International Space Planes and Hypersonic Systems and Technologies*, 2003.

[Bla94] Blanchard R., Larman K., and Moats C., Rarefied-flow shuttle aerodynamics flight model, *Journal of Spacecraft and Rockets*, vol. 31(4), pp. 550-556, 1994.

[Bow01] Bowcutt K.G., Multidisciplinary optimization of airbreathing hypersonic vehicles, *Journal of Propulsion and Power*, vol. 17(6), pp.1184-1190, 2001.

[Boy07] Boyd I.D., Modeling of associative ionization reactions in hypersonic rarefied flows, Journal of Physics of Fluids, vol. 19 (9), 2007.

[Boy10] Boyd I.D., Trumble K.A., and Wright M.J., Modeling of the stardust at high altitude, part 1: flowfield analysis, *Journal of Spacecraft and Rockets*, vol. 47, pp. 708-717, 2010.

[Boy10a] Boyd I.D., and Jenniskens P.M., Modeling of the stardust at high altitude, part 2: radiation analysis, *Journal of Spacecraft and Rockets*, vol. 47, pp. 901-909, 2010.

[Boy95] Boyd I.D., Candler G.V., and Levin D.A., Dissociation modeling in low density hypersonic flows of air, *Journal of Physics of Fluids*, vol. 7 (7), pp. 1757-1763, 1995.

[Boy97] Boyd I.D., Bose D., and Candler G.V., Monte Carlo modelling of nitric oxide formation based on quasi-classical trajectory calculations, *Journal of Physics of Fluids*, vol. 9 (4), pp. 1162-1170, 1997.

[Bur09] Burt J.M., and Boyd I.D., A hybrid particle approach for continuum and rarefied flow simulation, *Journal of Computational Physics*, vol. 228(2), pp. 460-475, 2009.

[Bur12] Burt J.M., Josyula E., and Boyd I.D., Novel Cartesian implementation of the direct simulation Monte Carlo method, Journal of Thermophysics and Heat Transfer, vol. 26(2), pp 258-270, 2012.

[Buy80] Byers R.V., and Hughes W.F., Theoretical and computational studies of hypersonic flowfields, *Annual Review of Fluid Mechanics*, vol. 12(1), pp. 61-94, 1980.

[Can93] Candler G.V., Boyd I.D., and Levin D.A., Continuum and DSMC analysis of bow shock flight experiments, *AIAA 31st Aerospace Sciences meeting*, paper 1993-0275, 1993.

[Ced02] Cédric V., A review of mathematical topics in collisional kinetic theory, *Handbook of mathematical fluid dynamics*, vol. 1, pp. 71–305, North-Holland, Amsterdam, 2002.

[Cer02] Cercignani C., The Boltzmann equation and fluid dynamics, *Handbook of mathematical fluid dynamics*, vol. 1, pp. 1–69, North-Holland, Amsterdam, 2002.

[Cer71] Cercignani C., and Lampis M., Kinetic models for gas-surface interactions, *Transport theory and statistical physics*, vol. 1, pp. 101-114, 1971.

[Cha61] Chambre P. A., and Schaaf S. A., Flow of rarefied gases, *Princeton Aeronautical Paperbacks, Princeton Legacy Library*, 1961.

[Che11] Chen X. Q., Hou Z. X., Liu J. X., and Gao, X. Z., Bluntness impact on performance of waverider, *Computers & Fluids*, vol. 48(1), pp. 30-43, 2011.

[Che12] Chen K.K., Tu J. H., and Rowley C. W., Variants of dynamic mode decomposition: boundary condition, Koopman, and Fourier analyses, *Journal of nonlinear science*, vol. 22(8), pp. 887–915, 2012.

[Cla05] Clavis Z., Wilmoth R.G., Plume modeling and application to Mars 2001 Odyssey aerobraking, *Journal of Spacecraft and Rockets*, vol. 42, pp. 450-456, 2005.

[Coc94] Cockrell Jr. C. E., Interpretation of waverider performance data using computational fluid dynamics, *Journal of aircraft*, vol. 31(5), pp 1095-1100, 1994.

[Cor88] Corda S., and Anderson J. Jr., Viscous optimized hypersonic waveriders designed from axisymmetric flow fields, *In 26th aerospace sciences meeting*, pp. 369, 1988.

[Cri03] Criminale W.O., Jackson T.L. and Joslin R.D.: Theory and Computation of Hydrodynamic Stability, *Cambridge University Press*, 2003.

[Del11] Delis A.I., Nikolos I.K. and Kazolea M., Performance and Comparison of Cell-Centered and Node-Centered Unstructured Finite Volume Discretizations for Shallow Water Free Surface Flows, *Archives of Computational Methods in Engineering*, vol. 18, pp. 57-118, 2011.

[Des08] Deschenes T.R., Alkandry H., and Boyd I.D., Application of a modular particle-continuum method to hypersonic propulsive decelaration, *42nd AIAA Thermophysics Conference*, paper 2008-3137, 2008.

[Des11] Deschenes T.R., Holman T.D.., and Boyd I.D., Effects of rotational energy relaxation on a modular particle-continuum method, *Journal of thermophysics and heat transfe*, vol. 25(2), pp. 218-227, 2011.

[Don09] Dongari N., Sambasivam R., and F. Durst, Extended Navier-Stokes equations and treatments of micro-channel gas flows, *Journal of Fluid Science and Technology*, vol. 4, pp. 454-467, 2009.

[Elm95] Elmendorf M. D., Dumas G. R., and Rausch R. D., Overview of the development and applications of the NASA-DFRC Navier-Stokes and Parabolized Navier-Stokes analysis capability, *In 33rd Aerospace Sciences Meeting and Exhibit*, p. 213, 1995.

[Erd94] Erdman P.W., Zipf E.C., Espy P., Howlett C.L., Levin D.A., and Collins R.J., Measurements of ultraviolet radiation from a 5-km/sec bow shock, *Journal of Thermophysics and Heat Transfer*, vol. 8, pp. 441-446, 1994.

[Eva92] Evans A., Marchant M.J., Weatherill N.P., Szmelter J. and Natakusumah D.K., A Point Enrichment Strategy for Polygonal Volume Meshes, *Applied Mathematical Modelling*, vol. 16, pp. 562-575, 1992.

[Fan01] Fan J., Boyd I.D., Cai C.P., Hennighausen K. and Candler G.V., Computation of rarefied gas flows around a NACA 0012 airfoil, *AIAA Journal*, vol. 39, pp. 618-625, 2001.

[Fer13] Ferras W.L., Nobregal J.M., and Pinho F.T, Implementation of slip boundary conditions in the finite volume method: new techniques, *International Journal for Numerical Methods in Fluids*, vol. 72, pp. 724-747, 2013.

[Flo63] Flower J. W., Configurations for high supersonic speeds derived from simple shockwaves and expansions, *Royal Aeronautical Society Journal*, vol. 67, pp. 287-290, 1963.

[Gad99] Gad-el-Hak M., The fluid mechanics of microdevices. The Freeman scholar lecture, *ASME Journal of Fluids Engineering*, vol. 121, pp. 5-33, 1999.

[Gal05] Gallis M.A., Boyles K.A., LeBeau G.J., DSMC simulations in support of the STS-107 accident investigation, *AIP conference proceedings*, vol. 762, p1211-1216, 2005

[Gal09] Gallis M.A., Torczynski, J.R., and Rader D.J., Convergence behavior of a new DSMC algorithm, *Journal of Computational Physics*, vol. 228, pp. 4532-4548, 2009.

[Gal11] Gallis M.A, and Torczynski, J.R., Effect of collision-partner selection schemes on the accuracy and efficiency of the direct simulation monte Carlo method, *International Journal of Numerical Methods in Fluids*, vol 67(8), pp 1057–1072, 2011.

[Gal14] Gallis M.A., Torczynski J.R., Plimpton S.J., Rader D.J., and Koehler T., Direct Simulation Monte Carlo: The quest for speed, *Proceedings of the 29th Rarefied Gas Dynamics (RGD) Symposium*, Xi'an, China, July 2014.

[Gal15] Gallis M.A., Koehler T.P., Torczynski J.R. and Plimpton S.J., Direct simulation Monte Carlo investigation of the Richtmyer-Meshkov instability, *Physics of Fluids*, vol. 27(8), p. 08410, 2015.

[Gal16] Gallis M.A., Koehler T.P., Torczynski J.R. and Plimpton S.J., Direct simulation Monte Carlo investigation of hydrodynamic instabilities in gases, *In AIP Conference Proceedings*, vol. 1786(1), p. 050002, 2016.

[Gal16a] Gallis M.A., Koehler T.P., Torczynski J.R. and Plimpton S.J., Direct simulation Monte Carlo investigation of the Rayleigh-Taylor instability, *Physical Review Fluids*, vol. 1(4), p. 043403, 2016.

[Gal17] Gallis M.A., Bitter N., Koehler T., Torczynski J.R., Plimpton S.J., and Papadakis G., DSMC simulations of turbulent energy decay in the Taylor–Green vortex flow, *Tech Max79nical report*, Sandia National Laboratories (SNL-NM), Albuquerque NM, 2017.

[Gal17a] Gallis M.A., Bitter N.P., Koehler T.P., Torczynski J.R., Plimpton S. J., and Papadakis G., Molecular-level simulations of turbulence and its decay, *Physical review letters*, vol. 6, p. 118, 2017.

[Gal18] Gallis M.A., Torczynski J.R., Bitter N.P., Koehler T.P., Plimpton S.J., and Papadakis G., Gas-kinetic simulation of sustained turbulence in minimal Couette flow, *Physical Review Fluids*, vol. 3(7), p. 071402, 2018.

[Gal20] Gallis M.A., Bitter N.P., and Torczynski J.R., DSMC simulations of Compressible Turbulence, Sandia National Lab. (SNL-NM), *No. SAND2020-0072C*. Albuquerque, NM (United States), 2020.

[Gal21] Gallis M.A., Torczynski J.R, Krygier M.C., Bitter N.P., and Plimpton S. J., Turbulence at the edge of continuum, *Physical Review Fluids*, vol. 6(1), 2021.

[Gar86] Garcia, A.L., Nonequilibrium fluctuations studied by a rarefied-gas simulation, *Physical review A*, vol. 31(2), pp. 1454-1457, 1986,

[Gar87] Garcia A.L., Malek M.M., Lie, G.C., Mareschal, M., and Clementi E., Hydrodynamic fluctuations in a dilute gas under shear, *Physical Review A*, vol. 36(9), 4348-4355, 1987.

[Gar90] Garcia A.L., Hydrodynamic fluctuations and the direct simulation Monte Carlo method, *Microscopic simulations of complex flows*, Springer, pp. 177-188, 1990.

[Gim19] Gimelshein, S. F., and Wysong, I. J., Nonequilibrium Air Flow Predictions with a High-Fidelity Direct Simulation Monte Carlo Approach, *Physical Review Fluids*, vol. 4(3), paper 033405, 2019.

[Gra70] Grantham W.L., Flight results of a 25,000 foot per second reentry experiment using microwave reflectometers to measure plasma electron density and standoff distance, *NASA technical note* D-6062, 1970.

[Gre00] Greenblatt D., and Wygnanski I., The control of flow separation by periodic excitation, *Progress in Aerospace Sciences*, vol 36, pp 487–545, 2000.

[Haa94] Haas B.L., Hash D.B., Bird G.A., Lumpkin III F.E., and Hassan H.A., Rates of thermal relaxation in direct simulation Monte Carlo methods. *Physics of Fluids*, vol. 6(6), 2191-2201, 1994.

[Has96] Hash D.B., and Hassan H.A., Assessment of schemes for coupling Monte Carlo and Navier-Stokes solution methods, *Journal of Thermophysics and Heat Transfer*, vol 10(2), pp. 242-249, 1996.

[Hass96] Hassan H.A., and Hash D.B., A decoupled DSMC/Navier-Stokes analysis of a traditional flow experiment, *In 34th AIAA aerospace sciences meeting and exhibit*, paper 96-0353, Reno, 1996.

[Het08] Hettiarachchi H. M., Golubovic M., Worek W. M., and Minkowycz W. J., Three-dimensional laminar slip-flow and heat transfer in a rectangular microchannel with constant wall temperature. *International Journal of Heat and Mass Transfer*, vol. 51:(21-22), pp. 5088-5096, 2008.

[Hir90] Hirsch C., Numerical computation of internal and external flows, vol. 2: Computational methods for inviscid and viscous flows, *John Wiley and Sons*, New York, 1990.

[Ho98] Ho C.M., and Tai Y.C., Micro-electro-mechanical- systems (MEMS) and fluid flows, *Annual Review of Fluid Mechanics*, vol. 30, pp. 579-612, 1998.

[Hol01] Holden M., and Wadhams T., Code validation study of laminar shock/boundary layer and shock/shock interactions in hypersonic flow. Part A: experimental measurements, AIAA, paper 1031, 2001.

[Hol09] Holman T.D., and Boyd I.D., Effects of continuum breakdown on the surface properties of a hypersonic sphere, *Journal of Thermophysics and Heat Transfer*, vol. 23(4), pp. 660-673, 2009.

[Hua11] Huang W., Ma L., Wang Z., Pourkashanian M., Ingham D.B., Luo S., and Lei J., A parametric study on the aerodynamic characteristics of a hypersonic waverider vehicle, *Acta Astronautica*, vol 69, pp. 135-140, 2011.

[Ill49] Illingworth C.R., Steady flow in the laminar boundary layer of a gas. *Procedures of Royal Society*, vol. A199, pp. 533–558, 1949.

[Jun13] Juniper M.P., Hanifi A., and Theofilis V., Modal stability theory lecture notes from the flow-nordita summer school on advanced instability methods for complex flows, *Applied Mechanics Reviews*, vol. 66(2). Stockholm, Sweden, 2013.

[Kal96] Kallinderis Y., and Baron J.R., A new adaptive algorithm for turbulent flows, *Computers & Fluids*, vol. 21, pp. 77-96, 1992.

[Kan00] Kannenberg K.C., and Boyd I.D., Strategies for efficient particle resolution in the direct simulation Monte Carlo method, *Journal of Computational Physics*, vol. 157 (2), pp. 727-745, 2000.

[Kar02] Karniadakis G.E., and Beskok A., Micro flows: fundamentals and simulation, *Springer*, New York, 2002.

[Kar23] Karpuzcu Irmak T., Matthew P. Jouffray, and Levin D.A., Effect of Oxygen Dissociation on Nitric Oxide Ultraviolet Emissions, *Journal of Thermophysics and Heat Transfer*, vol. 37(1), pp. 147-160, 2023.

[Kaw84] Kawata S., and Minami S.: Adaptive smoothing of spectroscopic data by a linear mean-square estimation, *Applications of Spectroscopy*, vol 38(1), pp 49–58, 1984.

[Kim03] Kim K., Three-Dimensional Hybrid Grid Generator and Unstructured Flow Solver for Compressors and Turbines, *PhD thesis*, Texas A&M University, 2003.

[Klo16] Klothakis A., Lygidakis G.N., and Nikolos I.K., Numerical analysis of rarefied gas flows using the academic CFD code *Galatea*, *Proceedings of the ECCOMAS Conference*, Heraklion, Crete, Greece, 2016.

[Klo17] Klothakis, A. G., Lygidakis, G. N., and Nikolos, I. K., Rarefied gas flow analysis of a suborbital shuttle with the academic CFD code *Galatea, In ASME International Mechanical Engineering Congress and Exposition*, vol. 58349, American Society of Mechanical Engineers, 2017.

[Klo20] Klothakis A., Quintanilha Jr H., Sawant S. S., Protopapadakis E., Theofilis V., and Levin, D. A., On the effect of velocity slip and temperature jump on flat plate boundary layer stability at Mach 4.5. *In APS Division of Fluid Dynamics Meeting Abstracts*, pp. H05-003, 2020.

[Klo21] Klothakis A., Sawant S.S., Quintanilha H.Jr., Theofilis V., and Levin D.A., Slip effects on the stability of supersonic laminar flat plate boundary layer, *AIAA Scitech 2021 Forum*, 2021.

[Klo22] Klothakis A., Quintanilha H. Junior, Sawant S. S., Protopapadakis E., Theofilis V., and Levin D.A., Linear stability analysis of hypersonic boundary layer computed by kinetic approach: a semi-infinite flat plate at $4.5 \leq M_{\infty} \leq 9$, *Theoretical and Computational Fluid Dynamics*, vol. 36, pp. 117-139, 2022.

[Koo00] Koobus B., Farhat C., and Tran H., Computation of Unsteady Viscous Flows around Moving Bodies Using the k-ε Turbulence Model on Unstructured Dynamic Grids, *Computer Methods in Applied Mechanics and Engineering*, vol. 190, pp. 1441-1466, 2000.

[Kou03] Koubogiannis D.G., Athanasiadis A.N., and Giannakoglou K.C., One and Two-equation turbulence models for the prediction of complex cascade flows using unstructured grids, *Computer & Fluids*, vol. 32, pp. 403-430, 2003.

[Kou91] Koura K., and Matsumoto H., Variable soft sphere molecular model for inverse-power-law or Lennard-Jones potential, *Physics of fluids*, vol. A3, pp. 2459-2465, 1991.

[Kou92] Koura K., and Matsumoto H., Variable soft sphere molecular model air species, *Physics of fluids*, vol. A4, pp. 1083-1085, 1992.

[Kre10] Kremer G. M., An introduction to the Boltzmann equation and transport processes in gases, *Springer Berlin Heidelberg*, 2010.

[Kuc78] Kuchemann D., The aerodynamic design of aircraft: a detailed introduction to the current aerodynamic knowledge and practical guide to the solution of aircraft design problems, *Oxford Pergamon Press*, 1978.

[Kum11] Kumar R.E.T., and Levin D.A., Compressible Laminar Boundary-Layer Flows with Statistical Bhatnagar–Gross–Krook Approaches, *Journal of Thermophysics and Heat Transfer*, vol. 24, no. 3, pp. 556–565, 2011.

[Lal88] Lallemand M.H., Etude de Schemas Runge-Kutta a 4 pas pour la Resolution Multigrille des Equations d' Euler 2D, *Raport de Recherche*, INRIA, 1988.

[Lan98] Laney C.B., Computational Gas Dynamics, *Cambridge University Press*, 1998.

[Lar74] Larsen P.S., and Borgnakke C., In rarefied gas dynamics, *DFVLR Press*, paper A7, Porz-Wahn, Germany, 1974.

[Leb03] LeBeau G., Boyles K., and Lumpkin F., Virtual sub-cells for the direct simulation Monte Carlo method, *AIAA paper 2003-1031*, 2003.

[Lee19] Lee M.N., Chen J.H. and Gallis M.A., Kelvin-Helmholtz instability with thermal nonequilibrium, Sandia National Lab. (SNL-CA), *No. SAND2019-11484C*, Livermore CA (United States); Sandia National Lab. (SNL-NM) Albuquerque NM (United States).

[Lev92] Levin D.A., Candler G.V., Collins R.J., Erdman P.W., Zipf E.C., and Howlett C.L., Examination of ultraviolet theory for bow shock rocket experiments-I, *Journal of Thermophysics and Heat Transfer*, *AIAA 27th Thermophysics Conference*, 1992.

[Lev93] Levin D.A., Candler G.V., Collins R.J., Howlett C.L., Espy P., Whiting E., and Pack C., Comparison of theory with atomic oxygen 130.4 nm radiation data from the bow shock ultraviolet 2 rocket flight, *AIAA 28th Thermophysics Conference*, 1993.

[Lin72] Linwood W.L., and Cross A.E., Electrostatic probe measurements of plasma parameters for two reentry flight experiments at 25,000 feet per second, *NASA technical note* D-6617, 1972.

[Lor91] Lord R. G, Some extensions to the Cercignani–Lampis gas–surface scattering kernel, *Physics of Fluids A: Fluid Dynamics*, vol 3, pp. 706-710, 1991.

[Luo05] Luo H., Baum J.D., and Lohner R., High-Reynolds viscous flow computations using an unstructured-grid method, *Journal of Aircraft*, vol. 42, pp. 483-492, 2005.

[Lyg11] Lygidakis G.N. and Nikolos I.K., An Unstructured Node-Centered Finite Volume Method for Computing 3D Viscous Compressible Flows on Hybrid Grids, *Proceedings of the 7th GRACM (Greek Association of Computational Mechanics) International Congress on Computational Mechanics*, Athens, 30 June - 2 July 2011.

[Lyg12] Lygidakis G.N., and Nikolos I.K., Using the finite-volume method and hybrid unstructured meshes to compute radiative heat transfer in 3-D geometries, *Numerical Heat Transfer Part B: Fundamentals*, vol. 62, pp. 289-314, 2012.

[Lyg13] Lygidakis G.N., and Nikolos I.K., Evaluating a parallel node-centered finite-volume algorithm, named Galatea, in simulation of 3D compressible flows, *Proceedings of the 10th HSTAM (Hellenic Society for Theoretical and Applied Mechanics) International Congress on Mechanics*, Chania, Crete, Greece, 2013.

[Lyg13a] Lygidakis G.N., and Nikolos I.K., Using a high-order spatial/temporal scheme and grid adaption with a finite-volume method for radiative heat transfer, *Numerical Heat Transfer Part B: Fundamentals*, vol. 64, pp. 89-117, 2013.

[Lyg14] Lygidakis G.N., and Nikolos I.K., Assessment of the Academic CFD Code "Galatea" Using the NASA Common Research Model (CRM), *Proceedings of the 12th Biennial Conference on Engineering Systems Design and Analysis, ASME-ESDA2014*, Copenhagen, Denmark, 25-27 June 2014, ESDA2014- 20265.

[Lyg14a] Lygidakis G.N., and Nikolos I.K., Using the DLR-F6 aircraft model for the evaluation of the academic CFD code "Galatea", *Proceedings of the 9th International Conference on Engineering Computational Technology, ECT 2014*, Naples, Italy, 2-5 September 2014.

[Lyg15] Lygidakis G.N., and Nikolos I.K., Numerical analysis of flow over the NASA Common Research Model using the academic Computational Fluid Dynamics code *Galatea*, *ASME Journal of Fluids Engineering*, Vol. 137, 071103-1, 2015.

[Lyg15a] Lygidakis G.N., On the numerical solution of compressible fluid flow and radiative heat transfer problems, *Technical University of Crete*, 2015.

[Lyg16] Lygidakis G.N., Sarakinos S.S, and Nikolos I.K., Comparison of different agglomeration multigrid schemes for compressible and incompressible flow simulations, *Advances in Engineering Software*, Vol. 101, pp. 77-97, 2016.

[Lun15] Lunan D. A., Waverider, a revised chronology, *20th AIAA International Space Planes and Hypersonic Systems and Technologies Conference*, 2015.

[Lum91] Lumpkin F.E., Haas B.L., and Boyd I.D., Resolution of differences between collision number definitions in particle and continuum simulations, *Physics of Fluids A: Fluid Dynamics*, vol 3(9), pp. 2282-2284, 1991.

[Mac65] Mack L.M., Computation of the stability of compressible laminar boundary layer, *In: Alder, B., Fernbach, S., Rotenberg, M. (Eds.) Methods in Computational Physics*, vol. 4, pp. 247–299, 1965.

[Mac66] Mack L.M., Boundary layer stability theory, *report 900-277 rev. a. Jet Propulsion Laboratory*, Pasadena, 1969.

[Mac84] Mack L.M., Boundary layer linear stability theory, *AGARD Report R-709* 1984.

[Mar07] Marxen O., Iaccarino G., and Shaqfeh E.S.G, Numerical simulation of hypersonic boundary layer instability using different gas models, *Center of Turbulence Research, Annual Research Briefs 2007*, pp. 15-27, 2007.

[Max79] Maxwell J.C., On stresses in rarified gases arising from inequalities of temperature, *Philosophical Transactions of the Royal Society*, vol. 170, pp. 231-256, 1879.

[Mil01] https://www.af.mil/About-Us/Fact-Sheets/Display/Article/104467/x-51a-waverider

[Mil63] Millikan R.C., and White D.R., Systematics of vibrational relaxation, *The Journal of chemical physics*, vol. 39(12), pp. 3209-3213, 1963.

[Mos05] Moss J.N., and Bird G.A., Direct simulation Monte Carlo simulations of hypersonic flows with shock interactions, *AIAA Journal*, vol. 43, pp. 2566-2573, 2005.

[Mul19] Mullen C. D., Turbeville F. D., Reed H. L., and Schneider S. P., Computational and experimental boundary-layer stability analysis on a hypersonic finned cone, *AIAA SciTech 2019 Forum*, *AIAA Paper 2019–1381*, 2019.

[Mun98] Munson B.R., Young D.F., and Okiishi T.I., Fundamentals of Fluid Mechanics, *John Wiley & Sons, Inc.*, New York, 1998.

[Mur69] Murman E.M., Experimental studies of a laminar hypersonic cone wake, *AIAA Journal*, 7(9), pp 1724-1730, 1969.

[Myo01] Myong R.S., A computational method for Eu's generalized hydrodynamic equations of rarefied and microscale gas dynamics, *Journal of Computational Physics*, vol. 168, pp. 47-72, 2001.

[Myo04] Myong R.S., A generalized hydrodynamic computational model for rarefied and microscale diatomic gas flows, *Journal of Computational Physics*, vol. 195, pp. 655-676, 2004.

[Myo05] Myong R.S, Reese J.M., Barber R.W. and Emerson D.R., Velocity slip in microscale cylindrical Couette flow: The Langmuir model, *Physics of Fluids*, vol. 17, pp. 87-105, 2005.

[Ott01] Otten H.B.A., Preliminary computational investigation on aerodynamic phenomena on DELFT aerospace reentry test vehicle, *Proceedings of the 4th Symposium on Aerothermodynamics for Space Applications*, Capua, Italy, October 2001, pp. 207-213, 2001.

[Osh84] Osher S., Riemann Solvers, the Entropy Condition and Difference Approximations, *SIAM Journal on Numerical Analysis*, vol. 21, pp. 217-235, 1984.

[Par18] Parks G. T., Developments and challenges in the coupling of DSMC and CFD, *Progress in Aerospace Sciences*, vol. 102, 1-23. doi: 10.1016/j.paerosci.2018.05.001

[Pec23] Peck M. M., Riha A. K., Reed H. L., Klothakis A., Dylewicz K., and Theofilis V., Comparative Studies on the Hypersonic Finned Cone, *AIAA SCITECH 2023 Forum*, pp. 0859, 2023.

[Pez16] Pezzella G., and Viviani A., Aerodynamic performance analysis of a winged re-entry vehicle from hypersonic down to subsonic speed, *Aerospace and Science Technology*, vol. 52, pp. 129–143, 2016.

[Pra17] Prakash P.K.S., and Ra A.S.K., R Deep Learning Cookbook, *PACKT*, 2017.

[Roe91] Roe P., Approximate Riemann Solvers, Parameter Vectors and Difference Schemes, *Journal of Computational Physics*, vol. 43, pp. 357-371, 1981.

[Qui17] Quintanilha H. Jr., Santos R., Alves L.S., and Theofilis V., Distributed solution of global eigenvalue problems on large clusters, *23rd AIAA Computational Fluid Dynamics Conference*, AIAA, 2017.

[Qui19] Quintanilha H. Jr., Theofilis V., and Hanifi A., Global transient-growth analysis of hypersonic flow on the HIFiRE-5 elliptic cone model, *AIAA Scitech 2019 Forum*, 2019.

[Qui21] Quintanilha H. Jr., Linear global nonmodal instability analysis of high-speed flows, *PhD thesis*, University of Liverpool, 2021.

[Red02] Reda D. C., Review and synthesis of roughness-dominated transition correlations for reentry applications, *Journal of spacecraft and rockets*, vol 39(2), pp. 161-167, 2002.

[Rov98] Roveda R, Goldstein D.B., and Varghese P.L., Hybrid Euler/particle approach for continuum/rarefied flows, *Journal of spacecraft and Rockets*, vol. 35(3), pp. 258-265, 1998.

[Rov00] Roveda R., Goldstein D.B., and Varghese P.L., Hybrid Euler/direct simulation Monte Carlo calculation of unsteady slit flow, *Journal of spacecraft and Rockets*, vol. 37(6), pp. 753-760, 2000.

[Row09] Rowley, C. W., Mezić, I., Bagheri, S., Schlatter, P., and Henningson, D. S., Spectral analysis of nonlinear flows, *Journal of fluid mechanics*, vol. 641, pp. 115–127, 2009.

[San09] Santos W.F., Bluntness impact on lift-to-drag ratio of hypersonic wedge flow, *Journal of Spacecraft and Rockets*, vol. 46(2), pp. 329-339, 2009.

[Sar14] Sarakinos S.S., Lygidakis G.N., and Nikolos I.K., Acceleration strategies for simulating compressible and incompressible flows, *Proceedings of the 4th International Conference on Parallel, Distributed, Grid and Cloud Computing for Engineering, PARENG 2015*, Dubrovnik, Croatia, 24-27 March 2015.

[Sav64] Savitzky A., and Golay M.J.: Smoothing and differentiation of data by simplified least squares procedures, *Analytical Chemistry*, vol 36(8), pp 1627–1639, 1964.

[Saw21] Sawant S.S., Levin D.A., and Theofilis V., A kinetic approach to studying low-frequency molecular fluctuations in a one-dimensional shock, *Physics of fluids*, vol. 33, pp. 104-106, 2021.

[Saw22] Sawant S.S., Theofilis V., and Levin D.A., On the synchronization of three-dimensional shock layer and laminar separation bubble instabilities in hypersonic flow over a double wedge, *Journal of Fluid Mechanics*, 941, 2022.

[Sch08] Schneider S. P., Effects of roughness on hypersonic boundary-layer transition. Journal of spacecraft and rockets, vol 45(2), pp 193-209, 2008.

[Sch10] Schmid P.J., Dynamic mode decomposition of numerical and experimental data. *Journal of fluid mechanics*, vol. 656, pp. 5-28, 2010.

[Sch11] Schmid P.J., Li L., Juniper M.P., and Pus, O., Applications of the dynamic mode decomposition. *Theoretical and computational fluid dynamics*, vol. 25, pp. 249-259, 2011.

[Sch06] Schwartzentruber T.E., and Boyd I.D., A hybrid particle-continuum method applied to shock waves, *Journal of Computational Physics*, vol. 215(2), pp. 402-416, 2006.

[Sch07] Schwartzentruber T.E., Scalabrin L.C., and Boyd I.D., A modular particle continuum numerical method for hypersonic nonequilibrium gas flows, *Journal of Computational Physics*, volume 225(1), pp 1159-1174, 2007.

[Sch07a] Schwartzentruber T.E., Scalabrin L.C., and I.D. Boyd, Modular implementation of a hybrid DSMC-NS solver for hypersonic non-equilibrium flows, *45th AIAA Aerospace Sciences Meeting and Exhibit*, paper 2007-613, 2007.

[Sch08a] Schwartzentruber T.E., Scalabrin L.C., and Boyd I.D., Hybrid particle-continuum simulations of nonequilibrium hypersonic blunt-body flowfields, *Journal of Thermophysics and Heat Transfer*, vol. 22(1), pp. 29-37, 2008.

[Sch08b] Schwartzentruber T.E., and Boyd I.D., Multiscale particle-continuum simulations of hypersonic flow over a planetary probe, *Journal of Spacecraft and Rockets*, volume 45, pp. 1196-1206, 2008.

[Sch08c] Schwartzentruber T.E., and Boyd I.D**.,** Hybrid particle continuum simulations of hypersonic flow over a hollow-cylinder-flare geometry, *AIAA Journal*, vol. 46(8), pp. 2086-2095, 2008.

[Ser12] Serdar Seckin, Flow visualization of a scramjet inlet-isolator model in supersonic flow, *B.Sc. Thesis, Istanbul Technical University*, 2012.

[She05] Shen C., Rarefied gas dynamics, *Springer*, Berlin Heidelberg, 2005.

[Sho14] Shoja-Seni A., Roohi E., Kahrom M. and Stefanov S., Investigation of aerodynamic characteristics of rarefied flow around NACA0012 airfoil using DSMC and NS solvers, *European Journal of Mechanics B/Fluids*, vol. 48, pp. 59-74, 2014.

[Smo98] von Smoluchowski M., Über Wärmeleitung in verdünnten Gasen. *Annalen der Physik*, vol. 300, pp. 101–130, 1898.

[Sor03] Sorensen K.A. O., Morgan H.K., and Weatherill N.P., A Multigrid accelerated hybrid unstructured mesh method for 3D compressible turbulent flow, *Computational Mechanics*, vol. 31, pp. 101-114, 2003.

[SPARTA21] SPARTA Code commands Manual, SPARTA Release November 21, 2021.

[Sun05] Sun Q., and Boyd I.D, Evaluation of macroscopic properties in the direct simulation Monte Carlo method, *Journal of Thermophysics and Heat Transfer*, vol. 19(3), pp. 329-335, 2005.

[Ste15] Stevanovic N.D., and Djordjevic V.D., An exact analytical solution for the second order slip-corrected Reynolds lubrication equation, *FME Transactions*, vol. 43, pp. 16-20, 2015.

[Str05] Struchtrup H., Macroscopic Transport Equations for Rarefied Gas Flows, *Springer Berlin Heidelberg*, 2005.

[Sut93] Sutherland W., LII. The viscosity of gases and molecular force. *The London, Edinburgh, and Dublin Philosophical Magazine and Journal of Science*, vol. 36(223), pp. 507-531, 1893.

[Swe84] Sweby P.K., High Resolution Schemes Using Flux Limiters for Hyperbolic Conservation Laws, *SIAM Journal on Numerical Analysis*, vol. 21, pp. 995-1011, 1984.

[Tai17] Taira K., Brunton S. L., Dawson S. T., Rowley C. W., Colonius T., McKeon B. J. Schmidt, O. T., Gordeyev S., Theofilis V., and Ukeiley L. S., Modal analysis of fluid flows: An overview, *AIAA Journal*, vol. 55(12), pp. 4013–4041, 2017.

[Tay64] Taylor R.L., Melcher B.W., and Washburn W.K., Studies of the luminous hypersonic wake, *AIAA Journal*, 2(10), 1964.

[The00] Theofilis V., On steady-state flow solutions and their nonparallel global linear instability, *Advances in turbulence VIII*, pp 35-38, 2000.

[The11] Theolifis V., Global linear instability, *Annual Reviews in Fluid Mechanics*, vol. 43, pp. 319-352, 2011.

[The20] Theofilis V., Massively parallel solution of the global linear instability non-symmetric complex generalized eigenvalue problem. *60th Israel Annual Conference on Aerospace Sciences (IACAS)*, 2020.

[Tin94] Tincher D. J., and Burnett D. W., Hypersonic waverider test vehicle-a logical next step, *Journal of Spacecraft and Rockets*, vol. 31(3), pp. 392-399, 1994.

[Tor97] Toro E.F., Riemann Solvers and Numerical Methods for Fluid Dynamics. A Practical Application. 2nd Edition, Springer, 1997.

[Tum18] Tumuklu O., Levin D. A., and Theofilis V., Investigation of unsteady, hypersonic, laminar separated flows over a double cone geometry using a kinetic approach, *Physics of Fluids*, vol. 30(4), 2018.

[Tur18] Turbeville F. D., and Schneider S. P., Boundary-layer instability on a slender cone with highly swept fins, *Fluid Dynamics Conference*, *AIAA Paper 2018–3070*, 2018.

[Tur18a] Turbeville F. D., Parametric study of a 7 half-angle cone with highly-swept fins at Mach 6, *Master's thesis*, Purdue University, 2018.

[Tur19] Turbeville F. D., and Schneider, S. P., Transition on a cone with a highly-swept fin at Mach 6, *AIAA Aviation 2019 Forum*, *AIAA Paper 2019–3217*, 2019.

[Tur21] Turbeville F. D., Measurements of transition in the corner formed by a highly-swept fin and a cone at Mach 6, *Ph.D. thesis*, Purdue University, 2021.

[Van82] Van Albada G.D., Van Leer B. and Roberts W.W., A Comparative Study of Computational Methods in Cosmic Gas Dynamics, *Astronomy and Astrophysics*, vol. 108, pp.46-84, 1982.

[Ven95] Venkatakrishnan V., Implicit Schemes and Parallel Computing in Unstructured Grid CFD, *Proceedings of the 26th Computational Fluid Dynamics Lecture Series Program*, Von Karman Institute for Fluid Dynamics, Rhode, Saint-Genese, Belgium,13-17 March 1995.

[Vin75] Vincenti W.G., Introduction to physical gas dynamics, *Huntington*, 1975.

[Viv20] Viviani A., Aprovitola A., Iuspa L., and Pezzella G., Aeroshape design of reusable re-entry vehicles by multidisciplinary optimization and computational fluid dynamics, *Aerospace and Science Technology*, vol 105, 2020.

[Vol06] Voland R. T., Huebner L. D., and McClinton C. R., X-43A Hypersonic vehicle technology development, *Acta Astronautica*, vol. 59, pp. 181-191, 2006.

[Vos10] Vos J.B. and Sanchi S., DPW4 Results Using Different Grids Including Near-Field/Far-Field Drag Analysis, *Proceedings of the 28th AIAA Applied Aerodynamics Conference*, Chicago, Illinois, USA, AIAA 2010-4552, 2010.

[Vos13] Vos J.B., Sanchi S. and Gehri A., Drag Prediction Workshop 4 Results Using Different Grids Including Near-Field/Far-Field Drag Analysis, *Journal of Aircraft*, vol. 50, pp. 1615-1627, 2013.

[Vou18] Voulodimos A., Doulamis N., Doulamis A., and Protopapadakis E., Deep learning for computer vision: a brief review, *Computational Intelligence and Neuroscience*, vol 66, 2018.

[Wag92] Wagner W., A convergence proof for Bird's direct simulation Monte Carlo method for the Boltzmann equation, *Journal of Statistical Physics*, vol. 66, pp. 1011-1044, 1992.

[Wan03] Wang W.L., and Boyd I., Hybrid DSMC-CFD simulations of hypersonic flow over sharp and blunted bodies, *In 36th AIAA thermophysics conference*, paper 2003-3644, Orlanda, FL, 2003.

[Whi96] Whiting E.E., Park C., Arnold J.O., and Paterson J.A., NEQAIR96, nonequilibrium and equilibrium radiative transport and spectra program, *user's manual*, NASA Reference publication 1389, 1996.

[Wij04] Wijesinghe H.S., Hornung R.D., Garcia A.L., and Hadjiconstantinou N.G., Three-dimensional hybrid continuum-atomistic simulations for multiscale hydrodynamics, *Journal of Fluids in Engineering*, vol. 126(5), pp. 768-777, 2004.

[Wil99] Wilmoth R.G., Mitcheltree R.A., and Moss J.N., Low-density aerodynamics of the stardust sample return capsule, *Journal of Spacecraft and Rockets*, vol. 42, pp. 436-441, 1999.

[Whi05] White F., Viscous Fluid Flow, *3rd edition McGraw-Hill*, 2005.

[Wys98] Wysong I.J., and Wadsworth D.C., Assessment of direct simulation Monte Carlo phenomenological rotational relaxation models. *Physics of Fluids*, vol. 10(11), pp. 2983-2994, 1998.

[Zha12] Zhang W.M., Meng G., and Wei X., A review on slip models for gas microflows, *Microfluidics and Nanofluidics*, vol. 13, pp. 845-882, 2012.

[Zho08] Zhong J., Ozawa T., and Levin D.A., Modeling of the stardust reentry ablation flows in the near-continuum flight regime, *AIAA Journal*, pp. 2568-2581, 2008.

[Zup14] Zuppardi G., Morsa L., Sippel M., and Schwanekamp T., Aero-thermodynamic analysis of the spaceliner-7.1 vehicle in high altitude flight, *Proceedings of the 29th International Symposium on Rarefied Gas Dynamics*, AIP Conference, Proceedings, vol. 1628, pp. 1268–1276, 2014.